

University of Nottingham

UK | CHINA | MALAYSIA

Robust Quantification of Cerebrovascular Reactivity using Magnetic Resonance Imaging and Hypercapnic Challenges

Thesis submitted to the University of Nottingham for the degree of Doctor of Philosophy, **January 2025**

Colette Clare Milbourn

20031322

Supervisors:

Dr. Nicholas P. Blockley

Prof. Paul L. Greenhaff

School of Life Sciences

University of Nottingham

0.1 Lay Abstract

How is the hose like a human brain? And more importantly why do we care? The hose is a long tubey thing which has fluid flowing through it and most importantly has a mechanism to control the flow - the nozzle Fig. 1. Under normal conditions you water the flowers, and they might survive without much water. However, during stress, e.g. a heatwave, you need to adjust the nozzle to increase water supply to the flowers or they will die. If the nozzle is broken it can't increase flow to match demand. It is important to work out what the problem is with the nozzle to save the flowers. However, if we were to cut it open then that would be the end of your hose. So what if we could measure a quantitative value for the quality of the hose nozzle, the mechanism that controls the flow? The same principle applies to the human brain. Here, the long tubey blood vessels deliver nutrients in the blood to the brain cells. Just as the nozzle of the hose opens and closes to adjust water flow, the blood vessels in the brain also expand and contract, and it can struggle to keep up with demand in ageing and disease. However, I'd really like to see what is going on inside your head without having to cut it open, and that is where brain scanners come in. Images from clinical brain scanners can look 'healthy' when the brain is at rest, and it's not until the brain is physically stressed that we see there is a problem keeping up with demand. My research involves using a special kind of brain scanning technique called Magnetic Resonance Imaging (MRI). This technique is used to quantify and map blood flow in the brain tissue, making scans more robust for clinical use. For brain diseases, this is especially important considering that 90% of strokes are considered to be preventable. My studies scanned healthy adults, giving them carbon dioxide (CO_2) to breathe to slightly stress the brain, and quantifying the blood flow in the brain tissue. I have also been optimising different scanner settings to make

the measurements more robust. Ideally, we would also be able to calibrate these scans to be able to check blood flow in the brain tissue without having to use any kind of extra kit, task or stressor at all, which is why I have been using more advanced data analysis methods.

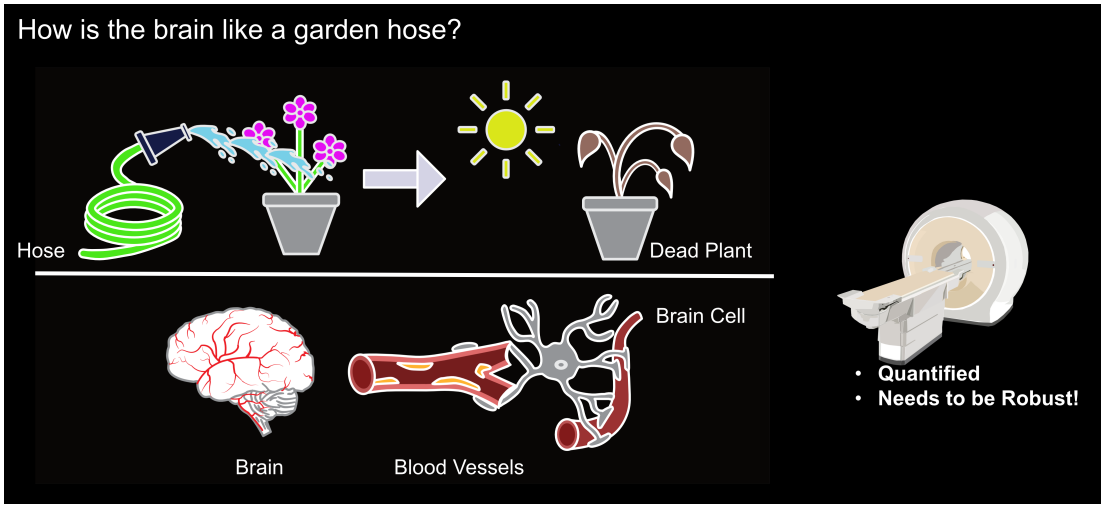


FIGURE 1: **Lay Visual Abstract.** Analogy of how the brain is like a garden hose, and how MRI can help us measure markers of brain health.

0.2 Abstract

Pseudocontinuous Arterial Spin Labelling (pCASL) magnetic resonance imaging (MRI) can quantify tissue cerebral blood flow (CBF) in the brain, providing a potential clinical biomarker of brain health. A cerebrovascular reactivity (CVR) response can be induced by increasing blood flow via a vasoactive stimulus, e.g. inhaling carbon dioxide during hypercapnic challenges. The overall aim of this thesis was to validate robust measures of CVR using MRI. Multiple investigations examined blood flow changes, magnetic field effects, pharmacological interventions, and advanced CVR analysis methods.

Findings demonstrated that pCASL blood flow measurements showed significant parameter dependent variations during hypercapnic challenges, with notable regional CBF variation. Magnetic field investigations revealed modest B_0 changes during hyperventilation and optimal B_1 field characteristics at the V3 vertebral artery segment.

A pharmacological intervention study examined the effects of anti-hypertensive medication during hypercapnic challenges. This was to alter the blood pressure and see what affect it had on CVR. While these interventions induced expected heart rate changes, they did not significantly alter blood pressure or carotid artery blood flow, suggesting robust compensatory mechanisms in healthy individuals.

Advanced CVR measurement techniques were explored using multiple post labelling delay "enhanced" ASL (eASL) and blood oxygen level dependent (BOLD) MRI, with a novel semi-automated gas delivery box. The eASL data

showed a substantial CVR response (∼60% increase in CBF, ∼22 s decrease in arterial transit time) during hypercapnia, which was a larger change than recent studies. The dynamically modelled BOLD (dCVR) analysis of the haemodynamic response function showed a 3.2% increase in magnitude. However, the processing was computationally intensive.

A study into the comparison of eASL, sinusoidal modelled BOLD CVR (sinCVR), and dCVR analyses showed no correlation between eASL and BOLD-based magnitude measures. There was a weak correlation between eASL and sinCVR timing metrics. sinCVR and dCVR magnitude were strongly positively correlated, whilst their timing metrics were weakly negatively correlated. This suggested the relationship between the different methods and physiology would require further investigation.

In conclusion, recent developments in acquisition and analysis of functional MRI were combined to resolve issues regarding CVR quantification. The intended impact was to improve the robustness of CVR results for diagnosis and prognosis of patients with cerebrovascular diseases.

0.3 Peer Reviewed Journal articles in preparation

1. **Milbourn, C. C.**, Francis S. T., Okell T., and Blockley, N. P., Moving Towards Robust Quantification of Cerebrovascular Reactivity using a Hypercapnia Challenge and Pseudocontinuous Arterial Spin Labelling. *In Preparation.*

0.3.1 Accepted Abstracts

1. **Milbourn, C. C.**, Rieger S. W., and Blockley, N.P., Multi Post Label Delay pCASL-MRI with a Semi-automated Gas Delivery System to Measure Cerebrovascular Reactivity via Hypercapnia (2023). Imaging Cerebral Physiology, 2023, Utrecht, Netherlands.

2. **Milbourn, C. C.**, Shams, S., and Chen, J.J., Age-related Differences in Dynamic Cerebrovascular Reactivity Based on CO_2-Response Modelling (2023). Organisation for Human Brain Mapping (OHBM) 2023, Montreal, Canada.

3. **Milbourn, C. C.**, Shams, S., and Chen, J.J., A Age-related Differences in Dynamic Cerebrovascular Reactivity Based on CO_2-Response Modelling (2023). International Society for Magnetic Resonance in Medicine (ISMRM) Annual Scientific Meeting 2023, Toronto, Canada.

4. **Milbourn, C. C.** and Blockley, N.P., Investigating Systematic Error in pseudocontinous Arterial Spin Labelling estimates of Cerebrovascular Reactivity (2023). ISMRM Annual Scientific Meeting 2023, Toronto, Canada.

5. **Milbourn, C. C.** and Blockley, N.P., Improving Measures of Cerebrovascular Reactivity using a Sinusoidal Hypercapnic Challenge and Dual-echo pseudocontinuous ASL (2022). ISMRM Annual Scientific Meeting 2022, London, England.

6. **Milbourn, C. C.**, Okell, T.W., and Blockley, N.P., Moving Towards Robust Quantification of Cerebrovascular Reactivity using pseudocontinuous ASL (2021). ISMRM Annual Scientific Meeting 2021, Online/ Vancouver, Canada.

Acknowledgements

First, of course thank you to my supervisors Dr Nicholas Blockley and Prof Paul Greenhaff.

I would like to gratefully acknowledge the funding support from the Bioscience and Bioscience Technology Research Council.

Many thanks to all of those who helped with the studies. Each of the chapters has a detailed break down of contributions to the chapter, but a special thank you to those at the Sir Peter Mansfield Imaging Centre and David Greenfield Human Physiology Unit, who helped with all aspects of these studies. Especially, Dr Natalie Shur, Dr Joseph Cullen, Dr Ayushman Gupta, Dr Abhishek Sheth, and Aline Nixon for the medical cover on the physiology study. Mia Keaton, Dr Joanne Mallinson, Melanie Marshall and Sara Brown who took bloods during the medical screenings. Andrew Cooper and Jan Paul for helping with MR training and scanning.

A huge thanks to Prof Jean Chen (and the Cranium lab) who hosted me for the Mitacs Globalink exchange programme, everyone who made me feel at home in Toronto, and Cerca Magnetics for hosting my professional internship placement.

x
Thanks to all the study volunteers who generously gave their time to make this research possible.

Thank you to the (extended) barn staff and students who helped motivate me throughout the writing process.

A heartfelt thank you to my dear friends and family, who have kept me going throughout. Especially, my Leicester lot, Cambridge Crew, and Claire for being the best friend and housemate I could ask for, providing tea, baked goods and TV time. Kalpana Tagore (who has been asking to read this since before I started the PhD), and Anna Lee for helping me, body and mind through various yoga and philosophies.

To my parents, and brothers, though especially my Mum, for putting up with reading and countless edits on Overleaf. To my grandparents for always supporting and inspiring me.

For Molly, forever in my heart.

COVID-19 Statement

0.4 COVID-19 Impact Statement

Initial Project Disruption The Biotechnology and Bioscience Research Council Doctoral Training Programme (BBSRC DTP) comprised three 6-week projects, from which students would select one for their main three-year PhD project. I started my third rotation in early March 2020. Due to COVID-19 restrictions, face-to-face data collection ceased during the week of 16th March 2020. The DTP cancelled the remainder of the rotation two weeks in, requiring students to select their main project within a few days. The University closed before the government lockdown, and students were advised to relocated to their permanent home addresses. My relocation to Cambridge (20th March 2020 – 20th April 2021) lasted longer than expected, with all work conducted online. The uncertainty of reopening complicated workload planning.

Facility Access and Equipment Challenges COVID-19 restrictions meant no study visits could take place at Sir Peter Mansfield Imaging Centre (SPMIC)from mid-March 2020 until April/May 2021, a time period of 13 months without being able to recruit any new participants or develop study protocols etc. Although funding for the project that had started during my second rotation had started before lockdown (supervised by Dr. Nicholas Blockley), and was extended to July 2020, this extension proved insufficient as in-person studies had not yet resumed. The study originally was to compare younger (18-30 years) to older

(50-60 years) age groups. However, there were strong ethical concerns about recruiting older vulnerable groups or patients. Therefore, it was decided that the project would no longer involve scanning older adults or carotid stenosis / stroke patients and became more methods focused.

In March 2020, BOC (supplier) recalled the medical gas cylinders needed for the hypercapnic challenges to be redistributed to hospitals. The project involved additional COVID-19 risks associated with the breathing apparatus and gas mixtures. Despite modifications, initial restrictions prevented gas challenges, or any cohorts outside of young, healthy adults. Upon reopening, SPMIC scanner availability was reduced due to 30-minute cleaning protocols between sessions, and a significant backlog of researcher demands on the booking system. As a new data collection project, my scanning time received a lower priority status. This delayed starting the first new scanner project until November 2021.

A physiological project began being planned in January 2021, to mitigate the problems with scanner access, but also encountered setbacks. Medical support in the David Greenfield Human Physiology Unit lapsed over lockdown, and the appointment of a new medical support clinical fellow was delayed, due to a university recruitment freeze. Extended NHS honorary contract processing postponed this recruitment further, until 15th June 2021. Supply chain delays affected equipment and pharmaceutical supplies. Participant recruitment was also difficult when in-person contact was still restricted, hence the medical screening for this project did not start until autumn 2021. Additional delays occurred in summer of 2022, when the medic left, which lead to a lack of medical cover, and another prolonged recruitment period.

After finally collecting the first three data scanner sets, the Gen 3 RespirAct^{TM}

failed, therefore that study was not included in this work, due to such a small dataset. Maintenance of this model was no longer supported, and there were no funds for a new one. Due to global supply shortages of basic electronic equipment, components and other commitments for my supervisor, it took Nic over two years to put together the new semi-automated gas delivery device made to replace the RespirAct^{TM} (Chapter 4 and 5).

Collaborations I applied to the Mitacs UK-Canada Globalink exchange programme in 2020/2021, which was postponed until travel restrictions for both UK and Canada were lifted. The university policy travel restrictions were until May 2022. I was able to get an extension on the funding for this and was able to attend Aug-Oct 2022. However, this meant that I did not learn the new analysis methods until much later in my PhD than planned. As a geriatric hospital, there were still many restrictions on data collection at Baycrest. During this time, with only a recent start to transition back to in-person workplace, the project moved to be data analysis focused. This placement had been timed to coincide with the global conference of the ISMRM in Vancouver, Canada in May 2021, which was moved entirely online. This impacted planned collaborations with other Canadian researchers.

Further impacts included my main supervisor's transition to one day per week from February 2023, and his move to more remote working for the preceding year.

Personal health issues, including COVID-19 infections, required a couple of months of leave in early 2022 and summer 2023.

Overall, the PhD did not exactly go as planned.

Anyway, here's a photo of my dog Molly 'woof-ing from home' to cheer you up after all that:



Contents

Abstract **ii**

0.1 Lay Abstract ii

0.2 Abstract iv

0.3 Peer Reviewed Journal articles in preparation vi

0.3.1 Accepted Abstracts vi

Acknowledgements **ix**

xi

0.4 COVID-19 Impact Statement xi

List of Figures **xxix**

List of Tables **lvii**

List of Abbreviations **lxiii**

1 Introduction **1**

1.1 Introduction to Cerebrovascular Reactivity 1

1.1.1 Cerebral Architecture 4

1.1.2 Cerebroautoregulation 7

1.1.3 Cerebrovascular Disease 9

1.2 Vasodilatory Stimuli 10

1.3 Theory of MR 13

1.3.1 Nuclear Magnetic Resonance 14
1.3.2 Nuclear Spin Angular Momentum 14
1.3.3 Quantum Energy States and Population Distribution . . 16
1.3.4 Quantum Transitions and Resonance 18
1.4 Classical Electromagnetic Behaviour 19
1.4.1 Classical Magnetisation Vector 19
1.4.2 Classical RF Excitation 22
1.4.3 Classical Relaxation Processes 24
T_1 Relaxation (Spin-Lattice) 24
T_2 Relaxation (Spin-Spin) 26
T_2* Decay (Free Induction Decay) 26
1.5 Pulse Sequences and Signal Generation 29
1.5.1 Spin Echo Sequences 29
1.5.2 Gradient Echo Sequences 31
1.5.3 Inversion Recovery Sequences 33
1.6 MR Hardware 34
1.7 IMAGING 38
1.7.1 Creating an Image 38
1.8 Functional MRI for Imaging Blood Flow in the Brain 39
1.8.1 Arterial Spin Labelling 40
pseudo-Continuous Arterial Spin Labelling 47
Balanced and Unbalanced pCASL 47
Multiple Post Labelling Delay ASL 50
Time-encoded MPLD ASL 53
1.8.2 Blood Oxygen Level Dependent Imaging 55
Haemodynamic Response Functions 59
Deconvolution 64

1.8.3 Phase Contract Velocity 68
1.9 Applications of fMRI CVR 69
1.9.1 Issues with CVR Measurements 74
1.10 Aims and Outline of the Thesis: 77
1.11 Overview of the Chapters 79

2 Optimising Robust Quantification of Cerebrovascular Reactivity using Pseudocontinuous ASL 81

2.1 Contributions to the Chapter 82
2.2 Visual Abstract 84
2.3 Introduction 85
2.3.1 ASL Parameters 86
ASL Preparation Parameters 87
2.3.2 Magnetic Field Inhomogeneity 88
2.4 Aims of the Study 92
2.5 Hypotheses 92
2.6 Methods 93
2.6.1 Ethics Approval and Participant Recruitment 93
2.6.2 Respiratory Stimulus 95
2.6.3 MR Imaging 103
Safety Requirements 103
MR Protocols 103
Image Analysis 108
2.6.4 Statistical Analysis 113
2.7 Results 114
2.7.1 Respiratory Stimulus 114
2.7.2 MR Imaging 116
Part 1 Effect of Hypercapnia on Different pCASL Parameters 116

Part 1 Effect of Hypercapnia on PCV across Arteries . . . 117
Part 2 Effect of Hyperventilation on B_0 . . . 120
Part 2 Effect of Labelling Plane Placement on B_1 . . . 122
2.8 Discussion . . . 124
2.8.1 Respiratory Stimulus . . . 124
2.8.2 pCASL: Systematic Variations in CVR Measured with Different pCASL Parameters . . . 125
2.8.3 PCV: Investigations of Potential Sources of Systematic Error due to Blood Velocities . . . 126
2.8.4 B_0: Investigations of Potential Sources of Systematic Error due to Hyperventilation . . . 127
2.8.5 B_1: Investigations of Potential Sources of Systematic Error due Placement of the Labelling Plane . . . 128
2.8.6 Limitations . . . 129
2.8.7 Conclusion . . . 130

3 Investigating the Effect of Pharmacological Interventions on Blood Pressure and Velocity during a Hypercapnic Challenge 133
3.1 Contributions to the Chapter . . . 134
3.2 Visual Abstract . . . 136
3.3 Introduction . . . 137
3.3.1 Blood Pressure as a Measure of Blood Flow . . . 137
3.3.2 Finger Cuff Methods of Measuring BP . . . 137
3.3.3 Problem: Understanding How Changes in BP Affect Cerebrovascular Reactivity . . . 138
3.3.4 Interventions to Model Changes in Blood Pressure . . . 138
3.3.5 Glyceryl Trinitrate – GTN . . . 139
3.3.6 Metoprolol - MET . . . 139

3.3.7 Aims of the Study . . . 140
3.3.8 Hypotheses . . . 141
3.4 Methods . . . 142
3.5 Participants . . . 142
3.6 Data Collection . . . 144
3.6.1 Study Day Design . . . 144
3.6.2 Dinamap Physiological Measurements . . . 146
3.6.3 Ultrasound . . . 148
3.6.4 Finapres . . . 151
3.6.5 Gases and Gas Analyser . . . 154
3.6.6 Gas Cylinders Setup . . . 154
3.6.7 Breathing Circuit . . . 154
3.6.8 Hypercapnic Challenge Paradigm . . . 156
3.6.9 Interventions . . . 156
3.7 Baseline Measurements . . . 157
3.8 Data Analysis . . . 157
3.8.1 Dinamap and Ultrasound Analysis . . . 158
3.8.2 Finapres Data Analysis . . . 159
3.8.3 End-tidal Data Analysis . . . 160
3.9 Statistical Analysis . . . 162
3.10 Results . . . 163
3.11 Participant Characteristics . . . 163
3.11.1 Baseline Measurements . . . 164
3.11.2 Respiratory Stimulus . . . 165
3.12 The Impact of GTN and MET Interventions on Mean Arterial Blood Pressure, Carotid Artery Blood Velocity and Heart Rate Responses during Normocapnia . . . 166

3.12.1 Normocapnia: Mean Arterial Pressure 166
3.12.2 Normocapnia: Blood Velocity 170
3.12.3 Normocapnia: Heart Rate 173
3.13 The Impact of GTN and MET Interventions on Mean Arterial Blood Pressure, Carotid Artery Blood Velocity and Heart Rate Responses during the Hypercapnic Challenge 176
3.13.1 Difference during the Hypercapnic Challenge: Mean Arterial Pressure 176
3.13.2 Difference during the Hypercapnic Challenge: Velocity . 178
3.13.3 Difference during the Hypercapnic Challenge: Heart Rate 180
3.14 Percentage Difference 182
3.14.1 Percentage Difference during Hypercapnic Challenge: Mean Arterial Pressure 182
3.14.2 Percentage Difference during Hypercapnic Challenge: Velocity Maximum 184
3.14.3 Percentage Difference during Hypercapnic Challenge: Heart Rate 185
3.15 Discussion 186
3.15.1 Pharmacological Interventions Did Not Alter Mean Arterial Blood Pressure or Carotid Artery Blood Velocity, but Did Alter the Heart Rate. 186
GTN Effect on Blood Pressure during Normocapnia . . . 187
GTN Effect on Blood Flow Velocity during Normocapnia 188
GTN Effect on Heart Rate during Normocapnia 189
MET Effect on Blood Pressure during Normocapnia . . . 190
MET Effect on Carotid Artery Blood Flow Velocity during Normocapnia 191

MET Effect on Heart Rate during Normocapnia 191
3.16 Response to Hypercapnic Challenge
after Pharmacological Interventions 192
The Impact of a Hypercapnic Challenge on Mean Arterial
Blood Pressure 193
The Impact of a Hypercapnic Challenge Effect on Blood
Velocity 193
Hypercapnic Challenge Effect on Heart Rate 197
3.16.1 Limitations 197
Blood Pressure Measurements 197
Participants Physical Characteristics and Sample Size . . 198
Single Sex Sample 199
Use of a Placebo and Double Blind Trials 200
3.16.2 Conclusions 200

4 Implementation of Advanced CVR methods 203
4.1 Contributions to the Chapter 204
4.2 Visual Abstract 206
4.3 Introduction 207
4.3.1 ASL 208
Multiple Post Labelling Delay ASL 208
Labelling Plane Placement 210
Hypercapnic Challenge 211
Bayesian Inference Analysis 212
4.3.2 BOLD 214
Multiband BOLD 214
BOLD CVR analysis 216
4.3.3 dCVR Analysis 218

4.4 Aims of the study . . . 222
4.5 Methods . . . 224
4.6 Participants . . . 224
4.7 Data Collection . . . 226
4.8 Respiratory Stimulus . . . 226
4.9 Gases, Gas Analyser and Gas Delivery Box . . . 226
4.10 Hypercapnic Challenge Paradigm . . . 231
4.10.1 Part 1 eASL . . . 231
4.10.2 Part 2 BOLD . . . 231
4.11 MR . . . 234
4.11.1 MR Safety Requirements . . . 234
4.11.2 MR Kit . . . 234
4.11.3 MR Scan Protocols . . . 234
4.11.4 Part 1 eASL . . . 237
4.11.5 Part 2 BOLD . . . 238
4.12 Data Analysis . . . 238
4.12.1 End-tidal Data Analysis . . . 238
4.13 MR Image Analysis . . . 240
4.13.1 Grey Matter Mask ROIs . . . 240
4.13.2 Part 1 eASL - BASIL . . . 242
4.13.3 Part 2 BOLD – dCVR . . . 243
4.13.4 Statistical Analysis . . . 244
4.14 Results . . . 247
4.15 Hypercapnic Challenges . . . 247
4.15.1 Part 1, eASL Hypercapnic Challenges . . . 247
4.15.2 Part 2, BOLD Response to Hypercapnic challenge . . . 249
4.16 Results: MR . . . 251

4.16.1 Results: Part 1 eASL 251
Cerebrovascular Blood Flow 251
Cerebral Blood Volume 254
Arterial Transit Time 256
4.16.2 Results: Part 2 dynamically Modelled BOLD CVR 258
BOLD dCVR: Magnitude 258
BOLD CVR: Time to Peak 260
4.17 Discussion 261
4.17.1 Respiratory Stimulus 261
4.17.2 eASL 261
eASL CVR Measured at Normo- and Hypercapnic Conditions 262
eASL aCBV Measured at Normo- and Hypercapnic Conditions 263
eASL ATT Measured at Normo- and Hypercapnic Conditions 264
4.17.3 BOLD dCVR 265
BOLD dCVR Magnitude Measured with a pseudo-Sinusoidal Hypercapnic Challenge 265
Comparison of Different Magnitude Analysis Methods . 267
BOLD dCVR Timing Measured with a pseudo-Sinusoidal Hypercapnic Challenge 268
Comparison of Different Timing Metric Analysis Methods 269
4.17.4 Limitations 269
Standardisation of MPLD ASL Acquisition and Analysis 269
dCVR Analysis Requirements 271
4.17.5 Conclusions 273

5 Comparing the Effect of a Hypercapnic Challenge on eASL, sinCVR and dCVR 275

5.1 Contributions to the Chapter 276

5.2 Visual Abstract . . . 277
5.3 Introduction . . . 278
5.3.1 Comparing Two Different BOLD Analysis Models to eASL 278
5.3.2 Comparing Different Brain Regions . . . 280
5.3.3 Aims . . . 283
5.3.4 Hypothesis . . . 283
5.4 Methods . . . 284
5.4.1 Data Collection . . . 284
5.4.2 Data Analysis . . . 284
5.4.3 Masks for Regions of Interest . . . 284
5.4.4 Data Analysis for eASL . . . 284
5.4.5 Data analysis for sinCVR and dCVR . . . 285
5.4.6 Statistical Analysis . . . 289
5.5 Results . . . 290
5.5.1 Comparison of CVR Magnitude . . . 290
Comparison of eASL CVR and sinCVR Magnitude . . . 290
Comparison of CVR and dCVR Magnitude . . . 292
Comparison of sinCVR and dCVR Magnitude . . . 293
5.5.2 Comparison of Timing Measures . . . 294
Comparison of eASL ATT and sinCVR Phase . . . 294
Comparison of eASL ATT and dCVR TTP . . . 296
Comparison of sinCVR Phase and dCVR TTP . . . 297
5.6 Discussion . . . 298
5.6.1 Respiratory Stimulus . . . 298
5.6.2 Magnitude . . . 300
eASL vs. BOLD Magnitude . . . 300
sinCVR vs. dCVR Magnitude . . . 301

Comparing Data Analysis Methods 303
5.6.3 Timing Metrics 305
eASL vs. BOLD Timing 305
sinCVR Phase vs. dCVR TTP Timing 305
Comparing Data Analysis Methods 306
5.6.4 Limitations 308
Respiratory Stimulus 308
5.6.5 Acquisition Methods Limitations 310
5.6.6 Analysis Methods Limitations 311
Modelling the Physiology 312
5.6.7 Conclusions 316

6 Discussion **319**

6.1 Summary of Interest 319
6.2 Optimising Robust Quantification of Cerebrovascular Reactivity using pseudocontinous ASL 320
6.3 Investigating the Effect of Pharmacological Interventions on Blood Pressure and Velocity during a Hypercapnic Challenge 322
6.4 Implementation of advanced CVR methods 323
6.5 Comparing the Effect of a Hypercapnic Challenge on eASL, sinCVR and dCVR 325
6.6 General Limitations and Future Directions 328
6.6.1 Recommendations 329

A Professional Internship Programme Reflective Statement **335**

A.1 Professional Internship Placement Reflective Statement 335

B Appendix Chapter 2 **339**

B.1 Chapter 2 Methods 339

B.2 Chapter 2 Results . . . 348
B.2.1 Respiratory Stimulus . . . 348
B.2.2 PETCO$_2$ Data for pCASL Params-1, -2 and -3 . . . 348

C Appendix Chapter 3 **357**
C.1 Chapter 3: Methods and Materials . . . 357
C.1.1 Withdrawn Participants . . . 366
C.1.2 Lower Body Negative Pressure Device . . . 368
C.1.3 Ultrasound . . . 369
C.2 Chapter 3: Dinamap Results . . . 370
C.3 Chapter 3: Finapres Results . . . 372
C.4 Finapres: Does the Pharmacological Intervention influence the Normocapnic Condition? . . . 372
C.4.1 Finapres: Mean Arterial Pressure . . . 373
C.4.2 Finapres: Difference Between Control and Intervention Normocapnia Conditions: Mean Arterial Pressure . . . 377
C.4.3 Finapres: Heart Rate . . . 378
C.4.4 Finapres: Heart Rate Difference in Control and Intervention Normocapnia conditions . . . 379
C.5 Finapres: Does the Intervention have an effect on the change between Normocapnia and Hypercapnia during the Hypercapnic Challenge? . . . 382
C.5.1 Finapres: Difference during Hypercapnic Challenge: Mean Arterial Pressure . . . 382
C.5.2 Finapres: Difference during Hypercapnic Challenge: Heart Rate . . . 384

D Appendix **387**

D.1 Chapter 4 Appendix: Methods and Materials 387
D.2 Chapter 4 Appendix: Results 389
D.2.1 Summary of Chapter 4 Results: Respiratory Stimulus . . 389
D.2.2 Summary of Chapter 4 Results: MR 391

E Appendix Chapter 5 **395**

E.1 Chapter 5 Results 395

List of Figures

1.1 **Cerebrovascular Reactivity.** A stimulus induces a CVR response which can be measured using MRI and then quantitive CVR maps of blood flow in the brain tissue can be calculated. Cerebrovascular reactivity (CVR), Magnetic Resonance Imaging (MRI). 2

1.2 **Respiratory and Circulatory Systems.** Components of the Respiratory system (Lungs), Circulatory System (Heart and blood vessels) that transport oxygen and carbon dioxide to and from the brain are involved in and influenced by cerebrovascular reactivity (CVR). (Created using Biorender.com) 3

1.3 **Basic Overview of Brain Vasculature.** A. Sagittal view of the major brain blood vessels, and a closer look at the B. Brain Vasculature Endothelial Cells. (Created using Biorender.com) 5

1.4 **3D Brain Artery Atlas.** The left column ("level 1") shows subdivisions of biological importance, based on probabilistic maps and/or anatomical landmarks. The right column ("level 2") represents the major vascular territories. 3D (three dimensional), ACA (anterior cerebral artery), MCA (middle cerebral artery), PCA (posterior cerebral artery), thalamoperfurat. (thalamoperforating arteries), VB (Vertebro-Basilar arteries). Figure credit to Liu and colleagues (2023) [140], reproduced under the creative common's licence open-access). Changes made: added a title and edited the figure legend. 6

1.5 **Cerebroautoregulation.** Autoregulation Curve changes blood flow with dilation and constriction of blood vessels within set limits (based on Klabunde cvphysiology.com and [181]). B. Time course of PO_2 in the capillary. Changes in oxygen uptake along pulmonary capillaries under normal, abnormal and grossly abnormal conditions, where the latter two struggle to reach the baseline seconds (s). PO_2 mmHg (Pulmonary Oxygenation per millimetres of mercury), mmHg (millimetres of mercury). Based on West and colleagues (2011) [246]. 8

1.6 **Precession.** A: A hydrogen nucleus precesses around the magnetic field B_0. 15

1.7 **Quantum Energy States** B: Populations of high and low-energy quantum spin states in relation to B_0. 17

1.8 **Classical Phase Coherence.** Comparison of magnetic moments that are in and out of phase, demonstrating classical electromagnetic behaviour of the bulk magnetisation. 21

1.9 **Classical Magnetisation Rotation.** A: The rotation of magnetisation between longitudinal and transverse planes. B: The effect of a 90° RF pulse on the bulk magnetisation vector. 23

1.10 **Classical T_1 Recovery.** Exponential recovery of longitudinal magnetisation for differentiation between different brain tissues. CSF (cerebrospinal fluid), ms (milliseconds), M_z (longitudinal magnetisation), TR (repetition time). Code edited from github and formatted in Affinity 2. 25

1.11 **Classical T2 Decay.** Exponential decay of transverse magnetisation showing differentiation between different brain tissues, with faster decay in brain tissue compared to CSF. CSF (cerebrospinal fluid), ms (milliseconds), Mxy (transverse magnetisation), TE (echo time). 28

1.12 **Spin Echo Pulse Sequence.** Classical evolution of magnetisation showing dephasing after the 90° pulse and rephasing to form an echo after the 180° pulse. FID (free induction decay), RF (radiofrequency pulse), TE (echo time), TR (repetition time). MATLAB code based on github code and formatted in Affinity 2. 30

1.13 **Gradient Echo Pulse Sequence.** Classical magnetisation evolution with gradient-induced dephasing and rephasing. FID (free induction decay), RF (radiofrequency pulse), TE (echo time), TR (repetition time). MATLAB code based on github code and formatted in Affinity 2. 32

1.14 **Inversion Recovery Pulse Sequence.** Classical magnetisation recovery following inversion, demonstrating T_1 weighting control through inversion time selection. RF (radiofrequency pulse), TE (echo time), TI (inversion time), TR (repetition time). MATLAB code based on github code and formatted in Affinity 2. 34

1.15 **Philips 3T Ingenia Scanner and Head coil.** A: shows the scanner with a 70 cm bore, with a maximum field of view of 55 cm. B: Shows the Philips dStream 32 channel head coil. Images from Philips website Link A and Link B. 35

1.16 **GE Healthcare 3T Premier Scanner and Head coil.** A: Shows the GE scanner with a 70 cm bore. B: Shows the GE Healthcare 48 channel head coil from above of the coil open with the top, bottom and spacer as three separate pieces, and also from the side view of the coil closed. 37

1.17 **Arterial Spin Labelling.** A. Creating the Perfusion-weighted Image (based on Elster, 2020). B. Time Scale of Imaging, 1. Magnetically label water in the blood upstream of the blood labelling plane. 2. Wait for blood to arrive at the imaging plane, 3. acquire images, 4. repeat in absence of labelled blood (control), 5. subtract the difference between the labelled and control images, 6. calculate cerebral blood flow (CBF) maps from amount of blood moved across the inversion time. Different sub-types of ASL can be created by changing the size, location and timing of the planes (Dai et al., 2008 [61], Elster, 2020 [70]). Post labelling delay (PLD). 42

1.18 **Continuous versus Pulsed ASL.** Basic concept diagram for comparing the pros and cons of continuous and pulsed ASL (arterial spin labelling). 46

1.19 **Unbalanced vs. Balanced pCASL.** A. Unbalanced labelling and a balanced control sequence. Gz (Gradient in the z-direction), pCASL (pseudocontinuous arterial spin labelling). 48

1.20 **Example of seven MPLD eASL sequence.** Schematic of post labelling delays (PLD) and label durations (LD) when encoding seven delays. The total LD is divided into 7 blocks, each with its own PLD and effective label duration (LD). A. For linear delays the blocks are divided equally. B. For exponential delays the blocks have exponentially increasing spacing. (multiple post labelling delay (MPLD), "enhanced" pseudocontinuous arterial spin labelling (eASL)(Based on the GE manual p12. DOC1685720, Rev:6. [91]) 52

1.21 **Time Encoded pCASL.** Schematic of post labelling delays (PLD) and label durations (LD) when encoding seven delays. A. 7x7 Hadamard Matrix representing the 7 MPLD eASL sequence used in Chapter 4, with red squares for the labelled blocks (+1) and blue squares for the control blocks (-1). B. Time-Encoded Labelling Scheme, with the different LD. C. Effective Post-Labelling Delays (TIs/PLDs). The label durations still follow an exponential pattern to compensate for T_1 decay, with the longest block (1183 ms) providing substantial signal for the last time points. Inversion times (TIs), "enhanced" pseudocontinuous arterial spin labelling (eASL), milliseconds (ms). 54

1.22 **Neurovascular Coupling and the Bold Effect.** Neurovascular Coupling (NVC) refers to the pathway from the neuronal activity to the vascular response seen in fMRI imaging. This is the basic concept of a (1) neuronal response resulting in downstream physiological effects that alters (2) Blood flow e.g. via vasoconstriction/vasodilation. This results in (3) changes in the blood e.g. metabolism of O_2 by the neurons, which produces deoxyhaemoglobin in the blood. Cerebral blood outflow washes this out, and also influences blood volume which decreases deoxyhaemoglobin. (4) This leads to an increase in the BOLD signal detected by the MRI. BOLD (blood oxygen level dependent), CBV (cerebral blood volume), MRI (magnetic resonance imaging), HR (haemodynamic response), O_2 (oxygen) RF (radiofrequency) (Based on [107, 180, 108, 115]). 57

1.23 **HRF Convolution.** A. A Gamma function across z. B. Gamma distribution curve across t (time). C. A Box car stimulus used to induce a BOLD response. D. HRF convolution based on B and C, across time (in s (seconds)) that peaks at around 5-6 s. Based on Glover (2024) [96] and Andrew Jahn (2024) [121]. 61

2.1 **Visual Abstract** Part 1: A hypercapnic challenge was used to induce a CVR response and create CVR maps. Three different preparation parameter sets were used with Params-1 giving the highest values. Part 2: The labelling plane was aligned with the V3 segment of the vertebral arteries in the neck. Hyperventilation (with clamped normocapnia) was used to investigate B_0 and B_1 effects. CO_2 (carbon dioxide), CVR (cerebrovascular reactivity). 84

2.2 **Robust CVR Part 1: Gas Delivery, Mask and Scanner Kit.** Photos of the Respiract^{TM} (A), gas delivery kit, mask set up (B) and the final set up in the MR scanner (C). Photo is not de-identified as CCM is in the photo. MRI (magnetic resonance imaging), PPU (peripheral pulse unit), SGD (sequential gas delivery mask), T (tesla). 96

2.3 **Robust CVR part 1 Gas Set up Diagram.** Diagram showing a conceptual set up of the in/outputs for the gas delivery in the Philips Ingenia scanner room for part 1. Not to scale. BNC (Bayonet Neill–Concelman cable), CO_2 (carbon dioxide), MRI (magnetic resonance imaging), PPU (peripheral pulse unit). . . 97

2.5 **Part 2, Gas Delivery Set up.** Example of the set up for the gas delivery kit used in Robust CVR part 2. Note, this photo was taken during set up development rather than during an actual scan. Hence, the laptop screen shows a screenshot of Labchart^{TM} within a notebook rather than the actual display screen. The final version did not require the extra connectors other than the gas line in /out. 100

2.6 **Robust CVR part 2 Gas Set up Diagram.** Diagram showing a conceptual set up of the in/outputs for the gas delivery in the Philips Ingenia scanner room for part 2. Not to scale. BNC (Bayonet Neill–Concelman cable), CO_2 (carbon dioxide), PPU (peripheral pulse unit), MRI (magnetic resonance imaging). . . 101

2.7 **Respiratory Data Analysis Preprocessing.** Part 1 used RespirAct^{TM} software on a Windows XP laptop to manually check the data and correct any breath-by-breath (BBB) markers. The BBB files were then exported and MATLAB was used to window the data using the RespirAct^{TM} 'event' files (marked during scanning for important time points) to give the end-tidal partial pressure of carbon dioxide ($PETCO_2$) data for each participant, MR scan and CO_2 condition. B. Part 2 used LabChart (by AD instruments) software during data collection. The data was exported as text files, the MATLAB files for the 'events' were then used to window the data into each scan and CO_2 condition, followed by extracting the peaks to give the $PETCO_2$ data. ms (milliseconds), %/mmHg (percentage change per millimetres mercury). (Logos references: ADInstruments link, Thornhill Medical link). 102

2.8 **Robust CVR Part 1 MRI Protocol.** The sequence for MR scanning was as follows; a survey, TOF (time of flight), PCV (phase contrast velocity) x3, pCASL (pseudocontinuous arterial spin labelling) x 3 sets of parameters, B_0 Map Axial, MPRAGE (Magnetization Prepared Rapid Acquisition of Gradient Echo). Images are an example set from one subject. 104

2.9 **Robust CVR Part 2 MRI Protocol.** The sequence for MR scanning was as follows; a survey, TOF (time of flight), pCASL (pseudocontinuous arterial spin labelling) x 3 sets of parameters, Axial B_0 Map, MPRAGE (Magnetization Prepared Rapid Acquisition of Gradient Echo). Images are an example set from one subject. 107

2.10 **Part 1 Methods, drawing ROIs.** Images showing the position of the ICA and VAs on a sagittal T1w image, an axial Time of flight image, and finally the coronal image used with the Segment software to draw ROIs of each artery. ICA (internal carotid artery), VA (vertebral artery), L (left), R (right), T1w (anatomical T1 weighted image). 110

2.11 **Part 2 Methods, planning the labelling plane and the B_1 and B_0 slices.** Example of using time of flight data to plan the labelling plane 90 mm below the anterior commissure-posterior commissure (AC-PC) line. ICAs (internal carotid arteries), mm (millimetres), L (left), R (right), ROI (region of interest), T1w (T1 weighted image), V3 (third vertebrae segment), VAs (Vertebral Arteries). Based on Bush et al., (2018) [42], McCarthy et al., 2022 [151]. . . 112

2.12 **Comparison of CVR estimates for each of the three pCASL (pseudocontinuous Arterial Spin Labelling) labelling parameter sets** A: The percentage change in cerebral blood flow (CBF) shows two outliers and did not show a difference between groups. B: The percentage change in CBF normalised by each individuals' change in end-tidal partial pressure of carbon dioxide ($P_{ET}CO_2$) in mmHg (millimetres of mercury). A significant difference was found between Params-1 and Params-2 (p=0.0315). 117

2.13 **Comparison across Hypercapnia Conditions.** Bars show mean±std. A: Average maximum velocity of feeding arteries (N=9, F=4, mean±std) at three carbon dioxide (CO_2) levels: hypocapnia (hypo, -10 mmHg below baseline), normocapnia (normo) and hypercapnia (hyper, +10 mmHg above baseline). Left/right (L/R) internal carotid arteries (ICA) and vertebral arteries (VA). B: Percentage difference in maximum velocity (%) between CO_2 levels by artery. C: Percentage difference in maximum velocity normalised by the change in the individual participants' end-tidal partial pressure of CO_2 (%/mmHg) between CO_2 levels by artery. % (percent), mmHg (millimetres of mercury). 119

2.14 **Comparing Median B_0 Across Different Arteries.** A: Comparing B_0 across arteries. B: Single slice data for the difference in B_0 between normal breathing and hyperventilation. C: Single slice data of the range of measured B_0 values calculated as the difference between the 2nd to 98th percentile. Left/right (L/R) internal carotid arteries (ICA) and vertebral arteries (VA), Hz (hertz). . . 121

2.15 **Comparing B_1 Across Different Arteries.** Box plots of the B_1 values across the group (black line) for the feeding arteries of the brain at two labelling locations prior to the hyperventilation protocol. A: Measurements made at the V3 segment of the vertebral arteries. B: Measurements made at a location 90 mm below the AC-PC line. AC-PC (anterior commissure - posterior commissure), Left/right (L/R) internal carotid arteries (ICA) and vertebral arteries (VA), mm (millimetres,) % (percent), (median±IQR (inter-quartile range)). 123

3.1 **Visual Abstract** A hypercapnic challenge was performed before and after a pharmacological intervention was administered. The physiological measures of blood pressure, heart rate and velocity were taken using a Dinamap, a Finapres and an ultrasound scanner. During control condition, after CO_2 there was no significant change in BP, velocity or HR. After GTN, there was an increase in HR, but no difference during the hypercapnic challenge. After MET, there was a decrease in HR, and after CO_2 there was an increase in BP and HR. BP (blood pressure), CO_2 (carbon dioxide/hypercapnic challenge), GTN (glyceryl trinitrate), MAP (mean arterial pressure), MET (metoprolol), mmHg (millilitres of mercury). Red Arrows indicates a change, NSF (not significant after multiple comparison correction). 136

3.2 **Study Timeline.** Time points at which measurements were taken. GTN (glyceryl trinitrate), Hyper (hypercapnia), mins (minutes) MET (metoprolol), Normo (normocapnia). 144

3.3 **Study Day Kit set up.** Set up of the kit used in this study including the Dinamap, Ultrasound, Mask kit, Finapres and gas delivery. BP (blood pressure), Finapres (FINger Arterial PRESsure). 145

3.4 **Dinamap Models.** Photos of the Dinamap models: A. Dash 3000 used in screening until replacement in 2023. B. used for data collection. Both are automatic, non-invasive blood pressure monitors. GE (GE Healthcare, Chicago, USA). 147

3.5 **Ultrasound Device.** Photo of the Toshiba Aplio 300 used for ultrasound measurements in this study. 149

3.6 **Ultrasound example trace.** Annotated photo of the ultrasound screen showing four cardiac cycles to give the average velocity measurements. 150

3.7 **Finapres Cuff.** Figures of Finapres cuff from the manual FMS, Finapres Medical Systems BV Version 1.10, dd: 2002.05.06. Images A (cuff sizing) and B (cuff wrapping) were edited and compiled together with C a photo of an example cuff position and D a photo of the calibration cuff at the same height as the heart. . . . 152

3.8 **Finapres and Gas Monitoring Kit Set.** Finapres on the left was used to monitor continuous blood pressure along with an ADInstruments® Gas Analyser (Product Code ML206) and Powerlab (26 Series with a 6 channel input). 153

3.9 **Breathing circuit set up.** Oxygen tubing from the medical flow meters was attached to the following breathing circuit and the expired gas was measured through a line out. Note size 4 (green) is shown in the photo, but both size 3 (yellow) and 4 were available for participants. F (female connecting), M (male connecting), L (litre), REF (reference number from manufacturer). 155

3.10 **Finapres and End Tidal Data Analysis process.** A: Data pre-processing: the LabChart® data file was exported as a text file both with and without comments (comments were used for marking important study day time points). In-house MATLAB scripts were used to create figures at each stage of the pre-processing to manually check the intervention times before windowing. B: Data were windowed for each physiological variable based on these intervention times for each intervention and condition. The 'FindPeaks' function was used to threshold each window. C: These data were used to calculate the mean of each individual's data across each window. D: Then the group median and interquartile ranges were calculated to display the median error bar and the difference between conditions was calculated and plotted as box plots. 161

3.11 **Dinamap: Mean Arterial Pressure.** Coloured lines are for showing change in MAP within each participant across the whole experiment chronologically, the black error bars represent group median and interquartile range. N=10. GTN (glyceryl trinitrate), Hyper (hypercapnia), MAP (mean arterial pressure), MET (metoprolol), mmHg (millimetres of mercury), Normo (normocapnia). 167

3.12 **Dinamap: Mean Arterial Pressure Comparing Normocapnia during Control and Intervention Conditions.** Shows the control (left side blue markers) and intervention (right side red markers) MAP during normocapnia. The circles show the individual participants and the black line represents group median and interquartile range. N=10. GTN (glyceryl trinitrate), MAP (mean arterial pressure), MET (metoprolol), mmHg (millimetres of mercury), Normo (normocapnia). 169

3.13 **Ultrasound: Velocity Maximum.** Coloured lines show the change in VMax within each participant across the whole experiment chronologically, the error bars represent the group median and interquartile range. N=10. cm/s (centimetres per second), GTN (glyceryl trinitrate), Hyper (hypercapnia), MET (metoprolol), Normo (normocapnia), VMax (velocity maximum). 170

3.14 **Ultrasound: Velocity Maximum Comparing Control and Intervention Normocapnia Conditions.** Shows the control (left side blue markers) and intervention (right side red markers) normocapnia velocities. The circles show the individual participants and the black line represents group median and interquartile range. N=10. There was no significant difference between the control and intervention velocity controls when GTN (p=0.770) or MET (p=1.000) was given. cm/s (centimetres per second), GTN (glyceryl trinitrate), MET (metoprolol), Normo (normocapnia), VMax (velocity maximum). 172

3.15 **Dinamap: Heart Rate.** Coloured lines show the change in HR for each participant across the whole experiment chronologically, the black line represents group median and interquartile range. N=10. BPM (beats per minute), GTN (glyceryl trinitrate), HR (heart rate), Hyper (hypercapnia), MET (metoprolol), Normo (normocapnia). 173

3.16 **Dinamap: Heart Rate Comparing Normocapnia during Control and Intervention Conditions.** Shows the control (left side blue markers) and intervention (right side red markers) normocapnia HRs. The circles show the individual participants and the black line represents group median and interquartile range. N=10. There was a significant difference between the control and intervention normocapnia conditions for HR when GTN (p=0.002) or MET (p=0.004) was given. BPM (beats per minute), GTN (glyceryl trinitrate), HR (heart rate), MET (metoprolol), Normo (normocapnia).175

3.17 **Dinamap: Difference Between Normo- and Hypercapnia for Control and Intervention Mean Arterial Pressure.** Shows the difference between hypercapnia and normocapnia for control (left side blue markers) and intervention (right side red markers) MAP. The circles show the individual participants and the black line represents group median and interquartile range. There were no significant differences between normo- to hypercapnia condition when comparing control to intervention change for MAP when GTN (p=0.336) or MET (p=0.883) were given. GTN (glyceryl trinitrate), MAP (mean arterial pressure), MET (metoprolol), mmHg (millimetres of mercury). 177

3.18 **Ultrasound: Velocity Maximum Difference Between Normo- and Hypercapnia for Control and Intervention.** Shows the difference between hypercapnia and normocapnia for control (left side blue markers) and intervention (right side red markers) velocities. The circles show the individual participants and the black line represents group median and interquartile range. There were no significant differences between the change from normo- to hypercapnia conditions when comparing control to intervention change for Vmax when GTN (p=0.4375) or MET were given (p=0.0625). cm/s (centimetres per second), CO_2, GTN (glyceryl trinitrate), MET (metoprolol), VMax (velocity maximum). 179

3.19 **Dinamap: Heart Rate Difference Between Normo- to Hypercapnia for Control and Intervention.** Shows the difference between hypercapnia and normocapnia for control (left side blue markers) and intervention (right side red markers) heart rates. The circles show the individual participants and the black line represents group median and interquartile range. There was no significant difference between the change from normocapnia to hypercapnia conditions when comparing control to intervention for HR when GTN (p=0.025) or MET (p=0.168) were given. BPM (beats per minute), GTN (glyceryl trinitrate), HR (heart rate), MET (metoprolol). 181

3.20 **Dinamap: Percentage Difference Between Normo- and Hypercapnia for Control and Intervention Mean Arterial Pressure.** Shows the difference between hypercapnia and normocapnia for control (left side blue markers) and intervention (right side red markers) MAP normalised by the individual's control condition. The circles show the individual participants and the black line represents the group median and interquartile range. GTN (glyceryl trinitrate), MAP (mean arterial pressure), MET (metoprolol), mmHg (millimetres of mercury). 183

3.21 **Ultrasound: Percentage Difference Between Control and Intervention Velocity Maximum under Normocapnia Condition.** Shows the control (left side blue markers) and intervention (right side red markers) normocapnia velocities. The circles show the individual participants and the black line represents the group median and interquartile range. N=10. GTN (glyceryl trinitrate), MET (metoprolol), Normo (normocapnia) VMax (velocity maximum). 184

3.22 **Dinamap: Percentage Difference Between Control and Intervention Heart Rate Normocapnia Conditions.** Shows the difference between the control and intervention normocapnia heart rates normalised by the individual's control condition. The circles show the individual participants and the black line represents group median and interquartile range. BPM (beats per minute), GTN (glyceryl trinitrate), HR (heart rate), MET (metoprolol). 185

4.1 **Visual Abstract for Chapter 4** Part 1 combined an enhanced pseudocontinuous arterial spin labelling (eASL) multiple post labelling delay (MPLD) sequence with placement of the labelling plane at the V3 segment of the vertebral arteries, a steady state hypercapnic challenge, and a more advanced Bayesian analysis toolbox Bayesian Inference for Arterial Spin Labelling (BASIL). The resulting cerebrovascular reactivity (CVR) and cerebral blood volume (CBV) was higher than in previous studies and the arterial transit time (ATT) was shorter. Part 2 combined a blood oxygen level dependent (BOLD) sequence with a pseudo-sinusoidal hypercapnic challenge and a novel dynamically modelled BOLD analysis method (dCVR), to give measures of CVR amplitude and timing response (time to peak (TTP)). 206

4.2 **Example of seven MPLD eASL at one example slice** The output from the GE eASL sequence shows the pre-subtracted control/label image. At each PLD the bolus appears 'brighter' during the hypercapnic condition. ms (milliseconds). 209

4.3 **Conceptual diagram of multiband BOLD imaging.** To create a multiband pulse a single slice pulse and frequency shift is used to excite a signal at the locations of interest. For example, by adding the pulses together to create a composite pulse it is possible to excite the other two brain slices along the z-axis. This is repeated, and the output images are compiled together to make the complete image. In this example the first slices are taken at the most inferior base of the brain and the subsequent slices are taken in the superior direction until the whole brain has been covered. When the signal is acquired by the scanner, all of the slices are combined together. The scanner then uses the spatial sensitivity of the coil (particularly in the z direction) to separate out the slices. BOLD (blood oxygen level dependent), RF (radio-frequency). 215

4.4 **Graphical explanation of the dCVR output parameters.** Haemodynamic response function curve in response to a CO_2 challenge i.e. hypercapnia. CO_2 (carbon dioxide), dCVR (dynamically modelled BOLD), TTP (time-to-peak), TTH (time-to-half-maximum), FWHM (full-width at half-maximum, area (the area of h(t), equivalent to the CVR amplitude). 217

4.5 **Semi-automated Gas Delivery Box Set Up.** The gas cylinders were connected via medical gas regulators and by gas hoses to the back of the gas delivery box. The gas delivery was controlled by an Arduino-based electronic control box. 228

4.6 **Semi-automated Gas Delivery Box Conceptual Diagram.** Diagram showing a conceptual set up of the inputs/outputs for the gas delivery in the GE Healthcare Premier scanner room. Not to scale. BNC (Bayonet Neill–Concelman cable), CO_2 (Carbon dioxide), MRI (magnetic resonance imaging), PPU (peripheral pulse unit). 229

4.7 **Mask Kit.** Tubing from the Y-piece was attached to the following mask set up with a reservoir made up of four 2 m pieces of tubing which were open to room air at one end. Note: the smaller size 3 yellow mask is shown in the photo above, but size 4 was also available and used for most participants. CPAP (Continuous positive airway pressure), F (female connecting), M (male connecting), L (litre), REF (reference number from manufacturer). 230

4.8 **Hypercapnic Challenge Paradigms.** A. A block protocol paradigm of normocapnia during the PCV (duration ∼120 s) and the pCASL (duration ∼330 s) scans, followed by hypercapnia for 30 s to account for lag time, and continued during repeated PCV and pCASL scans (total duration ∼480 s). B. A paradigm of 60 s normocapnia followed by 60 s hypercapnia repeated 3.5 times during the BOLD scan (duration ∼420 s). The BOLD scan was repeated twice. C. Example Respiratory trace showing the entire CO_2 trace for one participant. CO_2 (carbon dioxide), BOLD (blood oxygenation level dependent), ms (milliseconds), pCASL (pseudo continuous arterial spin labelling), phase contrast velocity (PCV), % (percent), s (seconds). 233

4.9 **MRI Protocol.** Images are an example set from one subject. The sequence for MR scanning was as follows, a localiser survey, MPRAGE (Magnetization Prepared Rapid Acquisition of Gradient Echo), TOF (time of flight) MRA (Magnetic resonance angiography), PCV (phase contrast velocity). eASL (enhanced ASL), BOLD (Blood Oxygen Level Dependent), SE (spin Echo). 236

4.10 **pCASL Data Analysis Pipeline.** PETCO$_2$ was windowed and calculated in MATLAB. MRI data were pre-processed using a BASH script and then analysed using Bayesian Inference for Arterial Spin Labelling (BASIL) using gamma dispersion modelling. The grey matter mask and perfusion images were used to calculate the percentage change (%) in blood flow, which was normalised to the individual's PETCO$_2$ to give the percentage change per mmHg. aCBV (arterial cerebral blood volume), ASL (arterial spin labelling), ATT (arterial transit time), BET (brain extraction tool), CVR (cerebrovascular reactivity), DeltaM (difference image i.e. difference between control and tag images), FAST (FMRIB advanced segmentation tool), FLIRT (FSL tool for linear registration), M_0(M zero scan), MNI (Montreal Neurological Institute), MRI (magnetic resonance imaging), PETCO$_2$ (end-tidal partial pressure of carbon dioxide). 239

l

4.11 **Creating GM ROIs.** Tools and transforms used to move the output data from ASL and BOLD datasets into the final M_0 image space. Black arrows denote transforms and blue arrows denote tools/analysis methods. ASL (arterial spin labelling), BASIL (BASIL basil toolbox), BET (brain extraction tool), BOLD (blood oxygen level dependent), dCVR (dynamically modelled BOLD), FAST (FMRIB advanced segmentation tool), FLIRT (FSL tool for linear registration), hyper (hypercapnia), MNI (Montreal Neurological Institute), MRI (magnetic resonance imaging), normo (normocapnia), T1w (T_1 weighted anatomical). 241

4.12 **dCVR HRF.** Concept diagram showing the respiratory stimuli (A), an example for respiratory trace (B) which was converted to $PETCO_2$, and then processed using the Findpeaks function (C), followed by normalisation (D), and integration with the Spherical Laguerres model (with Volterra kernels), to give an example HRF (E). $PETCO_2$ (end-tidal partial pressure of carbon dioxide), HRF (haemodynamic response function), dCVR (dynamically modelled BOLD (blood oxygen level dependent MRI (magnetic resonance imaging))), s (seconds). 245

4.13 **Comparing Cerebral Blood Flow (CBF) for Normo- and Hypercapnia Conditions.** Cerebral blood flow (CBF) increased from normo to hypercapnic conditions (p=0.0002). g (grams), hyper (hypercapnia), min (minute), ml (millilitres), normo (normocapnia). 252

4.14 **Cerebrovascular Response to Hypercapnic Challenge.** Percentage change of cerebral blood flow (CBF) from normo- to hypercapnia. The bar represents the group mean and the error bar represents the standard error of the mean. % (percent), mmHg (millimetres of mercury), $P_{ET}CO_2$ (end tidal partial pressure of carbon dioxide). 253

4.15 **Comparing arterial Cerebral Blood volume (aCBV) for Normo- and Hypercapnia Conditions.** aCBV increased from normo- to hypercapnic conditions (p=0.4545). hyper (hypercapnia), normo (normocapnia). 254

4.16 **Arterial cerebral Blood Volume Response to Hypercapnic Challenge.** Percentage change of aCBV (arterial cerebral blood volume) from normo- to hypercapnia. The bar represents the group mean and the error bar represents the standard error of the mean. % (percent), mmHg (millimetres of mercury), $P_{ET}CO_2$ (end tidal partial pressure of carbon dioxide). 255

4.17 **Comparing Arterial Transit Time (ATT) for Normo- and Hypercapnia Conditions.** Arterial transit time (ATT) decreased from normo- to hypercapnic conditions (p=0.0008). hyper (hypercapnia), normo (normocapnia), s (seconds). 256

4.18 **Arterial Transit Time Response to Hypercapnic Challenge.** Percentage change of ATT (arterial transit time) from normo- to hypercapnia. The bar represents the group mean and the error bar represents the standard error of the mean. % (percent), mmHg (millimetres of mercury), $P_{ET}CO_2$ (end tidal partial pressure of carbon dioxide). 257

4.19 **dCVR Cerebrovascular Reactivity Response to Hypercapnic Challenge: Magnitude.** A. A single slice, axial example of a dCVR CVR magnitude map showing the response to the hypercapnic challenge. The colour bar shows the higher CVR magnitude in yellow, and lower magnitudes are shown in blue. B. dCVR magnitude of response to a hypercapnic challenge as percentage change of cerebral blood flow (CBF) from normo- to hypercapnia, and C. normalised to the individual participants' $P_{ET}CO_2$. The bar represents the group mean and the error bar represents the standard error of the mean. dCVR dynamically modelled BOLD CVR), mmHg (millimetres of mercury), $P_{ET}CO_2$ (end tidal partial pressure of carbon dioxide), % (percent) 259

4.20 **dCVR Cerebrovascular Reactivity Response to Hypercapnic Challenge: Time to Peak.** A single slice, axial example of a dCVR dynamically modelled BOLD CVR (dCVR) time to peak (TTP) map showing the response to the hypercapnic challenge. The colour bar shows the longer TTP in yellow, and shorter TTP are shown in blue. , % (percent), s (seconds). 260

5.1 **Visual Abstract for Chapter 5.** This chapter compares the eASL and BOLD (dCVR) analyses from the previous chapter, along with an additional BOLD analysis (sinCVR), to investigate if there are correlations between these methods across five grey matter cortices. The measure of CVR magnitude from eASL did not correlate with those of sinCVR or dCVR. Measures of blood flow timing from eASL (ATT), correlated with those of sinCVR (phase), but not dCVR (TTP). sinCVR and dCVR CVR magnitude were positively correlated, but their timing measures were negatively correlated. ATT (arterial transit time), BOLD (blood oxygen level dependent), CVR (cerebrovascular reactivity), dCVR (dynamically modelled BOLD), eASL (enhstanced pseudocontinuous arterial spin labelling), sinCVR (sinusoidally modelled BOLD), TTP (time to peak). 277

5.2 **Grey matter cortices.** A: Shows the five main cortices of interest for grey matter CVR. B: Shows an example grey matter mask superimposed over the top of the five cortices. Frontal Lobe (cyan), Insula (red), Occipital Lobe (green), Parietal Lobe (blue) and Temporal Lobe (magenta). Created using the MNI (Montreal Neurological Institute) atlas and an example dataset from this chapter. 282

5.3 **sinCVR HRF.** Concept diagram showing the respiratory stimuli (A), an example for respiratory trace (B) which was converted to $P_{ET}CO_2$, and then processed using the Findpeaks function (C), and integration with the cos/sine model (D), to give an example HRF (E). $P_{ET}CO_2$ (end-tidal partial pressure of carbon dioxide), HRF (haemodynamic response function), sinCVR (sinusoidally modelled BOLD (blood oxygen level dependent MRI (magnetic resonance imaging))), s (seconds). 287

5.4 **Creating GM ROIs for the five main cortices.** Tools and transforms used for the eASL and BOLD datasets, moved into the eASL hyper M_0 space. Black arrows denote transforms and blue arrows denote tools/analysis methods. ASL (arterial spin labelling), BASIL (BASIL toolbox), BET (brain extraction tool), BOLD (Blood oxygen level dependent), dCVR (dynamically modelled BOLD), FAST (FMRIB advanced segmentation tool), hyper (hypercapnia), MNI (Montreal Neurological Institute), normo (normocapia), sinCVR (sinusoidally modelled BOLD, T1w ($T1_1$ weighted anatomical). 288

5.5 **Comparison of eASL CVR and sinCVR magnitude.** eASL and sinCVR were not correlated either before (A) or after normalisation to participant's individual $P_{ET}CO_2$ (B) (R^2=0.07 and R^2=0.00). Cerebrovascular reactivity (CVR), eASL (enhanced pseudocontinuous arterial spin labelling), hyper (hypercapnia), % (percent), mmHg (millimetres of mercury), $P_{ET}CO_2$ (end tidal partial pressure of carbon dioxide), sinCVR (sinusoidal modelled BOLD (blood oxygen level dependent)). 291

5.6 **Comparison of eASL CVR and dCVR magnitude** eASL and dCVR magnitdue were not correlated either before (A) or after normalisation to individuals' $P_{ET}CO_2$ (B) (R^2=0.07 and R^2=0.00). Cerebrovascular reactivity (CVR), dCVR (dynamically modelled BOLD) eASL (enhanced pseudocontinuous arterial spin labelling), hyper (hypercapnia), mmHg (millimetres of mercury), $P_{ET}CO_2$ (end tidal partial pressure of carbon dioxide). 292

5.7 **Comparison of sinCVR and dCVR magnitude.** sinCVR and dCVR magnitude values had a strong positive correlation (R^2=0.82). Cerebral vascular reactivity (CVR), dCVR (dynamically modelled BOLD), hyper (hypercapnia), normo (normocapnia), sinCVR (sinusoidal modelled BOLD). 293

5.8 **Comparison of eASL ATT and sinCVR phase.** sinCVR and dCVR timing measures had a weakly positively correlation (R^2=0.26). Timing delay and phase data had a small positive correlation. ATT (Arterial Transit Time), eASL (enhanced pseudocontinuous arterial spin labelling), s (seconds), sinCVR (sinusoidal modelled BOLD), BOLD (blood oxygen level dependent). 295

5.9 **Comparison of eASL Arterial Transit Time and dCVR Time To Peak.** Timing measures from eASL and dCVR were not correlated (R^2=0.05). dCVR (dynamically modelled BOLD), ATT (Arterial Transit Time) in s (seconds), eASL (enhanced pseudocontinuous arterial spin labelling), hyper (hypercapnia), normo (normocapnia), s (seconds), TTP (time to peak). 296

5.10 **Comparison of sinCVR phase and dCVR Time To Peak.** Timing measures from sinCVR and dCVR were weakly correlated (R^2=0.22). dCVR (dynamically modelled BOLD), hyper (hypercapnia), normo (normocapnia), s (seconds), TTP (time to peak), sinCVR (sinusoidal modelled BOLD), BOLD (blood oxygen level dependent). 297

C.4 **Dinamap Results Summary.** Summary table of chapter 3 results. BPM (beats per minute), cm/sec (centimetres per second), ΔPre (difference between normocapnia and hypercapnia, during the HC, pre-intervention), ΔPost (difference between normocapnia and hypercapnia, during the HC, post-intervention), GTN (glyceryl trinitrate), HC (hypercapnic challenge), Hyper (hypercapnia), Normo (normocapnia), N-N (normocapnia pre- vs. normocapnia post-intervention), MET (metoprolol), mmHg (millimetres of mercury).371

List of Tables

1.1 **Atomic Isotopes for MRI.** Table of different atomic isotopes, their nuclear spin quantum numbers, natural abundance, gyromagnetic ratio in megahertz (MHz) and abundance in the human body [32]. 18

2.1 **Part 1, Participants Characteristics Information.** Table of participants characteristics included in the data analysis. F (female), kg (kilograms), m (metres), M (male), std (standard deviation). 94

2.2 **Part 2, Participant Characteristics Information.** Table of participant characteristics for part 2. F (female), m (metres), M (male), kg (kilograms), std (standard deviation). 94

2.3 **Details of pCASL Parameter Sets.** Details of the Pseudo Continuous Arterial Spin Labelling (pCASL) preparation parameters used in Params-1, Params-2 and Params-3. G_{av} (average gradient amplitude) and G_{max} (maximum gradient amplitude), ms (milliseconds), μs (microsecond), mT/M (millitesla per meter). 106

2.4 **Part 1, Respiratory Challenges Results.** Part 1 Group mean end-tidal partial pressure of carbon dioxide ($P_{ET}CO_2$) levels during respiratory challenges (mean±standard deviation) for the PCV and pCASL data. N=10 for PCV, N=9 for pCASL. Change in $P_{ET}CO_2$ between normocapnia and hypercapnia (Δ), millimetres of mercury (mmHg), % (percentage), pseudocontinuous arterial spin labelling (pCASL), phase contrast velocity (PCV). 115

2.5 **Part 2, Respiratory Results.** Group mean end-tidal partial pressure of carbon dioxide ($P_{ET}CO_2$) levels during respiratory challenges (mean±std (standard deviation) for normocapnia, hyperventilation, and Δ (change in $P_{ET}CO_2$ between normocapnia and hyperventilation), millimetres of mercury (mmHg), % (percentage), N=6. 116

3.1 **Study Timeline Table.** Overview of the study day conditions in choronological order. CO_2 (carbon dioxide), GTN (glyceryl trinitrate), MAP (mean arterial pressure), MET (metoprolol), mmHg (millimetres of mercury). 158

3.2 **Participant Characteristics.** The mean and standard deviation for the participants of the low blood pressure study; Dose (MET) per kg, m (metres), mg (milligrams), F (female), kg (kilograms), std (standard deviation). 163

3.3 **Baseline Measurements.** Baseline measurements (group median±interquartile range, N=10) after participants had been resting, breathing room air for 30 minutes. BPM (beats per minutes), cm/s (centimetres per second), HR (heart rate), MAP (mean arterial pressure), mmHg (millimetres of mercury), VMax (velocity maximum). 164

3.4 **Respiratory Stimulus Response to a Hypercapnic Challenge.** ΔPRE (difference between normocapnia and hypercapnia, during the HC, pre-intervention), ΔPOST (difference between normocapnia and hypercapnia, during the HC, post-intervention), GTN (glyceryl trinitrate), HC (hypercapnic challenge), Hyper (hypercapnia), Normo (normocapnia), N-N (normocapnia pre- vs. normocapnia post-intervention), MET (metoprolol), mmHg (millimetres of mercury). 165

4.1 **Participant Characteristics** Table of participants characteristics recruited. kg (kilograms), m (metres), F (female), M2F (assigned male at birth, using gender affirming medication for female), M (male), PCV (phase contrast velocity), std (standard deviation). 225

4.2 **Response to Hypercapnic Challenge: eASL.** Table of participants characteristics and response to the hypercapnic challenge stimulus for the eASL datasets. m (metres), F (female), M (male), m (meters), kg (kilograms), std (standard deviation) % (percent), mmHg (millimetres of mercury), $P_{ET}CO_2$ (end tidal partial pressure of carbon dioxide). 248

4.3 **Response to Hypercapnic Challenge: BOLD.** Table of participants characteristics and response to the hypercapnic challenge stimulus for the BOLD datasets ($P_{ET}CO_2$). F (female), M (male), M2F (male to female medically transitioned) m (meters), kg (kilograms), std (standard deviation) % (percent), mmHg (millimetres of mercury), $P_{ET}CO_2$ (end tidal partial pressure of carbon dioxide). 250

B.1 Summary of participants characteristics for Chapter 2. Group mean±standard deviation. F (female), kg (kilograms), m (metres), M (male), std (standard deviation). 348

B.2 Respiratory Stimulus for B_1. Group mean±standard deviation. There was no significant difference between normal and hyperventilation $P_{ET}CO_2$. Analysis of Variance (ANOVA), Difference between normal and hyperventilation (Δ), End-tidal partial pressure of carbon dioxide ($P_{ET}CO_2$). 350

B.3 Part 1 Effect of Hypercapnia on Different pCASL Parameters. Group mean±standard deviation. Analysis of Variance (ANOVA), millimetres of mercury (mmHg), percentage change per mmHg (%/mmHg). 350

B.4 Part 1 Effect of Hypercapnia on PCV across Arteries. Group mean±standard deviation. Analysis of Variance (ANOVA), Centimetres per second (cm/s), Honestly Significant Difference (HSD). Not significantly difference (NSFD). 351

B.5 Range of B_0 offsets was estimated as the difference between 2nd and 98th, for normal breathing and hyperventilation. Left/right (L/R) internal carotid arteries (ICA) and vertebral arteries (VA), Hertz (Hz). 352

B.6 B_0 Arteries. Left/right (L/R) internal carotid arteries (ICA) and vertebral arteries (VA), Hertz (Hz). 353

B.7 B_0 across Conditions. Mann Whitney U test between conditions for individual arteries. Hertz (Hz). 354

B.8 Part 2 Effect of Labelling Plane Placement on B_1. median±interquartile range. Left/right (L/R) internal carotid arteries (ICA) and vertebral arteries (VA), Percentage (%). 355

C.1 **Baseline Measurements.** Baseline measurements (group median ± interquartile range, N=10) after participants had been resting, breathing room air, for 30minutes. BPM (beats per minutes), cm/s (centimeters per second), GTN (glyceryl trinitrate), MAP (mean arterial pressure), MET (Metoprolol), mmHg (millimetres of mercury), Vmax (Velocity Maximum). 372

D.1 **Respiratory Stimulus, Part 1, eASL Hypercapnic Challenges.** Group mean ± standard deviation, N=11. end-tidal partial pressure of carbon dioxide ($P_{ET}CO_2$), millimetres of mercury (mmHg). . 389

D.2 **Respiratory Stimulus, Part 2, BOLD Hypercapnic Challenges.** Group mean ± standard deviation, N=11. End-tidal partial pressure of carbon dioxide ($P_{ET}CO_2$), millimetres of mercury (mmHg). . 390

D.3 **Part 1, eASL Hypercapnic Challenges, MR.** Medians±group standard error of the mean, N=11. Difference between normo and hypercapnia (Δ), Normo (normocapnia), End-tidal partial pressure of carbon dioxide ($P_{ET}CO_2$), millimetres of mercury (mmHg). 391

D.4 **Part 2, BOLD Hypercapnic Challenges, MR.** Medians±group standard error of the mean, N=11. End-tidal partial pressure of carbon dioxide ($P_{ET}CO_2$), millimetres of mercury (mmHg), Time to Peak (TTP), percentage (%). 392

D.5 **Grey Matter Cortices eASL and BOLD data.** Break down of the metrics for each of the five main grey matter cortices. ANOVA (Analysis of Variance), ATT (arterial transit time), dCVR (dynamically modelled BOLD), s (seconds), sinCVR (sinusoidally modelled BOLD), TTP (Time to Peak). 393

E.1 **Chapter 5 Results Summary.** Average across the Five GM Cortices. Group mean of medians±group standard error of the mean, N=11. 397

List of Abbreviations

AAL	**A**utomatic **A**natomical **L**abelling
aCBV	**a**rterial **C**erebral **B**lood **V**olume
AC-PC	**A**nterior **C**ommisure - **P**osterior **C**ommisure
ACZ	**Ac**eta**z**olamide
ASL	**A**rterial **S**pin **L**abelling
ATT	**A**rterial **T**ransit **T**ime
AUC	**A**rea **U**nder the **C**urve
$\mathbf{B}_0$	$\mathbf{B}_0$ static magnetic field
$\mathbf{B}_1$	$\mathbf{B}_1$ radiofrequency field
BASIL	**B**ayesian **I**nference for **A**rterial **S**pin **L**abelling
BBB	**B**lood **B**rain **B**arrier
BET	**B**rain **E**xtraction **T**ool
BH	**B**reath **H**old(ing)
BP	**B**lood **P**ressure
BPM	**B**eats **P**er **M**inute
BOLD	**B**lood **O**xygen **L**evel **D**ependent
CASL	**C**ontinuous **A**rterial **S**pin **L**abelling
CBF	**C**erebral **B**lood **F**low
CBV	**C**erebral **B**lood **V**olume
cm/s	**C**entimetres per **S**econd
CO	**C**ardiac **O**utput

CO_2	**C**arbon **Dioxide**
CVD	**C**erebro**v**ascular **D**isease
CVR	**C**erebro**v**ascular **R**eactivity
Δ	**D**elta (to represent difference)
dCVR	**d**ynamically modelled BOLD **CVR**
DGHPU	**D**avid **G**reenfield **H**uman **P**hysiology **U**nit
DIA	**Dia**stolic blood pressure
DICOM	**D**igital **I**maging and **Co**mmunications in **M**edicine
eASL	**e**nhanced Pseudocontinuous **A**rterial **S**pin **L**abelling
ECG	**E**lectro**c**ardio**g**ram/phy
EEG	**E**lectro**e**ncephalo**g**ram/phy
EMS	**E**xperimental **M**anagement **S**ystem
EPI	**E**cho **P**lanar **I**maging
EVs	**E**xplanatory **V**ariables
FAST	**F**MRIB's **A**utomated **S**egmentation **T**ool
fMRI	**f**unctional **M**agnetic **R**esonance **I**maging
FOV	**F**ield **O**f **V**iew
FSL	**F**MRIB's **S**oftware **L**ibrary
G_{av}	**G**radient **A**verage
G_{max}	**G**radient **Max**imum
G_{ratio}	**G**radient **ratio**
GM	**G**rey **M**atter
GTN	**G**lyceryl **T**rinitrate
HC	**H**ypercapnic **C**hallenge
HR	**H**eart **R**ate
HRF	**H**aemodynamic **R**esponse **F**unction
Hz	**H**eart**z**

ICAs	**I**nternal **C**arotid **A**rteries
IQR	**I**nter **Q**uartile **R**ange
μ	**M**u
L	**L**eft
$\mathbf{M_0}$	$\mathbf{M_0}$ magnetic field
MAP	**M**ean **A**rterial **P**ressure
MATLAB	**Mat**hmatic **Lab**oratory (software)
MCA	**M**iddle **C**erebral **A**rteriea
MCFLIRT	**F**MRIB's **L**inear **I**mage **R**egistration **T**ool
MEG	**M**agneto**e**ncephalo**g**ram/phy
MET	**M**etoprolol
mg	**M**illi**g**rams
μ**g**	**M**icro**g**rams
m	**m**eters
mm	**M**illi**m**eters
mmHg	**M**illi**m**eters per **M**eter**m**ercury
MNI	**M**ontreal **N**eurological **I**nstitute
MPLD	**M**ulti **P**ost **L**abelling **D**elay
MR	**M**agnetic **R**esonance
MRI	**M**agnetic **R**esonance **I**maging
MPRAGE	**M**agnetisation **P**repared **R**apid **A**cquisition **G**radient **E**cho
N	**N**umber of participants
$\mathbf{N_2}$	**N**itrogen
$\mathbf{O_2}$	**O**xygen
OSIPI	**O**pen **S**cience **I**nitiative for **P**erfusion **I**maging
pCASL	**P**seudo**c**ontinuous **A**rterial **S**pin **L**abelling
PC	**P**hase **C**ontrast

PCV	**P**hase **C**ontrast **V**elocity
PET	**P**ositron **E**mission **T**omography
P$_{ET}$CO$_2$	**P**artial **E**nd **T**idal **P**ressure of **C**arbon dioxide
P$_{ET}$O$_2$	**P**artial **E**nd **T**idal **P**ressure of **O**xygen
PIS	**P**atient **I**nformation **S**heet
PLD	**P**ost **L**abelling **D**elay
R	**R**ight
RF	**R**adio **F**requency
ROI	**R**egion **O**f **I**nterest
rsfMRI	**R**esting **S**tate **f**unctional **M**agnetic **R**esonance **I**maging
σ	**s**igma
s	**S**econds
SAR	**S**pecific **A**bsorption **R**ate
sinCVR	**s**inosoidally modelled BOLD **CVR**
SGD	**S**equential **G**as **D**elivery
SYS	**Sys**tolic blood pressure
T	**T**esla
T$_1$	**T$_1$** weighted image
TCD	**T**rans **C**ranial **D**oppler
TE	**E**cho **T**ime
TOF	**T**ime **O**f **F**light
TR	**R**epetition **T**ime
TTP	**T**ime **T**o **P**eak
UoN	**U**niversity **o**f **N**ottingham
VAs	**V**ertibral **A**rteries
VMax	**M**aximum **V**elocity
VPeak	**M**aximum **Peak V**elocity

1 Introduction

This chapter will introduce the key concepts and background for the thesis including sections on the physiology of cerebrovascular reactivity (CVR), and how CVR can be measured using Magnetic Resonance Imaging (MRI) using stimuli such as a hypercapnic challenge (HC).

1.1 Introduction to Cerebrovascular Reactivity

Firstly, it is important to understand the biochemical, cellular, and physiological mechanisms of blood flow in the brain. Blood transports nutrients such as glucose and oxygen (O_2) around the body and removes waste products such as carbon dioxide (CO_2). The brain is made up of billions of neurons that require these nutrients to communicate with each other via synapses. The brain at rest requires 20% of your body's oxygen [209]. If neurons do not get enough nutrients, they are not able to communicate, leading to loss of brain function and in extreme cases neuron death.

CVR controls the amount of blood flow in the brain by altering multiple systems and is a marker of brain health. CVR is a measure of the response to vasoactive substances (e.g. inhaling CO_2), meaning substances that affect the vasculature and therefore change the cerebral blood flow to the brain (see Fig. 1.1). This can be measured using MRI (which will be discussed in more detail later), and is often normalised to the change in end-tidal CO_2 [225]. Cerebrovascular reserve

often also uses the abbreviation CVR, which refers to the maximum possible change in CBF from the baseline after stimulation, however this abbreviation will not be used in this way for this thesis.

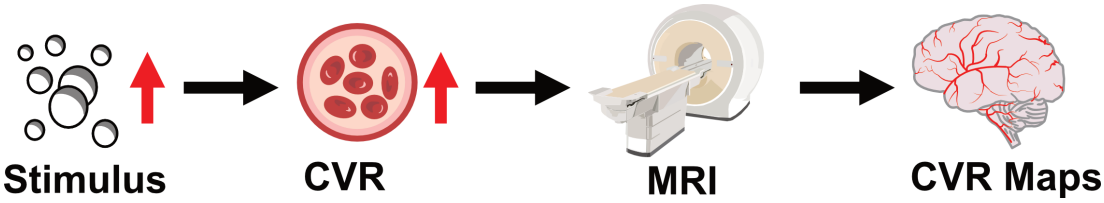


FIGURE 1.1: **Cerebrovascular Reactivity.** A stimulus induces a CVR response which can be measured using MRI and then quantitive CVR maps of blood flow in the brain tissue can be calculated. Cerebrovascular reactivity (CVR), Magnetic Resonance Imaging (MRI).

The respiratory and circulatory systems are heavily involved in the delivery of nutrients to the brain [181] (see Fig. 1.2). Changes in pH in the blood can provoke a CVR response. The pH of the blood is sensed by the respiratory centres, which then controls the respiratory rate via central and peripheral chemoreceptors. The lungs exchange fresh oxygen from the air across a thin, one cell thick surface around an air space called an alveoli. Blood vessels then transport this O_2 to the heart, which pumps the newly oxygenated blood around the body, including up to the brain. The O_2 is metabolised into CO_2, via the enzyme carbonic anhydrase, which rapidly forms carbonic acid [139]. Carbonic anhydrase catalyses the reversible hydration of CO_2 into bicarbonate ($HCO_3{}^-$) and protons (H^+), as seen in the following equation:

$$CO_2 + H_2O \Longleftrightarrow HCO_3^- + H^+). \tag{1.1}$$

Carbonic anhydrase activity therefore influences local pH changes, driving vasodilation (expansion/relaxation of the blood vessels) responses. This is because blood pH is largely regulated by the amount of CO_2 in the blood. So,

this is increase in pH (from the H^+) results in the removal of waste metabolic CO_2 from the blood, which is then breathed out via the lungs. This process facilitates gas exchange of O_2 and CO_2 in opposite directions i.e. from an area of high concentration to low concentration. Carbonic anhydrase II also influences the blood-brain barrier function, as expression in the brain capillary endothelium also regulates CO_2/HCO_3^- transport (across the barrier). It is also involved in the cerebrospinal fluid (CSF) secretion process, in the chorid plexus' (in the ventricles of the brain) epithelial lining.

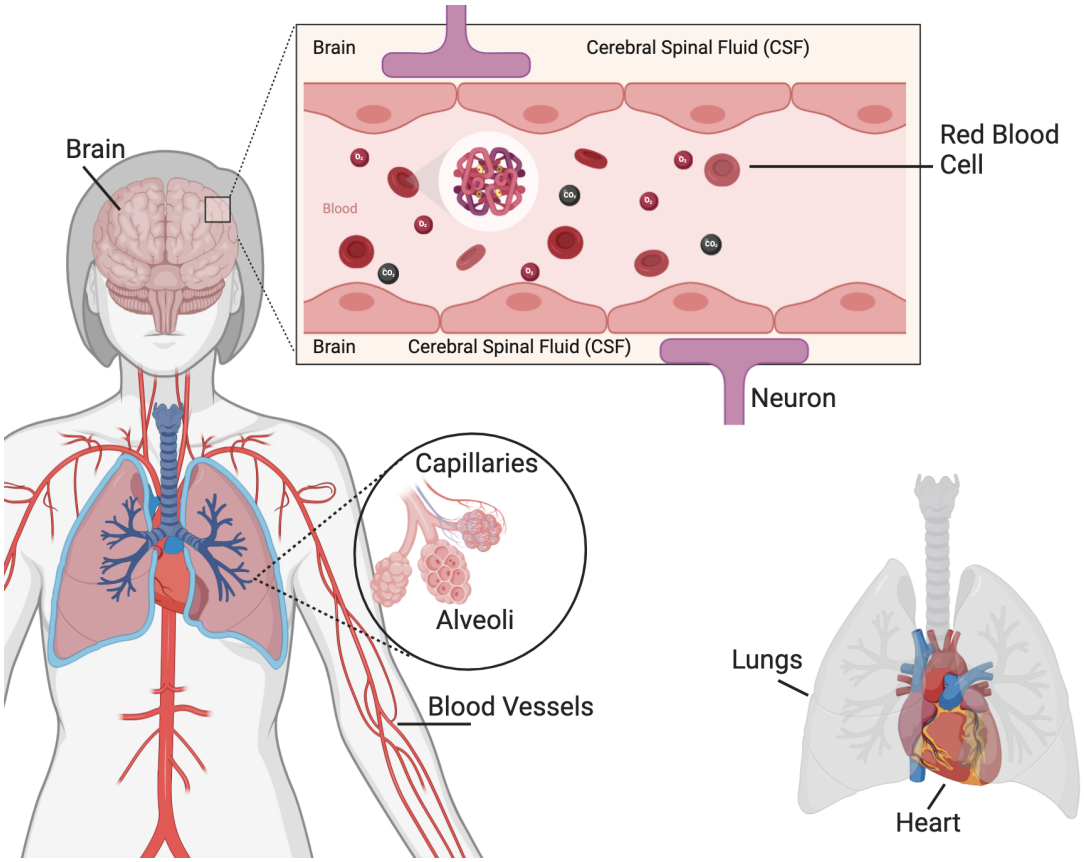


FIGURE 1.2: **Respiratory and Circulatory Systems.** Components of the Respiratory system (Lungs), Circulatory System (Heart and blood vessels) that transport oxygen and carbon dioxide to and from the brain are involved in and influenced by cerebrovascular reactivity (CVR). (Created using Biorender.com)

1.1.1 Cerebral Architecture

Figure 1.3 shows a basic overview of the brain vascular system, including a conceptual illustration of the smooth muscle cells (that contract and dilate for vasoconstriction/dilation), the pericytes (that help regulate blood flow), and the endothelial cells (that line the blood-brain barrier). Figure 1.4 shows the brain areas that the major blood vessels supply. Blood flow is controlled by four main mechanisms; the myogenic response (muscles e.g. of the artery walls that constrict and dilate), blood gas changes (e.g. an increase in CO_2 increases respiratory rate), neural activation, and sympathetic activity (involuntary neuronal control) [181]. Multiple mechanisms underlie these changes and not all are entirely understood, as they are so intertwined. For example, changes in pH caused by the dissociation of carbon dioxide into carbonic acid causes an increase in respiratory rate. This then also causes vasodilation via further myogenic response, and so on.

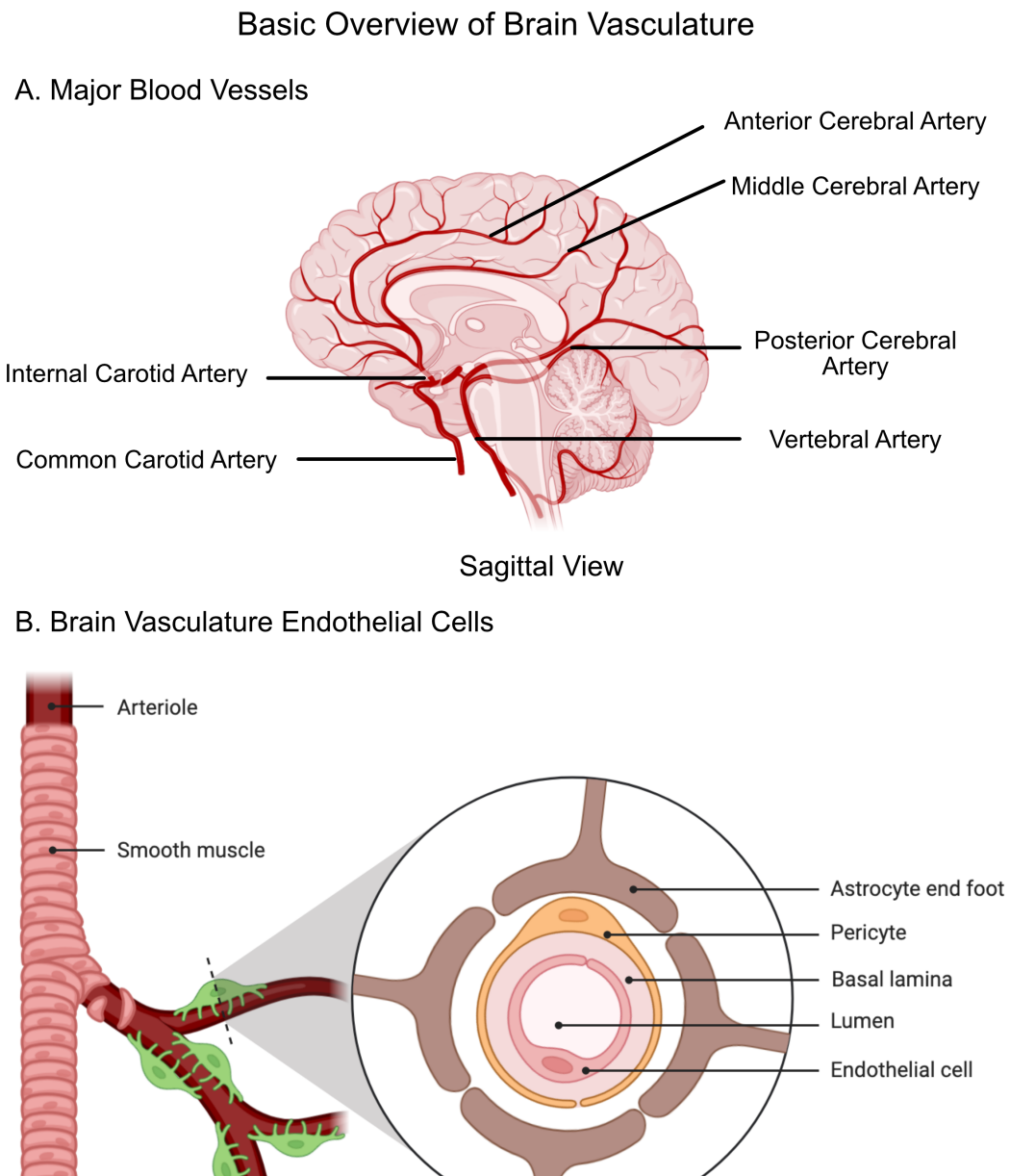


FIGURE 1.3: **Basic Overview of Brain Vasculature.** A. Sagittal view of the major brain blood vessels, and a closer look at the B. Brain Vasculature Endothelial Cells. (Created using Biorender.com)

Liu and colleagues (2023) brain atlas in figure 1.4 shows how different major arteries (anterior, middle and posterior cerebral arteries (ACA, MCA, PCA) supply different vascular territories and hence different brain regions and sub-regions (open source licence link [140]).

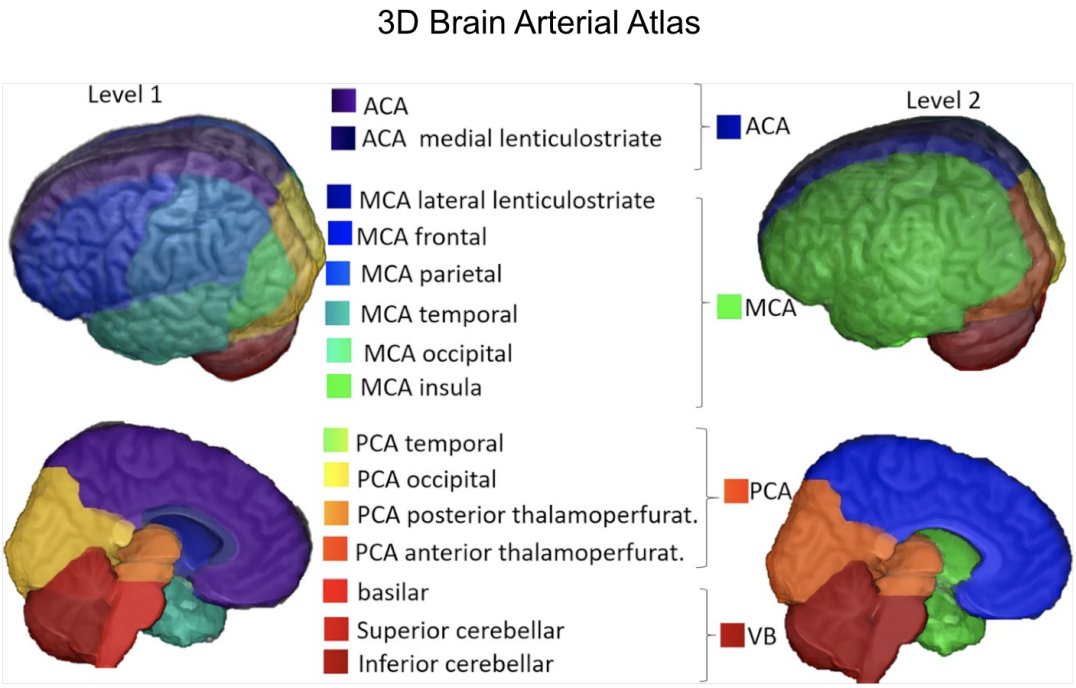


FIGURE 1.4: **3D Brain Artery Atlas.** The left column ("level 1") shows subdivisions of biological importance, based on probabilistic maps and/or anatomical landmarks. The right column ("level 2") represents the major vascular territories. 3D (three dimensional), ACA (anterior cerebral artery), MCA (middle cerebral artery), PCA (posterior cerebral artery), thalamoperfurat. (thalamoperforating arteries), VB (Vertebro-Basilar arteries). Figure credit to Liu and colleagues (2023) [140], reproduced under the creative common's licence open-access).

Changes made: added a title and edited the figure legend.

1.1.2 Cerebroautoregulation

Cerebroautoregulation refers to the ability to maintain the baseline blood flow in the brain. Of the mechanisms mentioned, vessel control is considered one of the most influential, as it can be controlled both locally (e.g. via CO_2 concentration) and globally (e.g. via long-distance neuronal signalling) (see Fig. 1.5A). The amount of blood delivered to the brain (Cerebral Blood Volume, (CBV)) and the rate at which it is delivered (Cerebral Blood Flow, (CBF)) can be tightly controlled by changing the arterial diameters. CBF is the quantity of blood (mL) reaching 100 g of brain tissue per unit of time (min), and is measured in mL/ 100 g/ min (which will be shown in more detail in Eqn 1.14). Arterial CBV (aCBV) can also be quantified, either as a fraction (0 to 1), as a percentage, or as ml blood per 100 ml of tissue, and is a measure of the intravascular volume of arteries and arterioles in the entire voxel volume [223]. Constriction and dilation of the vessels can alter vascular resistance, the blood pressure (BP), and subsequently the rate of blood flow. Control of the vasculature also includes vascular tone, which encompasses arterial tone, venous tone and capillary flow. For example, BP increases during exercise which causes the arteries constrict to maintain constant blood flow in the brain. Fig. 1.5B shows that changing the diameter of vessels in this way during exercise affects oxygen levels, in order to meet the increase in demand for O_2 throughout the body. Importantly, under normal conditions, CVR maintains a narrow baseline, within set limits, to prevent neuron damage, decline of cognition, or in the worst-case cell death. However, in ageing and disease this CVR, and therefore brain health, deteriorates [141].

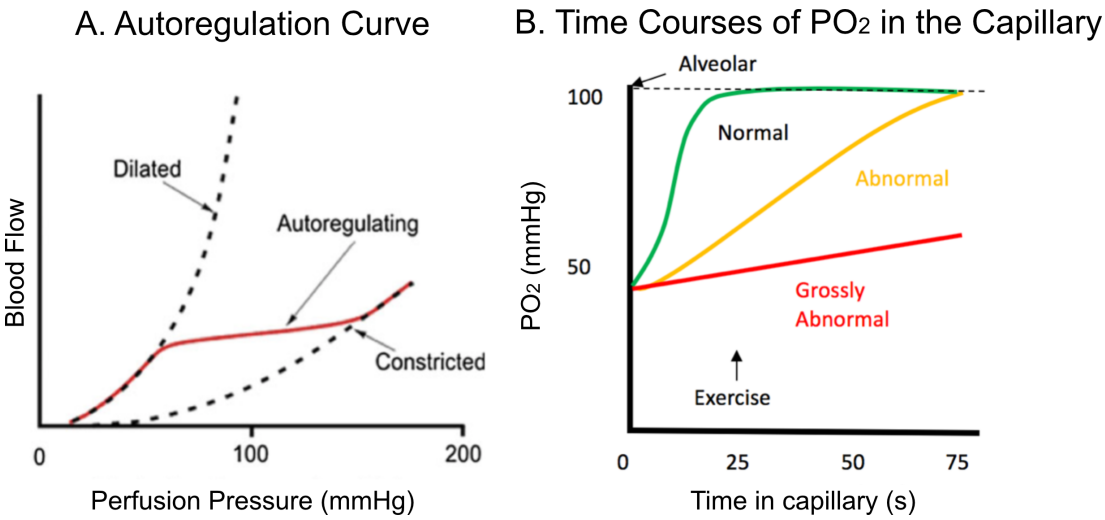


FIGURE 1.5: **Cerebroautoregulation.** Autoregulation Curve changes blood flow with dilation and constriction of blood vessels within set limits (based on Klabunde cvphysiology.com and [181]). B. Time course of PO_2 in the capillary. Changes in oxygen uptake along pulmonary capillaries under normal, abnormal and grossly abnormal conditions, where the latter two struggle to reach the baseline seconds (s). PO_2 mmHg (Pulmonary Oxygenation per millimetres of mercury), mmHg (millimetres of mercury). Based on West and colleagues (2011) [246].

1.1.3 Cerebrovascular Disease

As mentioned, one of the main motivations for investigating CVR is that it changes in health and disease. During healthy ageing, cerebral autoregulation at rest is often maintained consistently. However, the mechanisms that maintain cerebral autoregulation, including CVR, can change with ageing and and disease. This results in more complex and unpredictable effects than in a 'healthy' brain. Subsequently, measurements of CVR also become more difficult to model [181]. For example, cerebrovascular reserve can be returned to baseline if a person is healthy by simply increasing heart rate, CO_2 levels and BP. The compensatory mechanisms, such as receptors that monitor BP, become more sensitive with age. Therefore acting to maintain baseline CVR may be difficult compared to those who are younger [181]. For example, one short term protective mechanism used to maintain CVR is to increase BP. However, if this mechanism is used long term it can become a pathological problem, hypertension. Constantly raised BP leads to damaging and stiffening of the arteries in the long term. This impacts the ability of the arteries to constrict and dilates, which results in a decreased CVR response. Unfortunately, this can have a detrimental impact on blood supply to the brain.

Furthermore, ageing is a known risk of cerebrovascular disease (CVD), which is pertinent to our increasingly ageing population. The UK Government Office for Science reviewed the future of an ageing population. Data (last sampled in 2004) found older people from ethnic minorities were disproportionately affected by adverse health outcomes and co-morbidities associated with ageing [163, 21]. Although immensely heterogenous, older, ethnic populations faced a shared underlying disadvantage and deprivation caused by racism and discrimination. One of the most concerning aspects of this for CVD risk factors was the barriers faced when trying to access healthcare, which increased comorbid healthcare

problems. As a result using age as a risk factor for CVD may not be as simple as initially believed. More data is therefore needed for populations that are normally under-represented in research. Fortunately, there are recent initiatives to collect large, open source databases (e.g. UK BioBank of almost 49,000 participants (UKBioBank [220]), and in future these can be used to help elucidate more details of the relationships between age and CVD.

CVR also changes in other vascular diseases, which often increase with age such as neurodegeneration [94]. Understanding the relationship between age and CVD will also help to provide insight into the differences between healthy ageing and unhealthy ageing (i.e. neurodegenerative diseases such as vascular dementia). Furthermore, separating out the order of CVR deterioration and disease progression will hopefully help to separate out the cause and effect in neurodegenerative diseases. This would provide further applications for MRI CVR as a clinical biomarker (which will be discussed further in section 1.9.

1.2 Vasodilatory Stimuli

In order to more closely investigate CVR responses it is possible to research them in more detail. One option would be to monitor participants CO_2 change without any task (i.e. resting state). However a potential issue is that, during normal breathing, the natural variation in CO_2 varies considerably between people. Therefore, it would be important to study whether people with only a small change in CO_2 have correspondingly worse CVR images. Additionally, it would be important to consider what would be the minimum CO_2 variability required to produce MRI images of an acceptable quality [106]. In a clinical setting, analysis becomes particularly tricky due to such a small, often undetectable signal.

Methods of increasing CO_2 artificially can vary. CVR can also be altered through artificial stimulation (inhaled CO_2 [79], pharmacological substances (e.g. Acetazolamide [39]), and breath holding (BH) [231]). These can potentially be used to calibrate inter/intra-individual differences when measuring CVR.

Firstly, Acetazolamide is a pharmacological substance used clinically for glaucoma and other illnesses. Acetazolamide is a carbonic anhydrase inhibitor drug that causes vasodilation of vessels. Acetazolamide causes vasodilation in a similar way to hypercapnia, via pH/H+ ions. However, the pH is altered by preventing the excretion of H+ ions through the kidneys, rather than preventing the CO_2 from being expired by breathing. One disadvantage of acetazolamide that it is not recommended for use in the elderly. Another is that the main effects last around half an hour. Consequently, this does not allow for easy control of the stimulus over short periods of time, which is normally required for MRI research studies [168]. One benefit of acetazolamide is that it is stable, and clinicians may be more comfortable injecting something than administering CO_2, which requires more equipment and gas safety training etc.

In comparison, BH is very easy to perform, you simply ask participants to hold their breath for a set amount of time. However, CO_2 concentration for each participant is hard to determine and reproduce. Urback et al. (2017) [231] systematically reviewed 54 articles of MRI that used BH and concluded that measurement characteristics (e.g. normalizing signal to end-tidal CO_2) required comparison to non-BH induced methods of CVR to normalise the response.

In contrast, CO_2 gas can be inhaled via a medical mask so that the amount of CO_2 breathed in and out can be quantified. Delivering CO_2 artificially can be performed by inhaling air mixed with CO_2 and monitoring end-tidal

CO_2 (as a surrogate/proxy for arterial CO_2), which is often considered to be the most reliable and reproducible [81]. Unfortunately, around ¼ of patients are unable to perform the gas inhalation task, which can produce a sensation of breathlessness. CO_2 has other advantages such as quick washout times allowing for repeated stimuli.

The amount of CO_2 given is an important consideration when measuring CVR. Different participants have different ventilatory responses, so even if they all received a fixed amount of CO_2 'dose' during a gas inhalation challenge. Mark and colleagues (2010) compared fixed models to a newer automated feed-forward system (RespirAct^{TM}) that tailored the amount of CO_2 based on a participant's individual end-tidal results [146]. They showed that completely fixed CO_2 fraction inhalation was less beneficial than tailoring to an individual's $PETCO_2$. Tailoring the stimuli to each individual's baseline, where the stimulus can be the 'equivalent' amount of ventilatory stimulus across a number of individuals should result in a more uniform CVR response. Additionally, the newer method provided faster, more stable and more gradual transitions, which would also be more beneficial for diagnostics. Assumptions and potential drawbacks of the RespirAct^{TM} will be mentioned in more detail in relation to the other methods used in this thesis (i.e. manual gas delivery and a semi-automated gas delivery device), and the subsequent results of chapters 3, 4 and 5 in relation to other studies in their respective discussion sections.

The timing of CO_2 inhalation administration is another important consideration Blockley, Harkin and Bulte (2017) [31] demonstrated this by comparing a conventional steady state block of CO_2 gas inhalation stimulus [144], to a sinusoidally modulated stimulus. The sinusoidal stimulus so named due to presenting the increase and decrease of CO_2 as a sinusoidal waveform. Analyses suggested that with only 3–5 minutes of sinusoidal method data the quality of data was the same as 7

minutes of conventional data. This ability to rapidly acquire images without detriment to the quality of the data would be more practical for clinical settings. Additionally, this delivery can be tailored to the individual participants baseline levels. For example, using a machine called the RespirAct^{TM} (Thornhill Research Inc., Canada) gases are mixed to increase CO_2 levels in a controlled and quantifiable manner. However, one disadvantage of this is the expense of the kit required, as well as requiring extra training. Overall, of those mentioned, gas inhalation was the most stable and quantifiable 'stress test' for brain CVR measurements.

The next aspect of research to consider was how to measure these artificially induced changes in CVR. There are now several non-invasive, non-radiation related CVR measurements with various advantages and disadvantages. For example, transcranial Doppler Ultrasound (TCD) uses very high frequency sound waves to make non-invasive images of blood vessels and measure the velocity of blood within them. TCD has been used to validate the effects of CO_2 as a vasodilator and helped to determine how CO_2 narrows the blood vessels and consequently changes the vasculature tone through a process called the arterial baroreflex. Although TCD has a good temporal resolution, it has a poor spatial resolution, which makes it difficult to locate changes in CVR [4].

1.3 Theory of MR

This thesis will focus on MRI. MRI is a non-invasive method of measuring CVR. The next section will explain MR theory in more detail, beginning with the quantum mechanical foundations before progressing to the classical electromagnetic behaviour that enables imaging.

1.3.1 Nuclear Magnetic Resonance

Nuclear Magnetic Resonance (NMR) is the fundamental quantum mechanical basis for Magnetic Resonance. NMR is a quantum phenomenon where atomic nuclei in a magnetic field absorb and re-emit electromagnetic radiation at a specific resonant frequency [170, 28, 195]. Several quantum principles of NMR are essential for understanding Magnetic Resonance Imaging (MRI): nuclear spin, energy level transitions, and the quantum nature of resonance.

1.3.2 Nuclear Spin Angular Momentum

Nuclear spin angular momentum is an intrinsic quantum mechanical property of atomic nuclei. Nuclei with an odd number of protons and/or neutrons possess a non-zero nuclear spin quantum number (e.g., hydrogen ^{1}H with spin I = ½). This quantum mechanical spin creates an associated magnetic moment, which is quantised and can only exist in discrete orientations relative to an external magnetic field. The nuclear spin quantum number I can be either an integer or half-integer value. For example, deuterium ^{2}H has I = 1 (integer spin), whilst hydrogen ^{1}H has I = ½ (half-integer spin) [46]. The magnetic moment arises from this intrinsic quantum property and determines the nucleus's ability to interact with magnetic fields. Figure 1.7 shows the precession of the magnetic moment along the B_0 axis, and the equation of motion for the magnetic moment is:

$$\frac{d\boldsymbol{\mu}}{dt} = \gamma \boldsymbol{\mu} \times \mathbf{B_0} \tag{1.2}$$

where μ is the magnetic dipole moment vector, γ is the gyromagnetic ratio, B_0 is the static magnetic field vector and $\times$ denotes the cross product.

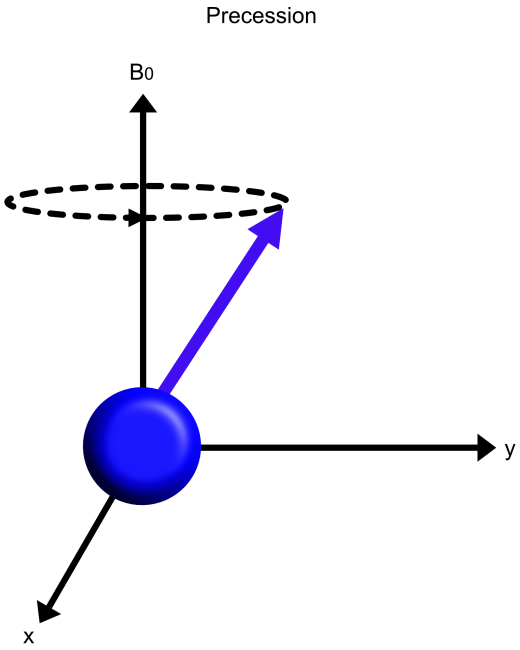


FIGURE 1.6: **Precession.** A: A hydrogen nucleus precesses around the magnetic field B_0.

1.3.3 Quantum Energy States and Population Distribution

When placed in a static magnetic field B_0, nuclear spins occupy discrete quantum energy states. For spin-½ nuclei like hydrogen, there are two possible orientations: spin-up (lower energy, $mI = -\frac{1}{2}$) and spin-down (higher energy, $mI = +\frac{1}{2}$) to the magnetic field (Fig. 1.7B). This gives the spins two different possible energy states (also known as Zeeman energy states) E+ and E-, and the energy difference (ΔE) between these quantum states is given by:

$$\Delta E = \gamma \hbar B_0 \tag{1.3}$$

where B_0 is the static magnetic field, γ is the gyromagnetic ratio and $\hbar$ is the reduced Planck constant.

The population distribution between these quantum states is shown in the following Boltzmann distribution Eqn. 1.4:

$$\frac{N_-}{N_+} = \exp\left(\frac{-\Delta E}{k_B T}\right) = \exp\left(\frac{-\gamma \hbar B_0}{k_B T}\right) \tag{1.4}$$

where ΔE is the difference between energy states, k_B is the Boltzmann constant and T is the absolute temperature. The thermal equilibrium at body temperature is calculated for 310° kelvin (37° C) at 3T. This results in a small population in the lower energy state, which is about approximately 10 nuclei per million hydrogen atoms at this thermal equilibrium.

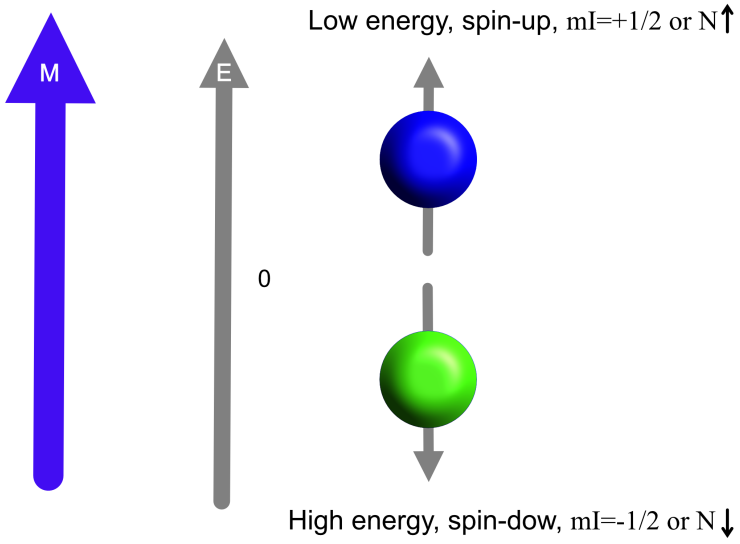


FIGURE 1.7: **Quantum Energy States** B: Populations of high and low-energy quantum spin states in relation to B_0.

TABLE 1.1: **Atomic Isotopes for MRI.** Table of different atomic isotopes, their nuclear spin quantum numbers, natural abundance, gyromagnetic ratio in megahertz (MHz) and abundance in the human body [32].

Atom Isotope	Nuclear Spin (I)	Natural Abundance (%)	Gyromagnetic Ratio MHz T^{-1}	Abundance (Body)
Hydrogen (^{1}H)	½	99.99%	42.58	High
Carbon (^{13}C)	½	1.10%	10.71	Medium Low
Fluorine (^{19}F)	½	100%	40.08	Low
Phosphorous (^{31}P)	½	100%	17.25	Low

Table 1.1 shows the nuclei most commonly used for MRI, selected for their spin-½ quantum properties and abundance in biological tissues. Hydrogen is particularly favoured due to its high natural abundance and prevalence in water molecules throughout the human body. Hence, hydrogen imaging will be the focus for the rest of the thesis.

1.3.4 Quantum Transitions and Resonance

Transitions between quantum energy states occur when electromagnetic radiation matches the energy difference between states. The resonance condition is:

$$h\nu = \Delta E = \gamma \hbar B_0 \tag{1.5}$$

where:

- *hbar* is Planck's constant, which relates the energy of electromagnetic radiation to its frequency
- ν is the frequency of the electromagnetic radiation in hertz (Hz)

- ΔE is the energy difference between two quantum energy states, measured in joules (J).
- γ is the gyromagnetic ratio
- B_0 is the strength of the external magnetic field, measured in tesla (T)

This gives the fundamental resonance frequency (Larmor frequency). Equation 1.6 shows that the precessional frequency (MHz) is proportional to the gyromagnetic ratio (MHz/T) multiplied by the strength of the magnetic field Tesla (T):

$$\omega_0 = \gamma B_0 \tag{1.6}$$

Radiofrequency (RF) pulses at this precise frequency can therefore induce quantum transitions, promoting nuclei from the lower to higher energy states or vice versa.

1.4 Classical Electromagnetic Behaviour

While the underlying physics is based on quantum mechanics, the macroscopic behaviour of large ensembles of nuclear spins can be described using classical electromagnetic theory. This classical description forms the basis for understanding MRI signal generation and manipulation.

1.4.1 Classical Magnetisation Vector

The small population excess in the lower energy quantum state creates a net classical magnetisation vector (M_0) aligned with B_0. This bulk magnetisation can be treated as a classical magnetic dipole that precesses around B_0 at the Larmor frequency. The precession of individual magnetic moments is coherent

(i.e. in-phase) initially, but environmental interactions cause gradual dephasing (i.e. incoherent / out of phase). This classical precession model, whilst derived from quantum origins, allows us to understand signal generation through electromagnetic induction.

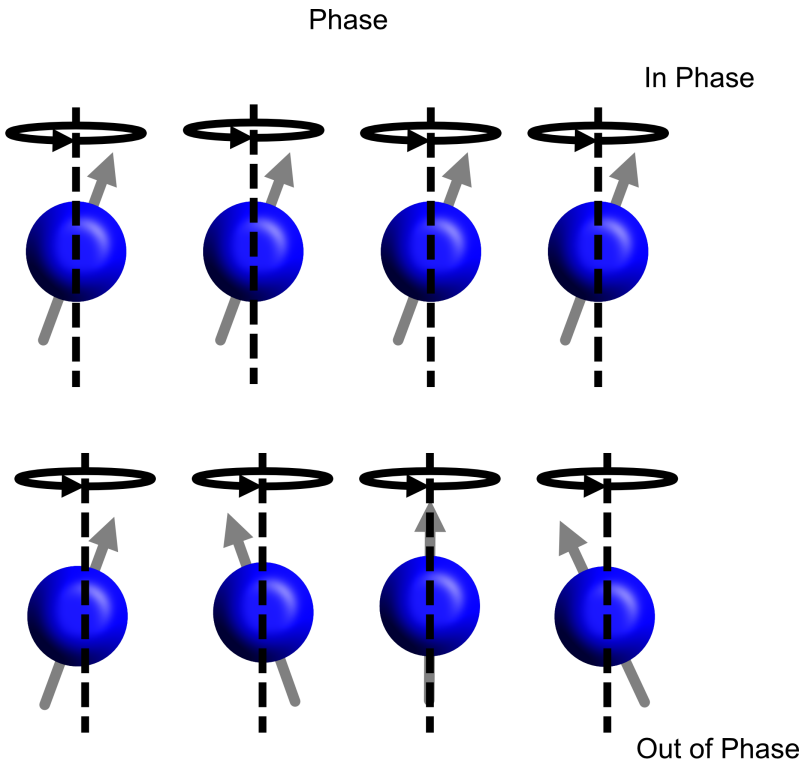


FIGURE 1.8: **Classical Phase Coherence.** Comparison of magnetic moments that are in and out of phase, demonstrating classical electromagnetic behaviour of the bulk magnetisation.

1.4.2 Classical RF Excitation

RF pulses applied at the Larmor frequency can rotate the net magnetisation vector away from its equilibrium position (Fig. 1.9A). For example, a 90° pulse rotates the bulk magnetisation completely into the transverse plane (Mxy)(in to phase)(Fig. 1.9B). Whereas, a 180° pulse inverts it into the longitudinal plane (Mz), so that Mz = -M_0 (Fig. 1.9C). A 180° flip angle pulse requires twice the energy of a 90° pulse. In MRI, this is performed using an RF coil that can both transmit and receive oscillating RF signals. The flip angle is determined by classical electromagnetic theory:

$$\text{Flip Angle} = \gamma B_1 \times \text{Duration of RF Pulse} \tag{1.7}$$

where B_1 is the amplitude of the RF magnetic field.

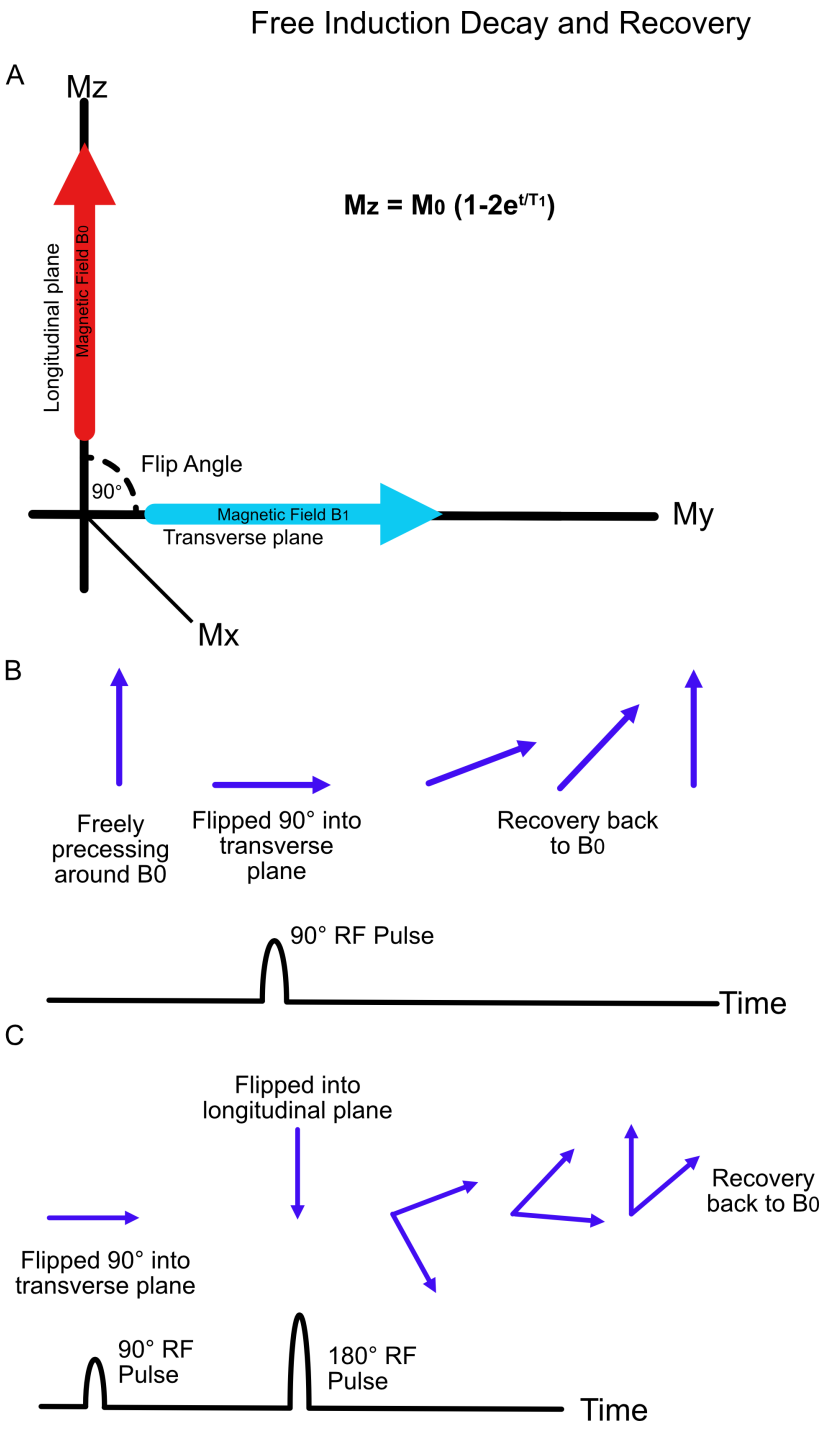


FIGURE 1.9: **Classical Magnetisation Rotation.** A: The rotation of magnetisation between longitudinal and transverse planes. B: The effect of a 90° RF pulse on the bulk magnetisation vector.

1.4.3 Classical Relaxation Processes

After RF excitation, the magnetisation returns to equilibrium through classical relaxation processes that have quantum mechanical origins, but are described phenomenologically.

T_1 Relaxation (Spin-Lattice)

T_1 recovery represents the classical return of longitudinal magnetisation to its equilibrium value. This process involves energy transfer from the excited nuclear spin system to the surrounding molecular environment (the "lattice"). The recovery follows exponential kinetics as defined by the following Eqn 1.8:

$$M_{z_t} = M_0 \left(1 - e^{-t/T_1}\right) \quad (1.8)$$

T_1 is defined as the time constant for 63% recovery of the longitudinal magnetisation (Fig. 1.10). The rate of T_1 recovery varies between tissues. Water has slower T_1 recovery compared to fat due to molecular environment differences. Water molecules have fewer interactions with their surroundings (primarily through O_2). In contrast, fat molecules have more opportunities for energy transfer, leading to faster T_1 recovery, via interactions with the carbon chains, .

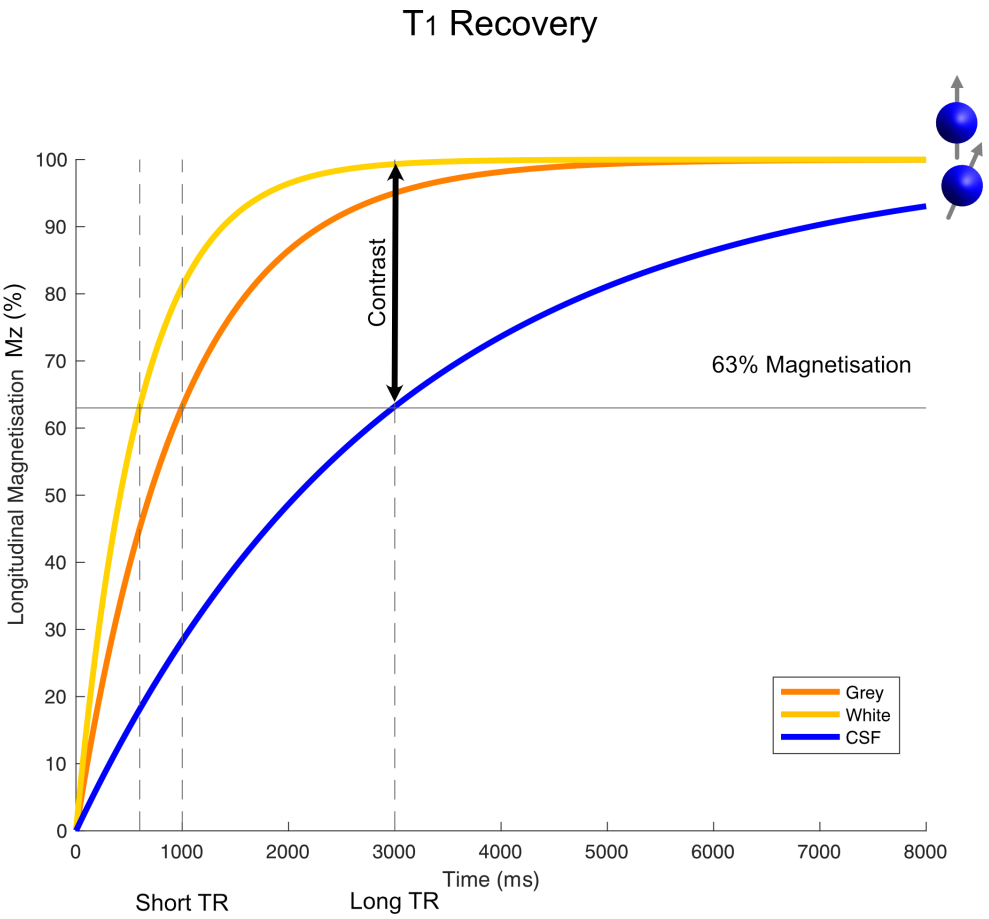


FIGURE 1.10: **Classical T_1 Recovery.** Exponential recovery of longitudinal magnetisation for differentiation between different brain tissues. CSF (cerebrospinal fluid), ms (milliseconds), M_z (longitudinal magnetisation), TR (repetition time). Code edited from github and formatted in Affinity 2.

T_2 Relaxation (Spin-Spin)

T_2 relaxation describes the classical loss of phase coherence in the transverse plane. This irreversible dephasing occurs due to local magnetic field variations experienced by individual spins, causing them to precess at slightly different frequencies:

$$M_{xy_t} = M_{xy} \cdot e^{-t/T_2} \quad (1.9)$$

T_2 is the time constant for 63% decay of transverse magnetisation (Fig. 1.11). The dephasing rate depends on molecular mobility as more rigid environments lead to faster T_2 decay. T_2 decay occurs at least 5-10 times faster than T_1 recovery. For example, in grey matter, T_1 is approximately 1200 ms while T_2 is about 80 ms. Notably, T_1 and T_2 values tend to converge for pure liquids like water. Fat has a faster T_2 decay than water due to its molecular structure.

T_2* Decay (Free Induction Decay)

T_2^* decay combines two components. Firstly, true T_2 decay, the irreversible spin-spin interactions. Secondly, T_2' decay, the reversible dephasing due to field inhomogeneities. B_0 field inhomogeneities arise from macroscopic sources (e.g., air-tissue interfaces in sinuses) and mesoscopic sources (e.g., susceptibility differences between deoxygenated blood and tissue) and subsequently cause regional differences in the Larmor frequency. These inhomogeneities cause spins to precess at slightly different frequencies, leading to more rapid dephasing than T_2 alone, and phase coherence is then lost. Consequently, T_2* decay is always faster than T_2 decay (Fig. 1.11).

In practice, the observed signal decay combines true T_2 relaxation with additional dephasing from macroscopic field inhomogeneities:

$$\frac{1}{T_2^*} = \frac{1}{T_2} + \frac{1}{T_2'} \tag{1.10}$$

where T_2' represents dephasing due to field inhomogeneities. These arise from air-tissue interfaces, blood vessels, and other susceptibility variations. Unlike T_2, the T_2' component is reversible through appropriate pulse sequences.

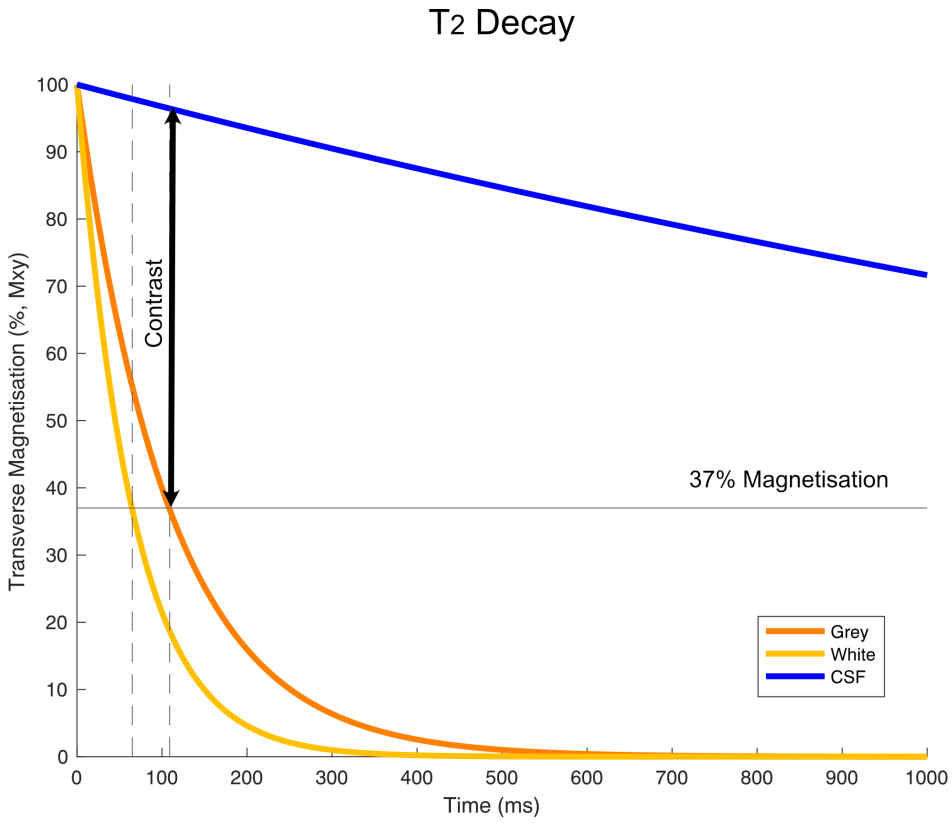


FIGURE 1.11: **Classical T2 Decay.** Exponential decay of transverse magnetisation showing differentiation between different brain tissues, with faster decay in brain tissue compared to CSF. CSF (cerebrospinal fluid), ms (milliseconds), Mxy (transverse magnetisation), TE (echo time).

1.5 Pulse Sequences and Signal Generation

MRI pulse sequences manipulate the classical magnetisation vector to generate contrast and spatial information. These sequences exploit the relaxation properties described above.

1.5.1 Spin Echo Sequences

A spin echo sequence uses a 90° excitation pulse followed by a 180° refocusing pulse (Fig. 1.12). The 180° pulse, applied at TE/2, reverses the dephasing caused by static field inhomogeneities, allowing (in theory) the measurement of true T_2 relaxation. The signal intensity is calculated with the following Eqn. 1.11:

$$S = \rho \left(1 - e^{-TR/T_1}\right) e^{-TE/T_2} \tag{1.11}$$

where ρ is the proton density, TR is the repetition time, and TE is the echo time. More specifically, repetition time (TR) is the time between repeated RF pulses and echo time (TE) is the time between the RF pulse and the read out of the signal.

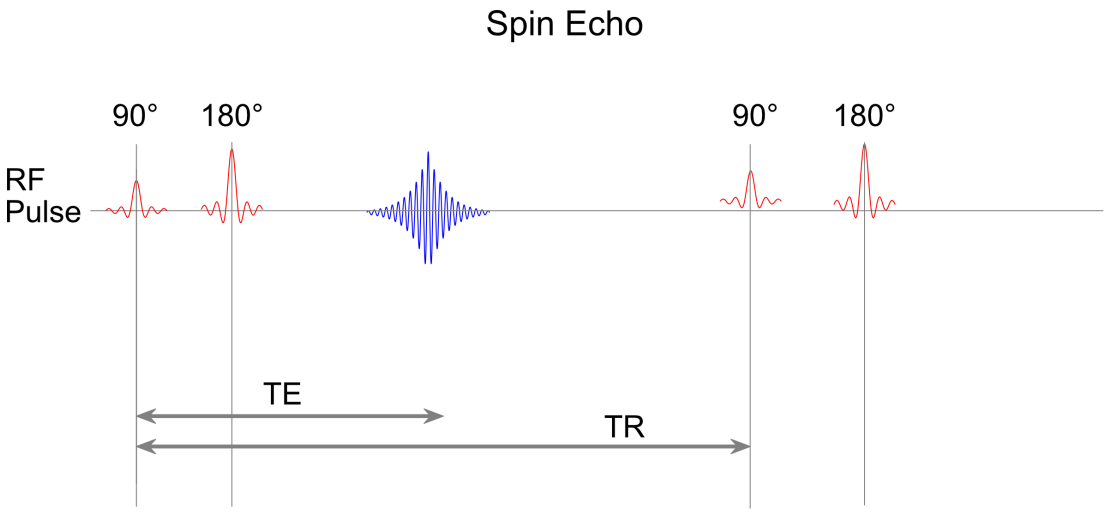


FIGURE 1.12: **Spin Echo Pulse Sequence.** Classical evolution of magnetisation showing dephasing after the 90° pulse and rephasing to form an echo after the 180° pulse. FID (free induction decay), RF (radiofrequency pulse), TE (echo time), TR (repetition time). MATLAB code based on github code and formatted in Affinity 2.

1.5.2 Gradient Echo Sequences

Gradient echo (GRE) sequences use magnetic field gradients rather than RF pulses to form an echo. A basic GRE sequence includes a dephasing gradient followed by a rephasing gradient Fig. 1.13. In GRE sequences, a negative gradient is used to dephase the magnetic moments spins, and so slowly precessing spins are slowed down more, and fast spins are sped up more. This accelerates the dephasing process. In contrast, the positive gradients reverse this effect, and cause slow spins to speed up, and fast ones to slow down. This causes rephasing and brings the spins back into coherence to form the gradient echo. When these two gradients are applied consecutively, it is called a bipolar application [147]. The signal equation for GRE includes T_2* weighting:

$$S = \rho \frac{\sin\alpha \left(1 - e^{-TR/T_1}\right)}{1 - \cos\alpha \cdot e^{-TR/T_1}} e^{-TE/T_2^*} \tag{1.12}$$

where α is the flip angle.

One limitation of GRE sequences is that they contain $T2^*$ effects, which increases the noise and amount of magnetic susceptibly artefacts resulting in a lower signal to noise ratio (SNR). Therefore, the choice of TE in GRE sequences becomes particularly important for controlling the $T2^*$ weighting and optimising the contrast.

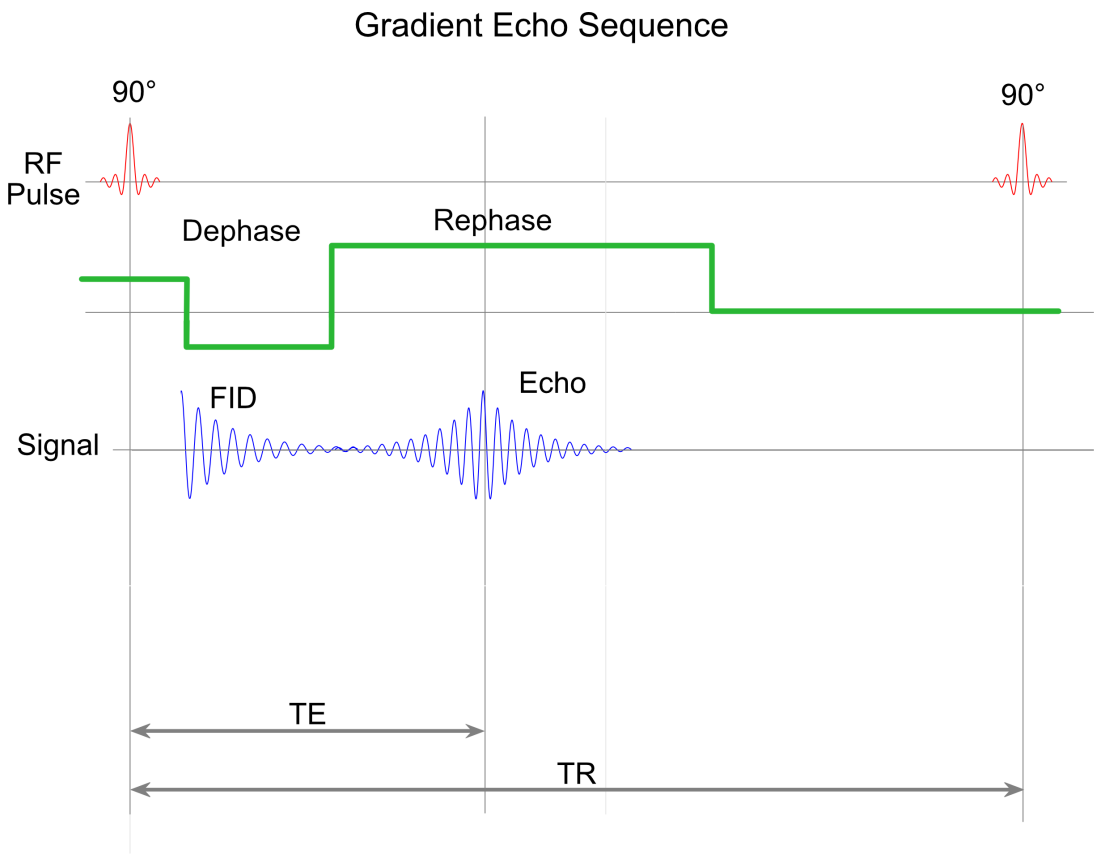


FIGURE 1.13: **Gradient Echo Pulse Sequence.** Classical magnetisation evolution with gradient-induced dephasing and rephasing. FID (free induction decay), RF (radiofrequency pulse), TE (echo time), TR (repetition time). MATLAB code based on github code and formatted in Affinity 2.

1.5.3 Inversion Recovery Sequences

Inversion recovery (IR) is the basis of the arterial spin labelling (ASL) method, which will be discussed later in section 1.8.1. IR can produce T_1 weighted images. The sequence begins with a 180° inversion pulse. After an inversion time (TI), a 90° pulse reads out the partially recovered magnetisation (Fig. 1.14). In the ideal case, the TE is as short as possible to minimise the T_2/T_2^* weighting of the signal. However, in reality, the TE varies depending on the acquisition method, e.g. around 2 ms for spiral acquisitions or longer for echo planar imaging (EPI) acquisitions. Therefore, the TI is important for controlling the weighting of the image. Additionally, although IR can be used to generate T_1 weighted images, it has broader applications beyond anatomical imaging, as the signal is based on reading the gradient echo rather than the FID. A variation of this sequence uses a 90° pulse instead of the 180° inversion pulse, which is known as saturation recovery.

The signal is calculated using the following Eqn 1.13:

$$S = \rho \left(1 - 2e^{-TI/T_1} + e^{-TR/T_1}\right) e^{-TE/T_2^*} \tag{1.13}$$

By choosing appropriate TI values, specific tissues can be nulled or highlighted, providing excellent T_1 contrast.

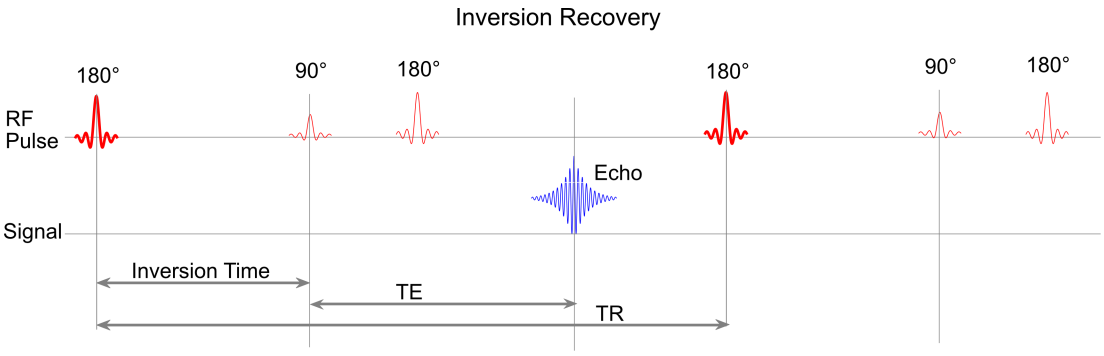


FIGURE 1.14: **Inversion Recovery Pulse Sequence.** Classical magnetisation recovery following inversion, demonstrating T_1 weighting control through inversion time selection. RF (radiofrequency pulse), TE (echo time), TI (inversion time), TR (repetition time). MATLAB code based on github code and formatted in Affinity 2.

1.6 MR Hardware

Figure 1.15 shows the official photos of the 3T Philips Ingenia scanner and head coil (Philips Medical Systems, Best, NL). Figure 1.15B shows the dStream 32 channel head coil in the closed configuration, with the two mirror options to the left of it.

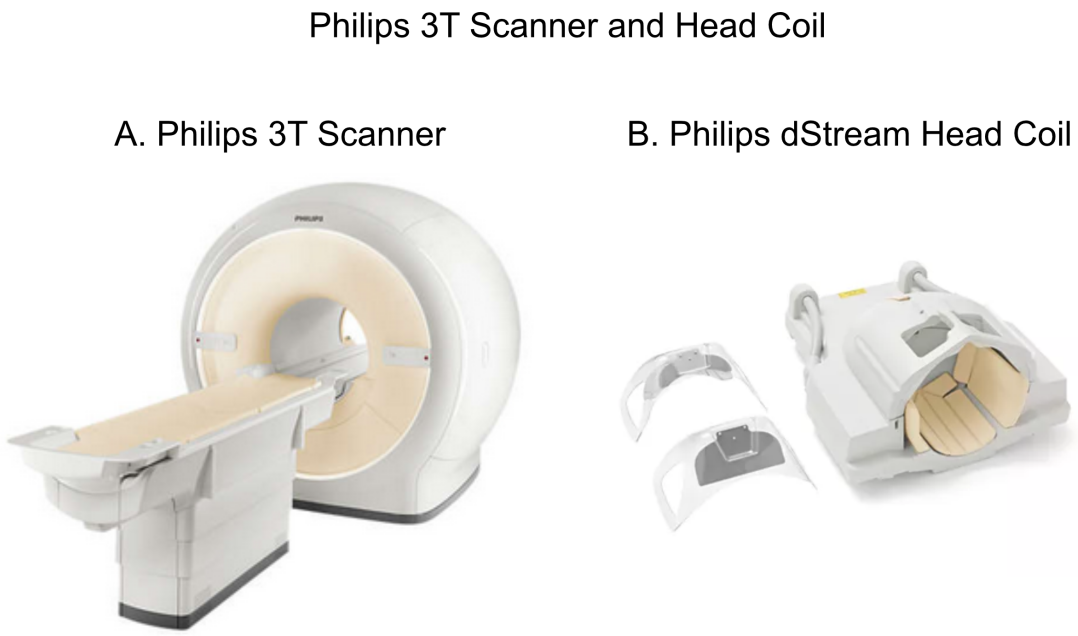


FIGURE 1.15: **Philips 3T Ingenia Scanner and Head coil.** A: shows the scanner with a 70 cm bore, with a maximum field of view of 55 cm. B: Shows the Philips dStream 32 channel head coil. Images from Philips website Link A and Link B.

Figure 1.16A shows a 3T GE Premier (Waukesha, WI, USA) scanner and the vendor's 48 channel head coil (Fig. 1.16B). The 'spacer', a piece of plastic that raised the top part of the head coil, was used to provide more room for the gas delivery mask kit. This was used for all participants for consistency. The peripheral pulse (PPU) and respiratory belt were also used to record participants' heart rate and respiratory rate.

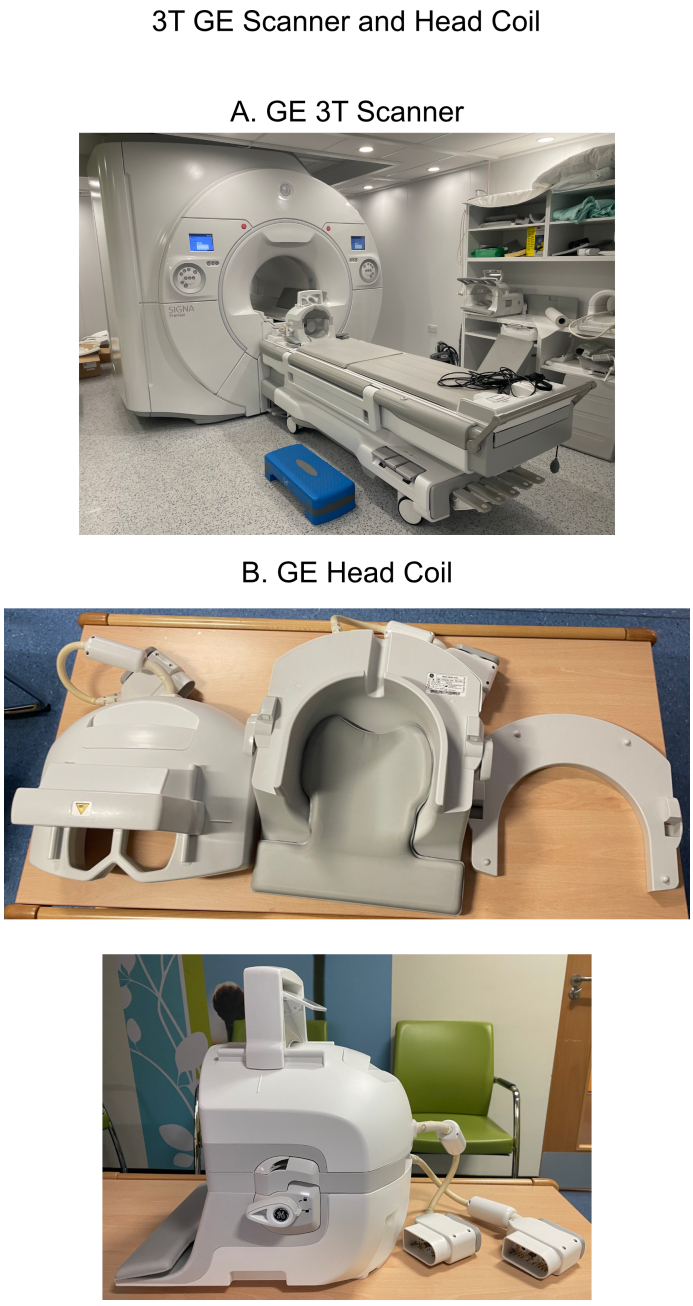


FIGURE 1.16: **GE Healthcare 3T Premier Scanner and Head coil.** A: Shows the GE scanner with a 70 cm bore. B: Shows the GE Healthcare 48 channel head coil from above of the coil open with the top, bottom and spacer as three separate pieces, and also from the side view of the coil closed.

1.7 IMAGING

1.7.1 Creating an Image

Slice section makes it possible to image one individual slice of the brain at a time. This is done by exciting a specific 'slice' of the brain by applying a gradient in the z direction, so that the nuclei will have different resonance frequencies across the z-axis. It is then possible to select for a slice by altering the frequency of the RF pulse, which is applied to 'flip' the nuclei and produce a signal. This frequency (and a range of nearby frequencies) only excites the slice along the z-axis that is at the Larmor frequency. The transmit range of frequencies (the bandwidth) therefore determines the thickness of the slice.

After slice selection, the spatial information needs to be encoded. This uses a y-direction (phase encoding gradient) and x-direction (frequency encoded gradient). As mentioned, frequency encoding works by applying a gradient in a particular direction, so that the Larmor frequency differs with position. Whereas, phase encoding is a spatially varying gradient which is briefly switched on to encode position in the phase of the signal. K-space is an abstract space which stores this information about spatial frequencies. The phase encoding gradients are applied at different strengths for each repetition, and the frequency encoding gradients are applied during signal readout fills the k-space with this important data. The centre of k-space provides the information about the low spatial frequencies (i.e. image contrast). In EPI, multiple phase encoding blips are applied after each frequency encoding gradient to step through k-space. The periphery of k-space provides information about the high spatial frequencies (i.e. edges and finer details). Hence, the image resolution is determined by the size of k-space, with larger k-space resulting in a higher resolution. The field of view is determined by the spacing between the k-space points. To

visualise the image from the MRI, a Fourier transform is applied to the k-space data to convert it into the spatial domain. Doing this for multiple slices helps to create the final 3 dimensional (3D) image.

1.8 Functional MRI for Imaging Blood Flow in the Brain

Functional Magnetic Resonance Imaging (fMRI) is a sub-type of MRI that has a high spatial resolution (<1 mm) compared to electrophysiological brain imaging techniques (e.g., magneto- and encephalography (MEG and EEG)) [255]. With the introduction of higher strength three Tesla scanners, Schmitt et al. (2004) [204] noted the higher level of detail acquired compared to 1.5T systems. Most clinical MRI scanners operate at 1.5-3T. While more complex scans can take up to an hour to conduct, attempts to decrease image acquisition time are constrained by decreased spatial resolution [47]. One major disadvantage of MRI is its poor temporal resolution [229], which refers to the acquisition time between and during scans. A human 11.7 T scanner is now operational in Paris, and construction of an 11.7 T scanner at Nottingham will soon be underway. These will provide much higher spatial resolution for fMRI. fMRI encompasses several physiological measurement methods, which can be used to investigate cerebral function and haemodynamics. For example, this covers ASL (see section 1.8.1), Blood oxygen level dependent (BOLD) (see section 1.8.2) and phase contrast velocity (PCV) (see section 1.8.3). There are other methods which are not used in this thesis (i.e. vascular space occupancy (VASO)), so will not be mentioned in any more detail.

fMRI is a useful tool for investigating both cognitive and systems level neuroscience. At a cognitive level, mapping brain activation can be used to create functional

connectivity networks associated with various cognitive processes e.g. sensory (vision, touch, taste), memory, language and more complex functions (executive functions etc). More recently resting-state fMRI has been used to determine intrinsic connectivity networks [27]. At a systems level, fMRI has been used to investigate more advanced, large-scale, connectivity maps, e.g. the default mode network and salience networks. Additionally, this has resulted in more detailed network organisation methods, for example dynamic functional connectivity and consciousness (e.g. graph theory approaches), which have been used to elucidate more information about how the brain functions. Hence, research into functionality in the brain has taken a step away from the traditional, purely structure based networks. This thesis will specifically focus on the functional applications within the brain vasculature via CVR, and more clinical applications of fMRI will be discussed in the fMRI CVR section 1.9.

1.8.1 Arterial Spin Labelling

Arterial spin labelling MRI is a quantitative measure of cerebral blood flow that involves magnetically labelling the blood to quantify tissue CBF [102]. ASL refers to an MRI method that uses an endogenous contrast (water) to generate contrast in an MR image. This contrast is created via the manipulation of the arterial blood magnetisation. It uses RF pulses prior to image acquisition, with the aim of isolating inflowing signal for the quantification of flow/perfusion [223]. The labelling part of ASL is in reference to the RF pulse, or train of RF pulses, that are used to change the magnetisation state of blood (i.e. hydrogen in the water in the blood, that flows into the brain tissue), in order to differentiate it from stationary tissue. The control pulse is an RF pulse, or train of pulses designed to match the static tissue, whilst causing minimal perturbation to arterial blood. The image acquired after the preparation by a control pulse

is called the control image. The next image acquired, is after the preparation from a labelling pulse, which is called the labelled image. The labelled image is then subtracted from the control image to create the ASL difference image, also known as the perfusion weighted image or ΔM. This subtraction removes the static tissue signal, and subsequently shows the perfusion signal produced by ASL preparation. Labelling pulses can be spatially selective, targeting the blood outside the imaging volume (upstream as in Fig. 1.17). The blood is labelled at a position called the labelling plane. Figure (Fig. 1.17) also shows how the control image is subtracted from the labelled image to create the perfusion weighted image. A single post labelling delay (PLD) ASL, shown here involves images acquired with only a single label delay time. The post labelling delay time is defined as the time interval between the end of the labelling pulse and when the image is read out (sometimes referred to specifically as the centre of the imaging excitation pulse). During the PLD, the labelled arterial blood has time to flow through to the tissue of interest. The time between when blood is labelled and when it first arrives in the imaging voxel/slice is also referred to as the arterial transit time (ATT). As blood velocity increases in response to CVR, the ATT tends to decrease, which makes it another useful measure of brain health. Another related measure of interest is the arterial blood flow (aBF), which is the blood flow per unit volume in the large arteries (measured in mL/mL/min). The aBF can be quantified under the assumptions of the indicator-dilution theory from dynamic MR angiography with sufficient spatial and temporal resolution, but that is beyond the scope of this thesis [223].

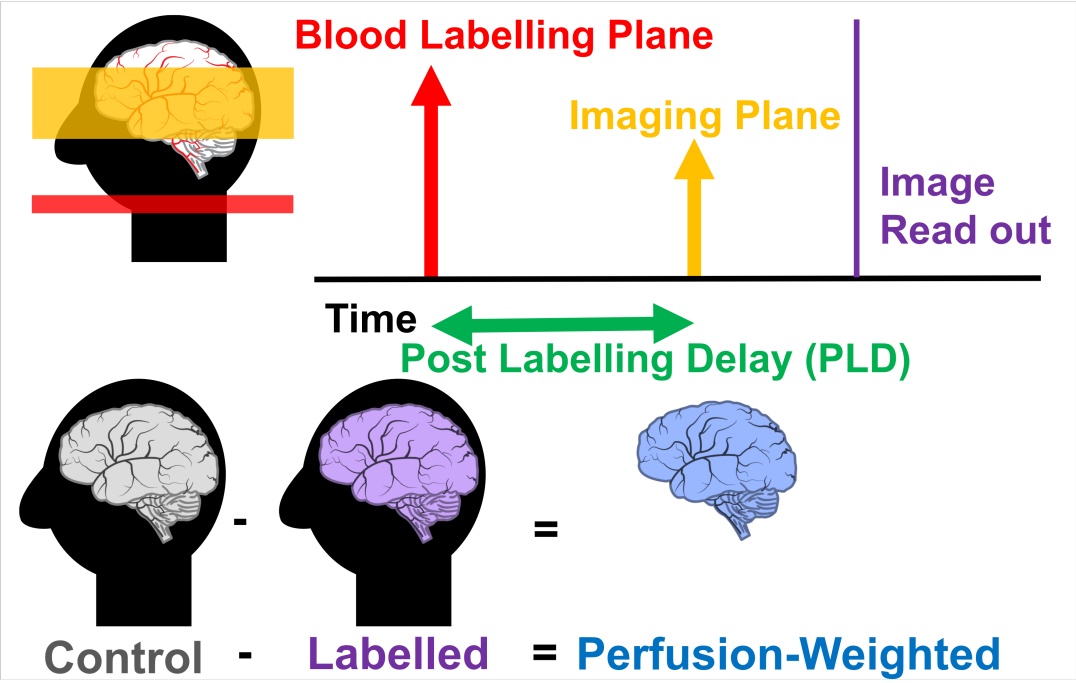


FIGURE 1.17: **Arterial Spin Labelling.** A. Creating the Perfusion-weighted Image (based on Elster, 2020). B. Time Scale of Imaging, 1. Magnetically label water in the blood upstream of the blood labelling plane. 2. Wait for blood to arrive at the imaging plane, 3. acquire images, 4. repeat in absence of labelled blood (control), 5. subtract the difference between the labelled and control images, 6. calculate cerebral blood flow (CBF) maps from amount of blood moved across the inversion time. Different sub-types of ASL can be created by changing the size, location and timing of the planes (Dai et al., 2008 [61], Elster, 2020 [70]). Post labelling delay (PLD).

Background 'noise' from the static tissue, present in a control image can cause problems for ASL SNR. Background suppression can therefore be used to decrease static tissue signal intensity through the use of RF pulses (e.g. saturation and inversion pulses) applied just before the images are read out. This method aims to improve SNR by reducing signal fluctuations in the labelled and control images. More specifically, saturation pulses applied just before and/or after the labelling/ control pulses aim to set the longitudinal magnetisation to zero, which should eliminate any label/control magnetisation transfer (MT) or slice profile mismatches.

Another method for increasing the SNR of the ASL images is via vascular suppression. This decreases the signal in the larger arteries during imaging, via application of crusher gradients after the excitation pulse. This dephases the signal based on the velocity profile of the spins specifically in the direction of the gradient [183]. The gradients target blood moving at a specific velocity (sometimes called vascular crusher gradients strength (VENC)) in the direction of the gradient to cause a 180° phase shift.

The following equation can be used for most kinds of ASL (with the need to make some modifications for PASL). This thesis will focus on pseudo-Continuous ASL (pCASL), which will be discussed in more detail in section 1.8.1. Equation 1.14 can be used to calculate CBF, for pCASL, which is based on Alsop and colleagues (2015)[7] and Buxton and colleagues (1998)[44]:

$$\text{CBF} = \frac{6000 \cdot \lambda \cdot \Delta M \cdot e^{\frac{\text{PLD}}{T_{1b}}}}{2 \cdot \alpha \cdot T_{1b} \cdot M_{0t} \cdot (1 - e^{-\frac{\tau}{T_{1b}}})} [\text{mL/min/100g}] \tag{1.14}$$

where:

- τ is the labelling duration (ms)

- PLD is the post-labelling delay (ms)
- α is the labelling efficiency (often assumed to be 0.85)
- λ is the blood-brain partition coefficient
- ΔM is the magnetisation difference
- T_{1b} is the longitudinal relaxation time of blood (ms)
- M_{0t} is the Equilibrium magnetisation of the tissue

It is important to note that several assumptions need to be met in order for this calculation to be robust. For example, labelling efficiency (α) refers to the inversion efficiency of the labelling pulse combined with loss of the label caused by background suppression. If all of the labelling pulse leads to a full inversion of blood magnetisation then the ASL labelling efficiency is said to be 1. Hence, the lower the labelling efficiency, the lower this number will be. The labelling efficiency for pCASL is generally assumed to be small enough to be ignored, or around 0.85. However, flow velocity (v), specifically the flow velocity of blood within the feeding arteries to the brain is known to effect the labelling efficiency of pCASL scans [13].

Labelling timings are also important. The Labelling duration (LD or τ) is the time of the labelling RF (or RF pulse train depending on the type of ASL), and the PLD is normally defined by the time of the first slice acquisition. However, the actual PLD for each slice may vary depending on the sequence used. These two measures together (LD + PLD) give the inflow time.

$T_1 b$ refers to the longitudinal relaxation time of the arterial blood. An assumption made with this value is that haematocrit levels are known to vary across populations, especially in patient groups. However, it is rare for people having a routine MRI to also require a blood test for haematocrit levels, for the calculation of the

T_1b value. Instead, T_1b is normally assumed to be ~1650 ms (for the healthy adult brain) at 3T [7, 64].

Next, an M_0 image is often used for the calibration of ASL to estimate the fully relaxed magnetisation. This is then separated into the M_{0b}, for the magnetisation of the blood and M_{0t} for the magnetisation of the tissue. These values are used to calculate the perfusion values, and to correct for the T_1 relaxation. The blood brain coefficient (λ) is scaled to the M_{0b} and the M_{0t}, and it is defined as the ratio between the blood and the tissue water concentration when at equilibrium (measured in mL of blood/g of tissue) [7]. Another assumption made about this equation is that λ of the tissue and veins are expected to be at an equilibrium. As eluded to, when these basic assumptions are not met, these issues can lead to under or over estimation of the ASL CBF values.

There are multiple types of ASL. In continuous ASL (CASL) blood is labelled as one single long pulse (~1000-3000 ms) via a continuous-wave RF pulse with a constant magnetic field gradient. The arterial blood that flows through a specific labelling plane is continuously inverted via adiabatic inversion [6, 8, 248]. Whereas, in pulsed ASL (PASL) blood water is labelled as it passes through a labelling 'slab' (of 15 - 20 cm thickness) instead of a large plane, with short RF pulses ~10-20 ms (Fig. 1.18)[7]. A common type of PASL used in clinical applications is Flow-Sensitive Alternating Inversion Recovery (FLAIR), which uses non-slice-selective global inversion pulses for the labelled image, and a slice-selective inversion pulse for the area of interest being imaged. This results in blood being labelled from both sides of the imaging volume [129]. Relatively new kinds of alternative ASL, such as velocity/acceleration selective (VS/Acc-ASL), target the blood with spatial selectivity (i.e. including blood flowing within the imaging volume) according to its velocity or acceleration [223]. This labels the blood nearer the capillaries, so that the signal decay is

decreased [250, 196, 75].

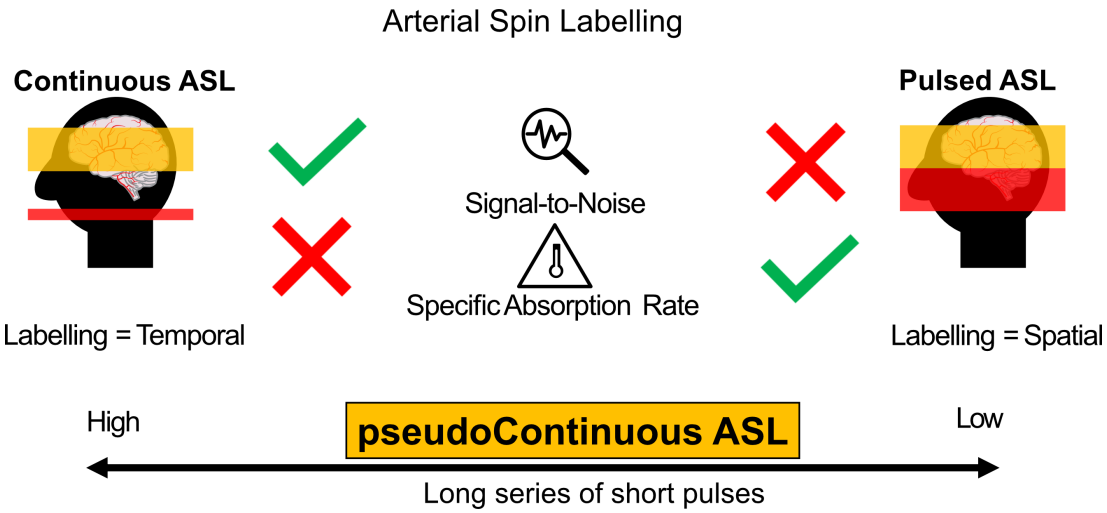


FIGURE 1.18: **Continuous versus Pulsed ASL.** Basic concept diagram for comparing the pros and cons of continuous and pulsed ASL (arterial spin labelling).

pseudo-Continuous Arterial Spin Labelling

Dai and colleagues (2008) [61] created a hybrid method of CASL and PASL called pseudo-Continuous ASL. pCASL uses a train of short RF pulses and aims to have the benefits of both CASL and PASL for measuring CBF. The pulses are applied at about ~ 1 per millisecond. The control image is creased using the phase modulation of the RF pulse train, so that the magnetisation transfer effects are the same as those during the labelling image, without disturbing the arterial blood magnetisation.

Balanced and Unbalanced pCASL

There are two main types of pCASL sequence, balanced and unbalanced (Fig. 1.19). The labelling pulse average gradient (G_{av}) is important for differentiating these two types. G_{av} is the average (mean) gradient applied simultaneously with the RF labelling pulses. These combine to create the flow-driven adiabatic inversion used to label the blood in pCASL. Balanced pCASL uses the same gradient waveform for both the label and control pulses, and the gradients are non-zero. This means that the G_{av} is also the same for the label and control pulses. In contrast, unbalanced pCASL uses different waveforms for the label and control pules. Here, the G_{av} for the label's pulse is non-zero, but the control pulse equals zero, because the refocusing gradient lobes are increased in amplitude so that the mean gradient is zero. One method to avoid problems with the MT effects is to use a separate RF transmission coil(s) to the coil(s) positioned over the arteries, so that power lose is decreased [9, 224, 257]. However, there still needs to be further improvements to the troublesome off-resonance effects at the labelling plane in unbalanced pCASL, to be equivalent to the smaller effects seen in balanced pCASL sequences.

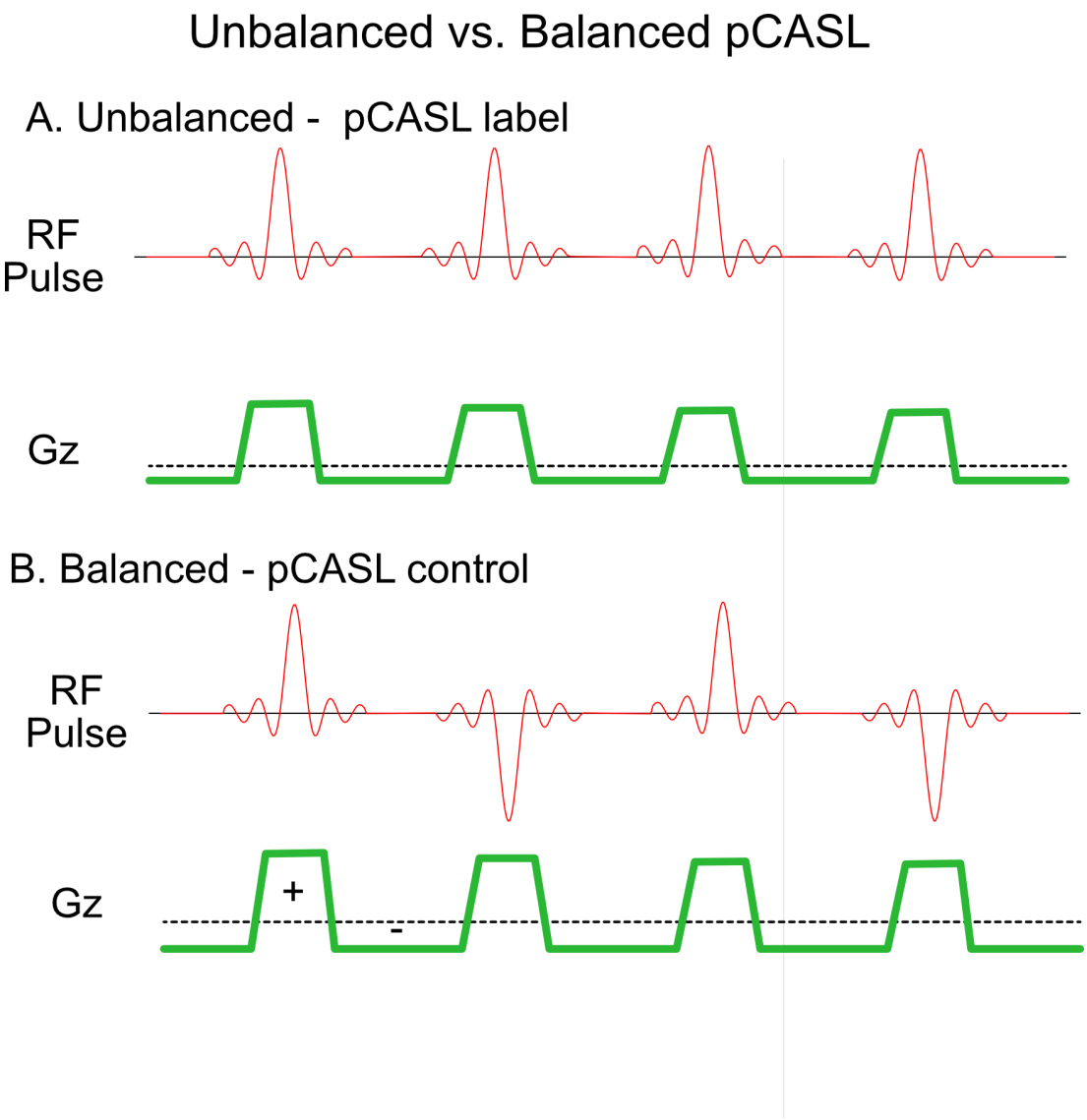


FIGURE 1.19: **Unbalanced vs. Balanced pCASL.** A. Unbalanced labelling and a balanced control sequence. Gz (Gradient in the z-direction), pCASL (pseudocontinuous arterial spin labelling).

Alsop and colleague's (2015)[7] 'White paper' proposed pCASL as the recommended ASL method, as its higher SNR provided more robust estimates of CBF (see Fig. 1.17). Although the paper published the protocol for use in Dementia, ASL has also proven useful for investigating multiple other diseases (e.g. stroke [241], brain tumours ([1]), Epilepsy ([132]), Neurodegeneration ((Alzheimer's [247]),(Huntingdon's disease [67])). ASL has also already proven useful in a range of diseases including cancerous tumours [171], microbleeds [59], lacunar stroke [26], sickle cell disease (most common cause of paediatric stroke) [92], and potentially many others. Additionally, this paper recommended specific PLD times depending on the cohort being scanned i.e. shorter for children (1500 ms), as they typically have a faster arterial transit time, around 1800 ms for healthy adults under 70 years, and a longer time of 2000 ms for older adults. A longer PLD was also recommended for patients, as there may be differences in their arterial arrival time.

Unfortunately, Aslan and colleagues (2010) [13] demonstrated that blood labelling efficiency decreased during the high flow, hypercapnic (high CO_2) conditions used to measure CVR. Essentially, the higher the velocity of the blood (induced by the CO_2), the lower the labelling efficiency. Hence, a major disadvantage of pCASL is that it is possible to underestimate CBF change during task and pathological conditions. They also proposed that labelling efficiency should be estimated on a participant-specific basis. As this method has not yet been standardised, models that include a calibration protocol for each individual may be required for use in a clinical setting until further refinement is standardised.

A major advantage of pCASL is that it is a quantitative measure of CBF. Additionally, newer versions of pCASL sequences include multiple post labelling delays. This makes it possible to calculate quantitative measures of arterial transit time, which can be used to establish CVR delay, and cerebral blood volume, to

separate out other physiological effects of the CVR response (discussed further in chapter 4). Multiple PLD (MPLD) methods allow the passage of the bolus through the tissue to be modelled. This has been useful in researching stroke and stenosis for the deficit in delay times. Another advantage is that ASL uses a natural endogenous tracer (water) rather than gadolinium [211].

A major disadvantage compared to other functional imaging (e.g. BOLD), is that pCASL has a low SNR. To increase the SNR, background suppression can be used to 'suppress' signal from specific tissues based on their T_1 value. By using special timing of multiple pulses it is possible to suppress as many T_1 values as possible, normally with the aim to suppress the T_1 of the fat tissue, so that the signal of the rest of the brain tissue is better. There are several physiological assumptions for basic ASL calculations. For example the labelling efficiency described above. Furthermore, there are other assumptions, such as that the T_1 of blood is also equal to the T_1 of tissue.

Multiple Post Labelling Delay ASL

Multiple PLD (MPLD) ASL refers to ASL protocols in which images are acquired with multiple (more than one) delay times [223]. In chapter 4, a MPLD pCASL sequence was used in order to measure changes in arterial transit time and arterial cerebral blood volume [228, 240]. MPLD, as the name suggests, uses more than one PLD and may also be referred to as 'multi-timepoint' ASL. This refers to tracking the bolus at multiple time points as it passes through the tissue (Fig. 1.20).

These are ASL sequences with varied time parameters (labelling delay and duration) used to investigate the kinetic ASL signal. These sequences can include repeated or successive PLDs. For example, Look-locker ASL uses a single labelling module, and then acquires several images at multiple time

points. It also uses a low flip angle during the image read out to decrease the saturation of the labelled blood, that was created by the earlier readouts [105].

This thesis used the MPLD "enhanced" pCASL technique provided by GE Healthcare which has 7 MPLDs, and was available on the GE MRI scanner at the University of Nottingham Medical school in the Sir Peter Mansfield Imaging Centre (SPMIC) [256]. The GE eASL pCASL sequence is a 'time-encoded' (also known as Hadamard encoded or te-pCASL) MPLD technique, which allows it to be more time efficient than other methods [244]. Each pCASL control/label module is split so that it has its own unique, varied control and labelling times, which are encoded into a matrix (Fig. 1.21). Typically these have short labelling and post labelling delays, which results in a mix of signals for each image. These images are then 'decoded' after acquisition. With this sequence it is possible to see the spatial flow of blood through the brain tissue over time. This results in a greater temporal efficiency as less acquisitions are needed per dataset [62, 104, 228, 238].

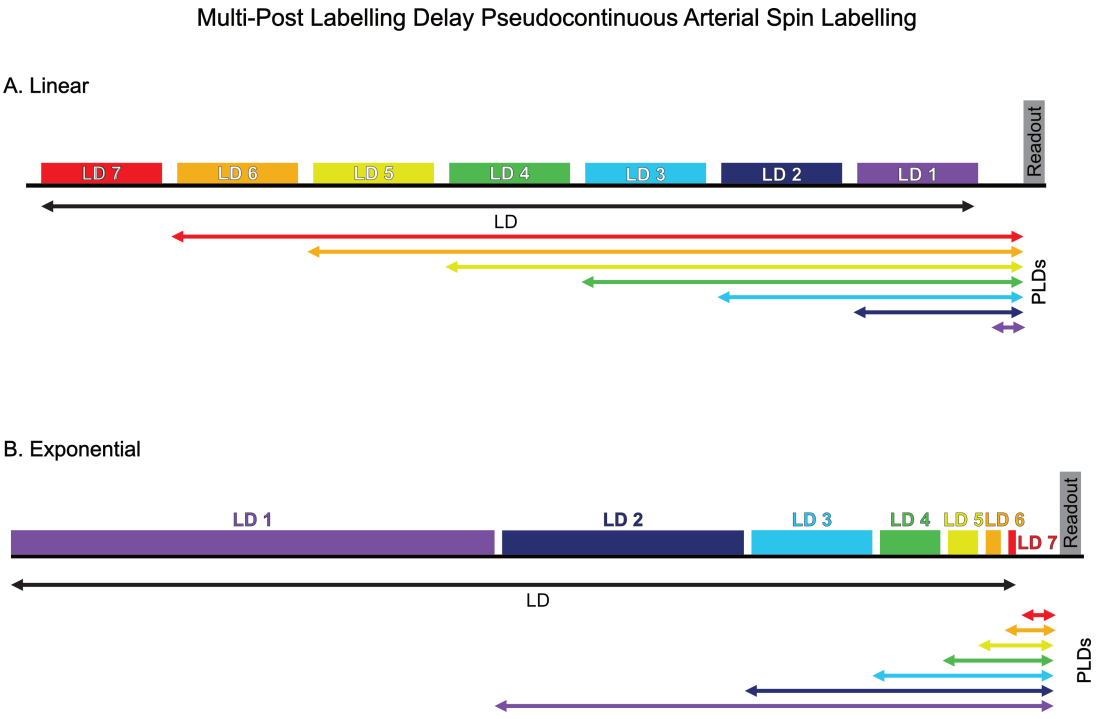


FIGURE 1.20: **Example of seven MPLD eASL sequence.** Schematic of post labelling delays (PLD) and label durations (LD) when encoding seven delays. The total LD is divided into 7 blocks, each with its own PLD and effective label duration (LD). A. For linear delays the blocks are divided equally. B. For exponential delays the blocks have exponentially increasing spacing. (multiple post labelling delay (MPLD), "enhanced" pseudocontinuous arterial spin labelling (eASL)(Based on the GE manual p12. DOC1685720, Rev:6. [91])

Time-encoded MPLD ASL

Hadamard-encoded ASL is an advanced MRI perfusion imaging technique that uses Hadamard encoding schemes to improve the temporal efficiency and SNR of ASL [244]. Hadamard-encoded ASL simultaneously labels multiple time points or arterial territories in a single acquisition, by applying different combinations of labelling/control conditions according to Hadamard matrices. This was later developed into time-encoded pCASL.

Figure 1.21 shows an example of a time-encoded pCASL labelling matrix, which was based on Hadamard encoded ASL [244]. Time-encoded pCASL labelling scheme uses control/label condition in a time-varying pattern (i.e. not simply alternated) [228]. For example, for a 7-MPLD scheme, there are seven different label (+1) and control (-1) conditions combinations within a 7x7 matrix. These each contribute to a signal that contains information about multiple PLDs.

Advantages of this method are that the resulting MPLD scan times are equal to that of a single PLD scan, but with more information about the arterial transit time etc. The main advantages of using this method is that it is more time efficient and also increases SNR. However, one disadvantage is that it requires a transform to extract the information from the composite signal into the different time points of the pCASL signal. Though, for eASL the scanner automatically outputs the pre-subtracted (i.e. decoded) data.

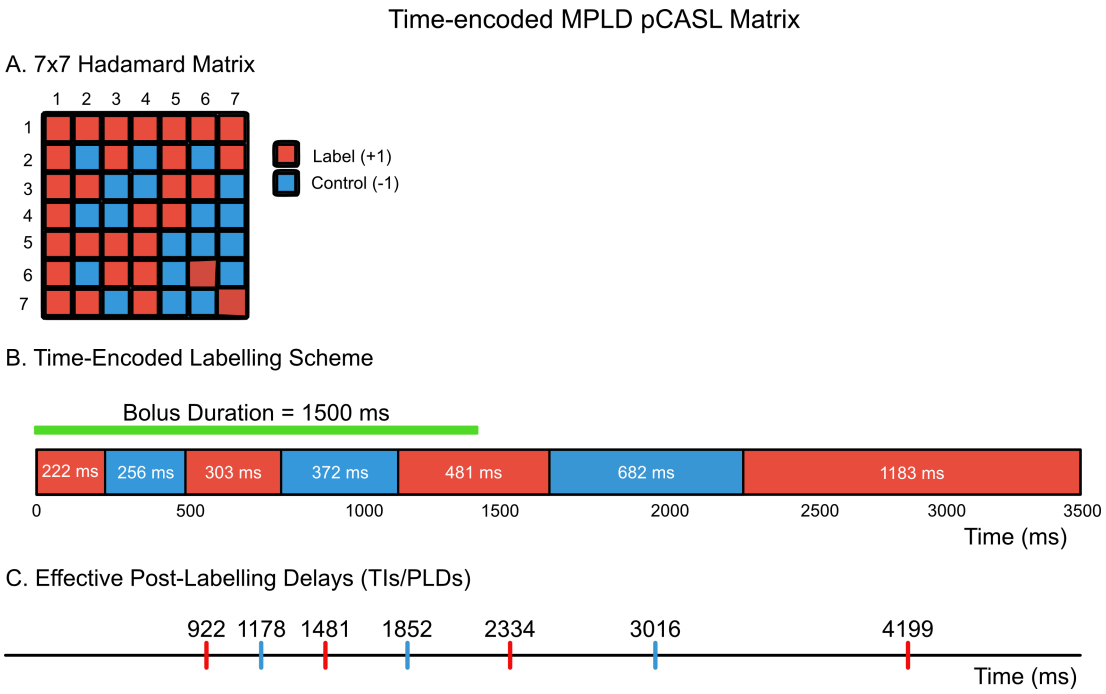


FIGURE 1.21: **Time Encoded pCASL.** Schematic of post labelling delays (PLD) and label durations (LD) when encoding seven delays. A. 7x7 Hadamard Matrix representing the 7 MPLD eASL sequence used in Chapter 4, with red squares for the labelled blocks (+1) and blue squares for the control blocks (-1). B. Time-Encoded Labelling Scheme, with the different LD. C. Effective Post-Labelling Delays (TIs/PLDs). The label durations still follow an exponential pattern to compensate for T_1 decay, with the longest block (1183 ms) providing substantial signal for the last time points. Inversion times (TIs), "enhanced" pseudocontinuous arterial spin labelling (eASL), milliseconds (ms).

Zhao and colleagues (2021) used ^{15}oxygen-water positron emission tomography (PET) to further validate MPLD pCASL for measuring CVR, with an ACZ challenge in healthy participants [262]. They found that simultaneously acquired CVR estimates (mean whole brain) were very similar for MPLD ASL (ASL = 42±19%) and PET (PET = 40±18%). In comparison, single PLD ASL CBF was 15±10% less than PET. Considering that PET has long been used as the gold-standard for CBF measurements, this validated MPLD ASL as a suitable non-invasive measure of CBF. Additionally, it highlighted the underestimation of CBF when measured with single PLD ASL.

1.8.2 Blood Oxygen Level Dependent Imaging

Blood oxygen level dependent MRI is another method of functional imaging. The BOLD method is an indirect measure of brain activity, as it relies on the principle of neurovascular coupling [172, 130, 18] (Fig. 1.22). This refers to the relationship between neuron activation and vascular responses, as the BOLD signal is technically based on the change in the magnetic properties of the blood. When the cell's haemoglobin are combined with oxygen (oxyhaemoglobin), they are diamagnetic. When neurons are 'active' they metabolise the oxygen and produce deoxyhaemoglobin, which is paramagnetic. The paramagnetic deoxyhaemoglobin has its own magnetic field gradient which leads to an increase in T_2^* weighted signal. The concept relies on the idea that the more 'functional' activity from the neurons, the more oxygen is metabolised. Therefore, the larger the difference between rest and task-based condition images, the larger the subsequent fMRI BOLD signal. During neural activity, blood flow increases much more than is required for oxygen metabolism, so deoxyhaemoglobin concentration is decreased downstream. This leads to an increase in the oxygenation of venous blood and hence a reduction in the amount of deoxyhaemoglobin.

This causes the T_2^* weighted signal to increase. This is because there is less dephasing due to the mesoscopic magnetic field inhomogeneity around the blood vessel caused by the paramagnetic deoxyhaemoglobin. The haemodynamic response specifically refers to the response of activity observed 1-2 seconds after a stimulus in the BOLD signal, peaking at about 6 seconds after the initial activity [33].

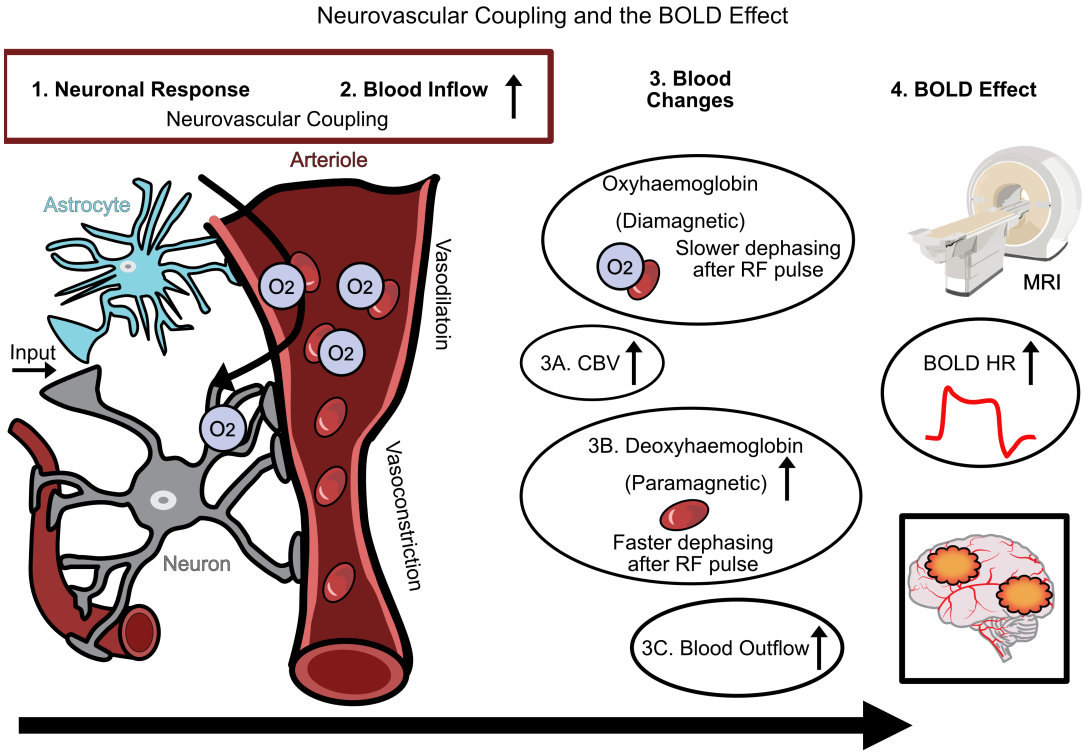


FIGURE 1.22: **Neurovascular Coupling and the Bold Effect.** Neurovascular Coupling (NVC) refers to the pathway from the neuronal activity to the vascular response seen in fMRI imaging. This is the basic concept of a (1) neuronal response resulting in downstream physiological effects that alters (2) Blood flow e.g. via vasoconstriction/vasodilation. This results in (3) changes in the blood e.g. metabolism of O_2 by the neurons, which produces deoxyhaemoglobin in the blood. Cerebral blood outflow washes this out, and also influences blood volume which decreases deoxyhaemoglobin. (4) This leads to an increase in the BOLD signal detected by the MRI. BOLD (blood oxygen level dependent), CBV (cerebral blood volume), MRI (magnetic resonance imaging), HR (haemodynamic response), O_2 (oxygen) RF (radiofrequency) (Based on [107, 180, 108, 115]).

A metric of interest derived from the BOLD effect is the cerebral metabolic rate of oxygen ($CMRO_2$), which is a measure of how much oxygen the brain metabolises per unit of time, which is typically expressed as millilitres of oxygen per 100 grams of brain tissue per minute (ml O_2/100g/min). Hence, $CMRO_2$ reflects the brain's metabolic activity and energy demands. $CMRO_2$ tends to decline slightly with age, and becomes uncoupled from CVR. Newer, calibrated BOLD fMRI approaches, to derive more quantitive metabolic parameters, to utilise $CMRO_2$ values. Additionally, oxygen extraction fraction (OEF) measured derived from BOLD MRI attempts to determine not just if there is an in/decrease in O_2, but also a more detailed idea of how much is actually metabolised by the neurons during brain activation / CVR changes. However, that is beyond the scope of this thesis.

An advantage of BOLD is that it has a higher spatial resolution than pCASL. BOLD sequences are generally based on EPI, which have a temporal resolution of around 1-3 seconds and detect small signal changes of around 1-5%. The temporal resolution can be improved with the use of multislice sequences (which will be discussed further in chapter 4). This high temporal resolution is beneficial for CVR measurements. Hence, BOLD is often used for qualitative CVR measurements, because the change in BOLD signal is also sensitive to vasodilatory responses and reliant on the concept of neurovascular coupling [186].

A major disadvantage of BOLD imaging is that the signal is relative to a baseline, which means that it is traditionally only ever qualitative. This was highlighted with the prevalence of 'resting state' BOLD fMRI, which showed that certain brain networks appear 'active' even when a participant is not given a task to perform [27]. Another major disadvantage of the BOLD method is that it is very sensitive to susceptibility artifacts described in section 1.4.3. Additionally,

head motion (which is common during respiratory tasks) also cause big artifacts in BOLD images. Furthermore, the relationship between the BOLD signal and the underlying physiological mechanisms is complex, so it is difficult to quantify even with newer modifications to data acquisition and analysis.

Haemodynamic Response Functions

A method of analysis that attempts to derive a more quantitive metric from BOLD MRI is using the haemodynamic response function (HRF), which aims to model more complex haemodynamic responses. After a stimulus, the haemodynamic response can be seen in the BOLD signal, and the HRF can be modelled using mathematical functions. A function being a mathematical equation that can be used to draw a curve. The simplest method is to model the HRF with a gamma distribution function (Eqn 1.15). This is shown as a probability density function in Eqn 1.16 and in Figure 1.23A.

$$\Gamma(z) = \int_0^\infty t^{z-1} e^{-t}\, dt \tag{1.15}$$

where the $\Gamma(z)$ is the gamma function symbol, using the integral from 0 to infinity using $\int_0^\infty$ and the integrand $t^{(z-1)}\, e^{(-t)}$, and dt represents the differential element of integration. The Gamma distribution curve can be seen in Figure 1.23B which is calculated as:

$$h(t) = \frac{t^{\alpha-1} \cdot e^{-t/\beta}}{\beta^{\alpha} \cdot \Gamma(\alpha)} \tag{1.16}$$

where time t is in seconds, α (alpha) is the shape parameter and β (beta) is the scale parameter (i.e. affecting the height of the HRF peak), with Γ as the gamma function. The time variable t is raised to the power of α-1, exponential term $e^{-t/\beta}$, with denominator with β raised to the power of α, and then multiplied

by the gamma function $\Gamma(\alpha)$.

This can be used to represent the temporal profile of the BOLD responses when convoluted with a stimulus functions function (Fig. 1.23C). Here, the gamma distribution from Eqn 1.16 and the stimulus are convolved (i.e. averaged). The basic gamma function used in HRF modelling is shown in Eqn 1.17:

$$h(t) = \frac{(t/\tau)^n \cdot e^{-(t-\tau)/\tau}}{n!} \tag{1.17}$$

where the HRF ($h(t)$) is calculated using τ (tau) as the time constant, t (time) in seconds, and n controls the function's shape. [33].

This is also called the canonical Gamma distribution function, which is used also referred to as an 'Impulse function', a term used to describe the response to the stimulus as an 'impulse'. An impulse response is the reaction of any dynamic system in response to some external change.

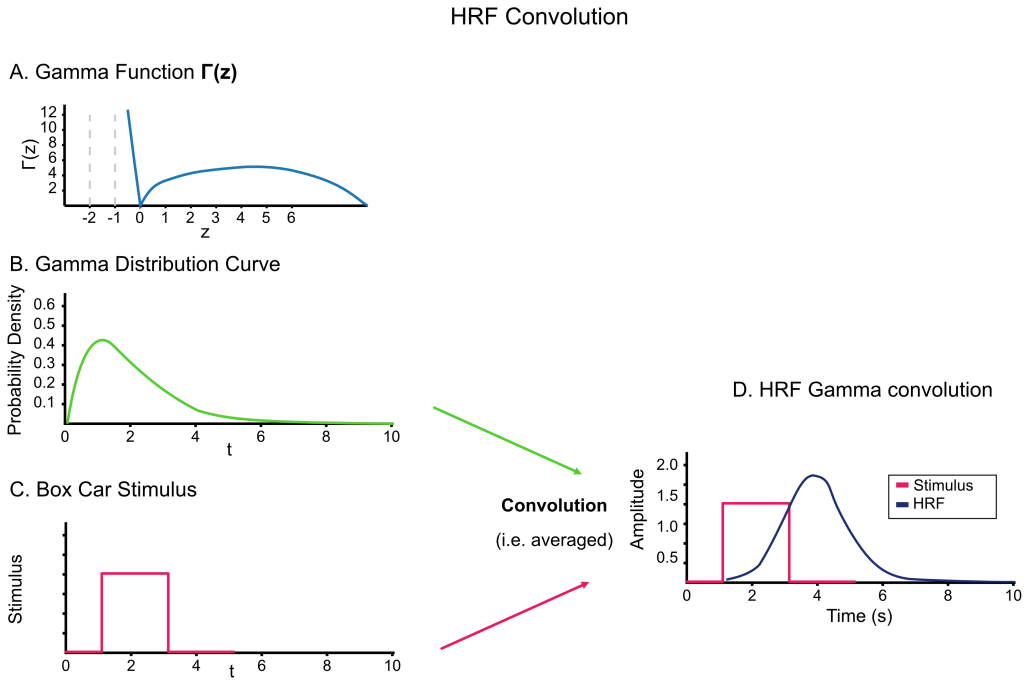


FIGURE 1.23: **HRF Convolution.** A. A Gamma function across z. B. Gamma distribution curve across t (time). C. A Box car stimulus used to induce a BOLD response. D. HRF convolution based on B and C, across time (in s (seconds)) that peaks at around 5-6 s. Based on Glover (2024) [96] and Andrew Jahn (2024) [121].

When analysing fMRI data, mass univariate analysis is required, i.e. calculated for each individual voxel's time-series. For example, for a simple boxcar stimulus, the HRF can be convolved from the stimulus shape, which is done by averaging both the stimulus shape as a function (e.g. a box car shape) and the gamma distribution function (as in Fig. 1.23D). Friston (1995) [88] later used a general linear model (GLM) (see Eqn 1.18) to characterise different fMRI responses using the fMRI time series as a linear combination of predictor variables, plus an error term.

$$y(t) = \beta_0 + \beta_1 X_1(t) + \beta_2 X_2(t) + \beta_3 X_3(t) + \varepsilon(t) \tag{1.18}$$

where $y(t)$ is the observed BOLD signal (the dependent variable) at time t, X_1, X_2 and X_3 are the predictor/ independent variables (regressors), β_1, β_2 and β_3 are the parameter weights to be estimated and $\varepsilon(t)$, the residuals, is the error term (assumed to be normally distributed).

This more complex model is able to also include the post-stimulus undershoot portion of the HRF. This uses a series of unknowns (parameter weights), that are dependent on the HRF to describe the longer lasting part of the process. In this context of convolving an HRF, the Gamma function is sometimes referred to as a 'kernel', which mathematically describes a function that measures the similarity between two data points and/ or a set of all vectors in the domain that are mapped to the zero vector in the codomain.

In matrix form, for all voxels and all time points, the GLM is written as:

$$\mathbf{Y} = \mathbf{XB} + \mathbf{E} \tag{1.19}$$

where **Y** is a matrix of dimensions $T \times V$ (time points $\times$ voxels), **X** is the design matrix of dimensions $T \times K$ (time points $\times$ regressors), **B** is a matrix of parameter estimates of dimensions $K \times V$ (regressors $\times$ voxels) and **E** is a matrix of error terms of dimensions $T \times V$ (time points $\times$ voxels).

Therefore, more complicated stimulus-related regressors can be convolved, to give the stimulus function with the GLM (Eqn 1.20):

$$x_j(t) = (s_j * h)(t) = \int_0^t s_j(\tau) \cdot h(t - \tau)\, d\tau \tag{1.20}$$

where $s_j(t)$ is the stimulus function for the condition j, $h(t)$ is the haemodynamic response function and $*$ denotes the convolution operation

Friston and colleagues (1995) also noted that the process of HRF looked like a couple of gamma variate functions. Therefore, an HRF could also be convolved using a set of statistical parametric maps of high probability of variation. The double Gamma HRF model is shown in Eqn 1.21.

$$h(t) = \frac{A_1(t/\tau_1)^{n_1} \cdot e^{-(t-\tau_1)/\tau_1}}{n_1!} - \frac{A_2(t/\tau_2)^{n_2} \cdot e^{-(t-\tau_2)/\tau_2}}{n_2!} \tag{1.21}$$

where, A_1 and A_2 are amplitude parameters, τ_1 and τ_2 are time constants for the positive response and undershoot, and n_1 and n_2 control the shape of each component.

Additionally, the parameter estimates **B** (from Eqn. 1.19 are obtained using the ordinary least squares (OLS method, which aims to minimise the differences

between the observed and predicted values, and is shown in Eqn 1.22:

$$\hat{\mathbf{B}} = (\mathbf{X}^T\mathbf{X})^{-1}\mathbf{X}^T\mathbf{Y} \tag{1.22}$$

where $\mathbf{B}$ is a matrix of parameter estimates of dimensions, $\mathbf{X}$ is the design matrix of dimensions, $\mathbf{Y}$ is a matrix of dimensions and T is for time.

This minimizes the sum of squared residuals (shown in Eqn 1.23) via the following:

$$\min_{\mathbf{B}} \sum_{i=1}^{T} \sum_{j=1}^{V} (y_{ij} - \hat{y}_{ij})^2 \tag{1.23}$$

where y is again the BOLD signal.

Overall, there a lot of different methods for the convolution of the BOLD response to stimuli. A major disadvantage of convolution methods are that they tend to struggle with distinguishing one larger BOLD response as several overlapping BOLD responses, that other methods might otherwise be interpret separately.

Deconvolution

Some problems with estimating the HRF are that the HRF lags behind neural activity (typically peaking 4-6 seconds later), it is temporally dispersed (can last 20-30 seconds) and this potentially obscures the true timing and shape of neural events. As a results, the response of neural events (or in the case of this thesis the CVR response) can become merged within the various BOLD responses. It is therefore important to properly understand the precise timing and distinguish between distinct, but similar, processes [96]. Different stimuli have been used to determine what an average deconvolved HRF might look like. For example, Glover (1999) [95] used a simple finger tapping task as a

stimulus to calculate an HRF:

$$HRF(t) = h_1 te^{-t/\tau_1} + h_2 te^{-t/\tau_2} \tag{1.24}$$

where:

- $HRF(t)$ is the haemodynamic response function as a function of time t, representing the BOLD signal response
- t is the time variable, typically measured in seconds after stimulus onset
- h_1 and h_2 are amplitude parameters or weighting coefficients that determine the relative contributions of the two exponential components
- τ_1(tau$_1$) and τ_2 (tau$_2$) are time constants that control the decay rates of the two exponential components, measured in seconds

The basic deconvolution of the BOLD signal in the fMRI experiment by Glover (1999)[95] can be simplified as a linear equation shown below in Eqn 1.25:

$$m(t) = s(t) * h(t) + n(t) \tag{1.25}$$

where $m(t)$ is the BOLD signal measurement, $s(t)$ is the task stimulus design, $h(t)$ is the haemodynamic response function (HRF) and $n(t)$ is the noise. Stimulus-related BOLD fMRI can also be deconvolved from an impulse response.

Which can be rearranged to deconvolve $h(t)$ by calculating the stimulus using the Wiener filter $d(t)$:

$$s'(t) = d(t) * m(t) \tag{1.26}$$

where $d(t)$ is the Wiener filter in time domain.

However, not all HRFs are assumed to be a linear function, and these can be filtered. Hence, there is a need to converts signals to the frequency domain, via Fourier transforms, using the following Eqn 1.28:

$$D(\omega) = \frac{H^*(\omega)}{|H(\omega)|^2 + N(\omega)} \tag{1.27}$$

where:

- $D(\omega)$ is the deconvolution filter in frequency domain
- $H^*(\omega)$ is the complex conjugate of HRF in frequency domain
- $|H(\omega)|^2$ is the squared magnitude of HRF in frequency domain
- $N(\omega)$ is the noise power spectrum.

Multiplying the filter by the measured signal then gives the response, and is estimated using Eqn 1.28, which is then converted back to the time domain using the full Wiener filter expression shown in Eqn 1.29:

$$s(t) = \mathcal{F}^{-1}\{D(\omega)M(\omega)\} \tag{1.28}$$

where: $s(t)$ is the estimated stimulus, $\mathcal{F}^{-1}$ is the inverse Fourier transform, and $M(\omega)$ is the measurement in frequency domain.

The N_0^2 term in the denominator prevents noise amplification when $H(\omega)|^2$ is small:

$$s(t) = \mathcal{F}^{-1}\left\{\frac{H^*(\omega)M(\omega)}{|H(\omega)|^2 + N_0^2}\right\} \tag{1.29}$$

where N_0^2 is the constant noise power spectral density.

Overall, deconvolution is important for analysing stimulus-related fMRI designs, where timing precision matters, as it makes it possible to separate out overlapping BOLD responses. This also makes it possible to compare temporal differences brain activation across different brain regions, which may differ from the more traditional 'canonical' convolution models [226]. Analysis methods that extract events from resting-state fMRI data would also be useful, in order to remove the use of the hypercapnic challenges when measuring CVR [55].

However, some disadvantages of using deconvolution analysis methods include problems with low signal to noise data, as these methods are very sensitive to noisy data [2]. This can include noise from physiological confounds e.g. heart rate, breathing, movement. Furthermore, these methods may struggle more when there are variations in HRF shape across brain regions and individuals, which may be more pronounced when comparing older adults and patients to healthy controls [227]. There are also many more models that can be used for both convolution and deconvolution of the HRF. Selecting which parameters and models to use can be complex. The ones used in this thesis will be explained in more detail in Chapter 4.

1.8.3 Phase Contract Velocity

Phase contrast velocity MRI (PCV) uses bipolar gradient pulses, so that when the blood (H^+) pass through the gradients the spins accumulate a phase shift [40, 80]. More specifically, this uses gradient pulses with opposing polarities across an equal area. A static spin results in no net phase shift. Therefore, only the moving spins (i.e. blood flow) result in a phase shift, which can be converted to quantitative velocity values (as mL/s). The net phase is proportional to the velocity as follows:

$$\phi = -\gamma v M_1 \tag{1.30}$$

where ϕ is the net velocity dependent phase shift, v is the velocity and M_1 is the product of the gradient amplitude plus the time of application of the gradient field.

This method is therefore useful for measuring changes in cerebral blood vessels to provide a value of CBF and subsequently CVR measurements. The resulting PCV output provides both a magnitude image (anatomical information) and phase image (velocity as greyscale values). The phase images show flow in one direction as bright, flow in the opposite direction as dark, and stationary tissue as grey. The velocity values can also be used to create flow-time curves for more detailed haemodynamic analysis at the macrovascular level [78].The velocity encoding (VENC) value, which is set relative to the expected velocity. This is also important, as a VENC value that is too low will cause wrap-around from aliasing. Whereas, a VENC value that is too high will decrease the sensitivity to slower blood flow.

Advantages of the PCV method are that it is a direct measure of velocity, with high accuracy. Hence, it can be used to calibrate / normalise pCASL labelling efficiency. Additionally, PCV performs well for measuring CBF at large feeding

vessels to the brain, which is useful for CVR. However, some disadvantages include the low spatial resolution of PCV. PCV has a limited spatial coverage (i.e. one slice used in this thesis) and does not perform well for estimates of blood velocity in smaller blood vessels. Therefore, it is not possible to compare all brain regions simultaneously, though this is also an area of current development. In contrast to pCASL MRI, which tends to underestimate CBF, PCV tends to overestimate CBF. Additionally, this method is sensitive to motion artifacts.

1.9 Applications of fMRI CVR

The importance of fMRI is based on the clinical diagnostic applications, which is the main motivation for improving fMRI measurements of CVR. Clinical applications of CVR have so far mainly focused on cerebrovascular diseases. As mentioned there are multiple other CVDs and associated disorders that would benefit from new diagnostics based on CVR. These range from blood cell abnormalities such as Sickle Cell Anaemia [13] to Moyamoya disease (where additional blood vessels grow to bypass blockages) [153] to carotid stenosis and stroke.

Some of the common applications of fMRI CVR include pre-surgical planning, (e.g. for brain tumours or epilepsy localisation), and cerebrovascular assessment. Firstly, pre-surgical evaluation for neurosurgery patients is important to ensure that the surgery avoids unnecessarily damaging the 'eloquent' brain areas. Performing tasks such as language lateralisation, verb generation and semantic decision making can help with locating the specific functional areas in each individual patient. These important functional areas can then be avoided, where possible, during the surgical procedure. Secondly, Epilepsy surgery

aims to alleviate epileptic seizures via the removal or ablation of brain areas. In addition to protecting eloquent brain areas in epilepsy patients, using fMRI for epilepsy localisation can be used to increase the accuracy and precision of the area that needs to be removed. Functional tasks are used to determine the epileptogenic focus, which is often in an area that has abnormal connectivity patterns or pathways, and aims to remove the smallest amount of brain tissue possible.

Another reason for neurosurgery is the removal of brain tumours [185, 187, 186]. CVR has also been used to detect brain tumours via the abnormal growth of blood vessels diverting/ monopolising the vascular blood flow to increase the growth of the tumour. Therefore, CVR mapping can help to distinguish between tumour tissue and normal brain tissue. It can also assist with surgical planning, by identifying areas that have compromised vascular reserve.

There are many other cerebrovascular diseases that can benefit from CVR measurements. CVR has already been shown to be impaired in carotid stenosis, a condition where arteries narrow due to the build-up of material, normally fatty deposits [169]. In arterial stenosis ([65, 144], CVR is useful for accessing the cerebrovascular reserve in patients, which can determine if a patient will need surgery to remove the stenosis or could be managed with pharmacological treatment. Carotid stenosis is also a very common cause of stroke, as parts of the plaque break off, flow into the brain vasculature system, and cause blockages (i.e. ischaemic stroke). Leoni and colleagues (2012) [136] also showed that in carotid stenosis CVR was a good candidate to predict strokes, as CVR was no longer evenly spread (homogenously) across both sides of the brain (hemispheres) before a stroke occurred. In stroke ([177], CVR mapping can also be used to determine the cerebrovascular reserve, both acutely and chronically, which can determine available treatment options.

Moyamoya disease has a lot in common with carotid stenosis, however the vessels in this condition are stenosed above the circle of Willis (higher up in the brain). Simultaneous PET-MRI has been used with ACZ challenges to investigate Moyamoya disease [261]. The PET/MRI included ^{15}oxygen-water PET, single and multi-PLD pCASL. Overall, CVR was significantly lower in occluded regions compared to normal regions across all modalities (PET = 68±12% vs. single PLD-ASL = 52±5% vs. multi PLD ASL = 56±9%). In affected vascular territories, MPLD ASL was slightly better correlated with PET (concordance correlation coefficient (0.36)) than single PLD (0.35), and performed even better in unaffected territories (MPLD ASL = 0.32 vs. single PLD = 0.16). Additional information from the MPLD ASL showed that the ATT was 15-18% higher in the affected territories than the healthy ones, which means that blood took longer to perfuse to these regions. This shows there can be a benefit to using a non-invasive, non-ionising method of neuroimaging, without compromising the quantitive measures of CBF. Ideally, once CVR based diagnostics have been validated, then this biomarker could be further tailored to specific CVDs.

In cerebral small vessel disease, another high risk condition for severe ischaemic stroke, white matter hyperintensities (lesions that appear bright on some MR scans) generally denote worsening disease progression and are a marker for small vessel disease [213]. CVR has been shown to be inversely related to white matter hyperintensity severity, suggesting another link to cerebrovascular health and disease.

Traumatic brain injury ([126]) is another disorder where CVR has a potential clinical application. Amyot and colleagues (2018) investigated traumatic cerebrovascular injuries (TCVI) in patients with traumatic brain injury (TBI) [10]. They used ASL to investigate biomarkers in N=27 TBI chronic (> 6 months post-injury)

patients and N=15 matched controls. The results showed a decrease in the GM (controls GM CVR = 0.191±0.016 %BOLD/mmHg vs patients 0.154±0.025%BOLD/mmHg (median)) and WM CVR (as a global mean) compared to healthy controls. There was also cerebrovascular dysfunction, in that these decreases in whole brain CVR were asymmetrical in patients, but symmetrical in controls (controls=0.173±0.014 %BOLD/mmHg vs. patients = 0.140±0.23 %BOLD/mmHg). In contrast to the CVR response, the CBF values did not correlate well with each other or the neurobehavioural test scores (controls median GM CBF = 43.9±13.3 mL/100 g/min vs. patients = 37.9±8.8 mL/100 g/min). As a result, CBF estimates did not differentiate well between patients and controls. This studies' combination of structural and functional vascular measures provided a comprehensive assessment of cerebrovascular dysfunction and supported clinical implementation of CVR, over CBF, as a biomarker and potential candidate for interventions for TCVI [11].

Sickle cell disease (SCD) is a blood disorder in which red blood cells are 'sickle' shaped (i.e. abnormal), and are therefore not as efficient at carrying oxygen. Additionally, the misshapen cells can accumulate and block blood vessels, further restricting blood flow and oxygen around the body and brain. Václavů and colleagues (2019) studied N=36 patients with sickle cell disease with pCASL MRI. They used an ACZ challenge to induce a CVR response, and patients GM CBF increased by 82.8±20.1 mL/100g/min, compared to only a 51.3±4.8 mL/100g/min increase controls (median±interquartile range). They also showed that the cerebrovascular reserve in patients was reduced by about half (34.1%), compared to healthy controls (69.5%). Less reserve results in less ability to increase dilation when required to increase blood flow demand to the brain. This difference was likely due to patients adapting to SCD by increasing blood flow to compensate for the disorder, even at rest, leaving less room for this

'reserve' when needed. Here, only baseline CBF correlated with CVR, and the two metrics became dissociated in patients during the ACZ challenges. Additionally, these problems with blood flow lead to a high occurrence of 'silent' brain damage from cerebral infarcts (i.e. small ischaemic strokes) in patients (patients = 81%, controls = 45%), and larger areas of damage (median volume of patients = 0.34 mL vs. controls=0.02 mL) where the infarcts occurred. Such infarcts are also thought to lead to the decline in cognition in SCD. This suggests there is a need to take CVR into consideration for SCD treatments, as increasing haemoglobin and blood flow reserve may help with the reduced capacity to maintain a sufficient vascular reserve. CVR has been shown to be important in normal ageing [64, 90], and comparing this to what may be considering "abnormal ageing" in neurodegenerative diseases. Various vascular risk factors are known to contribute to cognitive decline. More specifically, poor CVR response has been associated with cognitive performance. This association extends to neurodegenerative diseases such as Vascular Dementia and Alzheimer's disease (AD). This was investigated in a stage II clinical trial, by Aslanyan and colleagues (2024) called the Systolic Blood Pressure Intervention Trial Memory and Cognition in Decreased Hypertension (SPRINT-MIND) [14]. This ASL and BOLD MRI study aimed to access older adults who also had hypertension over a longitudinal period, with a particular interest in the brain areas that degenerate in AD. The results showed a protective element to CVR, in that patients with a better CVR response had a lower mild cognitive impairment (MCI) risk, even after developing AD. This supported the growing theory that vascular dysfunction contributes to the underlying aetiology (in the associated brain regions), not just the subsequent behavioural symptoms. A poor CVR was also negatively associated with MCI, which is a degenerative, memory impairment disorder. MCI is often a pre-cursor and/or risk factor to Dementia

and AD. In MCI patients, a CVR response to a HC resulted in a decreased CVR in the medial temporal lobe (which is an important area for memory) compared to control regions. This evidence showed that CVR deterioration is a potential mechanism for AD and cognitive impairment, via vascular dysfunction, and therefore also a potential treatment target. For example, attempting to maintain a 'normal' CVR range may provide a protective, and even preventative therapeutic treatment. A greater understanding of the biological pathways that underpin CVR would therefore also be useful for this clinical application as a predictive marker of these diseases.

Overall, there are a variety of CVDs and other clinical applications that would benefit from using fMRI CVR for diagnosis, prognosis and treatment planning/efficiency testing.

1.9.1 Issues with CVR Measurements

pCASL methods of CVR measurements are the focus of this thesis, as in theory the measurements are quantitative. However, certain conditions need to be met for these measurements to be precise. Exploring how to make the sequences more robust under less strict assumptions (i.e. under increased blood velocity) would therefore be beneficial for optimising pCASL CVR for clinical use. In summary, there is a variety of issues with the current use of CVR.

Firstly, there are some technical limitations of inducing a CVR response. Some patient groups may have difficulty performing breath holds or tolerating inhaling high CO_2, which may make it harder to validate CVR in these populations. Ideally, there would be no need for inducing a CVR response artificially, instead a simple, resting-state data collection would be more suitable for clinical use. Unfortunately, the natural fluctuations in CO_2 are very small, and analysis of

this data type is still a challenge. Therefore, this thesis aimed to compare a variety of different CO_2 delivery methods. Additionally, optimising the HRF in BOLD analysis method may make it more feasible to analyse resting-state pCASL CVR data more effectively in future.

A second problem is standardisation. There are many different types of MRI protocols used for measuring CVR, from the method of MRI sequences (e.g. BOLD/ pCASL), to the specific parameters used within the MR sequence, and the method of inducing CVR (e.g. breath holds vs. delivery of CO_2). These vary both within and across both academic and clinical research centres, which results in difficulty making direct comparisons between results. Furthermore, even if the same data was collected, the analysis methods used to calculate CVR also varies considerably, from in-house scripts, to open-source toolboxes to commercially available algorithms. Subsequently, the clinical value of such results is harder to determine. Therefore, another aim of this thesis was to optimise pCASL CVR measurements by comparing different parameter sets and types of analysis. Currently, the spatial resolution and temporal resolution (compared to electrophysiology) needs to be refined in order to provide a deeper understanding of where and when cerebrovascular deterioration occurs in disease states. Hence, there is a need to improve the balance between the spatial and temporal resolution. Therefore, this thesis aimed to compare different pCASL CVR sequences including single PLD pCASL and whole brain coverage using MPLD, and to explore the benefits of MPLD over single PLD sequences.

If pCASL CVR is to be used to determine precise changes between healthy brains, disease progression and effectiveness of treatments then confidence in the quantitative nature of the data is important for translation to more routine clinical applications. Validating the pCASL estimations of CVR to PCV (another direct, quantitative measure of CBF) provides another way to increase confidence

in these measures. This includes the need to be able to detect small changes at the very onset of cerebrovascular decline, in order to prevent, rather than just cure cerebrovascular deterioration.

Together these limitations contribute to problems with quantification of CVR measurements. Consequently, CVR measurements need to be more robust, reproducible, and feasible in clinical settings. This may include decreasing scan times, to standardising both data collection and analysis, to accessibility of the cost and application of these methods.

1.10 Aims and Outline of the Thesis:

Clinically, the main motivation for investigating CVR is as a biomarker for cerebrovascular disease and the associated risk factors of CVD. As mentioned, CVR reduction is associated with risk factors including vessel stenosis, occlusion in sickle cell disease, deposition of vasoconstrictors in AD, as well as damage to both small and large vessels. CVR mapping provides valuable information about cerebrovascular reserve and deterioration of the cerebral blood vessels, hence it is complementary to traditional imaging measures. Moreover, CVR is increasingly important for assessing brain vascular health across a diverse range of neurological conditions in both research and clinical settings.

The original overall aim of this PhD was to look at the dynamic response of CVR in health and disease. Unfortunately, it was no longer possible to scan patients or older adults, therefore the focus moved away from applications to optimisation of CVR methodology.

The main aim of this thesis was then focused on the optimisation of each stage of CVR measurement including: data acquisition - using different MRI methods, sequences and parameter sets, the hypercapnic challenge - using different gas delivery methods, and the data analysis - using standard, Bayesian and more complex HRF analysis.

This project aims to use arterial spin labelling (ASL) magnetic resonance imaging (MRI) to optimise the quantification of cerebrovascular reactivity (CVR) including:

Short term aims:

- To validate robust measures of the change in blood flow in the brain using MRI to provide new insight into CVR measurements. For example,

comparing different pCASL parameters' estimates of CVR to PCV measures of CVR.

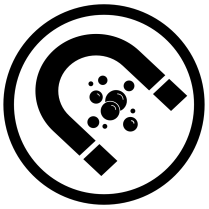
- To advance the implementation of hypercapnic challenges for inducing CVR, and investigate CVR measurements. For example, by comparing manual, semi-automated and computer controlled gas delivery methods.
- To advance the implementation of ASL analysis for investigating CVR measurements, including timing metrics. For example, using MPLD pCASL sequences to determine arterial transit times.
- To advance the implementation of BOLD analysis for investigating CVR measurements, including timing metrics. For example, using dCVR analysis to model the HRF response to a hypercapnic challenge.

Longer term impact:

- Optimising CVR measurements to improve diagnosis and prognosis of cerebrovascular diseases (applicable to those both common and rare) addresses the need to save lives and increase 'disability free' years of life.
- To provide a diagnostic that performs well across age, specifically in older people who are more at risk of CVDs.
- To advance science & healthcare as general awareness of disorders (in association with how research is being progressed) encourages patients to join clinical group studies, for people to consider preventative measures, and seek diagnosis earlier.

1.11 Overview of the Chapters

This thesis is divided into six Chapters, including the current introduction chapter. All of the experimental chapters are studies of young, healthy, adult participants.



Chapter 2 part 1 explores the effect of increasing blood velocity in the feeding arteries of the brain due to a hypercapnic challenge, and its effect on the labelling efficiency of pseudo-continuous ASL and subsequent measures of CVR.



Chapter 2 part 2 investigates if hyperventilation with an artificially maintained normocapnic condition and changing the pCASL labelling plane placement affects the B_0/B_1+ inhomogeneity, and subsequently if this influences CVR measures.



Chapter 3 assesses the feasibility of using pharmacological interventions to alter blood flow. This study was performed outside of the MR scanner as a pilot and involved non-invasive measures of blood pressure, heart rate and blood velocity in the carotid artery with Doppler ultrasound.



Chapter 4 part 1 incorporates aspects of the previous chapters with the addition of: multiple post labelling

delay pCASL; a new gas delivery device for a steady state hypercapnic challenge; and a more advanced analysis method for ASL quantification using Bayesian modelling, with macrovasculature and gamma dispersion modelling.



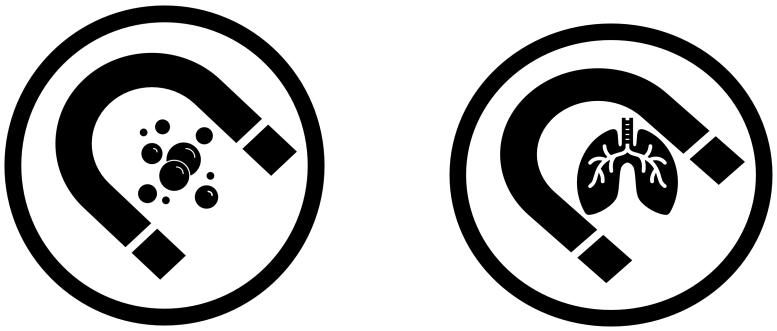
Chapter 4 part 2 explores the use of BOLD with a pseudo-sinusoidal hypercapnic challenge with the new gas delivery device. The analysis involved a more traditional method of analysis for CVR measurements and a newer, more advanced dynamically modelled CVR method.



Chapter 5 compares the amplitude and timing CVR parameters described in chapter 4. It compares the multiple post labelling delay pCASL analysis to two sets of BOLD analyses (sinusoidal CVR and dynamic CVR), and considers if there are correlations between these measures of CVR.

Chapter 6 provides a summary of findings and highlights the contributions of this thesis to creating more robust measurements of CVR using pCASL, BOLD and hypercapnic challenges for acquisition and more advance analysis / modelling methods. It also identifies the limitations of the work and lists potential future research ideas.

2 Optimising Robust Quantification of Cerebrovascular Reactivity using Pseudocontinuous ASL



2.1 Contributions to the Chapter

The first part of this study (the effect of blood velocity changes) was already underway when I started my PhD in September 2019. During my second DTP Rotation (6th January to 21st February 2020) with Dr Nicholas Blockley I observed data collection, helped to set up the RespirAct^{TM} and performed data analysis. The original project plan included data collection of both 'younger' (18-30 years) and 'older' (50-60 years) participants. However, due to the UK COVID-19 lock down, data collection stopped in March 2020. A funding extension was given to continue data collection until July 2020. Unfortunately, the university had not allowed scanning to be re-started until May 2021. Therefore, only the 'younger' participants datasets are included in this chapter, as there were an insufficient number of datasets from the 'older' cohort to be used for a comparison study.

In the second part of this study (the effect of B_0 and B_1), I did the participant advertisement, recruitment, screening and assisted as an MR assistant during data collection, then wrote the scripts for data analysis and manuscript writing/editing etc.

Dr Nicholas Blockley provided support as the main supervisor, for set-up of the study, and revisions to the manuscript.

Prof Susan Francis helped with the MR protocol parameters for the B_0/B_1 map sequences.

Jan Paul and Andrew Cooper were scanner operators for the 3T Philips scanner and the screening for the first part of the study.

Thanks to Dr Joanna Pinto for introducing me to the Findpeaks function in Matlab.

This study received funding from the Biotechnology and Biosciences Research Council (BBSRC) and the National Institute for Health Research (NIHR) Nottingham Biomedical Research Centre (BRC).

2.2 Visual Abstract

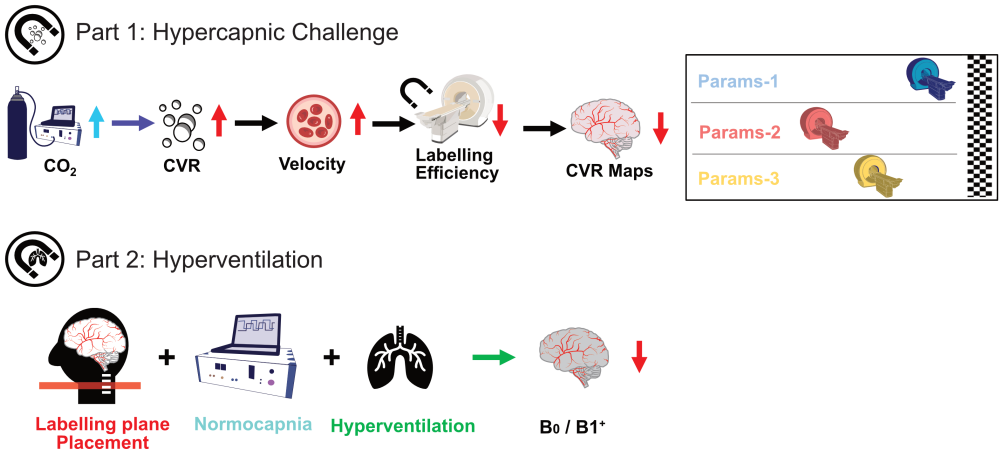


FIGURE 2.1: **Visual Abstract** Part 1: A hypercapnic challenge was used to induce a CVR response and create CVR maps. Three different preparation parameter sets were used with Params-1 giving the highest values. Part 2: The labelling plane was aligned with the V3 segment of the vertebral arteries in the neck. Hyperventilation (with clamped normocapnia) was used to investigate B_0 and B_1 effects. CO_2 (carbon dioxide), CVR (cerebrovascular reactivity).

2.3 Introduction

As mentioned previously, cerebrovascular reactivity (CVR) is a potential clinical marker for brain health (see section 1). CVR is the ability of blood vessels in the brain to react to changes in metabolic demand by regulating cerebral blood flow (CBF). CVR is a component of autoregulation that maintains a narrow baseline within set limits to prevent neuronal damage and decline of cognition [201, 141]. CVR is also altered in healthy ageing [64] and disease. Findings generally show a lower CVR in cerebral steno-occlusive diseases, dementia and cognitive impairment, small vessel disease and normal ageing [214]. Therefore, robust clinical measures of CVR would be advantageous to clinicians. A CVR response can be induced artificially via a vasoactive stimulus, which causes a change in CBF without altering metabolism. For example, inhaling air with an elevated carbon dioxide (CO_2) content interleaved with breathing air is referred to as a hypercapnia challenge. Acetazolamide (ACZ), a medication that causes vasodilation, has also been used to induce CBF, but it takes 30 minutes to peak, which is considerably slower than a hypercapnic challenge. ACZ may be more easily implemented in a clinical setting as it does not require gas canisters and equipment. These two stimuli have been shown to produce robust and reliable changes in CBF which can be used to map CVR [141, 235]. However, measuring the effect of these types of challenge requires measurements of both baseline and intervention conditions to calculate CBF change.

2.3.1 ASL Parameters

The two most common methods to map CVR using MRI are the blood oxygen level dependent (BOLD) and arterial spin labelling (ASL) techniques. Measurements of CVR using BOLD are not directly proportional to the percentage change in CBF as the amplitude of the response is dependent on baseline physiological parameters such as the oxygen extraction fraction (OEF) and cerebral blood volume (CBV) [30]. In contrast, ASL magnetically labels blood as it passes through the feeding arteries of the brain to measure tissue CBF and is considered to be a quantitative measure of perfusion. Pseudocontinuous ASL (pCASL) has been recommended for clinical patients because its higher signal-to-noise ratio results in more robust estimates of CBF compared to traditional pulsed ASL (PASL) methods [7]. However, it is important to recognise that there are substantial variations across the different pCASL implementations. Variations in PASL labelling modules are typically named (e.g., Fluid-Attenuated Inversion Recovery (FLAIR) and Simultaneous Transmit and Receive (STAR)), whereas a multitude of variations in the pCASL labelling module come under the umbrella term of pCASL. For pCASL the labelling modules fall in to one of two categories (mentioned in section 1.8.1); balanced [250], which is the most common, and unbalanced sequences [61] that are parametrised by the mean and maximum gradient strength and the RF pulse amplitude, duration and spacing. These variations have differing sensitivity to blood velocity, RF pulse amplitude and magnetic field inhomogeneity at the labelling plane. Together these factors determine the labelling efficiency observed *in vivo*, which is an important factor in the quantification of CBF [44] and is expected to vary across different pCASL implementations [234]. Therefore, it is important to determine which pCASL preparation parameters most influence the labelling efficiency and subsequent CVR estimations.

Aslan and colleagues (2010) [13] investigated the effect of blood velocity on pCASL labelling efficiency and whether it is altered during a hypercapnia challenge. By comparing pCASL measurements of the percentage change in CBF due to hypercapnia with whole brain measurements of total CBF using phase contrast (PC) MRI, they found that pCASL underestimated the change in CBF. They attributed this error to a reduction in labelling efficiency. For hypercapnia based CVR, the percentage change in CBF is typically calculated as the ratio of the CBF-weighted signal at baseline and during hypercapnia, rather than absolute quantification in both conditions. The labelling efficiency is therefore implicitly assumed to be constant between conditions in this kind of analysis. Hence, if labelling efficiency is reduced, this results in the underestimation of CBF change.

ASL Preparation Parameters

Three sets of pCASL preparation parameters were used in this chapter. This was to compare the local Philips scanner pCASL sequence to the current literature recommendations. The first set of parameters (Params-1) were the default parameters for the Philips Ingenia 3T scanner (Vaclavu and colleagues (2018)[233]). The second set (Params-2) were based on the recommended parameters from the Alsop and colleagues (2015) ([7]) white paper that first recommended the use of pCASL for clinical use. The third set (Params-3) were the parameters from the (Aslan and colleagues (2010) ([13]) paper, which recommended improving labelling efficiency for measures taken during an increased velocity of blood flow in the brain tissue. Although more than one parameter was changed in each set, the main difference between them was the change in Gaverage:Gmaximum

ratio. The labelling pulse maximum gradient (G_{max}), measured in mT/m, is defined as the maximum amplitude of the slice-selection gradient applied within the train of labelling pulses. The labelling pulse average gradient (G_{av}), also measured in mT/m, is defined as the non-zero average (mean) gradient applied with the RF labelling pulses. These create the flow-driven adiabatic inversion required for pCASL imaging. The highest ratio for the preparation parameter sets used was Params-1 (0.36 mT/m : 5 mT/m), followed by Params-2 (1.00 mT/m : 10 mT/m), and then Params-3 (0.60 mT/m : 6 mT/m). The parameter sets can be seen in more detail in Table 2.3.

Bush and colleagues (2018) [42] performed experiments comparing healthy participants with hyperaemic anaemic patients (high CBF). They found that an interaction between the blood velocity and reduced radiofrequency (RF) amplitude resulted in a reduction in the labelling efficiency. This caused baseline CBF to be underestimated in pCASL measurements, when compared with PCV MRI CBF measurements. In addition, they suggested the use of a two-compartment model to account for tissue transit time, and subsequently showed transit time was reduced in anaemic patients. Whilst these experiments were only conducted at baseline, the implication for CVR studies is that the labelling efficiency is expected to change between the baseline and the hypercapnia/ACZ condition. Therefore, for ACZ based CVR, where absolute quantification between conditions is required, knowledge of the labelling efficiency is important for accurate quantification.

2.3.2 Magnetic Field Inhomogeneity

Magnetic field inhomogeneity at the labelling plane is known to affect the labelling efficiency. There have been attempts to improve quantification of CBF by optimising the parameters of the pCASL labelling module [263]. A major

point of difference between balanced and unbalanced pCASL approaches is their differing sensitivity to magnetic field offsets. In both types of pCASL sequence the label, as a function of off resonance frequency, is the same, but the control condition differs. For the balanced approach the control response is a shifted version of the label by a phase of π, whilst for the unbalanced approach the control is largely independent of the phase shift. Since magnetic field inhomogeneity is expected to be greater in the neck, unbalanced pCASL was originally recommended for clinical use [7]. Typically, it would be assumed that the magnetic field inhomogeneity remains constant between normocapnic and hypercapnic conditions during a hypercapnic challenge (HC). However, the hyperventilation that occurs during hypercapnia may also influence the magnetic field detrimentally. Breathing deeply introduces movements in the chest and abdomen, as well as air volume changes in the lungs [236]. This can result in susceptibility changes in the tissue-air interface, changes in the magnetic susceptibility boundaries and changes in tissue density [120]. This is an important consideration in pCASL as the labelling efficiency requires a consistent magnetic field at the labelling plane in the neck, where the feeding arteries to the brain are labelled [254]. Additionally, the long pCASL labelling times create a higher chance for the magnetic field to fluctuate within the data acquisition time.

Furthermore, blood oxygenation may also change, via gaseous exchange, and would then subsequently alter the T_1 of blood. Hence, corrections have often been used to deal with these off-resonance problems e.g. through shimming [23]. Zhao and colleagues' [260] simulations showed that high velocities were particularly vulnerable to off-resonance effects and that unbalanced pCASL was more robust than balanced pCASL. Therefore, field inhomogeneities may also contribute to changes in the labelling efficiency for balanced pCASL implementations,

which are currently more common than unbalanced. The overall effect is likely to reduce the CBF estimates measured with pCASL.

Each of these sources of error could potentially be corrected via post-processing using additional information (PC velocity, magnetic field map, RF field map), which requires additional scan time [42, 256]. This may be particularly impractical when a hypercapnia stimulus is used, due to the need for an additional challenge and delays in reaching a stable steady-state. Therefore, selecting pCASL labelling parameters which minimise their effect on labelling efficiency may be a more pragmatic approach to improving the accuracy of hypercapnia CVR measurements.

The B1 mapping sequence used in this chapter is called Dual Refocusing Echo Acquisition Mode (DREAM). Dream is an 'ultrafast' method that combines the Stimulated Echo Acquisition Mode (STEAM) preparation sequence with a tailored single-shot gradient echo sequence [86, 85]. This allows it to simultaneously measure the stimulated echo (STE) from the STEAM-prepared, i.e. dephased, magnetisation, and the free induction decay (FID) from the unprepared i.e. in-phase magnetisation. The flip angle is determined from the ratio of these two signals using the following method:

$$I_{\mathrm{STE}} = \sin(\beta) M_{z,\mathrm{STE}} = \frac{1}{2}\sin(\beta)\sin^2(\alpha)\cdot M_0 \tag{3}$$
$$I_{\mathrm{FID}} = \sin(\beta) M_{z,\mathrm{FID}} = \sin(\beta)\cos^2(\alpha)\cdot M_0$$

Next, dividing the two equations of gives:

$$I_{\mathrm{STE}} / I_{\mathrm{FID}} = \tan^2(\alpha)/2 \tag{4}$$

where:

- I_STE is the stimulated echo signal intensity
- I_FID is the free induction decay signal intensity
- $M_{z,STE}$ is the STEAM-prepared (dephased) longitudinal magnetisation
- $M_{z,FID}$ is the Unprepared (in-phase) longitudinal magnetisation
- M_0 is the equilibrium magnetisation
- $(alpha)$ is the STEAM pulse flip angle
- $(beta)$ is the imaging pulse flip angle

Therefore, the 'actual' flip angle α of the STEAM pulses can be calculated from the ratio of the measured echo signals via the following Eqn (assuming the range is between 0 to 90):

$$\alpha = \arctan \sqrt{2 I_{\mathrm{STE}} / I_{\mathrm{FID}}} \tag{5}$$

where α is the actual flip angle, and arctan is the arctangent, the inverse function of the tangent function.

Due to the these timing schematics, a major advantage of this method is that this sequence is robust to susceptibility and chemical shift effects it is not so reliant on T_1 or T_2 relaxation times, and using a single acquisition for both echoes means it is more resistant to motion artifacts. Furthermore, it has a low specific absorption rate (SAR) and provides B_0 phase maps and transceive phase maps "for free". Most importantly, the data acquisition is very quick at ∼130 ms per slice (1.1 seconds for 8 slices), compared to 18 seconds for comparable methods. For example, DREAM is ∼16 times faster than the 'actual flip angle imaging' (AFI). For reference, the AFI pulse sequence uses two identical RF pulses, followed by two delays of different duration ($TR_1 < TR_2$). After each

pulse, a gradient echo (GRE) signal is acquired. Hence, the DREAM sequence was chosen to investigate the B_0/ B_1 inhomogeneties during hyperventilation.

2.4 Aims of the Study

The aim of this study was to investigate systematic differences in balanced pCASL measurements of CVR from a hypercapnia challenge for three different sets of pCASL preparation parameters. This study also aimed to characterise the blood velocity changes in the feeding arteries of the brain during a hypercapnia challenge, the effect of suboptimal radio-frequency (B_1) and static magnetic (B_0) fields, including changes in B_0 during a hyperventilation challenge.

2.5 Hypotheses

Part 1 Effect of different pCASL parameters and velocity

The hypothesis of this part of the study was that different pCASL preparation parameters will have different levels of efficiency depending on the velocity of the blood in the feeding arteries. Estimates of the change in CBF in response to a hypercapnic stimulus are therefore expected to vary with different pCASL preparation parameters.

Part 2 Effect of B_0 and B_1 inhomogeneity

The hypothesis of this part of the study was that magnetic field inhomogeneity and RF inhomogeneity at the labelling plane will affect the efficiency of the pCASL preparation and cause errors in pCASL CVR measurements.

2.6 Methods

2.6.1 Ethics Approval and Participant Recruitment

Written informed consent was obtained from healthy volunteers following local ethics committee approval (Robust CVR: 246-1902, Robust CVR part 2: 288-1904). Inclusion criteria included: participant was able to give written informed consent for participation in the study, in good health, male or female, aged 20 to 60 years. Exclusion criteria included: contraindication for MRI, pregnancy, does not have adequate understanding of verbal and written information in English sufficient to complete an MRI safety screening, suffers from severe chronic obstructive pulmonary disease (COPD). All datasets presented in this chapter are of young, healthy volunteers (self-reported). For the first part, there were N=10 complete phase contrast velocity (PCV) datasets (5 female, 5 male, aged 21.7±1.6 years, N=9 pCASL datasets (4F, 5M, aged 21.3±1.2 years). For part 2, there was a separate cohort of N=6 participants (2F, 4M, aged 25.8±1.7 years) with complete datasets. Tables 2.1 and 2.2 provide more detailed information on participants characteristics.

Screening was the same as chapter 2, which included: a review of the participant information sheet, checklist of in/exclusion criteria consent form, height and weight, MR Safety screening form (and tattoo form if applicable) (see appendix B.1).

TABLE 2.1: **Part 1, Participants Characteristics Information.** Table of participants characteristics included in the data analysis. F (female), kg (kilograms), m (metres), M (male), std (standard deviation).

Participant Number	Age (years)	Sex	Weight (kg)	Height (m)
1	23	M	65	1.69
2	22	M	90	1.61
3	23	F	49	1.58
4	21	F	52	1.57
5	20	M	57	1.73
6	20	F	69	1.75
7	25	F	60	1.60
8	22	M	64	1.78
9	21	F	85	1.63
10	20	M	50	1.62
Group mean±std	**21.7±1.6**	**5M & 5F**	**64.1±14.1**	**1.66±0.10**

TABLE 2.2: **Part 2, Participant Characteristics Information.** Table of participant characteristics for part 2. F (female), m (metres), M (male), kg (kilograms), std (standard deviation).

Participant Number	Age	Sex	Weight (kg)	Height (m)
1	27	F	55	1.65
2	25	F	89	1.66
3	26	M	66	1.63
4	24	M	95	1.88
5	27	M	80	1.78
6	26	M	75	1.76
Group mean±std	**25.8±1.7**	**4M, 2F**	**76.7±14.5**	**1.73±0.10**

2.6.2 Respiratory Stimulus

Two systems were used to administer respiratory stimuli: a computerised system and manual control. In both cases a sequential gas delivery (SGD) breathing circuit mask was fitted outside the scanner (Fig. 2.2B). It was fitted to the participant's face with an airtight seal using medical tape (Tegaderm, 3M Healthcare, St. Paul, Minnesota, USA). Gas cylinders were stored outside of the scanner in an adjacent room, with gas hoses connected to the gas delivery system (RespirAct^{TM}).

Unfortunately, after part 1 had been completed, the RespirAct^{TM} oxygen sensor broke during an interim study, and it was therefore no longer possible to use it for experiments. The RespirAct^{TM} Gen 4^{TM} has since been released, but there were no funds available to replace the existing Gen 3^{TM} (Reference for Gen 4^{TM} [81]). The gas delivery kit for part 2 was then created from other available kit, and had a simpler gas challenge.

For part 1, hypercapnic challenges were delivered using a prospective end-tidal targeting system via a computer-controlled gas blender [215] (RespirAct Gen 3^{TM}, Thornhill Medical, Toronto, Canada) (Fig. 2.2A). This device is able to administer inspired gases and measure expired gases, in addition to being able to target specific $P_{ET}CO_2$and partial pressure of end-tidal ($P_{ET}CO_2$) values and oxygen (O_2)). It is able to deliver more complex paradigms using a prospective end-tidal targeting algorithm via a computer-controlled gas blender. This makes it possible to deliver more complex paradigms e.g. ramps, sinusoidal or block paradigms [215]. The prospective algorithm was tuned for each participant by first estimating their baseline maximum volume of O_2 and CO_2 (VO_2 and VCO_2) and then adjusting to maintain an isocapnic condition. Participants were then given a 60 s demonstration of the hypercapnic condition, at +10

mmHg of their baseline $P_{ET}CO_2$, to ensure that they would be comfortable with it in the scanner. Figure 2.3 shows the full set up as a conceptual diagram.

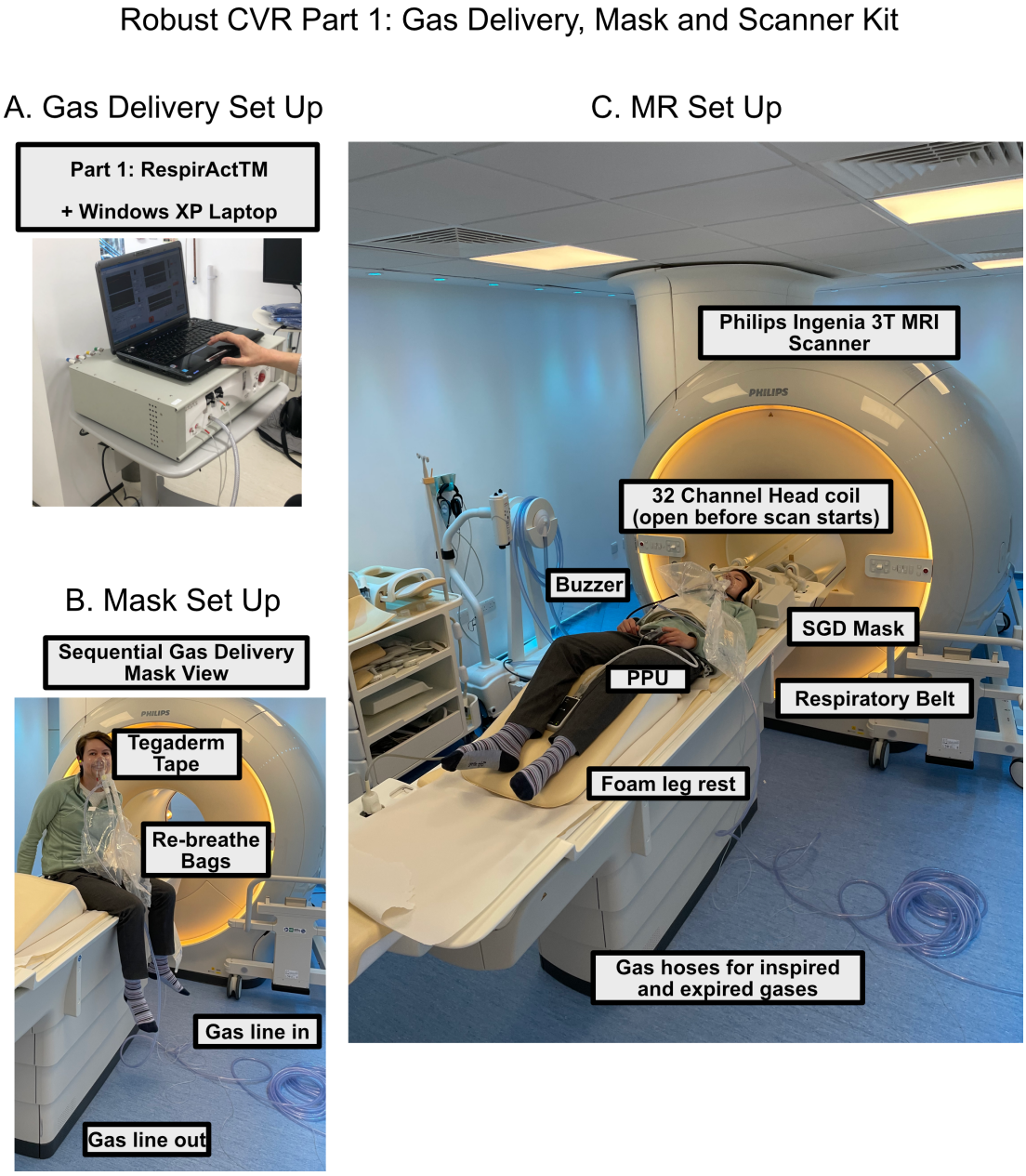


FIGURE 2.2: **Robust CVR Part 1: Gas Delivery, Mask and Scanner Kit.** Photos of the Respiract^{TM} (A), gas delivery kit, mask set up (B) and the final set up in the MR scanner (C). Photo is not de-identified as CCM is in the photo. MRI (magnetic resonance imaging), PPU (peripheral pulse unit), SGD (sequential gas delivery mask), T (tesla).

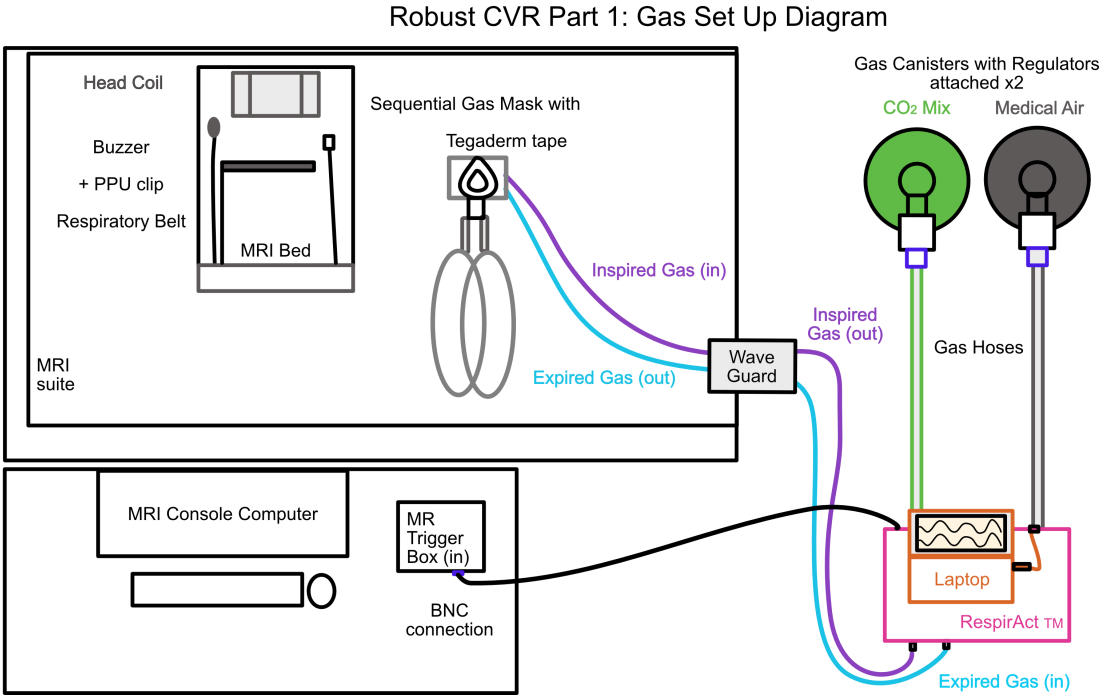
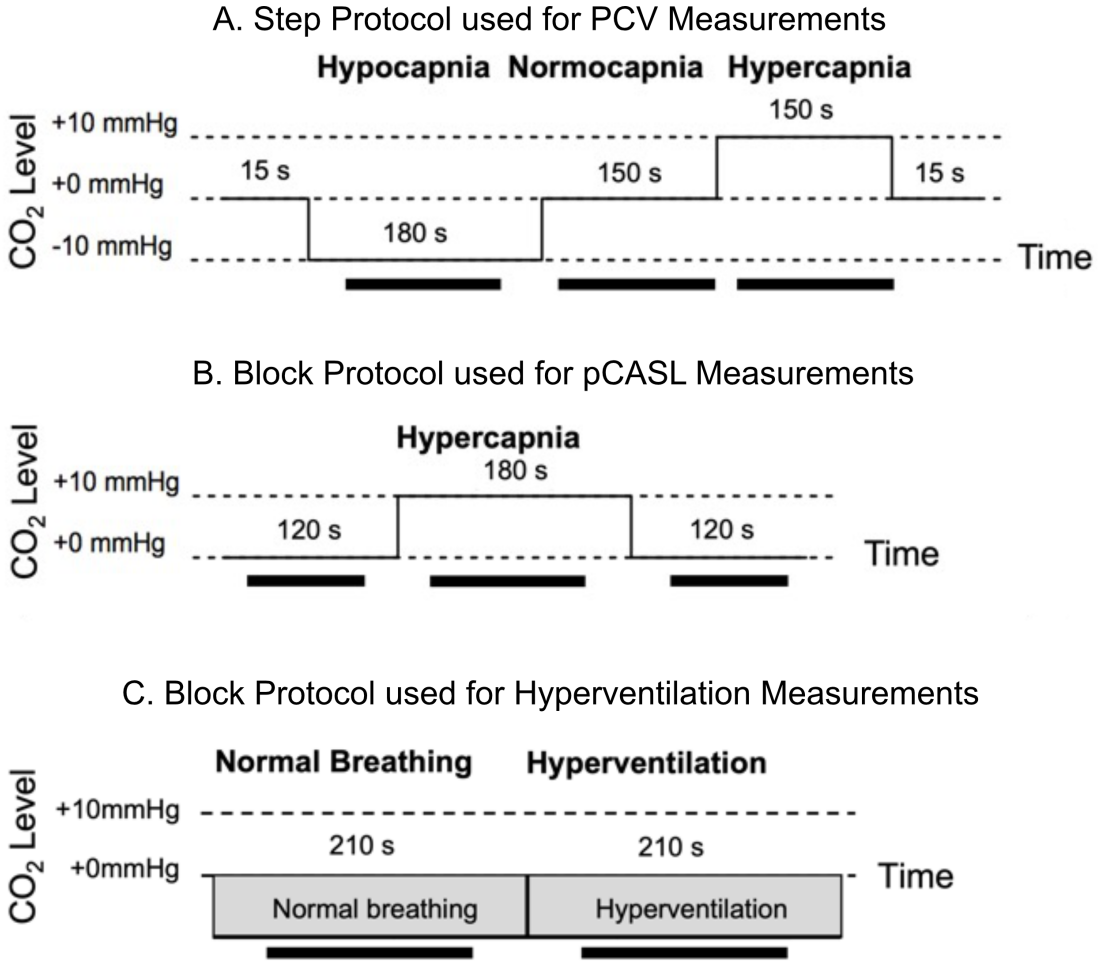


FIGURE 2.3: **Robust CVR part 1 Gas Set up Diagram.** Diagram showing a conceptual set up of the in/outputs for the gas delivery in the Philips Ingenia scanner room for part 1. Not to scale. BNC (Bayonet Neill–Concelman cable), CO_2 (carbon dioxide), MRI (magnetic resonance imaging), PPU (peripheral pulse unit).

For the part 1 PCV measurements, a step protocol of hypocapnic, normocapnic and hypercapnic levels was used (Fig. 2.6.2A). The PCV protocol targeted the $P_{ET}CO_2$ at ±10 mmHg above and below the participant's resting $P_{ET}CO_2$. Participants were asked to increase their ventilation rate during the hypocapnic condition to decrease their $P_{ET}CO_2$ and, once stable, they were told to breath normally. This was maintained for 180 s below their baseline normocapnic condition, followed by 150 s at baseline and a further 150 s at hypercapnia. Total time 480 s. The hypocapnic condition block was slightly longer to allow the $P_{ET}CO_2$ level to stabilise. The breath-by-breath values for $P_{ET}CO_2$ from the RespirAct^{TM} software were extracted from the 120 s time windows for the hypocapnia, normocapnia and hypercapnic conditions (see black bars in Fig.

2.6.2A) for the analysis. These values were then averaged across participants to give a group mean value during each of the three conditions.

For part 1 pCASL measurements, a single block of hypercapnia interleaved with normocapnia was used (Fig. 2.6.2B). The pCASL protocol consisted of 120 s baseline, 180 s at +10 mmHg $P_{ET}CO_2$, then 120 s baseline for a total time of 420 s per parameter set. The breath-by-breath values for $P_{ET}CO_2$ from the RespirAct^{TM} software were extracted similarly to the PCV data, though this time using a window of 180 s for normocapnia and a window of 120 s for hypercapnia. The window was used to clip the start and end of the block to capture a more stabilised $P_{ET}CO_2$ level. Figure 2.7A shows example respiratory data, including pre-processing.



mmHg (millimetres of mercury), s (seconds).

mmHg (millimetres of mercury), s (seconds).

FIGURE 2.4: **Respiratory protocols.** A: Step protocol used for Phase Contrast Velocity (PCV) measurements, in part 1, made in the main feeding arteries of the brain by altering the participants CO_2levels. The hypercapnia condition was performed by targeting end-tidal partial pressure of CO_2 ($P_{ET}CO_2$) at 10 mmHg above the participant's resting $P_{ET}CO_2$. The hypocapnic condition was achieved by asking participants to increase their ventilation rate. B: A block protocol was used for Pseudo Continuous Arterial Spin Labelling (pCASL) measurements in part 1, with three different sets of pCASL preparation parameters. Black bars denote the time windows used for analysis were taken from the middle of each block. C: A block protocol, for part 2, involved 210 s of normal breathing followed by 210 s of hyperventilation for three parameter sets, which was then windowed to 200 s.

mmHg (millimetres of mercury), s (seconds).

For part 2, the flow of medical air into the SGD breathing circuit was adjusted using a medical flow meter to clamp $P_{ET}CO_2$ [19]. The readout of the participant's $CO_2$was determined via live observation of the expired CO_2levels. During normal breathing the breathing rate and CO_2level were determined, and this level was manually matched during the hyperventilation condition via addition of O_2 gas into the SGD. An ADInstruments Gas Analyser (Product Code ML206) and Powerlab (26 Series with a 6-channel input) were connected to a 2016 Macintosh Macbook Pro (Apple, Cupertino, USA) with LabChart V8.1.24 (ADInstruments, NZ Limited) (Fig. 2.5). A custom Labchart^{TM} template was used to record continuous O_2 and CO_2, measurements. These were recorded as a percentage and later converted to $P_{ET}O_2$ and $P_{ET}CO_2$. Figure 2.6 shows the full set up as a conceptual diagram.

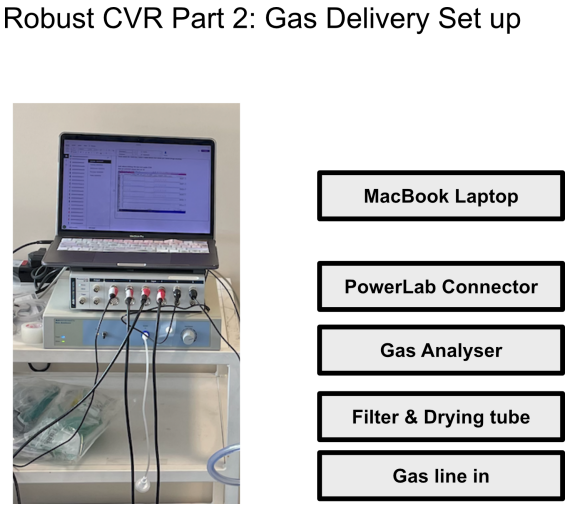


FIGURE 2.5: **Part 2, Gas Delivery Set up.** Example of the set up for the gas delivery kit used in Robust CVR part 2. Note, this photo was taken during set up development rather than during an actual scan. Hence, the laptop screen shows a screenshot of Labchart^{TM} within a notebook rather than the actual display screen. The final version did not require the extra connectors other than the gas line in /out.

For part 2, during the single slice temporally resolved B_0 mapping technique, participants were asked to breathe normally for the first half (210 s) of the

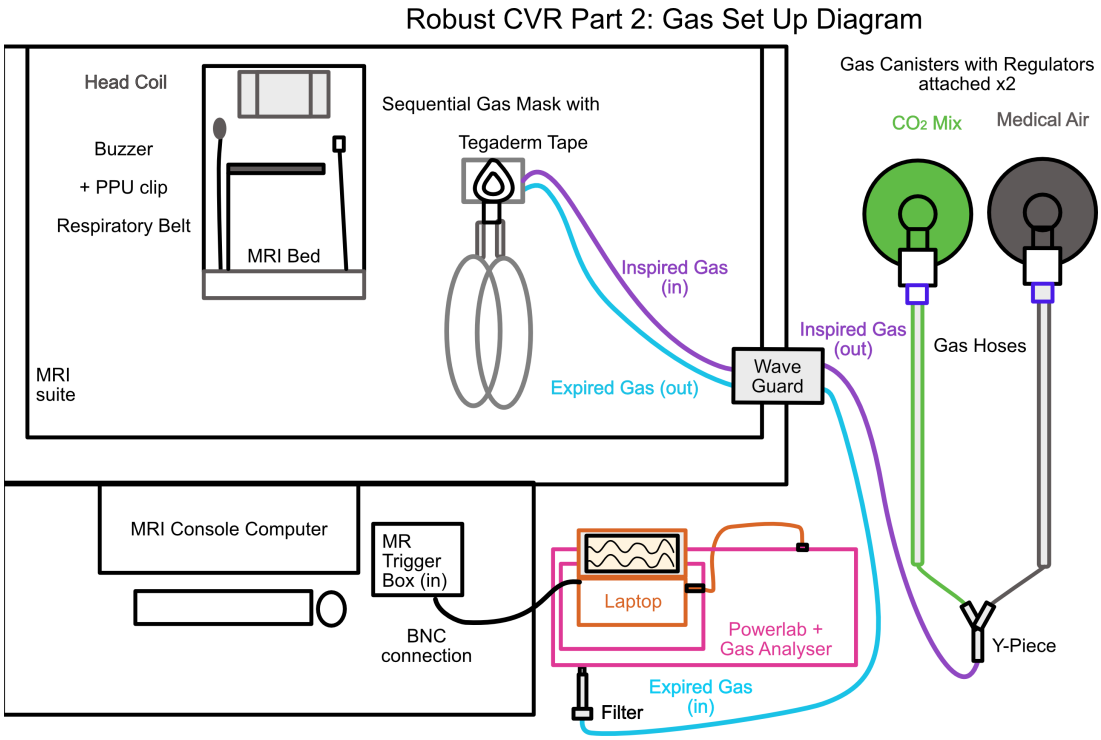


FIGURE 2.6: **Robust CVR part 2 Gas Set up Diagram.** Diagram showing a conceptual set up of the in/outputs for the gas delivery in the Philips Ingenia scanner room for part 2. Not to scale. BNC (Bayonet Neill–Concelman cable), CO_2 (carbon dioxide), PPU (peripheral pulse unit), MRI (magnetic resonance imaging).

protocol whilst their $P_{ET}CO_2$ was passively monitored. Then they were asked to hyperventilate for the second half (210 s) of the scan whilst the $P_{ET}CO_2$ was maintained at their normocapnic level via the SGD mask (Fig. 2.6.2C). Figure 2.7B shows example respiratory data, including pre-processing. Expired CO_2 data were collected as a percentage and converted to $P_{ET}CO_2$ by multiplying by 713 mmHg to account for atmospheric pressure of dry gas (assuming pATM = 760 mmHg, minus lung partial pressure of water vapour pH_2O = 47 mmHg at body temperature).

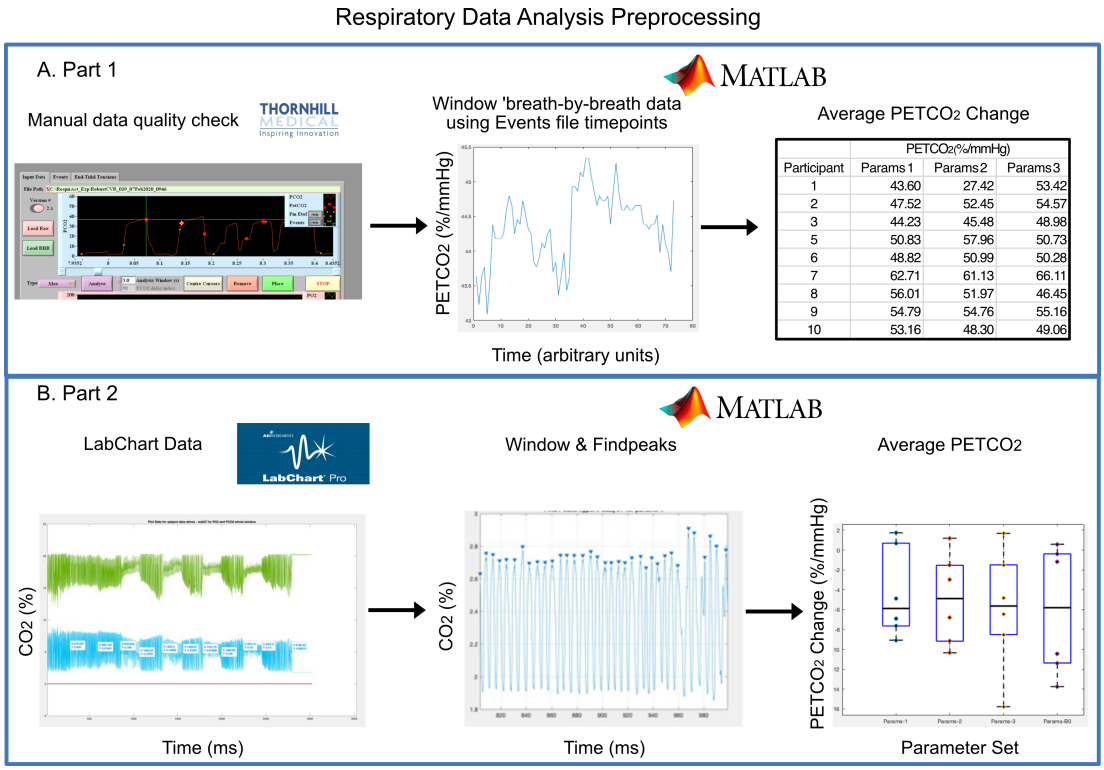


FIGURE 2.7: **Respiratory Data Analysis Preprocessing.** Part 1 used RespirAct™ software on a Windows XP laptop to manually check the data and correct any breath-by-breath (BBB) markers. The BBB files were then exported and MATLAB was used to window the data using the RespirAct™ 'event' files (marked during scanning for important time points) to give the end-tidal partial pressure of carbon dioxide ($PETCO_2$) data for each participant, MR scan and CO_2 condition. B. Part 2 used LabChart (by AD instruments) software during data collection. The data was exported as text files, the MATLAB files for the 'events' were then used to window the data into each scan and CO_2 condition, followed by extracting the peaks to give the $PETCO_2$ data. ms (milliseconds), %/mmHg (percentage change per millimetres mercury). (Logos references: ADInstruments link, Thornhill Medical link).

2.6.3 MR Imaging

Safety Requirements

An MR screening form (see appendix section D), and if applicable a Tattoo safety form (see appendix section D), were signed by the participant and the MR assistant/operator. Participants were given ear plugs to reduce audio noise from the scanner.

Participants were scanned using a 3T Ingenia scanner for both parts of this study using the vendor's 32-channel head receive coil and body transmit coil (Philips Healthcare, Best, Netherlands) (see images in theory section 1.15). The peripheral pulse unit (PPU) and respiratory belt were also used to record the participants' heart rate and respiratory rate, which can be seen in Fig. 1.15C.

MR Protocols

In both parts of the study an Magnetization Prepared Rapid Acquisition of Gradient Echo (MPRAGE) was performed for use in registration during the image analysis stage [160]. The MPRAGE was acquired with FOV 256 x 256 mm x 162 slices. TR/TE 8.1 / 3.7 ms, flip angle 8°, total scan time 3 mins 44 s.

For part 1, the MRI protocol is shown in figure 2.8. A time of flight (TOF) image was first acquired to determine where to place the imaging plane for the PCV and the labelling plane for the pCASL. The PCV scan was planned for hypocapnia, then repeated for both normo- and hypercapnia. The pCASL labelling plane was planned to coincide with the PCV imaging plane. The hypercapnic challenge (Fig. 2.6.2B) was then repeated for three different sets of pCASL preparation parameters. This was followed by an axial B_0 map scan, and lastly, the anatomical MPRAGE. The full text files of the scan protocols can

be found in the Zenodo repository (Study 1 Robust CVR Part 1: 10.5281/zenodo.10018201, Study 4 Robust CVR Part 2: 10.5281/zenodo.10018214).

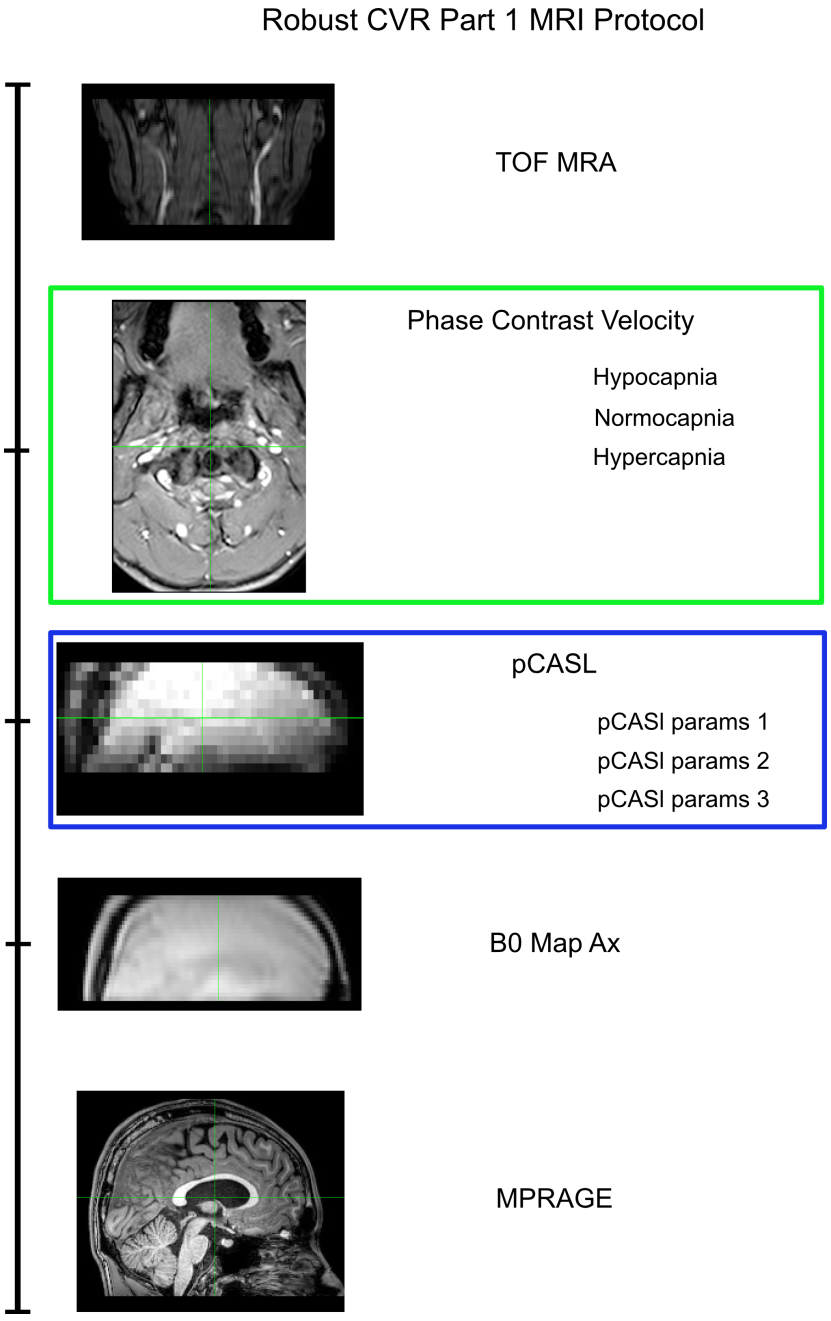


FIGURE 2.8: **Robust CVR Part 1 MRI Protocol.** The sequence for MR scanning was as follows; a survey, TOF (time of flight), PCV (phase contrast velocity) x3, pCASL (pseudocontinuous arterial spin labelling) x 3 sets of parameters, B_0 Map Axial, MPRAGE (Magnetization Prepared Rapid Acquisition of Gradient Echo). Images are an example set from one subject.

For part 1, PCV measurements were made in a single slice, positioned through the V3 segment of the vertebral arteries (VA) and the internal carotid arteries (ICA), across 30 cardiac phases (FOV = 150x101 mm, 254x171 matrix, one 4 mm slice, TR/TE = 9 ms/5.3 ms, VENC = 90/120 cm/s – higher for hypercapnia). The slice was positioned axially to match the placement of the pCASL labelling plane. Measurements were made during each of the three conditions of the step protocol (Fig. 2.6.2A). For the PCV, the RespirAct^{TM} was synchronised with the imaging by placing a time marker in the respiratory recordings file.

For part 1, single post-labelling delay (PLD) pCASL data were acquired (FOV=240 mm^2, 64x64 matrix, twelve 5 mm slices, 1 mm gap, TR/TE=4s/14 ms, bandwidth=2056.7 Hz/px, PLD=1800 ms, label duration=1500 ms). For reference, the flip angle in pCASL is the single labelling pulse in the pCASL labelling pulse train and the label duration is the duration of each pCASL labelling pulse [223]. Three sets of pCASL preparation parameters were used: Params-1 (Vaclavu and colleagues (2018)[233]), Params-2 (Aslsop and colleagues (2015)[7]) and Params-3 (Aslan and colleagues (2010) [13]) (see Table 2.3). The RespirAct^{TM} protocol was synchronised with the start of the imaging protocol. The hypercapnia block protocol was repeated for each parameter set (Fig. 2.6.2B).

For part 2, the MR scan protocol is shown in Figure 2.9. B_0 mapping was conducted using two sequences; the first was to measure changes in B_0 during the hyperventilation protocol in a single slice (single slice, temporally resolved) and the second to map B_0 over multiple slices during normal breathing (multi-slice, single time point). Multislice B_1 mapping was also performed.

The single slice B_0 map was acquired at the labelling plane with multiple repetitions (FOV = 240x240 mm, matrix 128x128, one 3 mm slice, TR/TE =

TABLE 2.3: **Details of pCASL Parameter Sets.** Details of the Pseudo Continuous Arterial Spin Labelling (pCASL) preparation parameters used in Params-1, Params-2 and Params-3. G_{av} (average gradient amplitude) and G_{max} (maximum gradient amplitude), ms (milliseconds), μs (microsecond), mT/M (millitesla per meter).

pCASL Preparation Parameters			
	Params-1	Params-2	Params-3
Interval	1.21 ms	1.20 ms	1.00 ms
G_{av}	0.36 mT/m	1.00 mT/m	0.60 mT/m
G_{max}	5 mT/m	10 mT/m	6 mT/m
Flip angle	27.8°	27.3°	18°
Duration	480 μs	500 μs	500 μs
Spacing	730 μs	700 μs	500 μs
G_{max}/G_{av}	13.9	10.0	10.0

1 s/4.6 ms, flip angle 3°, 420 repetitions), with shimming performed over the volume. Participants performed the hyperventilation block protocol during this scan (Fig. 2.6.2C).

The multislice B_0 map was centred on the labelling plane (FOV = 240x240 mm, matrix 128x128, forty 6 mm slices, TR/TE = 9.2 ms/4 ms, flip angle 3°). A shim box was placed to cover the imaging volume in order to replicate the magnetic field inhomogeneity that occurs at the labelling plane in the pCASL measurements under similar conditions.

Multislice B_1 mapping was performed using the dual refocusing echo acquisition mode (DREAM) technique [164] during normal breathing centred on the labelling plane (FOV= 240x240 mm, matrix 80x80, twenty-two 5 mm slices, TR/TE_1/TE_2 = 6 ms/ 1.8 ms/ 3.4 ms, flip angle 8°). DREAM is

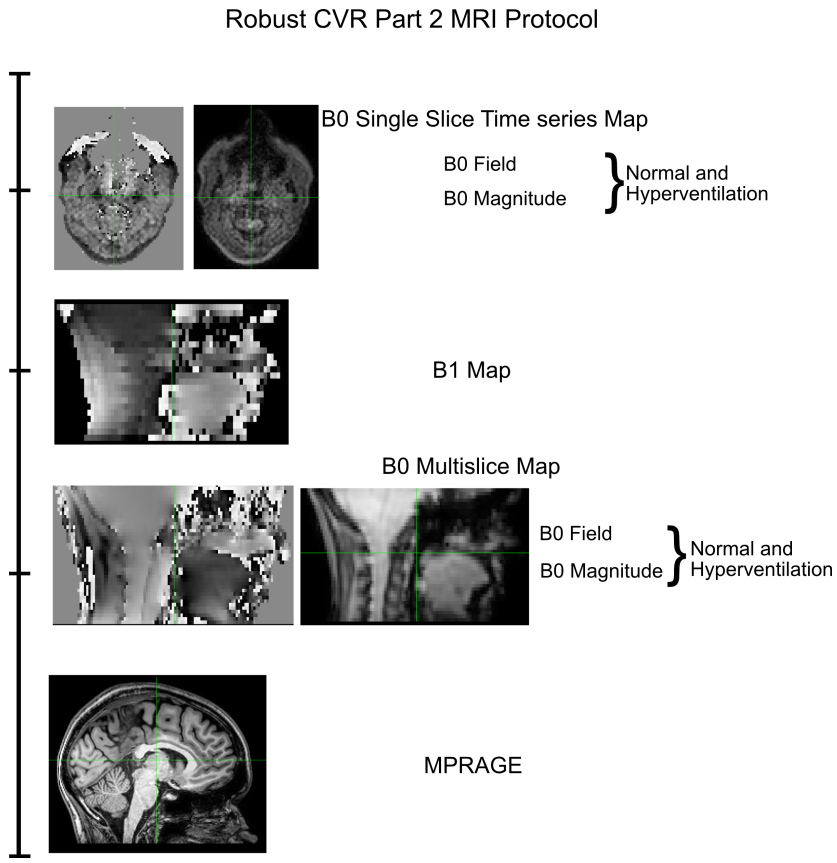


FIGURE 2.9: **Robust CVR Part 2 MRI Protocol.** The sequence for MR scanning was as follows; a survey, TOF (time of flight), pCASL (pseudocontinuous arterial spin labelling) x 3 sets of parameters, Axial B_0 Map, MPRAGE (Magnetization Prepared Rapid Acquisition of Gradient Echo). Images are an example set from one subject.

Image Analysis

For the pCASL data, pre-processing was performed using FMRIB Software Library (FSL) [252]. Non-brain tissue was removed using the Brain Extraction Tool (BET) [216]. Motion correction and registration were performed with FMRIB's Linear Image Registration Tool (MCFLIRT) [123]. Spatial smoothing was performed with a FWHM kernel (5 mm). High pass temporal filter cut off was set at 240 s. Analysis was performed using a full perfusion signal model using FEAT [252]. The model consisted of three explanatory variables (EVs): alternating control and label (EV1) representing the baseline perfusion, the $P_{ET}CO_2$ time course to remove BOLD contamination (EV2), and the interaction between EV1 and EV2 (EV3) representing the change in perfusion in response to the hypercapnia challenge. Regions of interest (ROI) were generated by first segmenting the participant's T_1-weighted structural using FMRIB's Automated Segmentation Tool (FAST) to create a grey matter (GM) partial volume estimate (PVE) map [258]. For reference, PVE refers to the probability (an estimate) of a specific voxel containing a mixture of GM, white matter (WM) and cerebrospinal fluid (CSF). This is because an average voxel size (i.e. a 3D volume) in an ASL perfusion image is larger than the average cortical thickness, and therefore likely to, partially, contain some of each of the three tissues/fluid [15, 49]. Each of the three components can be further defined as fractional tissue volume or tissue partial volumes of the total voxel volume (P_{GM}, P_{WM} and P_{CSF}). By separating these tissues out, by only including voxels with a probability of having the desired tissue (above a certain threshold, often >50%), it is then possible to estimate the tissue specific perfusion using ROIs to give CBF_{GM} and CBF_{WM}.

This pipeline was therefore further refined by restricting the ROI to cortical GM so that the results would present the CBF specifically of the GM. This was

done by co-registering the Montreal Neurological Institute (MNI), McConnell Brain Imaging Centre, Montreal Neurological Institute, McGill University, Montreal, Quebec, Canada) Cortical Atlas via the MNI standard brain to the structural image [136, 150]. Finally, the masked PVE map was thresholded at 50% and transformed to the pCASL images. Further analysis was performed in MATLAB (Mathworks, Natick, MA). The median flow was calculated as the percentage change to give a measure of CVR for the grey matter in the brain (see Eqn 2.1. The median CVR values were then normalised by the change in $P_{ET}CO_2$ (Δ $P_{ET}CO_2$). Then the change in $P_{ET}CO_2$ was calculated as the mean hypercapnia values minus the mean baseline values and gave the resulting flow change as %/ mmHg.

$$Percentage\ Difference = \frac{Hypercapnia - Normocapnia}{Normocapnia} \tag{2.1}$$

For part 1 PCV data, ROIs were manually defined using Segment v3.0 [110] for all four feeding arteries (left (L) and right (R) ICAs and VAs), which were then propagated across all cardiac phases. The maximum velocity from each ROI and cardiac phase was extracted for all three CO_2 levels. The mean across cardiac phases was then calculated. The group mean maximum velocity was used to minimise contamination from static tissue included in the ROI, which may bias estimates when averaging across the whole ROI (see Fig. 2.10). The percentage change in velocity was calculated relative to normocapnia for hypercapnia and hypocapnia (using Eqn 2.1), and then also normalised by the Δ $P_{ET}CO_2$ recorded for each participant resulting in units of %/mmHg. In addition, for all participants, the maximum velocity in each artery was averaged for each CO_2 level to give the group mean and standard deviation.

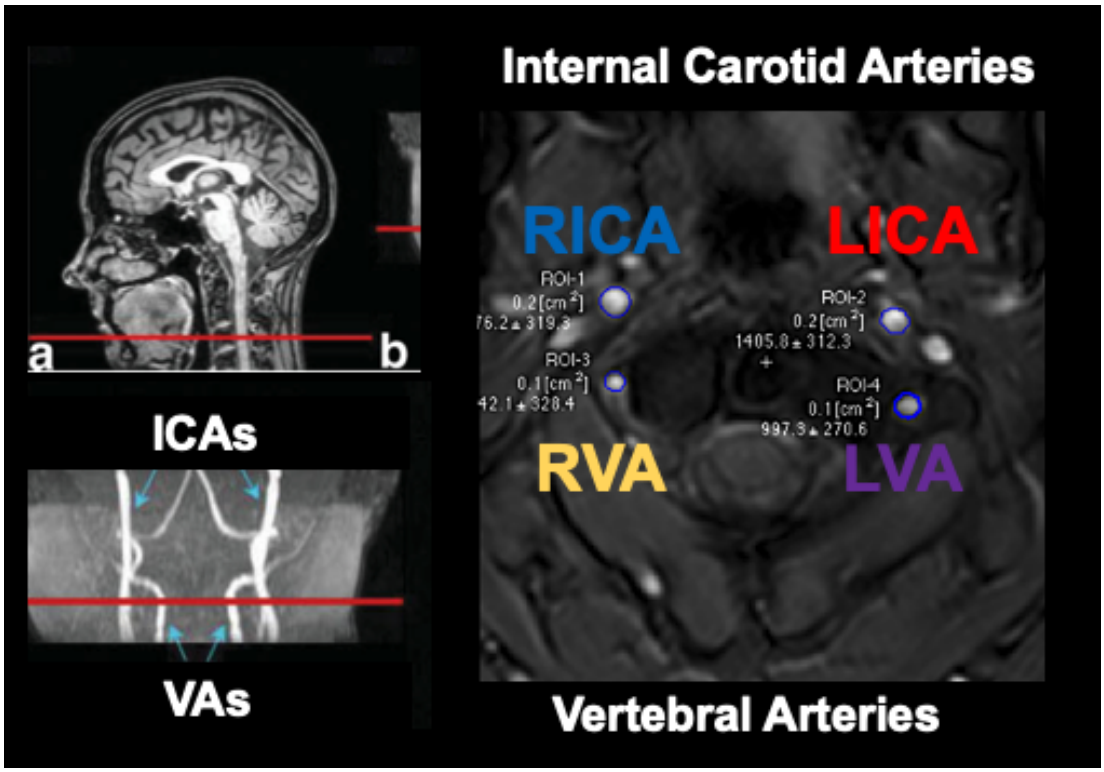


FIGURE 2.10: **Part 1 Methods, drawing ROIs.** Images showing the position of the ICA and VAs on a sagittal T1w image, an axial Time of flight image, and finally the coronal image used with the Segment software to draw ROIs of each artery. ICA (internal carotid artery), VA (vertebral artery), L (left), R (right), T1w (anatomical T1 weighted image).

For part 2, the B_0 single slice, time resolved MR volumes were split into two halves, the first half (volumes 1 to 200) and second half (220 to 400), to separate out the normo- and hypercapnic conditions using FSLROI. Volumes 201 to 219 were not included in the analysis to enable the new hyperventilation steady state to be established. The change in B_0 due to hyperventilation was calculated from the single slice data as the B_0 during hyperventilation (first 200 s) minus the B_0 during normal breathing (last 200 s). The difference between the 2^{nd} and 98^{th} percentiles over time was also calculated for normal breathing and hyperventilation as a more robust measure of the range of B_0 values during hyperventilation. The B_0 offset during normal breathing prior to the hyperventilation task was estimated from the multislice data as the mean across each artery ROI at the labelling plane.

For part 2, the B_1 was estimated as a percentage of the nominal flip angle and was measured in artery ROIs at both the labelling plane and at 90 mm below the anterior commissure-posterior commissure (AC-PC) line to compare with previously reported results [42] (see Fig. 2.11). Median values of B_0 (both the single slice temporally resolved and the multi-slice single time point) and B_1 were extracted from all four arteries using ROIs of 5x5 pixels (B_0) and 3x3 pixels (B_1) created using FSLeyes [151] manually. The B_0 images were low resolution, so the higher resolution images (MPRAGE) were overlayed with the B_0 and B_1 images when defining ROIs (see Fig. 2.11). A MATLAB (MATLAB, Mathworks, Natick, MA) script was used to extract the B_0 and B_1 from the artery ROIs and for creating graphs of the results.

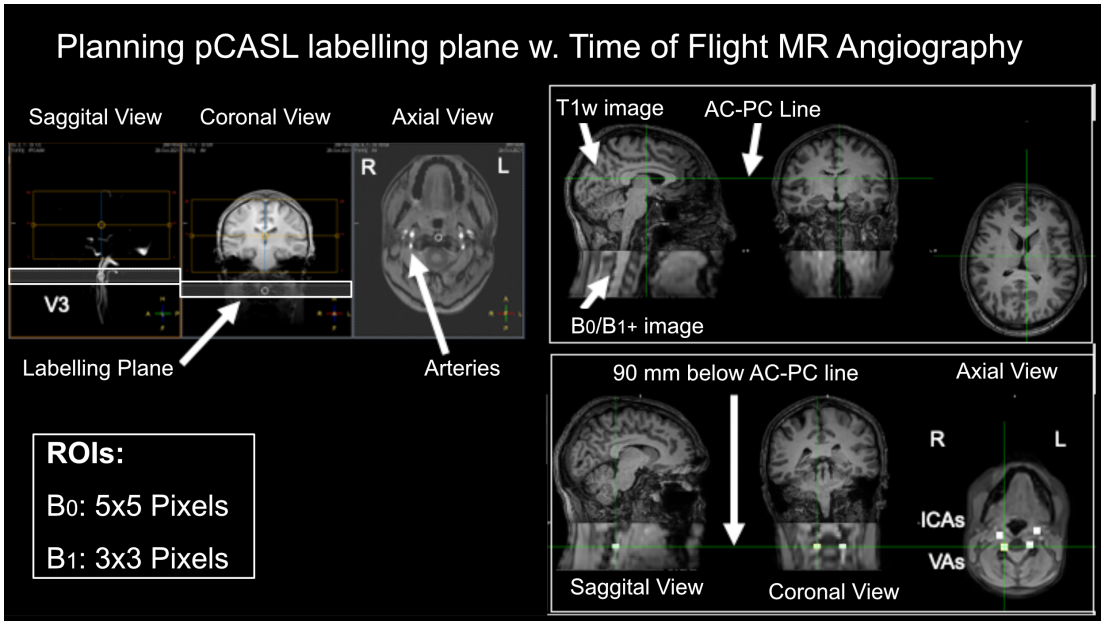


FIGURE 2.11: **Part 2 Methods, planning the labelling plane and the B_1 and B_0 slices.** Example of using time of flight data to plan the labelling plane 90 mm below the anterior commissure-posterior commissure (AC-PC) line. ICAs (internal carotid arteries), mm (millimetres), L (left), R (right), ROI (region of interest), T1w (T1 weighted image), V3 (third vertebrae segment), VAs (Vertebral Arteries). Based on Bush et al., (2018) [42], McCarthy et al., 2022 [151].

2.6.4 Statistical Analysis

For all statistical tests, the alpha threshold for significance was set at 0.05. The pCASL data were tested with a Shapiro-Wilks test (Params-1, 2 and 3 $p>0.05$). For the PCV data, the Shapiro-Wilks results suggested non-normal data ($p<0.05$), but the kurtosis was near zero (-0.0482) which suggests a distribution shape close to normal, positive skewness (0.7603). This indicates the distribution is slightly right-skewed, so in order to match the pCASL data, parametric statistical tests were still used. For the respiratory challenge, pCASL data, one-way ANOVAs were performed to compare multiple groups (e.g. $P_{ET}CO_2$ values across different parameter sets) to investigate the null hypothesis that the group mean values were equal. In the case that group means were found to be significantly different, post-hoc pairwise comparisons between groups were justified using the Tukey-Kramer test, to determine if specific group means were different. The Tukey-Kramer method controls for multiple comparisons by correcting for the family wise error rate. In this sense it is less conservative than multiple T-tests with Bonferroni correction.

The B_0 and B_1 data were tested with a Shapiro-Wilks test and was shown to be non-parametric ($p<0.05$) for some arteries. There were also some extreme outliers. Therefore a Kruskal-Wallis test was performed, with the null hypothesis being that there would be no difference between groups. In the case that group means were found to be significantly different, post-hoc pairwise comparisons between groups were justified using the Mann Whitney U test, with inbuilt Bonferroni correction, to determine if specific group means were different.

2.7 Results

There are summary tables of the results for this chapter in the appendix

2.7.1 Respiratory Stimulus

In part 1 of this study, one of the 10 participants scanned did not complete the study due to a technical issue with the scanner. Hence the results show N=10 for PCV data and N=9 for pCASL data. The summary of group mean CO_2 levels across the respiratory protocols are shown in Table 2.4. These results confirm that the hypercapnia challenges were sufficient to change the participants' $PETCO_2$ levels. The full table for Params-1, Params-2, and Params-3 $PETCO_2$ levels for normo- and hypercapnia as well as the difference data is in the appendix (see table B.1). There was no significant difference between the three parameters for the pCASL data $PETCO_2$ levels during normocapnia conditions, and there was no significant difference during the three hypercapnia conditions. However, the normocapnia conditions was significantly different to the hypercapnia conditions as expected (ANOVA p=0.0000).

In part 2, of the seven participants scanned, six who were in the "younger" category of 18-30 years were included in these results (see table 2.5) with N=6 completing both B_0 scans and the B_1 scan. There was no significant difference in $PETCO_2$ to one another in terms of percentage change (ANOVA, p=0.9374), which infers that the hyperventilation challenge maintained a consistent normocapnia level during the B_0 scans.

TABLE 2.4: **Part 1, Respiratory Challenges Results.** Part 1 Group mean end-tidal partial pressure of carbon dioxide ($PETCO_2$) levels during respiratory challenges (mean±standard deviation) for the PCV and pCASL data. N=10 for PCV, N=9 for pCASL. Change in $PETCO_2$ between normocapnia and hypercapnia (Δ), millimetres of mercury (mmHg), % (percentage), pseudocontinuous arterial spin labelling (pCASL), phase contrast velocity (PCV).

Participant No.	**PCV**				**pCASL**		
	Hypocapnia (mmHg)	**Normocapnia (mmHg)**	**Hypercapnia (mmHg)**	**Δ (mmHg)**	**Normocapnia (mmHg)**	**Hypercapnia (mmHg)**	**Δ (mmHg)**
1	31.8±1.5	38.3±1.1	45.0±1.4	6.7	40.0±1.5	45.8±0.6	5.8
2	37.7±1.2	42.5±1.8	48.4±0.3	6.0	42.2±0.7	49.5±1.2	7.2
3	33.6±0.7	40.6±1.8	46.8±0.4	6.2	40.6±0.5	47.1±0.2	6.5
4	35.9±1.5	40.2±1.7	48.1±2.1	7.0	NA	NA	NA
5	33.8±1.9	39.1±1.3	47.0±0.6	7.9	40.5±0.4	47.9±0.9	7.5
6	30.9±0.7	37.7±0.9	43.9±2.8	6.1	38.9±0.1	45.9±0.1	7.0
7	28.2±4.4	36.8±1.7	45.2±0.4	8.4	35.8±0.3	44.7±0.1	8.9
8	36.7±0.7	45.2±3.8	48.3±1.3	3.1	39.9±1.1	47.2±1.7	7.2
9	34.2±1.0	40.4±0.3	48.0±0.6	7.7	39.5±0.2	47.2±0.2	7.7
10	38.3±2.7	44.2±3.0	50.7±0.2	6.5	43.3±1.5	50.3±1.2	7.0
Group mean±std	**34.1±1.6**	**40.5±1.7**	**47.1±1.0**	**6.6±1.5**	**40.1±0.7**	**47.3±0.1**	**7.2±0.8**

TABLE 2.5: **Part 2, Respiratory Results.** Group mean end-tidal partial pressure of carbon dioxide ($P_{ET}CO_2$) levels during respiratory challenges (mean±std (standard deviation) for normocapnia, hyperventilation, and Δ (change in $P_{ET}CO_2$ between normocapnia and hyperventilation), millimetres of mercury (mmHg), % (percentage), N=6.

	Condition		
Participant No.	**Normal ventilation (mmHg)**	**Hyperventilation (mmHg)**	**Δ (mmHg)**
1	19.3±0.2	19.4±0.4	0.1
2	52.0±0.7	51.4±0.7	-0.6
3	60.9±2.1	60.7±2.0	-0.2
4	52.8±3.3	45.5±1.7	-7.3
5	59.1±0.6	52.4±2.0	-6.7
6	57.3±0.7	51.4±2.9	-6.0
Group mean±std	**50.2±1.3**	**46.8±1.6**	**-3.4±3.5**

2.7.2 MR Imaging

Part 1 Effect of Hypercapnia on Different pCASL Parameters

The pCASL data from part 1 is presented in Figure 2.12 and shows the grey matter CVR for each set of pCASL parameters. Figure 2.12A shows the percentage change in CBF in response to hypercapnia. Figure 2.12B plots the percentage change in CBF normalised to each individual's change in $P_{ET}CO_2$ in mmHg (group mean±std: Params-1 = 6.08±1.45 %/mmHg, Params-2 = 4.05±1.61 %/mmHg, Params-3 = 5.06±1.51 %/mmHg). Outliers observed in Fig. 2.12A for Params-1 and Params-3 appear reduced, suggesting some participants may have experienced a slightly different change in $P_{ET}CO_2$. One-way ANOVA showed that the group means (after normalisation) were not all the same (p=0.0315). Post-hoc pairwise comparisons between groups using the Tukey-Kramer test revealed the means of Params-1 and Params-2 were significantly different (p=0.030).

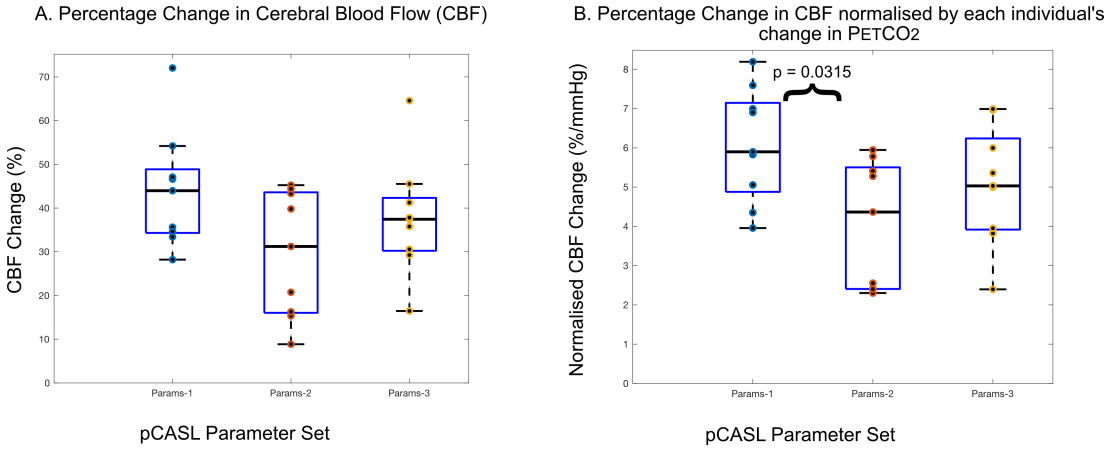


FIGURE 2.12: **Comparison of CVR estimates for each of the three pCASL (pseudocontinuous Arterial Spin Labelling) labelling parameter sets** A: The percentage change in cerebral blood flow (CBF) shows two outliers and did not show a difference between groups. B: The percentage change in CBF normalised by each individuals' change in end-tidal partial pressure of carbon dioxide ($PETCO_2$) in mmHg (millimetres of mercury). A significant difference was found between Params-1 and Params-2 (p=0.0315).

Part 1 Effect of Hypercapnia on PCV across Arteries

Figure 2.13A displays the PCV mean maximum velocity averaged across the cardiac cycle and participants for each of the ROIs (arteries) and CO_2 conditions (group mean±std): ICAnormo = 44.4±9.3 cm/s, ICAhyper = 52.6±11.7 cm/s, VAnormo = 22.6±5.1 cm/s, VAhyper = 27.5±6.8 cm/s. Figure 2.13B showed the difference between hypo- and normocapnia, and an ANOVA showed statistical differences at p=0.0121, however post-hoc Tukey's HSD test showed that no individual pairwise comparisons reach statistical significance when controlling for multiple comparisons. This suggests that while there were differences between the groups (particularly between RVA and the other arteries), these differences are not large enough to reach significance in post-hoc testing. Figure 2.13B also shows the difference between normo- and hypercapnia, and again

ANOVA showed a significant overall effect (p=0.0017). The ICAs appeared to have higher mean maximum velocities than the VAs for all CO_2 conditions and the maximum velocities, and were slightly higher in the left arteries compared to the right. However, the Tukey's HSD showed no pairwise comparisons reached statistical significance.

The percentage changes normalised by individual participant's $PETCO_2$ are shown in Figure 2.13C. For hypo- to normocapnia, ANOVA showed a significant overall effect (p=0.0036), but none of the pairwise comparisons reached statistical significance in the Tukey's HSD test. For normo- to hypercapnia, ANOVA showed a significant overall effect (p=0.0032). None of the pairwise comparisons reached statistical significance in the Tukey's HSD test. There was considerable within-group variability relative to between-group differences. Overall, blood velocity showed an effect, as $PETCO_2$ increased so did velocity from hypocapnia to normocapnia, and from normocapnia to hypercapnia.

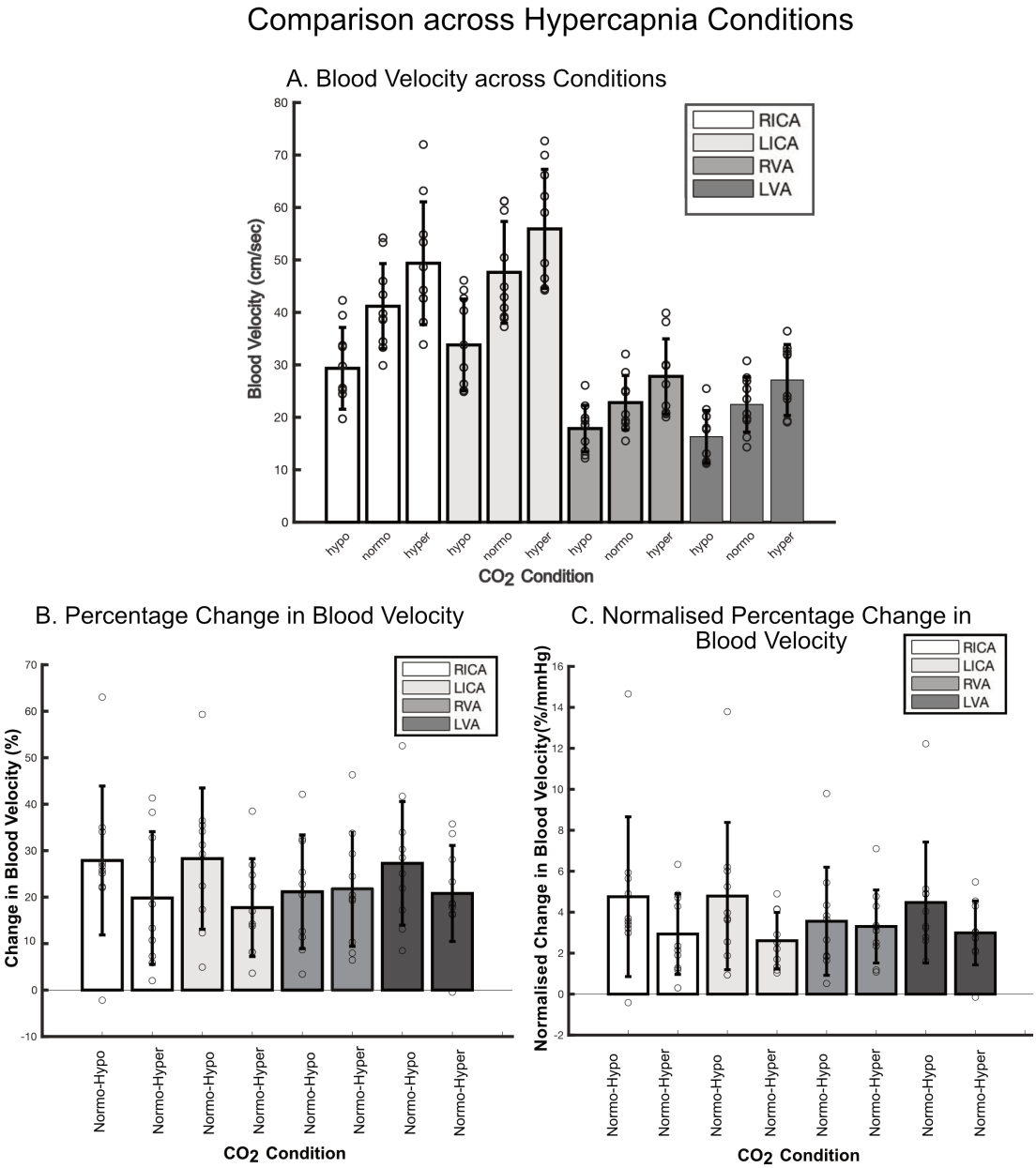


FIGURE 2.13: **Comparison across Hypercapnia Conditions.** Bars show mean±std. A: Average maximum velocity of feeding arteries (N=9, F=4, mean±std) at three carbon dioxide (CO_2) levels: hypocapnia (hypo, -10 mmHg below baseline), normocapnia (normo) and hypercapnia (hyper, +10 mmHg above baseline). Left/right (L/R) internal carotid arteries (ICA) and vertebral arteries (VA). B: Percentage difference in maximum velocity (%) between CO_2 levels by artery. C: Percentage difference in maximum velocity normalised by the change in the individual participants' end-tidal partial pressure of CO_2 (%/mmHg) between CO_2 levels by artery. % (percent), mmHg (millimetres of mercury).

Part 2 Effect of Hyperventilation on B_0

From part 2, the impact of B_0 and B_1 at the labelling plane was investigated in a separate cohort of participants to determine if this was having a compounding influence on the labelling efficiency.

Figure 2.14 presents the variations in B_0 for the four arteries at the labelling plane. The absolute B_0 offset prior to the hyperventilation protocol was measured from the multislice B_0 map (Fig. 2.14A). The change in B_0 was measured as the difference between normal breathing and hyperventilation using the single slice temporally resolved data (Fig. 2.14B). Group average difference (median±IQR) RICA = 4.8±2.9 Hz, LICA = 3.5±9.3 Hz, LVA = 3.6±3.6 Hz and RVA = 4.4±6.6 Hz. The Kruskal-Wallis test showed there was no significant difference between any of the arteries (p=0.2611) or conditions (p=0.3312).

The range of B_0 offsets was estimated as the difference between 2nd and 98th percentiles, and is presented for normal breathing and hyperventilation (Fig. 2.14C), Group averages were: RICA = -1.8±8.1 Hz, LICA = -3.2±2.7 Hz, LVA = 9.1±16.6 Hz and RVA = 8.1±14.9 Hz (median±IQR). There was a significant difference between the arteries (p=0.0162), but no significant difference between breathing conditions (p=0.4704). Of the post-hoc pairwise comparisons using Mann Whitney U test between conditions for individual arteries there was a significant difference between the following arteries: RICA vs LICA (p=0.0086), RICA vs RVA (p=0.0056). Whereas there was no significant difference between the following: RICA vs LVA (p=0.2145), LICA vs LVA (p=0.4355), LICA vs RVA (p=0.2364), LVA vs RVA (p=0.1658).

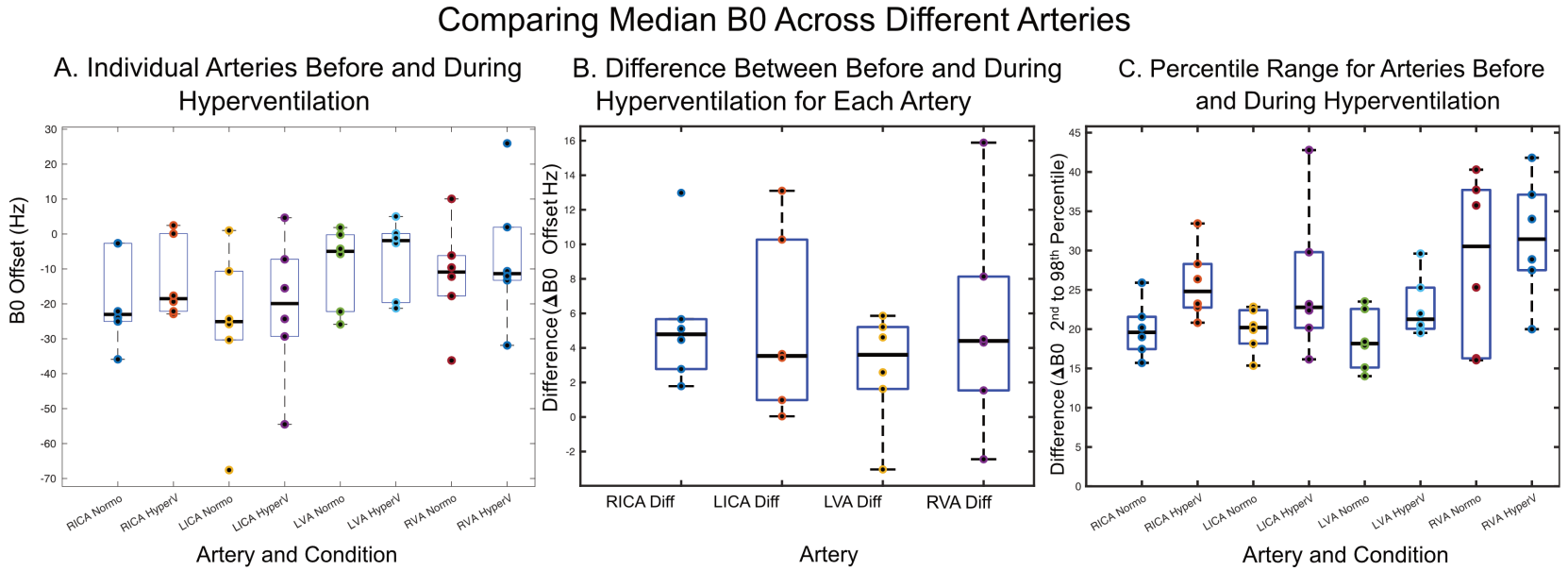


FIGURE 2.14: **Comparing Median B_0 Across Different Arteries.** A: Comparing B_0 across arteries. B: Single slice data for the difference in B_0 between normal breathing and hyperventilation. C: Single slice data of the range of measured B_0 values calculated as the difference between the 2nd to 98th percentile. Left/right (L/R) internal carotid arteries (ICA) and vertebral arteries (VA), Hz (hertz).

Part 2 Effect of Labelling Plane Placement on B_1

Figure 2.15A shows the B_1 data from part 2. This shows the percentage of the nominal flip angle from the B_1 map for the four arteries at the level of the V3 segment of the VAs, representing the labelling plane location used in the first part of this study. The group averages here were RICA (94.2±2.9%), LICA (98.2±3.4%), LVA (100.3±5.9%), RVA (94.5±7.7%) (median±IQR). The Kruskal-Wallis test showed there was no significant difference between any of the arteries at this position (p=0.0934).

Figure 2.15B shows the B_1 values in the same arteries, but located at 90 mm below the AC-PC line. The group median values were: RICA (78.5±10.4%), LICA (83.3±7.2%), LVA (94.2±15.9%), RVA (93.0±8.4%) (median±IQR). The Kruskal-Wallis test showed there was no significant difference between any of the arteries at this position (p=0.0419).

The Kruskal-Wallis test showed that there was a statistically significant main effect of position (V3 vs. 90 mm below AC-PC line) (V3 = 96.3±6.4%, 90 mm below = 85.8±14.7%, median±IQR, p=0.0010). Post-hoc tests using the Mann Whitney U test showed that there was a statistical difference between the two positions for the RICA (+12.9±-8.1%, p=0.0374), LICA (+14.5±-4.8%, p=0.0065), but not for the LVA (+3.7±-11.8%, p=0.4233), RVA (0.0±+0.0%, p=0.7488) (median±IQR).

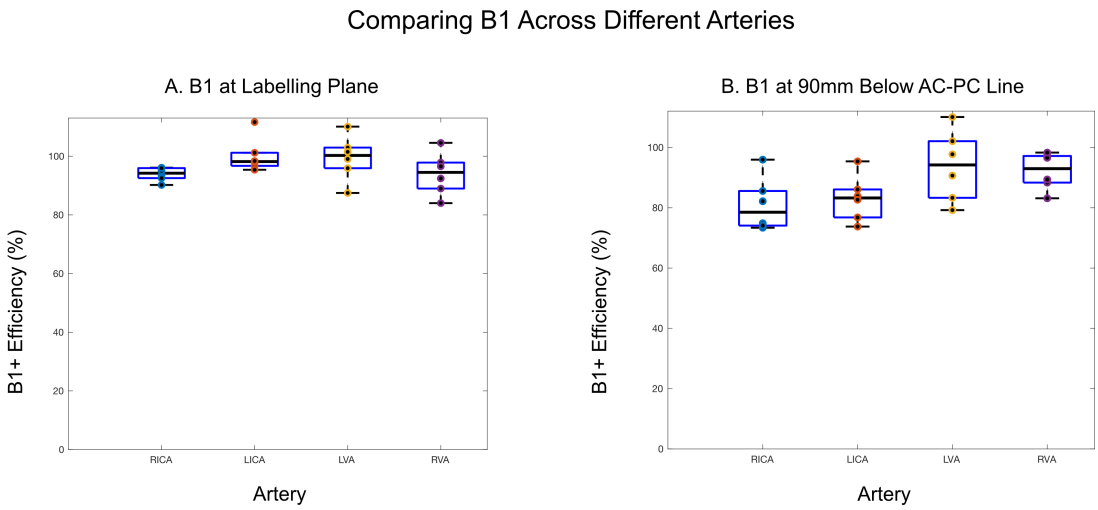


FIGURE 2.15: **Comparing B_1 Across Different Arteries.** Box plots of the B_1 values across the group (black line) for the feeding arteries of the brain at two labelling locations prior to the hyperventilation protocol. A: Measurements made at the V3 segment of the vertebral arteries. B: Measurements made at a location 90 mm below the AC-PC line. AC-PC (anterior commissure - posterior commissure), Left/right (L/R) internal carotid arteries (ICA) and vertebral arteries (VA), mm (millimetres,) % (percent), (median±IQR (inter-quartile range)).

2.8 Discussion

The prospect of robust quantification of CVR using pCASL is enticing, however previous studies have shown there are a number of sources of systematic error that may be detrimental to the quantification of CVR with pCASL [13, 42, 233, 260]. Investigations were performed to consider the physiological and physical parameters which could explain any systematic differences in CVR measurements across three sets of pCASL preparation parameters. Initial investigations in the first part of the study focussed on the change in blood velocity in the arteries at the labelling plane. This was followed up in the second part with a separate cohort of participants with measurements of B_0 (during normal breathing and hyperventilation) and B_1(considering two labelling locations). The hypercapnic challenge used in this study was sufficient to induce a CVR response, and the estimates of CVR varied depending on the pCASL preparation parameter set used. A systematic difference in quantified CVR was observed, with a statistically significant difference between two of the sets of pCASL parameters (Params-1 and Params-2). Investigations of the source of this difference found a $\sim$12% increase in blood velocity in the ICAs and VAs. Additionally, at the pCASL labelling plane (which in this case was at the level of the V3 segment of the VAs), there was a group median B_0 offset of 29 Hz, and a change in B_0 of $\sim$5 Hz due to the hyperventilation accompanying the hypercapnic challenge. There was also a group average B_1 percentage of nominal flip angle of 96.9%.

2.8.1 Respiratory Stimulus

Respiratory stimuli were consistent across runs and participants, and no significant difference was observed between repeats of the pCASL block hypercapnia

challenge. This consistency was particularly important in this study to dissociate the effects of stimulus administration and systematic differences between pCASL preparation parameters.

In contrast to similar studies which used Acetazolamide [256], a hypercapnia stimulus was administered to participants. Hypercapnia based studies differ from ACZ studies in that the former are based on the ratio of the CBF-weighted signal between hypercapnia and normocapnia, whereas for the latter absolute quantification pre- and post-ACZ is required.

When using $P_{ET}CO_2$ as a surrogate for CO_2 levels in the blood, there may be small differences between the absolute values measured and the 'true' values. However, Duffin and colleagues (2011) [68] have shown that breath by breath measurements of $P_{ET}CO_2$ using sequential gas delivery (i.e. the RespirAct^{TM}), as used in this study, are equivalent to the arterial CO_2 level. It also reduces the error in calculating the $P_{ET}CO_2$ and has been shown to be a reliable measure for observing induced CO_2 changes [119].

2.8.2 pCASL: Systematic Variations in CVR Measured with Different pCASL Parameters

The hypothesis that CVR measurements would vary depending on pCASL preparation parameters was supported. Measurements of perfusion and the subsequent estimates of CVR were found to vary systematically with different pCASL preparation parameters. Params-1 showed the highest values and Params-2 showed the lowest values of CVR. The difference between different pCASL preparation parameter sets conform with previous studies that used ACZ and similar parameters [233]. However, the previous ACZ study involved two separate scans, with a delay of 30 minutes for the drug to have an effect.

In contrast, for a hypercapnic challenge only one scan is required to measure CVR, which would reduce intra-individual confounds. Therefore, a single scan would be more viable in a clinical setting.

2.8.3 PCV: Investigations of Potential Sources of Systematic Error due to Blood Velocities

The hypothesis that blood velocities would change in the feeding arteries to the brain during hypercapnia was supported, with a large difference observed between the ICAs and VAs. Changes in blood velocity are often assumed to be negligible during hypercapnia, but were found to increase by 10-12% from normo- to hypercapnia conditions in this chapter. As arteries had different velocities, this supports the idea that the global mean average velocity across all arteries is not representative of the velocity in arteries feeding different territories of the brain. Therefore, calculations for the different vascular territories of the brain could be weighted according to measurements from the artery that feeds it [175]. Knowing there is an increase in velocity is important for evaluating the effects this will have on the labelling efficiency of the pCASL and subsequent CVR estimates. Alternatively, when planning a clinical scan, it would be important to consider if the global CVR value best suits the reasons for the scan.

Physiological differences in the blood vessels to the brain explain some of the differences between the measurements of CVR taken at different arteries. The ICAs ($\sim$7 mm) [201] are bigger in diameter than the VAs ($\sim$3 mm) [239], which would also explain why there was a notable difference between the ICA and VA velocity values. When measured with ultrasound, Vural & Çiçek (2019) [239] observed that the left VA diameters (3.50$\pm$0.55 mm) were generally

larger than the right (3.13±0.34 mm) (N=771, 290 M, 554 F, 52.2±12.6 years), which corresponded with a higher artery flow volume in the left (151.45±57.26 mL/min) compared to the right (119.21±44.98 mL/min) VA. Additionally, there was no difference between right- or left-handed participants. The velocity measurements in the left ICA and VA are likely to be higher than their right counterparts because the right common carotid artery bifurcates before reaching the brain [165]. This may also have resulted in less change in vasodilation between normo- and hypercapnia and therefore less overall change in velocity between conditions.

2.8.4 B_0: Investigations of Potential Sources of Systematic Error due to Hyperventilation

The hypothesis that the static magnetic field (B_0) would be affected by the hyperventilation associated with a hypercapnia stimulus was observed, but to a lesser extent than has been shown previously [42]. Although the absolute change in B_0 was relatively small ($\sim$5 Hz), a $\sim$10% increase in the range of B_0 values was observed. B_0 was measured because shimming, used to reduce B_0 field inhomogeneities, is not typically performed at the level of the labelling plane.

When looking at the B_0 there was no difference between arteries or conditions. This would suggest there is not too much of a problem with B_0 inhomogeneities when comparing normocapnia to hyperventilation and therefore, less of a problem with deep breathing caused by hypercapnia challenges. However, when looking the 2nd and 98th percentile of the B_0 offset there was a significant difference between the arteries but not the conditions (normocapnia vs. hyperventilation). More specifically there was a difference between the measurements at the RICA

vs the LICA, and the RICA vs. the RVA, which suggests that there would be differences in the B_0 measured across the different arteries.

Therefore, measuring any changes in B_0 could be critical to understanding any errors in pCASL CBF quantification. Even if they are quite small, if position of the labelling plane can be moved to remove a small amount of error it would still be beneficial to make the measurements more robust. Additionally, this would have a particular impact on hypercapnia CVR, where CVR is measured dynamically. Despite the measured change at the labelling plane, it was considered too small to influence labelling efficiency between normal breathing and hyperventilation.

2.8.5 B_1: Investigations of Potential Sources of Systematic Error due Placement of the Labelling Plane

The hypothesis that the effect of suboptimal radiofrequency (B_1) would be detrimental to pCASL measurements was subtle. In contrast to previous work, only a small, non-significant reduction in B_1 was observed of ∼97% compared with ∼83% at 90 mm below the AC-PC line seen previously [42]. The B_1 at the V3 vs. B_1 90 mm below the AC-PC line were significantly different, which was most pronounced in the RICA and LICA values. LVA and RVA showed no significant differences between conditions, but had higher standard deviations, so noise may have been a factor. LICA showed the largest condition effect (∼15%). Therefore, this suggests there is a difference in the B_1 when measured at across different arteries. Overall, vessel differences were less pronounced at the V3 segment than at 90 mm below the AC-PC line.

Therefore, placing the labelling plane at V3 appears to be more optimal than at 90 mm below AC-PC. Bush et al., 2018 [42] measured at 90 mm below the AC-PC line so this would be better compared with our measurement at this

level i.e. 83% vs. 88% (the rounded average of the measurements from the 4 arteries at 90 mm) which are much more comparable. Using a balanced pCASL sequence may also have had an impact as the reduction in B_1 is likely to have an effect on the labelling efficiency. Likewise this may not have been an issue for Bush and colleagues (2018)[42] because they used an unbalanced pCASL.

2.8.6 Limitations

Most obviously, the small study sample size of both parts of the study was a large limitation because it reduced the power of the study. One extensive systematic review of the literature that aimed to determine the most common and most useful measures of CVR with MRI found that the majority (45 studies) had less than 10 subjects, compared to nine which had N>100 [214].

This study used a single PLD, whereas comparisons to Positron Emission Tomography (PET) show that multiple PLD methods provide more reliable and robust measurements of CVR, as it is considered to have a higher signal to noise ratio [256]. This study also demonstrated a significant change in arterial transit time, which cannot be accounted for in a single PLD acquisition. However, the systematic difference in pCASL parameters shown in these results suggests that labelling efficiency is a fundamental component of CVR measurements and should therefore still be carefully considered.

The spatial resolution of the PCV acquisition was limited in order to obtain a practical scan duration and enough cardiac phases to sample the peaks of the cardiac cycle. In this study the maximum velocity from each artery ROI was extracted under the assumption of laminar flow, to minimise the error from including stationary parts of the vessel wall. However, it is possible that this method still underestimated the maximum velocity since the native in-plane

resolution of the data was 1.14x1.14 mm and the average arteries looked at here have diameters of ∼3-7 mm. Hence the voxel with maximum velocity may be an average over a relatively large fraction of the diameter of these vessels, particularly the VAs.

Additionally, the relatively low temporal resolution of the single slice B_0 mapping may underestimate rapid changes in B_0 during hyperventilation, so it may not have been possible to characterise the full effect. Furthermore, a shim box was not placed over the nominal imaging volume for a pCASL acquisition, as was the case for the multislice B_0 map. This might have affected the magnitude of any changes in B_0 during hyperventilation.

The practical aspects of the hypercapnia challenge add additional requirements to the scan (e.g. extra set-up time, equipment and cost), which would still be suboptimal for clinical scans. Some recent studies have used resting state BOLD imaging (no task or extra equipment) [98]. However, approaches such as this are challenging to perform using ASL data due to the much lower SNR compared with BOLD. Furthermore, it is currently unclear whether a stress test, such as a hypercapnia challenge or ACZ, is required to provoke response in an a brain that appears health at rest, but shows pathology when 'stressed'. There is a collective aim to remove this limitation in future [206].

2.8.7 Conclusion

In conclusion, hypercapnia challenges were performed to determine if CVR varies systematically with different pCASL parameter variants due to changes in feeding artery blood velocity. The results showed that the CVR measurements varied depending on the artery, the CO_2 condition and the pCASL preparation parameters used. These differences in CVR would have a fundamental impact

on physiological/clinical interpretation. Therefore, this study adds to the consensus that selecting pCASL preparation parameters to optimise labelling efficiency is an important consideration for robust CVR measurements. However, further work is still required to better understand the origin of these systematic differences in pCASL based CVR. The investigation into measuring B_0 (during normal breathing and hyperventilation) and B_1 (at two labelling locations) also showed variation in results depending on condition and labelling placement. The effect was smaller than expected but could still contribute to some differences in pCASL CVR measurements. Therefore, it is also important to take these factors into consideration when planning a pCASL experiment.

3 Investigating the Effect of Pharmacological Interventions on Blood Pressure and Velocity during a Hypercapnic Challenge



3.1 Contributions to the Chapter

Colette Milbourn was involved in all stages of the study; the study design, ethics approval, set-up, participant recruitment, participant screening and data collection (except for the invasive blood sampling and insertion of the cannula), writing the scripts for data analysis and presentation, manuscript writing/editing

Dr Nicholas Blockley provided support as the main supervisor and setup of the study and data analysis, and revisions to the manuscript.

Prof Paul Greenhaff provided support as the second supervisor for setting up the study for the physiology background, data analysis, interpretation and manuscript revisions.

Aline Nixon provided support during the study design, setup and medical cover for the study days.

Dr Joseph Cullen, Dr Ayushman Gupta and Dr Abhishek Sheth provided medical support/cover for the screenings and study days.

Sarah Brown provided support as manager of the David Greenfield Human Physiology Unit.

Dr Liz Simpson provided support for the lower body negative pressure (LBNP), which was eventually not used in the final experiment, and also helped with the ethics approval design.

Dr Natalie Shur provided support for the ethics approval design and additional medical cover.

Intermediate life support cover was provided by Mia Keaton, Dr Joanne Mallinson, Melanie Marshall and Sara Brown.

Dr Richard Simpson helped with introduction to ultrasound and visit day to the vascular clinic at the Queen's Medical Centre, Nottingham.

3.2 Visual Abstract

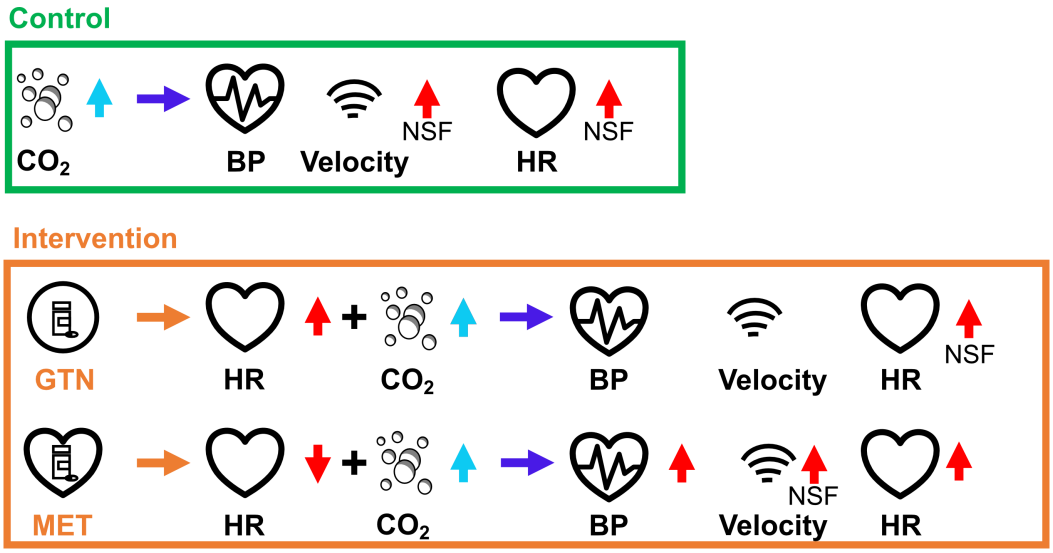


FIGURE 3.1: **Visual Abstract** A hypercapnic challenge was performed before and after a pharmacological intervention was administered. The physiological measures of blood pressure, heart rate and velocity were taken using a Dinamap, a Finapres and an ultrasound scanner. During control condition, after CO_2 there was no significant change in BP, velocity or HR. After GTN, there was an increase in HR, but no difference during the hypercapnic challenge. After MET, there was a decrease in HR, and after CO_2 there was an increase in BP and HR. BP (blood pressure), CO_2 (carbon dioxide/hypercapnic challenge), GTN (glyceryl trinitrate), MAP (mean arterial pressure), MET (metoprolol), mmHg (millilitres of mercury). Red Arrows indicates a change, NSF (not significant after multiple comparison correction).

3.3 Introduction

3.3.1 Blood Pressure as a Measure of Blood Flow

Blood pressure (BP) is the pressure required to move blood through the circulatory system. It is useful for diagnostic purposes since it is closely related to the force and rate of contraction of the heart, and the diameter and elasticity of the arterial walls in the circulatory system. Systolic blood pressure (SYS) is measured when the heart contracts, to force blood through the arteries, and diastolic blood pressure (DIA) is the measure of pressure when the heart relaxes, to rest and refill with blood. These mechanisms regulate how blood flows throughout the body to match organ metabolic requirements, although the pressure measured throughout the descending arterial branches may vary. Arterial cannulation is the most direct method to measure BP, but is also considered to be invasive, as this method involves insertion of the sensor directly into the artery. Therefore, it is recommended for critical care use, but not for less extreme circumstances [145]. In contrast, sphygmomanometery (involving a BP cuff on the arm) provides a non-invasive, quick, and cheap measure of BP, and is used in standard clinical practice. However, due to the method of constricting the brachial artery to take this recording, it is not possible to acquire continuous measurements. Additionally, due to the mercury in traditional manual sphygmomanometers, these have generally been replaced with aneroid (without liquid) or digital monitors (also known as oscillometers) in clinical settings ([173]).

3.3.2 Finger Cuff Methods of Measuring BP

Finger cuff measures of BP (i.e. the Finapres, FINger Arterial PRESsure) provide a continuous estimate of BP as a reliable and non-invasive alternative to traditional

arm cuff measures of BP. The Finapres device uses a finger cuff to measure BP using an algorithm based on Peňáz and colleagues (1973)[182] (the original volume clamp theory for measurement of BP at the finger. However, the algorithm is protected by intellectual property rights and is therefore not transparent [182]. Silke and Audley (1998) [210] claimed that the Finapres is accurate for BP measurements as a non-invasive measure, if used with a calibration to deal with 'offset' i.e. using the return to flow calibration method introduced in 2002 [210, 203]. This method involves in/deflating the arm cuff to measure the brachial BP and therefore calibrate the peripheral BP measured at the finger cuff. The development and validation of the device was provided by [245, 118, 131]. These devices work best within set assumptions, i.e. that the person is lying down and still, to remove the possibility of movement artifacts that have been seen during use of the device during exercise [203].

3.3.3 Problem: Understanding How Changes in BP Affect Cerebrovascular Reactivity

3.3.4 Interventions to Model Changes in Blood Pressure

There are many pharmacological interventions that are routinely used to alter BP, either by lowering abnormally high BP (anti-hypertensive), or by increasing abnormally low BP (anti-hypotensive). Two anti-hypertensive pharmacological interventions were considered in this study. These vasoactive compounds are used clinically to modulate BP systemically (glyceryl trinitrate) and centrally (metoprolol).

3.3.5 Glyceryl Trinitrate – GTN

Glyceryl trinitrate (GTN), (often referred to as nitroglycerin due to its origins as an explosive) causes both arterial and venous vasodilation (independent of endothelial nitric oxide synthase), and is known to alter blood flow. The effects of sublingual GTN are rapid, transient and cause vasodilation throughout the circulatory system. In smooth muscle cells (i.e. throughout the body), GTN is converted by an enzyme called mitochondrial aldehyde dehydrogenase (ALDH2) into nitric oxide (NO), which subsequently acts as a vasodilator. In turn, this activates guanylate cyclase, which converts guanosine triphosphate (GTP) into cyclic guanosine 3′, 5′-monophosphate (cGMP) [117, 56, 128]. cGMP is also a vasodilator that activates protein kinase-dependent phosphorylation resulting in a downstream cascade and subsequent relaxation and increases blood flow in veins, arteries and heart tissue.

GTN has a half-life of 1-4 minutes. As a global vasodilator, GTN has been used to treat angina (chest pains associated with heart problems), hypertension after cardiac surgery and anal fissure (BNF.nice.org.uk, 2024 [166]).

3.3.6 Metoprolol - MET

Metoprolol is as a cardiac specific, beta-1 adrenergic receptor inhibitor. Metoprolol doses of less than 100 mg (milligrams) are considered to have a negligible effect on beta-2 receptors. MET has negative chronotropic and inotropic effects (decreases heart rate by altering electrical impulses via ion exchange). MET does this without altering membrane stabilisation or intrinsic sympathomimetics [159]. Overall, MET decreases cardiac output with a standard half-life of 3 to 4 hours for standard (i.e. not slow release) formulations.

MET is clinically used to treat hypertension, angina, arrhythmias, migraine, hyperthyroidism and early intervention of infarction (BNF.nice.org.uk, 2024 [167]).

3.3.7 Aims of the Study

The main aim of this study was to investigate cardiovascular physiological responses to a hypercapnic challenge (HC) in young, healthy volunteers, both before and after administration of a centrally (MET) or peripherally (GTN) acting pharmacological intervention, to lower mean BP. In the longer term, these temporary changes in BP in healthy participants might also allow a comparison to patients with cerebrovascular diseases, where BP is often altered.

This study aimed to investigate two primary outcome measures; changes in measures of mean arterial BP (MAP) and changes in carotid artery blood velocity (Vmax). Heart rate (HR) was used as a secondary end-point measure of adaptive changes in response to changes in blood flow.

The Primary outcome was to observe the change in systemic BP (measured with non-invasive BP cuffs) and the change in carotid artery blood velocity during a HC task (measured with duplex Doppler ultrasound) i.e. changes observed between hypercapnia and normocapnia. The secondary outcome was to observe the change in BP and carotid artery blood velocity response to hypercapnia after administration of hypotensive interventions (compared to the response prior to these interventions). The other outcome measurements included a non-invasive measure of HR via pulse oximeter.

3.3.8 Hypotheses

The first hypothesis was to see if the pharmacological interventions actually resulted in a lowered BP, and would be determined with the physiological measures mentioned above during the normocapnia condition. The second hypothesis was that the pharmacological interventions would affect the physiological measures mentioned above during the HC i.e. that the response would be different during the pharmacological intervention. Additionally, it was hypothesised that the GTN/MET would reduce BP in a controlled and repeatable manner.

3.4 Methods

3.5 Participants

Local ethics committee approval was provided for this study (Faculty of Medicine and Health Sciences, University of Nottingham, ethics code 212-0321). Participants were sent the patient information sheet (PIS) via email and the in/exclusion criteria were checked (shown on the last page of Fig. C.1). Participants were invited for a medical screening session of up to 60 minutes at the David Greenfield Human Physiology Unit (DGHPU). Prior to screening, participants were given the opportunity to ask questions about the study and if they wished to join the study informed, written consent was acquired. As part of screening, participants were asked to fill in a basic health questionnaire (previous/current medical problems, age, etc.) including some lifestyle questions (smoking/drinking/change in fitness) (Fig. C.1). Participants had their height and weight measured, body mass index (BMI) was calculated, followed by BP measurements first lying and then standing (1 min & 3 mins) (Dash 3000 and Dinamap 8100 BP machine, GE Healthcare, Chicago, USA). HR and blood oxygen saturation (via a pulse oximeter) were also measured. HR and rhythms were checked with a 12-lead electrocardiogram (ECG) (AT-10 plus, Baar, Switzerland). Venous blood samples were taken (from the antecubital vein) to confirm that urea and electrolyte concentrations, liver function and blood counts were within healthy clinical ranges.

Although both male and female participants were invited to volunteer, only 10 females (N=10) completed both study days (see Table 3.2) in the Results section for participant physical characteristics)and the appendix for excluded participants Table C.1).

Outline of study days:

Study day 1 and 2

1. Review paperwork
2. Rest for 30 minutes
3. Cannulation
4. Baseline observations
5. Pre-intervention observations with HC
6. Medication (wait for peak)
7. Post-intervention observations with HC
8. Recovery and food

3.6 Data Collection

3.6.1 Study Day Design

A brief overview of the study day is shown in Figure 3.2. On the day of the study, it was confirmed that participants had fasted since midnight, had not consumed caffeine or alcohol, and had not exercised excessively in the last 24 hours. This was to ensure that these potential factors did not influence the baseline state physiological measurements. Participants were fed at the end of the study day. The study day events are detailed in Table 3.1.

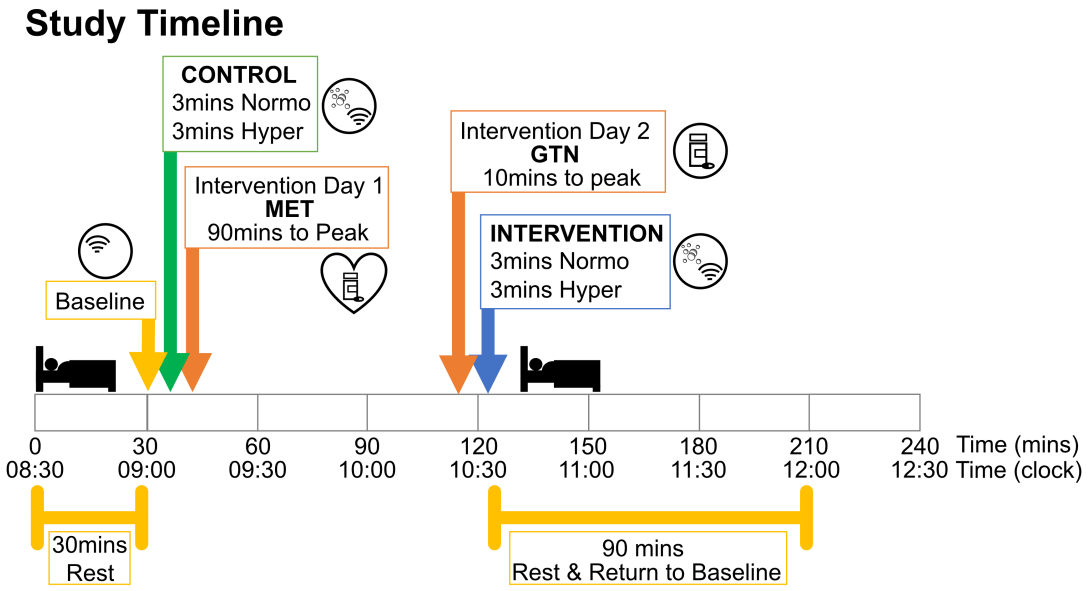


FIGURE 3.2: **Study Timeline.** Time points at which measurements were taken. GTN (glyceryl trinitrate), Hyper (hypercapnia), mins (minutes) MET (metoprolol), Normo (normocapnia).

The following figure 3.3 shows the experimental set up for the study day.

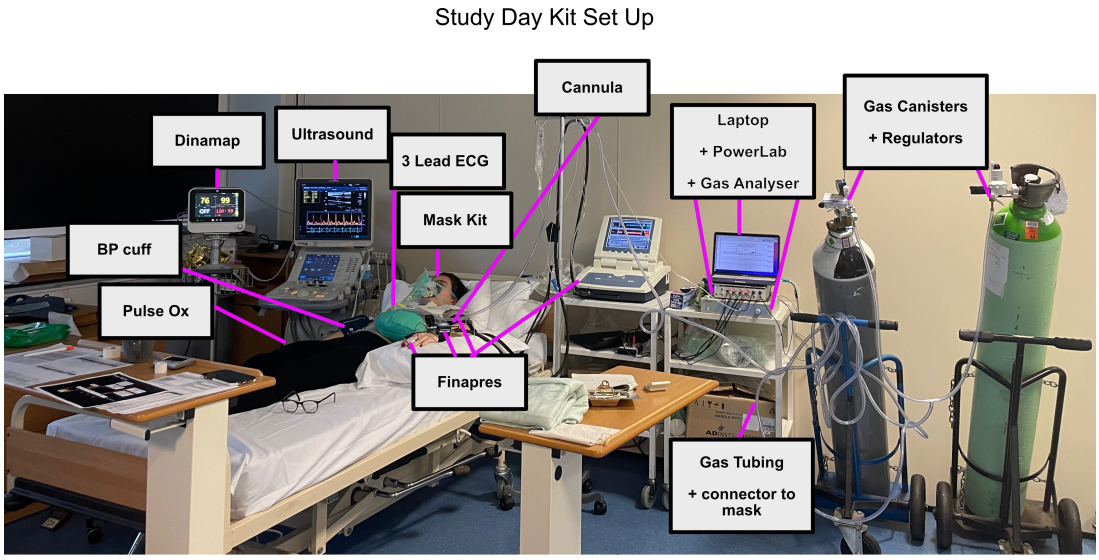


FIGURE 3.3: **Study Day Kit set up.** Set up of the kit used in this study including the Dinamap, Ultrasound, Mask kit, Finapres and gas delivery. BP (blood pressure), Finapres (FINger Arterial PRESsure).

3.6.2 Dinamap Physiological Measurements

Dinamap^{TM} vital signs monitor 8100 blood pressure machine (GE Healthcare, Chicago, USA) arm cuff (adult size 23-33 cm) was placed on the right upper arm of the participant across the brachial artery, and the pulse oximeter clip was placed on a finger on their right hand. The Dinamap was used to record measurements of the SYS, DIA and MAP BP. The Dinamap ProCare device is accredited internationally for clinical use [63]; BHSOC, (accessed 2023)[24]) (Fig. 3.4). After 30 minutes of rest, a baseline check of physiological measurements was performed to ensure SYS was above 100 mmHg and HR was above 50 BPM before continuing with the rest of the study day. These thresholds were chosen based on a previous DGHPU ethics approval (GTN and ultrasound measurements at the brachial artery [212]). A cannula was placed in the antecubital vein with a slow drip of saline (0.9 percent sodium chloride), as a precaution in case of a drop in SYS below 100 mmHg following drug administration. BP, HR and blood oxygen saturation levels were monitored throughout the study day. Five participants were withdrawn due to a low BP and/or HR, and one due to failure to cannulate. One participant had the second study day re-scheduled due to failure to cannulate on the second study day.

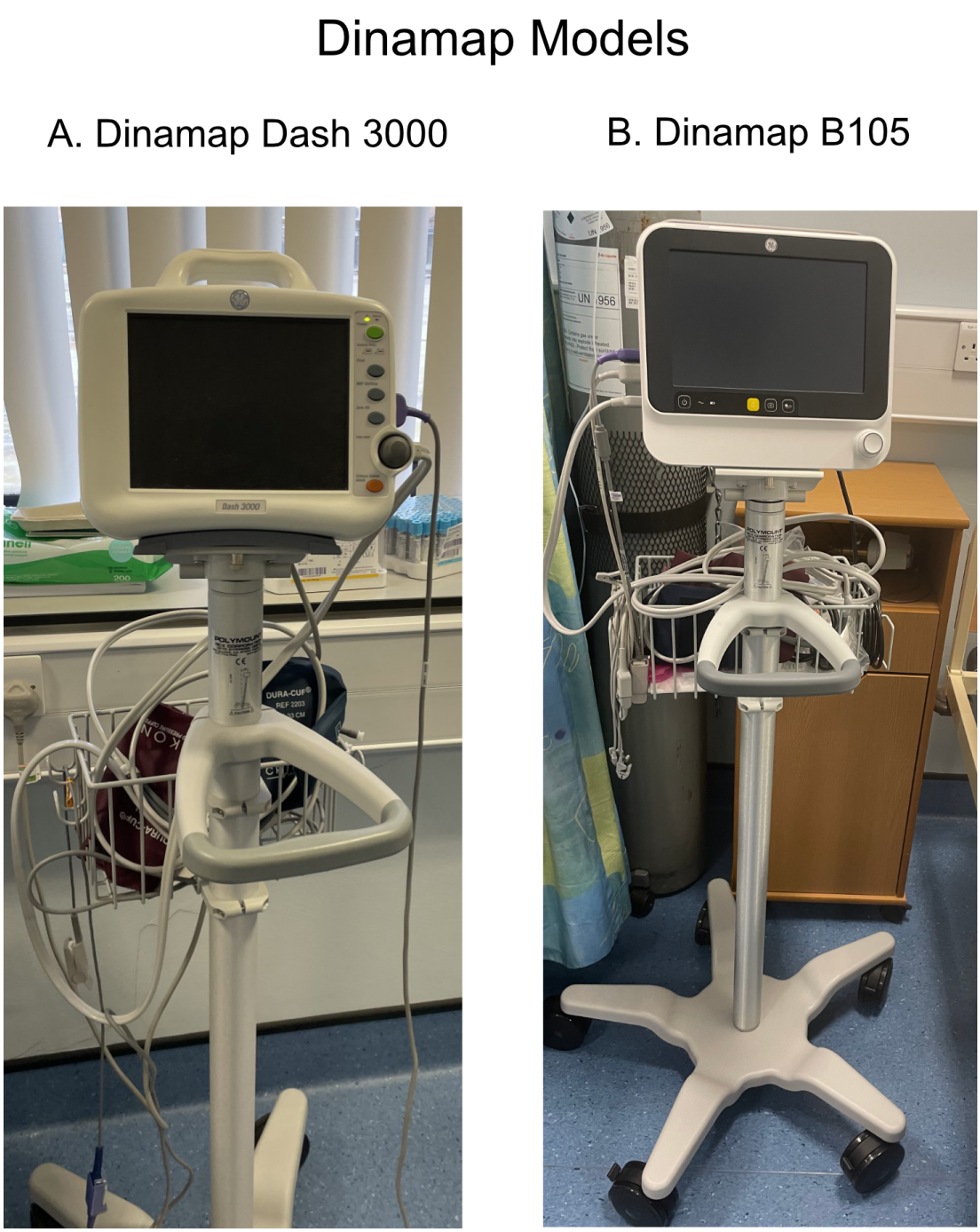


FIGURE 3.4: **Dinamap Models.** Photos of the Dinamap models: A. Dash 3000 used in screening until replacement in 2023. B. used for data collection. Both are automatic, non-invasive blood pressure monitors. GE (GE Healthcare, Chicago, USA).

3.6.3 Ultrasound

Ultrasound was used to measure blood velocity in the common carotid artery (CA) to determine if there were changes in blood velocity towards the brain following drug administration. A Toshiba Aplio 300 (now a subsidiary of Cannon Medical, Ōtawara, Tochigi, Japan) ultrasound and 11L (Linear array) probe were used with a custom Carotid 11L4 pre-set (see Fig. 3.5). A 3-lead ECG was used to synchronise the ultrasound measurements with the cardiac cycle. The gate size was set at 5 for both normocapnia and hypercapnia conditions. Transmission gel (Skintact, now Fannin, Leopardstown, IE) was applied to the scanning probe. A longitudinal scan with clearly defined intima edges was acquired (the probe 'T' was placed perpendicular to the artery). Once a clear image was obtained, the pulse wave function was selected and the Doppler window positioned so it was aligned within the vessel. The beam was aligned with the artery to see the walls of the vessel on both sides and the carotid sinus bulb on the far left of the screen. Probe placement was then marked on the participants neck with a marker for consistency across conditions. The Doppler angle was set at <60° to maximise accuracy, and this was achieved by setting the marker at an angle <60°, and manoeuvring the probe so that the artery was at the same angle as shown by the marker. Recordings of more than four complete cardiac cycles were made and then averaged across the cardiac cycle. Three repeats of these measurements were taken at each of the key time points (see Fig. 3.6). Velocity maximum data were recorded as, according to the laminar flow model, the highest flow rate is present in the centre of the artery. In contrast, a mean average would be adversely affected by the turbulent noise around the artery edges and the gate placement.



FIGURE 3.5: **Ultrasound Device.** Photo of the Toshiba Aplio 300 used for ultrasound measurements in this study.

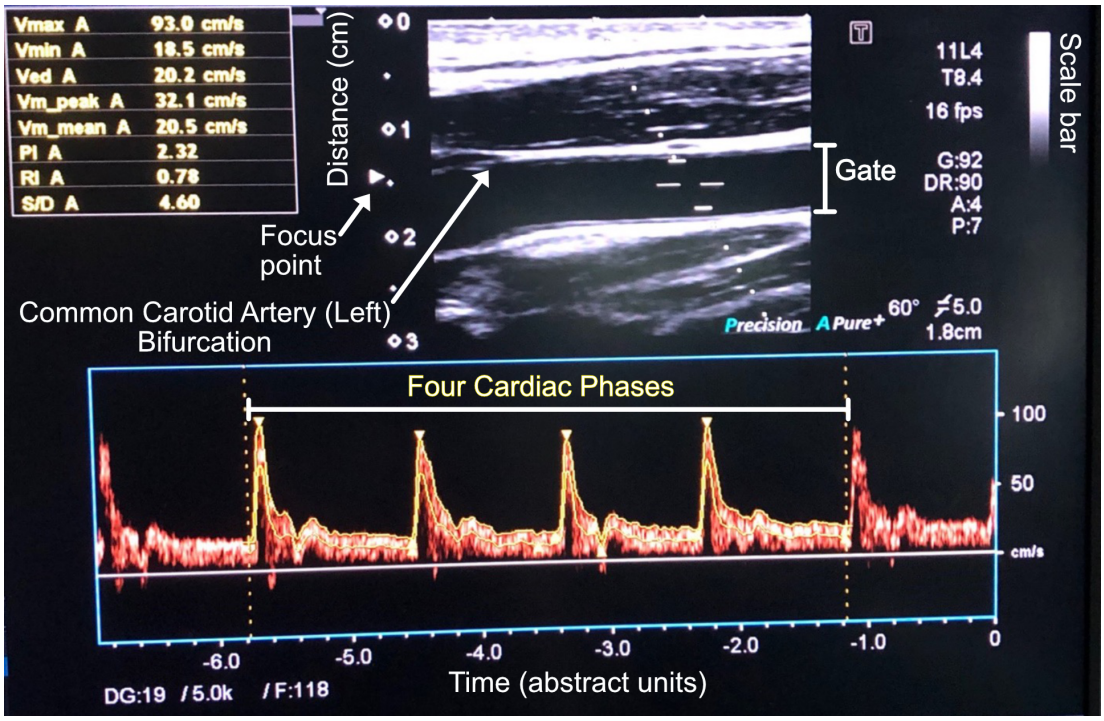


FIGURE 3.6: **Ultrasound example trace.** Annotated photo of the ultrasound screen showing four cardiac cycles to give the average velocity measurements.

3.6.4 Finapres

The Finapres (1998 version of the TNO Finometer PRO) was set up using the Research option and then the participant information (i.e. sex, age, weight) was entered. Figure 3.7A shows how the finger cuff was fitted for size and figure 3.7B shows the positioning on the participant's left middle finger. The wrist box was firmly attached on the left wrist. The arm cuff was placed on the upper part of the left arm, and 3.7D shows how the calibration cuff was placed at the same height as the heart. Figure 3.8 shows how the Finapres was connected to the laptop via the connector box. Recordings were calibrated by waiting for the 'physiological measurements' on the screen to indicate 'great' or 'excellent' and then the 'RTF' ramp calibration setting was used for calibration. RTF stands for 'return to flow' calibration. The arm cuff was used to calibrate the finger cuff, so that continuous recordings of SYS, DIA, HR and cardiac output (CO) could be calculated.

Figure 3.7 shows the Finapres cuff equipment used for the data collection for the study.

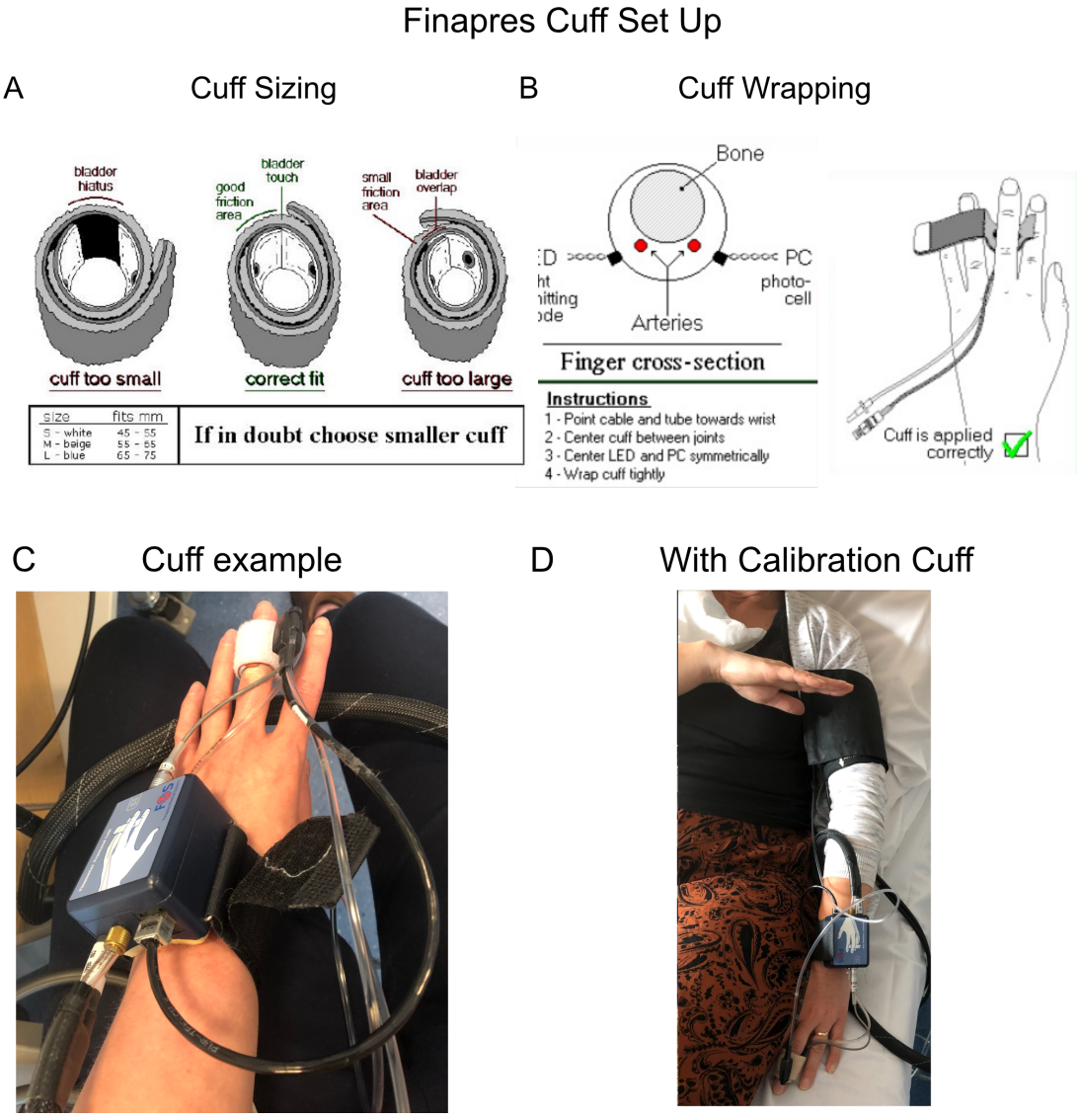


FIGURE 3.7: **Finapres Cuff.** Figures of Finapres cuff from the manual FMS, Finapres Medical Systems BV Version 1.10, dd: 2002.05.06. Images A (cuff sizing) and B (cuff wrapping) were edited and compiled together with C a photo of an example cuff position and D a photo of the calibration cuff at the same height as the heart.

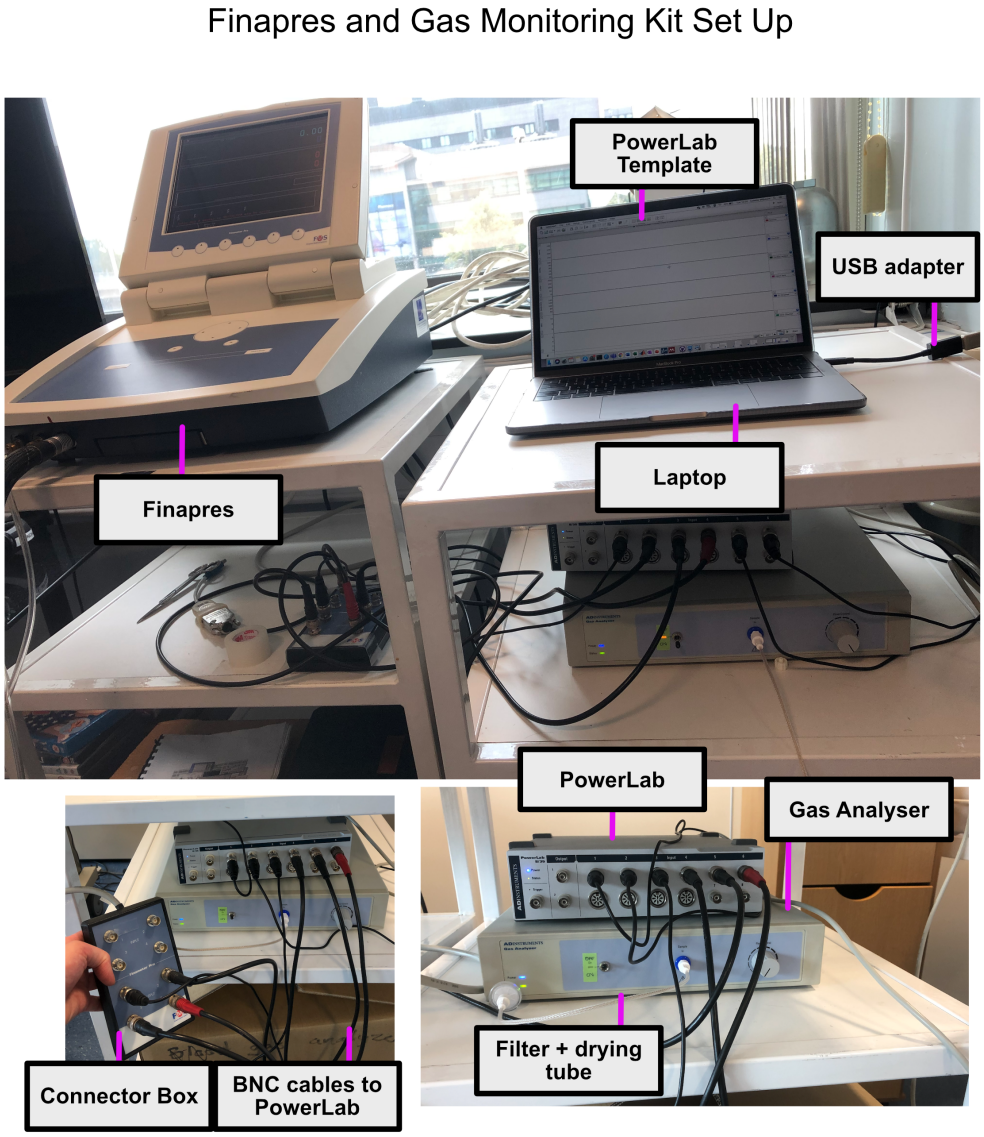


FIGURE 3.8: **Finapres and Gas Monitoring Kit Set.** Finapres on the left was used to monitor continuous blood pressure along with an ADInstruments® Gas Analyser (Product Code ML206) and Powerlab (26 Series with a 6 channel input).

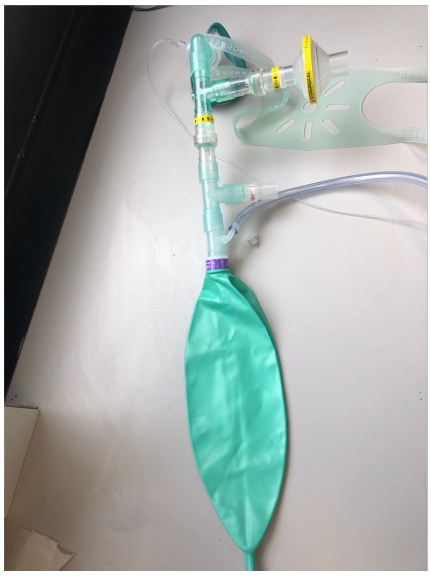
3.6.5 Gases and Gas Analyser

3.6.6 Gas Cylinders Setup

Figure 3.3 shows how the gases were set up for the HCs and for recording the participants' expired oxygen (O_2) and carbon dioxide (CO_2). Both gases were attached via gas regulators and medical flow meters. Tubing to the flow meters was then joined at a Y-piece. Next the breathing circuit was attached using a further length of tubing. Gas cylinders contained a medical air mix (21% O_2, 79% nitrogen (N_2)), and a custom hypercapnic gas mix (5% CO_2, 21% O_2, 74% N_2).

3.6.7 Breathing Circuit

The breathing circuit was assembled from single use, disposable plastic components (Intersurgical and Cole-Palmer), based on Suri and colleagues (2021)[221], with a line in from the gas canisters, and a line out to the Gas Analyser for gas analysis (Fig. 3.9).



REF 7294001: ClearLite, anaesthetic face mask, size 4, adult, green seal
Bradel on right - REF892.00 Vygon: Gas Analyser F-2-F LL clear
REF 7089000: Plastic Hook Ring
REF 2715000: Masterflex Fitting, Nylon, Straight, Female Luer to Smooth Bore Hose Barb Adapter, 3/32" ID; 25/PK filter to the hole.
REF 2734000: Gas Monitoring Line, 1.2MM ID, M/M Luer Lock, 3M
REF 1992000: Fixed elbow
REF 1981000: T-piece 22M-22F-22M
REF 1921000: One-way directional valve 22M (flow in) - 22M (flow out)
REF 1690000: Flo-Guard breathing filter
REF 1921000: One-way directional valve 22M (flow in) - 22M (flow out)
REF 1983000: T-piece 22M/15F-22F-22F
REF 1950000: 22M-22V (flow in) - 22M
REF 1963000: straight connector 22M - 6mm OD stem and cap - 22F
REF 2830000: Reservoir bag, 3L with anti occlusion cage mount, 22F neck
REF 2224000: Harness for CPAP mask adult, medium/large

FIGURE 3.9: **Breathing circuit set up.** Oxygen tubing from the medical flow meters was attached to the following breathing circuit and the expired gas was measured through a line out. Note size 4 (green) is shown in the photo, but both size 3 (yellow) and 4 were available for participants. F (female connecting), M (male connecting), L (litre), REF (reference number from manufacturer).

A PowerLab 26 Series with 6 input channels (AD Instruments, Dunedin, New Zealand) was connected to a 2016 MacBook Pro (Apple, Cupertino, USA) running LabChart V8.1.24. A Gas Analyser (ML206, AD Instruments, Dunedin, NZ) and the Finapres were connected to the 6 channels of the PowerLab. A custom LabChart® template was used to continuously record SYS (mmHg), DIA (mmHg), HR (BPM), CO (l/min), fraction of expired O_2 (%) and fraction of expired CO_2 (%). This was also used to continuously record the expired gases during the HCs (see Fig. 3.8).

3.6.8 Hypercapnic Challenge Paradigm

During the hypercapnic challenge the medical flow meters were set to 15 L/min and switched manually between the two gases. The HC involved breathing medical air for 3 minutes followed by the hypercapnic gas for 3 minutes. Finapres and Gas Analyser measurements were continuously recorded during the HC, whilst Doppler ultrasound measurements were recorded during the steady state i.e. after 3 mins of breathing the normocapnic mixture and 3 mins after switching to the hypercapnic mixture.

The first HC was performed straight after the baseline observations were taken, and a second HC was performed at the expected peak time for the pharmaceutical interventions.

3.6.9 Interventions

Interventions given on the study days were GTN and MET. GTN was given as a single 400 μg (micrograms) sublingual tablet with an estimated time to peak GTN plasma concentration of 10 minutes (average 5-10 mins). MET was given as a single 50 mg tablet with an estimated time to peak MET plasma

concentration of 90 minutes. In order for the second set of physiological measurements to be acquired at the same time on both days, MET was given straight after the first hypercapnia challenge and the GTN was given 1 hr 20 minutes after the first hypercapnia challenge on their given study day visits (to peak $\sim$ 11:00). Tablets were used to ensure the dose given was the same for all participants without the need for invasive intravenous (invasive) administration.

3.7 Baseline Measurements

Once participants had been rested supine on the bed for 30 minutes, a set of baseline measurements were taken. This was to ensure that they had a stable baseline after travelling to the unit. The saline intravenous (IV) cannula was normally inserted within the first 30 minutes of resting before the baseline, but on the first session for one participant it was placed after the first set of baseline observations. Table 3.1 shows the timeline in more detail. Measurements were taken at each time point in the following order; the time point was marked in LabChart® with a comment, current values from the Finapres were written down on the case report form (CRF) as a paper backup. Then a Dinamap measurement was acquired and added to the CRF, three ultrasound recordings of the vessel diameter were made followed by three velocity measurements and all recorded on the CRF.

3.8 Data Analysis

Data analysis was performed to determine the outcomes of any changes in BP, velocity, or HR for both control and intervention conditions. This was to determine if there was an influence on the HC after the interventions had been given.

TABLE 3.1: **Study Timeline Table.** Overview of the study day conditions in choronological order. CO_2 (carbon dioxide), GTN (glyceryl trinitrate), MAP (mean arterial pressure), MET (metoprolol), mmHg (millimetres of mercury).

Condition	Details
Baseline	Measurements taken 30 minutes after lying down resting breathing room air.
Control Normocapnia	After baseline. Measurements taken after breathing medical air for 3 minutes.
Control Hypercapnia	Air mix switched straight from normocapnia to hypercapnia mix, and then measurements taken after breathing 5% CO_2 mix for 3 minutes.
Intervention Given	GTN: Given 1 hr 20 mins after completing HC, 10 minutes to peak time. MET: Given after completing the HC, 1 hr 30 mins to peak time.
Intervention Normocapnia	At peak intervention time. Measurements taken after breathing medical air for 3 minutes.
Intervention Hypercapnia	At peak intervention time. Air mix switched straight from normocapnia to hypercapnia mix, and then measurements taken after breathing 5% CO_2 mix for 3 minutes.

3.8.1 Dinamap and Ultrasound Analysis

Dinamap measurements were taken throughout the experiment to ensure BP and HR did not exceed the discontinuation criteria (SYS below 100 mmHg, HR below 50 BPM) and for each of the different conditions. Three repeats of each time point for the ultrasound measurements were recorded on the CRF for each individual. The mean for each time point was calculated in an Excel (Microsoft, Redmond, USA) spreadsheet and the result was then added to one spreadsheet to collate data from all participants. A comma-separated values

(csv) format file was exported from Excel and then imported into MATLAB (The Mathworks, Natick, USA), where in-house scripts were used to plot the median and interquartile range (IQR) for the whole group analysis. These data were then used to calculate the differences between pre- and post- intervention conditions.

3.8.2 Finapres Data Analysis

Although the Finapres data was not used in the final results, they are shown in the appendix for comparison to the Dinamap. The methods for how the data was collected is here for completeness as the LabChart® data for the Finapres outputs were collected simultaneously with the PETCO_2 and O_2 (end-tidal partial pressure of CO_2 and O_2) data. LabChart® data files were exported as text files and anonymised further e.g. from participant number Low15 to subject number (completed datasets only) sub01. Figure 3.10A shows the steps of how in-house MATLAB scripts were then used to pre-process and analyse the Finapres data to create the figures seen in the results section. Data windows were taken once steady state had been reached, creating a 2 minutes long window for each of the 3 minute sections of the HCs, these windows were calculated using the noted time points of each gas condition from the exported LabChart® data files and then manually checked in order to ensure the trace had stabilised. MAP was calculated as:

$$MeanArterialPressure = \frac{Systolic + (2 * Diastolic)}{3} \tag{3.1}$$

The median and IQR of the groups were also calculated to compare the group response to the interventions and HCs (Fig. 3.10C and D).

3.8.3 End-tidal Data Analysis

Figure 3.10B shows how the average end-tidalCO_2 ($PETCO_2$) was calculated using a custom built MATLAB script. The MATLAB function 'FindPeaks' was used to find the peak of the expired CO_2 trace, to extract the breath by breath end-tidal value of CO_2. Each window was manually checked to ensure the thresholds for minimum peak height, minimum peak prominence, and minimum peak distance were appropriate. The recordings of the CO_2 trace from the gas analyser were measured as a fraction of the participant's expired gases ($FeCO_2$). Therefore, the PET CO_2 was calculated to account for atmospheric pressure (pATM=760 mmHg) minus lung partial pressure of water vapour (pH_2O=47 mmHg) at body temperature i.e. $FeCO_2 \times$ 713. The mean $PETCO_2$ was calculated over the same time window as the Finapres data for each subject, intervention (GTN and MET), and hypercapnia challenge gas condition (normocapnia and hypercapnia). For the BP, HR, and $PETCO_2$ the group median and IQR were also calculated to compare the group response to the HC. These data were used to create box plots shown in the Results Section.

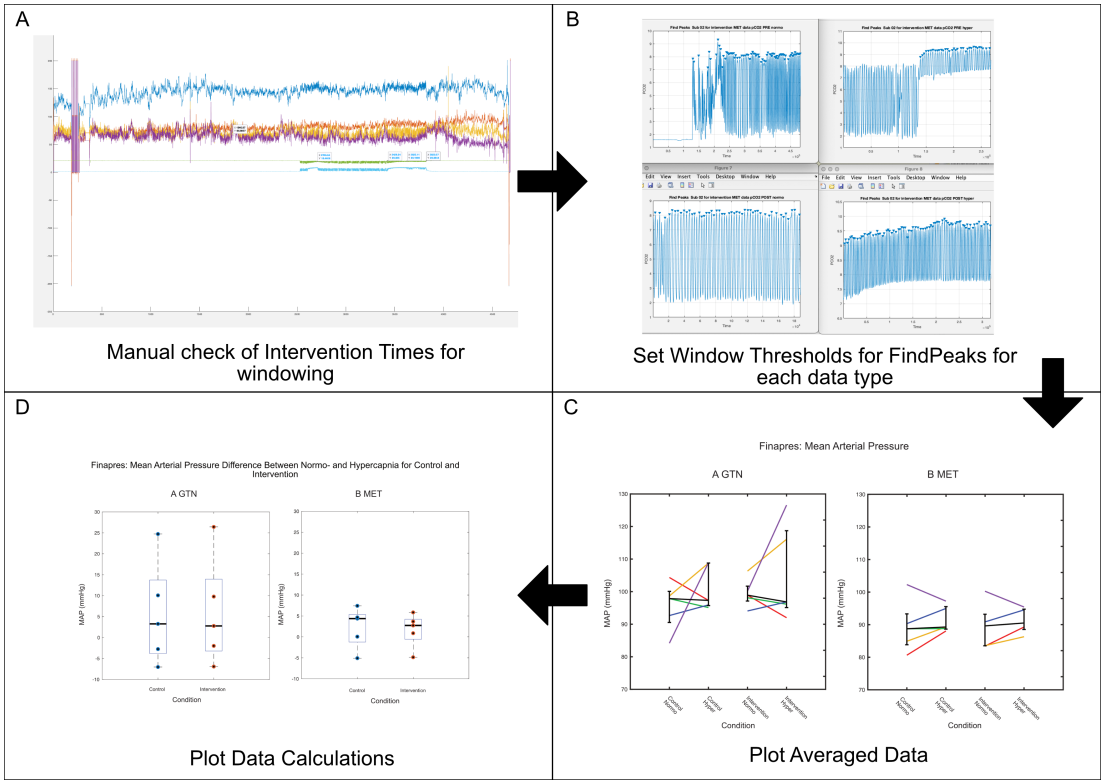


FIGURE 3.10: **Finapres and End Tidal Data Analysis process.** A: Data pre-processing: the LabChart® data file was exported as a text file both with and without comments (comments were used for marking important study day time points). In-house MATLAB scripts were used to create figures at each stage of the pre-processing to manually check the intervention times before windowing. B: Data were windowed for each physiological variable based on these intervention times for each intervention and condition. The 'FindPeaks' function was used to threshold each window. C: These data were used to calculate the mean of each individual's data across each window. D: Then the group median and interquartile ranges were calculated to display the median error bar and the difference between conditions was calculated and plotted as box plots.

3.9 Statistical Analysis

To compare the baseline measurements on day 1 and day 2, the coefficient of variance (CV) was calculated as:

Mean of means (μ_i) = (day 1 μ + day 1 μ)/2

Standard deviation of means (σ_i) = [((day 1 μ - μ_i)^2 + (day 2 μ - μ_i)^2)/(2-1)]

CV = (σ_i / μ_i) × 100%

A CV of more than 5% was considered to be variable.

Data were deemed non-parametric due to the small sample size. Additionally, kurtosis plots were made to check for skew. In-house MATLAB scripts were used to perform Wilcoxon Sign Rank tests for each of the physiological variables to determine if there were differences between the pre- and post-intervention conditions for baseline, as well as if there were differences between normocapnia and hypercapnia conditions.

Multiple comparison correction was performed using an alpha of 0.05, which when using the Bonfferoni correction for five tests was therefore divided by five to give an alpha of 0.01.

3.10 Results

3.11 Participant Characteristics

Ten participants completed the screening and both study days, the physical characteristics of the participants are shown in Table 3.2. Although both male and female participants were recruited, only female participants completed all study days and all of the male participants recruited were withdrawn at the medical screening or on the first study day due to exclusion criteria (see more detail in methods section 3.5). The study sessions were run at two time points, one September 2021 - June 2022, and a second September - December 2023. See the Appendix for total list of screened participants with reasons for withdrawal C.1.

TABLE 3.2: **Participant Characteristics.** The mean and standard deviation for the participants of the low blood pressure study; Dose (MET) per kg, m (metres), mg (milligrams), F (female), kg (kilograms), std (standard deviation).

Participant Number	Age (years)	Height (m)	Weight (kg)	Dose (MET) (mg) per kg	Sex
1	21	1.65	59	0.86	F
2	21	1.67	70	0.72	F
3	30	1.59	57	0.88	F
4	21	1.55	54	0.92	F
5	20	1.68	70	0.71	F
6	19	1.69	64	0.78	F
7	22	1.78	61	0.82	F
8	19	1.65	66	0.76	F
9	20	1.67	70	0.71	F
10	21	1.64	60	0.83	F
Mean±std	21.4±3.2	1.66±6.1	63±5.8	0.80±0.07	NA

3.11.1 Baseline Measurements

Table 3.3 shows the baseline measurements taken at the beginning of the study day for the 10 participants. The results show the measurements from the Dinamap (MAP and HR) and ultrasound (VMax). These measurements were similar for both study days, showing a relatively consistent baseline before starting the experiment. When comparing day 1 to day 2, the coefficient of variance for all measurements was less than 5%, so was considered to be within acceptable limits of variation across the two days for Dinamap. Another reason for focusing on the Dinamap data over the Finapres data was that the Finapres algorithm was proprietary, so data acquisition would not have been as transparent. The Finapres would sometimes struggle to get up to the required 'great' or 'excellent' level of calibration, so this suggested the calibration was not very good. Furthermore, the Finapres BP was consistently higher at around 20 mmHg more than the Dinamap, though the trends were similar it was less physiologically plausible.

TABLE 3.3: **Baseline Measurements.** Baseline measurements (group median±interquartile range, N=10) after participants had been resting, breathing room air for 30 minutes. BPM (beats per minutes), cm/s (centimetres per second), HR (heart rate), MAP (mean arterial pressure), mmHg (millimetres of mercury), VMax (velocity maximum).

Measurement	Day 1	Day 2	Coefficient of variance (%)
Finapres MAP (mmHg)	93.9±11.6	88.5±8.1	4.2
HR (BPM)	69.5±13.5	64.5±8.1	5.3
Dinamap MAP (mmHg)	80.0±4.2	76.5±6.0	3.2
HR (BPM)	67.1±13.5	66.4±11.7	0.7
VMax (cm/s)	99.2±22.9	94.6±19.1	3.3

3.11.2 Respiratory Stimulus

Table 3.4 shows the response to the hypercapnic challenge.

TABLE 3.4: **Respiratory Stimulus Response to a Hypercapnic Challenge.** ΔPRE (difference between normocapnia and hypercapnia, during the HC, pre-intervention), ΔPOST (difference between normocapnia and hypercapnia, during the HC, post-intervention), GTN (glyceryl trinitrate), HC (hypercapnic challenge), Hyper (hypercapnia), Normo (normocapnia), N-N (normocapnia pre- vs. normocapnia post-intervention), MET (metoprolol), mmHg (millimetres of mercury).

	Pre Intervention			**Post Intervention**			**Difference Pre- to Post Intervention**		
	Normo (mmHg)	Hyper (mmHg)	ΔPRE (mmHg)	Normo (mmHg)	Hyper (mmHg)	ΔPOST (mmHg)	Pre Normo to Post Normo (mmHg)	Difference N to N (mmHg)	ΔPRE to ΔPOST (mmHg)
GTN	33.3±27.6	41.1±32.1	7.8±9.0	33.1±25.1	40.5±25.5	7.1±4.6	0.2±3.1	p=0.770	p=0.557
MET	15.6±24.1	39.1±33.0	8.1±22.5	25.1±17.5	40.7±30.0	9.2±9.7	0.2±6.3	p=0.492	p=0.846

3.12 The Impact of GTN and MET Interventions on Mean Arterial Blood Pressure, Carotid Artery Blood Velocity and Heart Rate Responses during Normocapnia

3.12.1 Normocapnia: Mean Arterial Pressure

The Dinamap results are presented here as there was a greater variance in the Finapres data than the Dinamap data. The Finapres results are in appendix (section C.3). Figure 3.11 shows the BP data represented by the MAP value for each individual participant (coloured lines) along with the group median and interquartile range (IQR) (black error bars) measured using a Dinamap. Qualitatively, both before and after an intervention was administered, the MAP did not vary much.

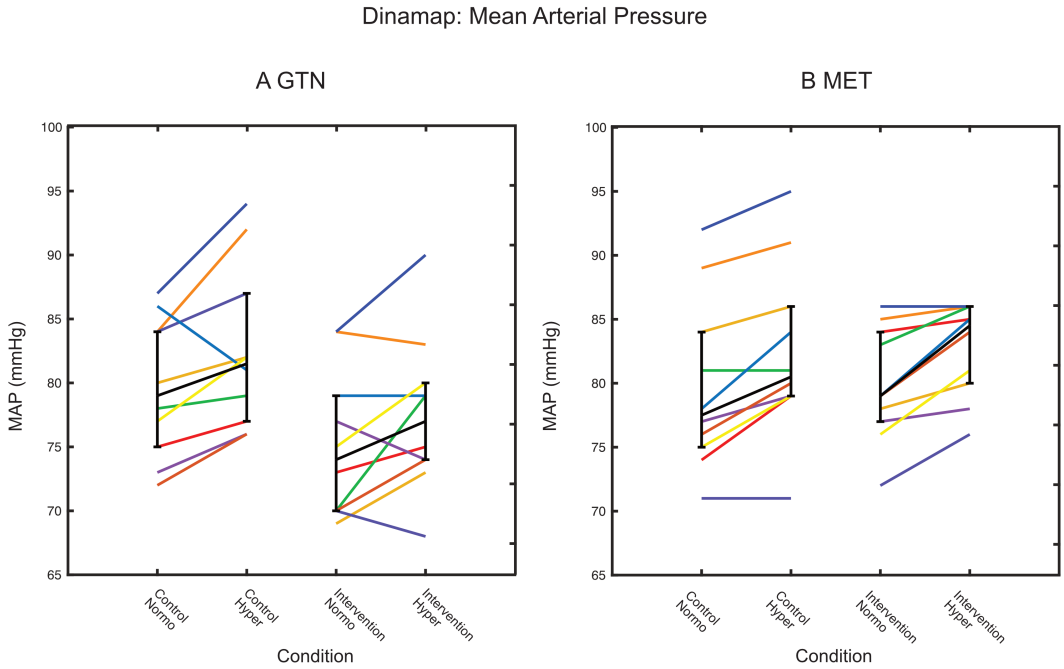


FIGURE 3.11: **Dinamap: Mean Arterial Pressure.** Coloured lines are for showing change in MAP within each participant across the whole experiment chronologically, the black error bars represent group median and interquartile range. N=10. GTN (glyceryl trinitrate), Hyper (hypercapnia), MAP (mean arterial pressure), MET (metoprolol), mmHg (millimetres of mercury), Normo (normocapnia).

The BP during control and intervention normocapnia conditions was compared to see if there was a noticeable effect of the pharmacological interventions on lowering the BP i.e. did the hypotensive medications produce the expected drop in BP. When BP was measured with a Dinamap (shown in Figure 3.12) the control and intervention MAP on the day the GTN was administered was 79.0±9.0 mmHg during the control normocapnia (Fig. 3.12A), followed by 74.0±9.0 mmHg during the intervention normocapnia (median±IQR), a difference of -2.5±6.0 mmHg, p=0.035 (median±IQR) i.e. not significant after multiple comparisons correction. On the days MET was administered, MAP was 77.5±9.0 mmHg during the control normocapnia (Fig. 3.12B), followed by 79.0±7.0 mmHg (median±IQR) during post-intervention normocapnia. This was a difference of 1.0±6.0 mmHg (median±IQR), p=0.895, which was also not significant.

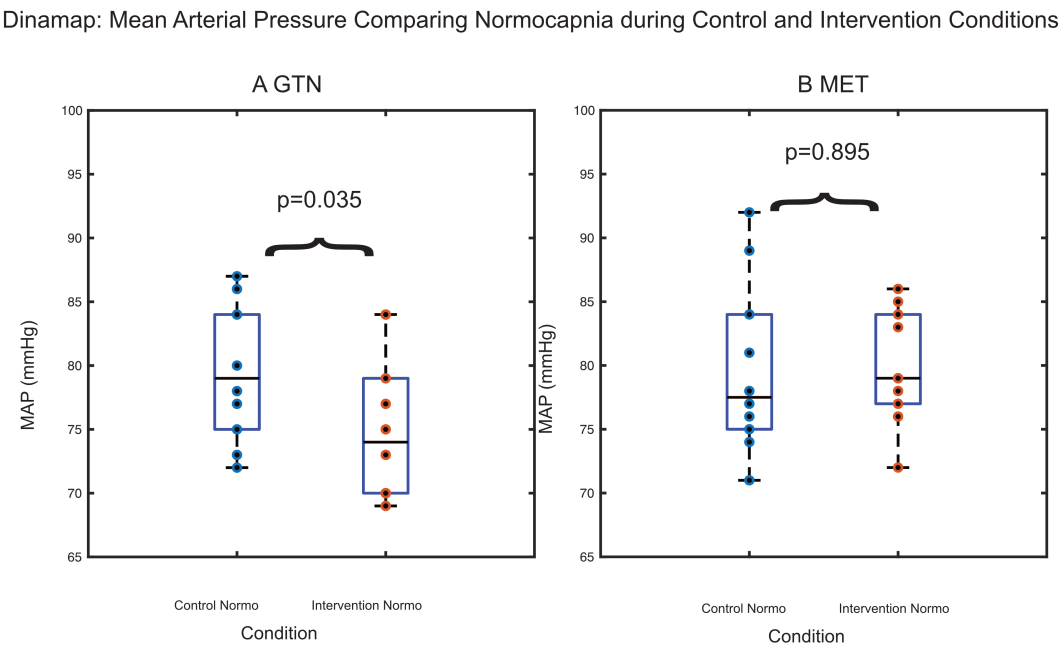


FIGURE 3.12: **Dinamap: Mean Arterial Pressure Comparing Normocapnia during Control and Intervention Conditions.** Shows the control (left side blue markers) and intervention (right side red markers) MAP during normocapnia. The circles show the individual participants and the black line represents group median and interquartile range. N=10. GTN (glyceryl trinitrate), MAP (mean arterial pressure), MET (metoprolol), mmHg (millimetres of mercury), Normo (normocapnia).

3.12.2 Normocapnia: Blood Velocity

Figure 3.13 shows the velocity maximum measurements, represented by Vmax for all data, for each individual participant (coloured lines) and the group median and IQR (black error bars) data. Qualitatively, there appears to be slightly more variability in the GTN data (Fig. 3.13A) compared to the MET data (Fig. 3.13B).

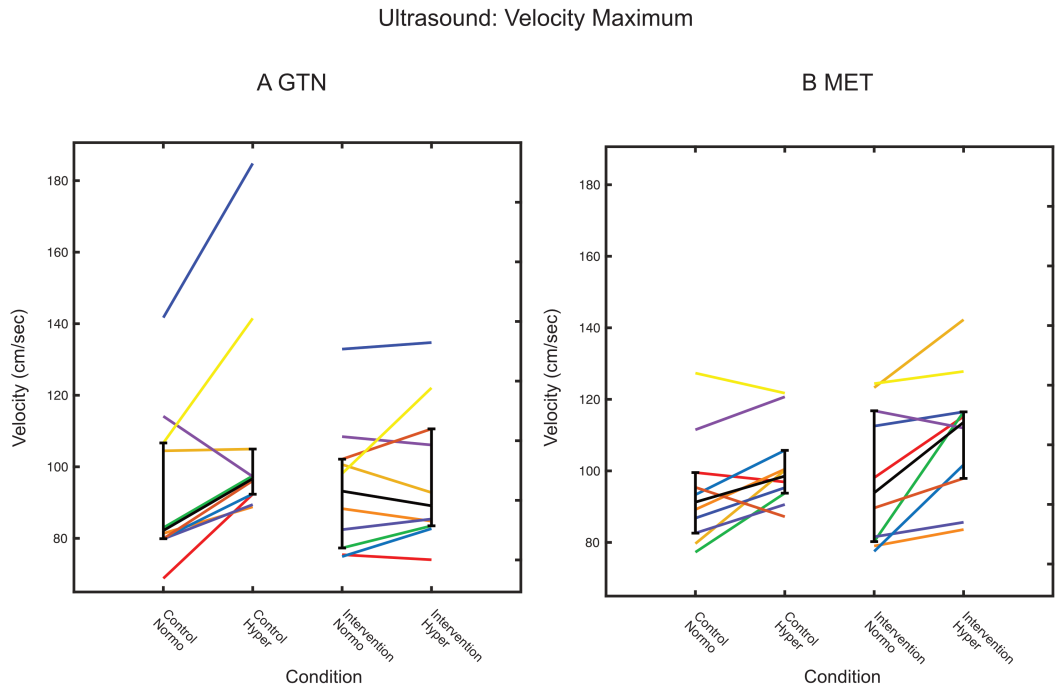


FIGURE 3.13: **Ultrasound: Velocity Maximum.** Coloured lines show the change in VMax within each participant across the whole experiment chronologically, the error bars represent the group median and interquartile range. N=10. cm/s (centimetres per second), GTN (glyceryl trinitrate), Hyper (hypercapnia), MET (metoprolol), Normo (normocapnia), VMax (velocity maximum).

The differences between the blood velocity during the normocapnia condition for control and intervention conditions was compared to see if there was a change in velocity due to the interventions. For GTN, velocity during the control normocapnia was 82.2±26.8 cm/s, followed by 93.2±24.8 cm/s (median±IQR) during the GTN intervention normocapnia (Fig. 3.14A). This was a difference of -4.5±12.3 cm/s (p=0.770) (median±IQR), which was not significantly different. For MET, velocity during control normocapnia was 91.3±16.9 cm/s, followed by 93.9±36.6 cm/s (median±IQR) during post-intervention normocapnia (Fig. 3.14B). The difference was -1.2±11.1 cm/s (median±IQR), p=1.000, which was also not significantly different after the intervention.

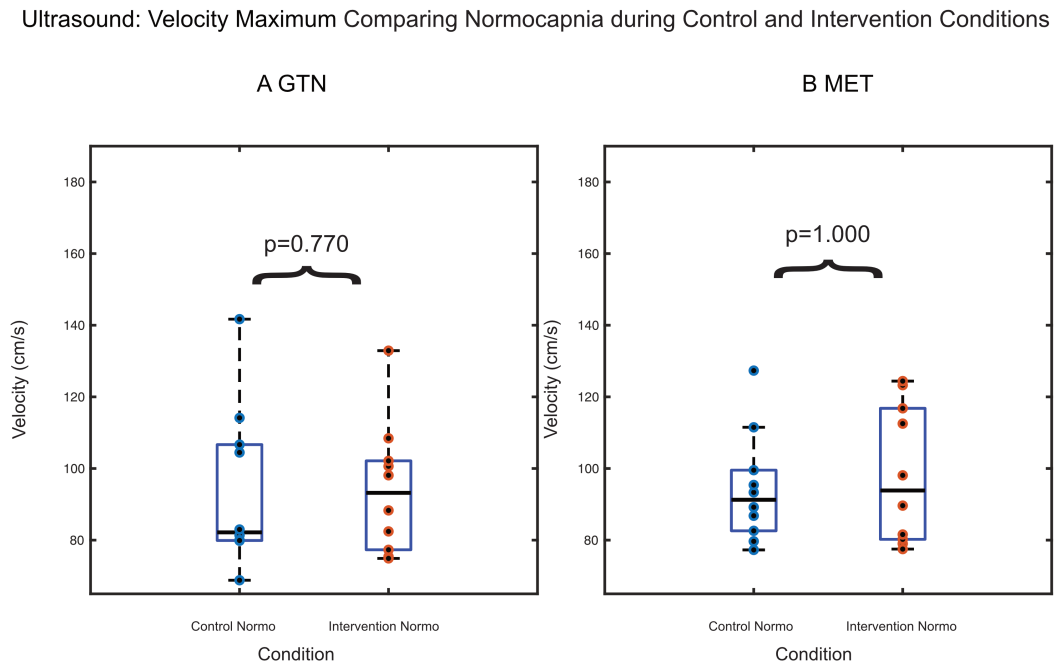


FIGURE 3.14: **Ultrasound: Velocity Maximum Comparing Control and Intervention Normocapnia Conditions.** Shows the control (left side blue markers) and intervention (right side red markers) normocapnia velocities. The circles show the individual participants and the black line represents group median and interquartile range. N=10. There was no significant difference between the control and intervention velocity controls when GTN (p=0.770) or MET (p=1.000) was given. cm/s (centimetres per second), GTN (glyceryl trinitrate), MET (metoprolol), Normo (normocapnia), VMax (velocity maximum).

3.12.3 Normocapnia: Heart Rate

The heart rate (in BPM) was measured as a secondary finding to investigate HR as an adaptation or compensatory mechanism to the GTN or MET influence on BP. Figure 3.15 shows the HR for each individual participant (coloured lines) with the group median and IQR (black error bars) (Fig. 3.15A GTN compared (Fig. 3.15B MET).

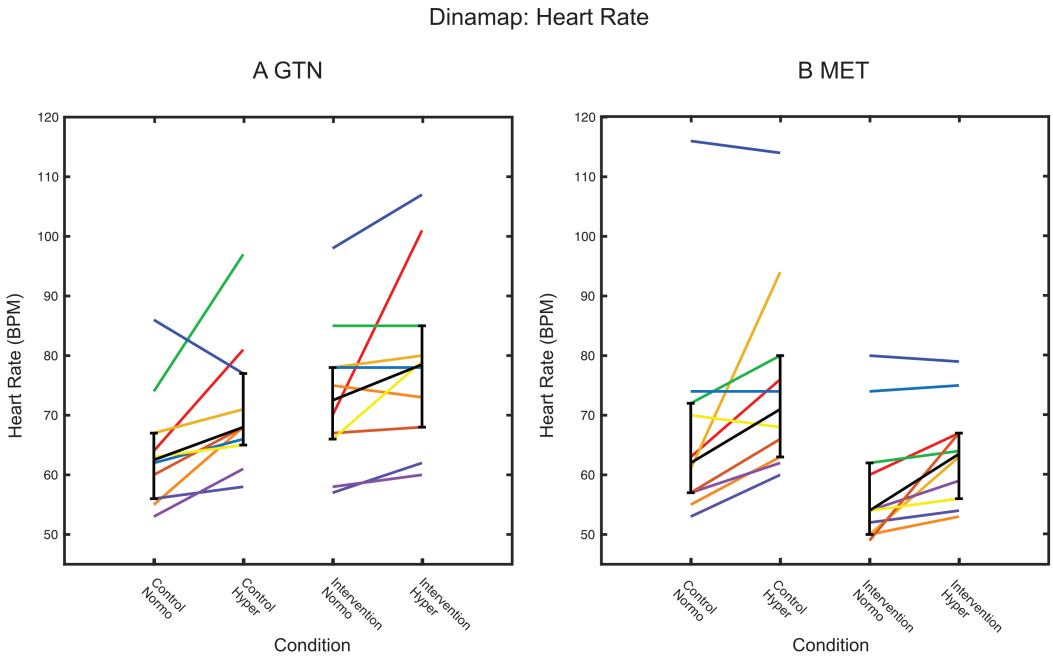


FIGURE 3.15: **Dinamap: Heart Rate.** Coloured lines show the change in HR for each participant across the whole experiment chronologically, the black line represents group median and interquartile range. N=10. BPM (beats per minute), GTN (glyceryl trinitrate), HR (heart rate), Hyper (hypercapnia), MET (metoprolol), Normo (normocapnia).

Figure 3.16 shows there was a significant difference between the control (left side blue markers) and intervention (right side red markers) normocapnia conditions. For GTN, an increase in HR during normocapnia was measured from control normocapnia 62.5±11.0 BPM to intervention normocapnia 72.5±12.0 BPM (median±IQR)) (Fig. 3.16A). The difference was calculated as an increase of 9.0±7.0 BPM (median±IQR), p=0.002, which was significant after correction for multiple comparisons.

In contrast, for MET, HR was 62.0±15.0 BPM during control normocapnia which decreased to 54.0±12.0 BPM during intervention normocapnia (median±IQR), (Fig. 3.16B). The difference was calculated as a decrease of -6.5±8.0 BPM (median±IQR), p=0.004, which was significant after correction for multiple comparisons.

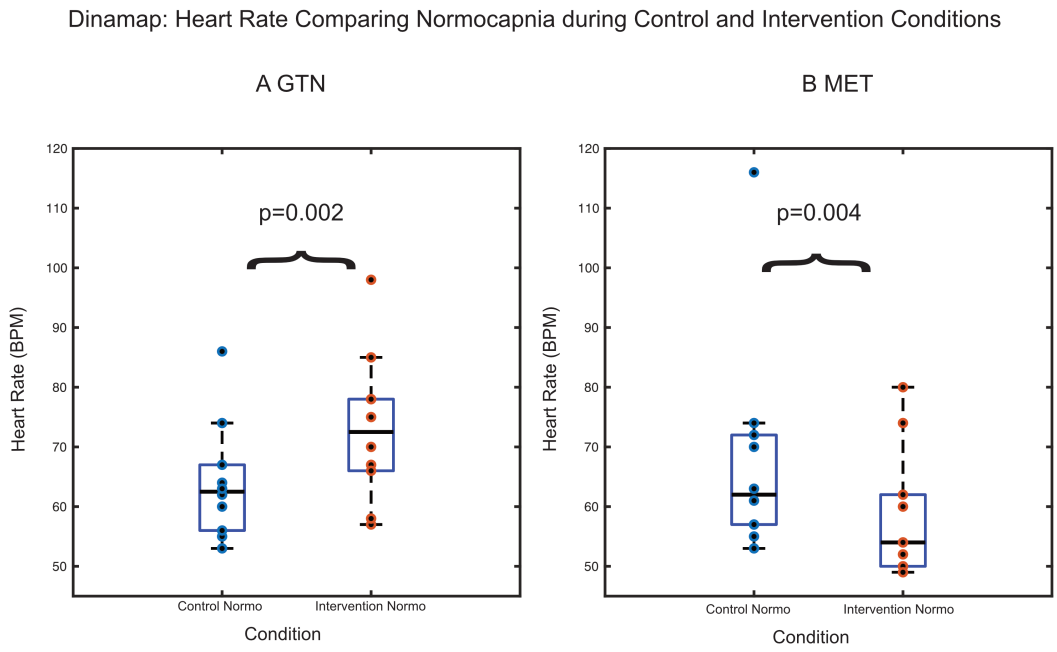


FIGURE 3.16: **Dinamap: Heart Rate Comparing Normocapnia during Control and Intervention Conditions.** Shows the control (left side blue markers) and intervention (right side red markers) normocapnia HRs. The circles show the individual participants and the black line represents group median and interquartile range. N=10. There was a significant difference between the control and intervention normocapnia conditions for HR when GTN (p=0.002) or MET (p=0.004) was given. BPM (beats per minute), GTN (glyceryl trinitrate), HR (heart rate), MET (metoprolol), Normo (normocapnia).

3.13 The Impact of GTN and MET Interventions on Mean Arterial Blood Pressure, Carotid Artery Blood Velocity and Heart Rate Responses during the Hypercapnic Challenge

The following results show the difference between the normocapnic and hypercapnic measurements for both control (pre-intervention) and intervention (post-intervention) conditions.

3.13.1 Difference during the Hypercapnic Challenge: Mean Arterial Pressure

On the day that GTN was given, MAP during the pre-intervention hypercapnic challenge was 79.0±9.0 mmHg (normo) followed by 81.5±10.0 mmHg (hyper), a difference (ΔPre) of 0.5±4.0 mmHg (median±IQR), which was not significantly different (p=0.557). Post-intervention MAP during the HC was 74.0±9.0 mmHg (normo) followed by 77.0±6.0 mmHg (hyper) (median±IQR), a difference (ΔPost) of 3.0±6.0 mmHg, which was also not significantly different (p=0.074). Additionally, there was no significant difference between the HC responses when comparing ΔPre to ΔPost (p=0.336) (Fig. 3.17A) (i.e. no difference between the responses pre- to post-intervention).

On the day that MET was given, pre-intervention MAP during the HC was 77.5±9.0 mmHg (normo) followed by 80.5±7.0 mmHg (hyper), a difference (ΔPre) of 2.5±4.0 mmHg (median±IQR), which was not significantly different (p=1.000). Post-intervention MAP significantly increased from 79.0±7.0 mmHg (normo) to 84.5±6.0 mmHg (hyper), a difference (ΔPost) of 3.2±3.1 mmHg

(median±IQR) (p=0.004). However, when comparing the HC responses of ΔPre to ΔPost there was no significant difference (p=0.883) (Fig. 3.17B).

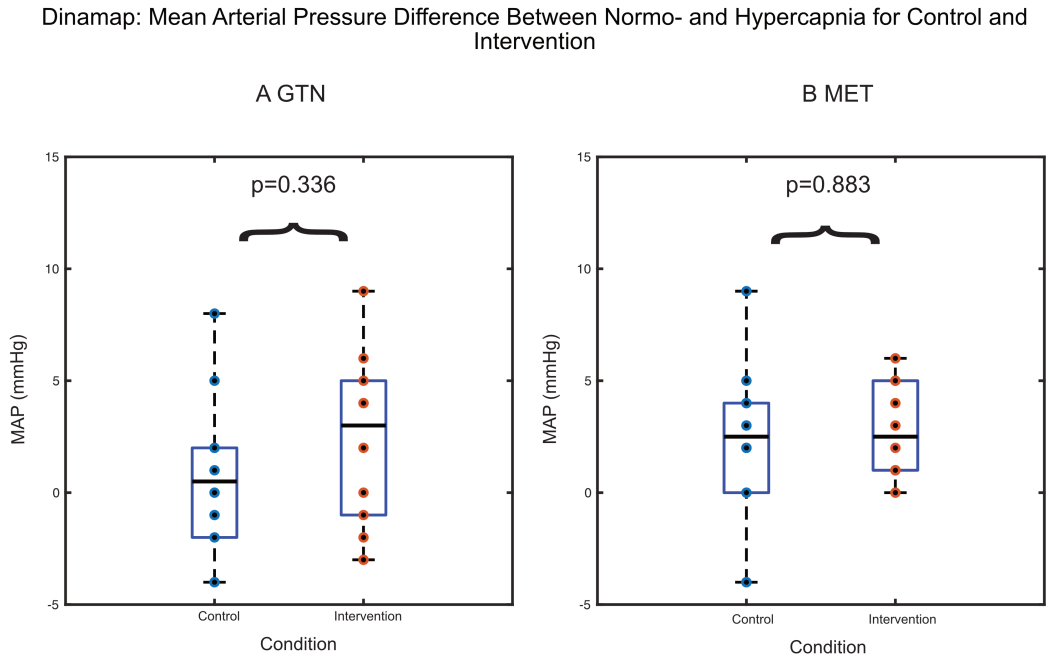


FIGURE 3.17: **Dinamap: Difference Between Normo- and Hypercapnia for Control and Intervention Mean Arterial Pressure.** Shows the difference between hypercapnia and normocapnia for control (left side blue markers) and intervention (right side red markers) MAP. The circles show the individual participants and the black line represents group median and interquartile range. There were no significant differences between normo- to hypercapnia condition when comparing control to intervention change for MAP when GTN (p=0.336) or MET (p=0.883) were given. GTN (glyceryl trinitrate), MAP (mean arterial pressure), MET (metoprolol), mmHg (millimetres of mercury).

3.13.2 Difference during the Hypercapnic Challenge: Velocity

On the days that GTN was administered, the pre-intervention VMax was 82.2±26.8 cm/s (normo) followed by 96.7±12.6 cm/s (hyper) during the hypercapnic challenge, a difference (ΔPre) of 3.3±10.1 cm/s (median±IQR), which was not significantly different (p=0.846). Post-intervention MAP was 93.2±24.8 cm/s (normo) followed by 89.1±27.1 cm/s (hyper) (median±IQR) during the HC, a difference (ΔPost) of -2.4±10.13 cm/s, which was also not significantly different (p=0.32). Additionally, there was no significant difference between the HC responses, when comparing ΔPre to ΔPost response to the HC (p=0.922) (Fig. 3.18A).

On the days that MET was administered, pre-intervention VMax was 91.3±16.9 cm/s (normo) followed by 98.5±112.0 cm/s (hyper) during the HC, a difference (ΔPre) of 0.3±17.5 cm/s (median±IQR), which was not significantly different after multiple comparisons correction (p=0.037). Post-intervention VMax was 93.9±36.6 cm/s (normo) followed by 113.6±18.6 cm/s (hyper), a difference (ΔPost) of 6.4±15.0 (median±IQR), which was not significantly different after multiple comparisons correction (p=0.020). Additionally, when comparing the HC responses of ΔPre to ΔPost there was no significant difference to the HC (p=0.0273) (Fig. 3.18B).

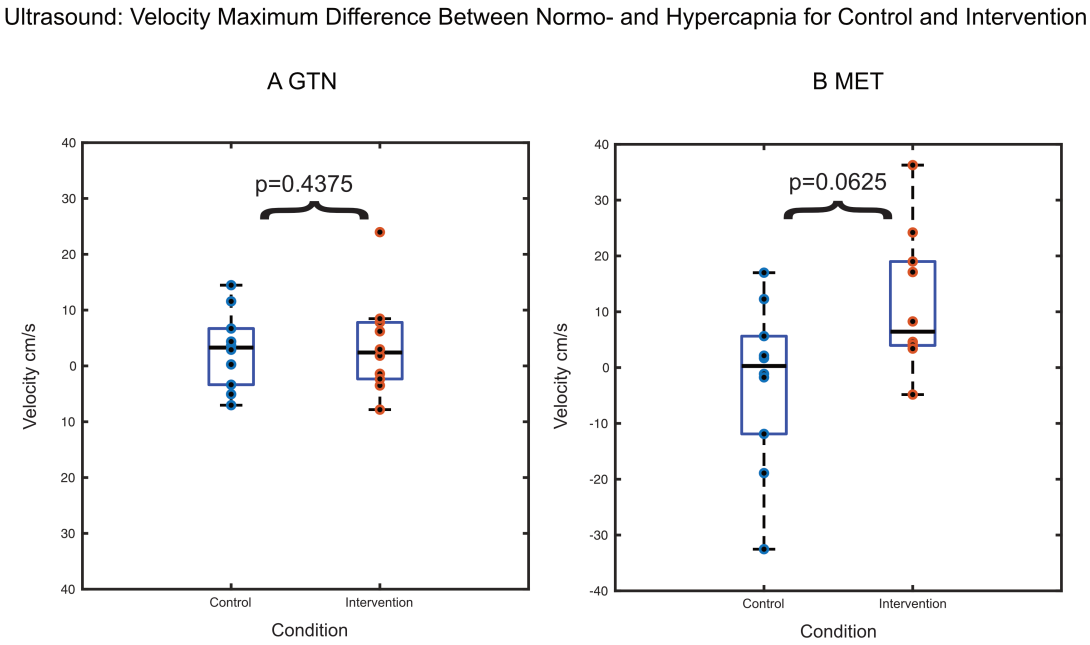


FIGURE 3.18: **Ultrasound: Velocity Maximum Difference Between Normo- and Hypercapnia for Control and Intervention.** Shows the difference between hypercapnia and normocapnia for control (left side blue markers) and intervention (right side red markers) velocities. The circles show the individual participants and the black line represents group median and interquartile range. There were no significant differences between the change from normo- to hypercapnia conditions when comparing control to intervention change for Vmax when GTN (p=0.4375) or MET were given (p=0.0625). cm/s (centimetres per second), CO_2, GTN (glyceryl trinitrate), MET (metoprolol), VMax (velocity maximum).

3.13.3 Difference during the Hypercapnic Challenge: Heart Rate

On the day that GTN was given, pre-intervention HR was 62.5±11.0 BPM (normo) followed by 68.0±12.0 BPM (hyper) during the hypercapnic challenge, a difference (ΔPre) of -1.5±5.0 BPM (median±IQR), which was not significantly different (p=0.027). Post-intervention HR was 72.5±12.0 BPM (normo) followed by 78.5±17.0 BPM (hyper) (median±IQR), a difference (ΔPost) of 2.0±9.0 BPM, which was also not significantly different (p=0.039). Additionally, there was no significant difference between the HC responses, when comparing ΔPre to ΔPost (p=0.025) (Fig. 3.19A).

On the day that MET was given, pre-intervention HR was 62.0±15.0 BPM (normo) followed by 71.0±17.0 BPM (hyper) during the HC, a difference (ΔPre) of -0.5±8.0 BPM (median±IQR), which was not significantly different (p=0.846). Post-intervention HR was 54.0±12.0 BPM (normo) followed by 63.5±11.0 BPM (hyper), a difference (ΔPost) of 2.5±5.0 BPM (median±IQR), which was a significant increase (p=0.006). When comparing the HC responses of ΔPre to ΔPost there was no significant difference (p=0.168)(Fig. 3.19B).

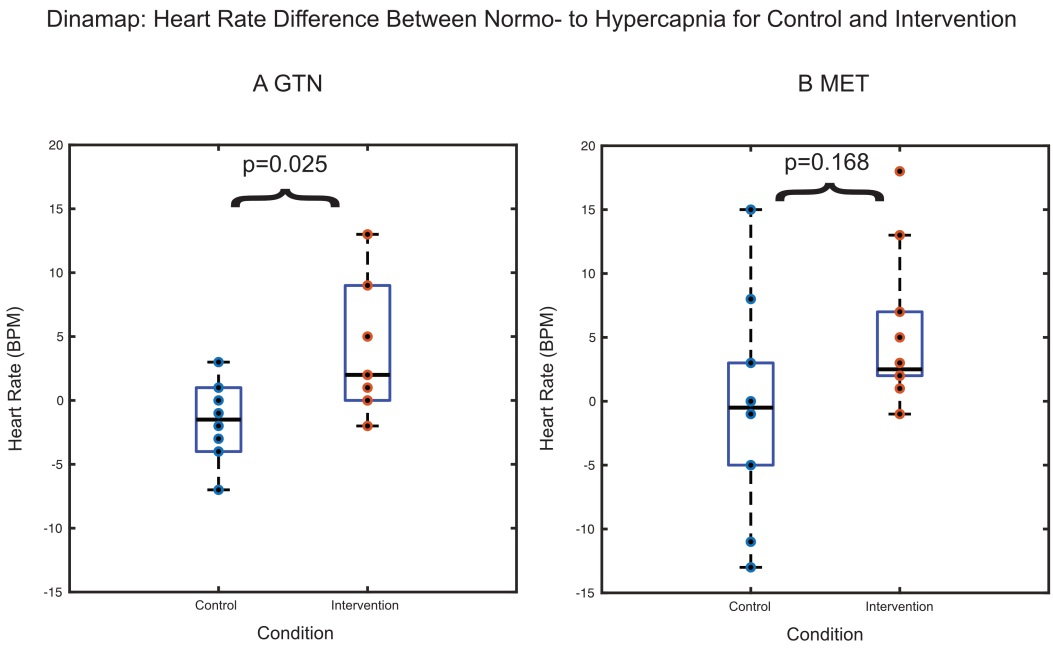


FIGURE 3.19: **Dinamap: Heart Rate Difference Between Normo- to Hypercapnia for Control and Intervention.** Shows the difference between hypercapnia and normocapnia for control (left side blue markers) and intervention (right side red markers) heart rates. The circles show the individual participants and the black line represents group median and interquartile range. There was no significant difference between the change from normocapnia to hypercapnia conditions when comparing control to intervention for HR when GTN (p=0.025) or MET (p=0.168) were given. BPM (beats per minute), GTN (glyceryl trinitrate), HR (heart rate), MET (metoprolol).

3.14 Percentage Difference

The percentage difference of each individual was calculated to normalise the data by each individual participants' baseline. This was to make it easier to compare these results to the previous MRI (magnetic resonance imaging) data presented in Chapter 2.

3.14.1 Percentage Difference during Hypercapnic Challenge: Mean Arterial Pressure

Figure 3.20 shows that when comparing pre- to post intervention response to hypercapnia (i.e. percentage difference ΔPre to ΔPost), MAP after GTN ΔPre was 0.6±5.2%, and ΔPost was 4.2±7.9% (median±IQR), which was not significantly different (p=0.557). For MET, ΔPre was 3.2±5.5% and ΔPost was 3.1±5.1% (median±IQR), which was not significantly different (p=1.000). So, was not statistically significant for either intervention.

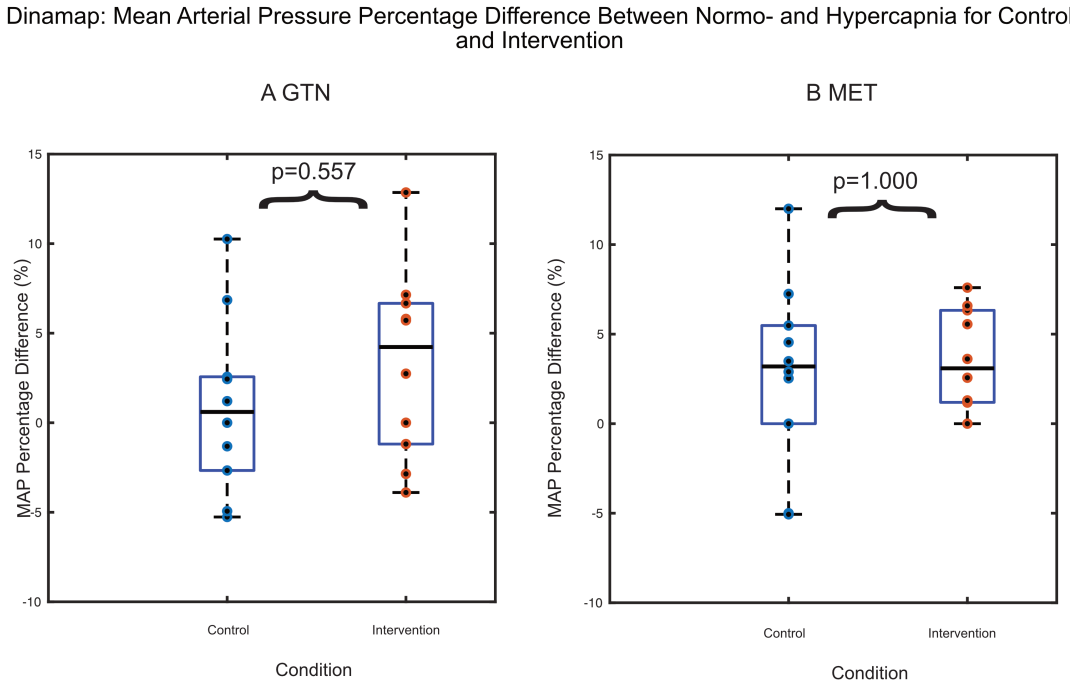


FIGURE 3.20: **Dinamap: Percentage Difference Between Normo- and Hypercapnia for Control and Intervention Mean Arterial Pressure.** Shows the difference between hypercapnia and normocapnia for control (left side blue markers) and intervention (right side red markers) MAP normalised by the individual's control condition. The circles show the individual participants and the black line represents the group median and interquartile range. GTN (glyceryl trinitrate), MAP (mean arterial pressure), MET (metoprolol), mmHg (millimetres of mercury).

3.14.2 Percentage Difference during Hypercapnic Challenge: Velocity Maximum

Figure 3.21 shows that when comparing pre- to post intervention responses to the hypercapnic challenge (i.e. percentage difference ΔPre to ΔPost), VMax for GTN ΔPre was 4.7±10.9%, and ΔPost was 2.5±10.4% (median±IQR), which was not significantly different (p=0.846). For MET, ΔPre was 0.2±14.8%, and ΔPost was 7.5±13.9%, (median±IQR), which was not significantly different (p=0.064).

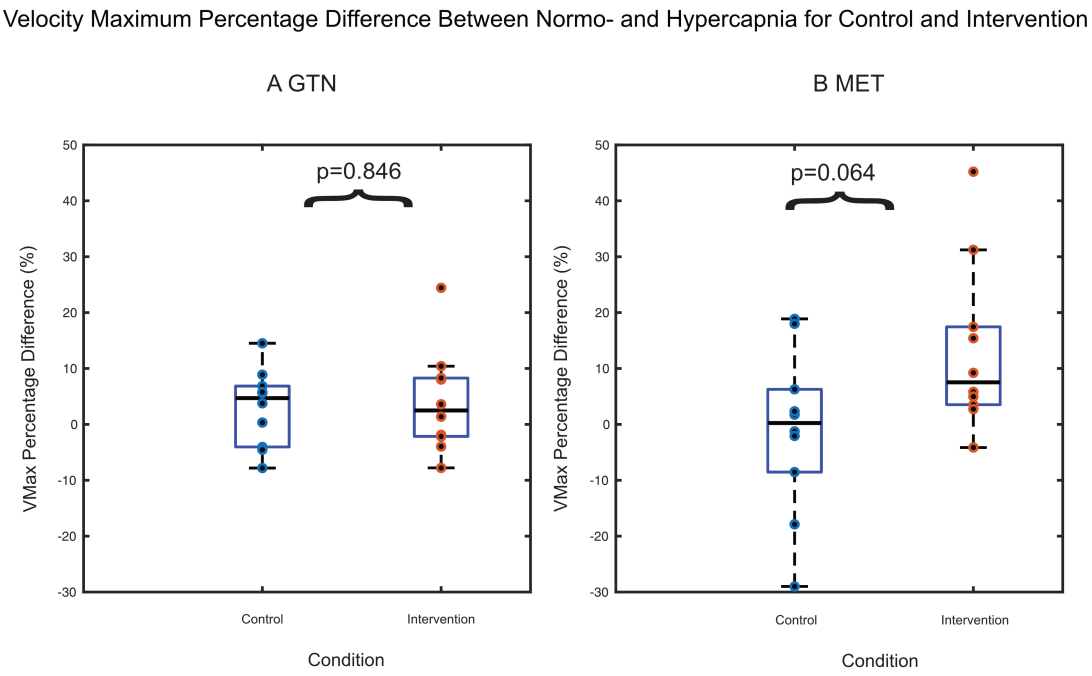


FIGURE 3.21: **Ultrasound: Percentage Difference Between Control and Intervention Velocity Maximum under Normocapnia Condition.** Shows the control (left side blue markers) and intervention (right side red markers) normocapnia velocities. The circles show the individual participants and the black line represents the group median and interquartile range. N=10. GTN (glyceryl trinitrate), MET (metoprolol), Normo (normocapnia) VMax (velocity maximum).

3.14.3 Percentage Difference during Hypercapnic Challenge: Heart Rate

Figure 3.22 shows that when comparing pre- to post intervention responses to the hypercapnic challenge (i.e. percentage difference ΔPre to ΔPost), HR for GTN ΔPre was -2.6±6.3%, and ΔPost was 3.0±9.2% (median±IQR), which was not significantly different (p=0.027). For MET, HR ΔPre was -0.9±12.6%, and ΔPost was 4.9±8.4% (median±IQR), which was not significantly different (p=0.193). So, was not statistically significant for either intervention.

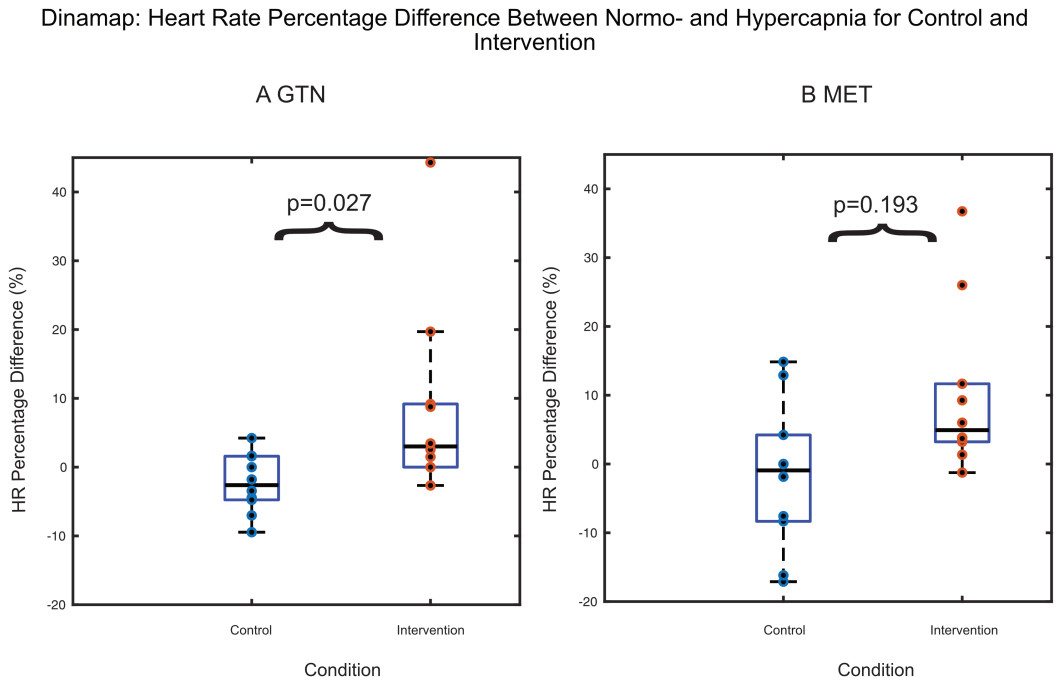


FIGURE 3.22: **Dinamap: Percentage Difference Between Control and Intervention Heart Rate Normocapnia Conditions.** Shows the difference between the control and intervention normocapnia heart rates normalised by the individual's control condition. The circles show the individual participants and the black line represents group median and interquartile range. BPM (beats per minute), GTN (glyceryl trinitrate), HR (heart rate), MET (metoprolol).

3.15 Discussion

This study aimed to investigate the changes in systemic blood pressure, heart rate and carotid artery blood flow velocity during a normocapnic and hypercapnic challenge, both before and after pharmacological interventions. This intervention was administered to alter central and peripheral haemodynamic responses. The overarching objective was to establish an *in vivo* model for reducing systemic BP and carotid artery blood flow, as an intermediate step towards developing robust measures of blood flow in the brain tissue using MRI. Hence, the study was conducted as a feasibility study for a future study in involving MRI.

In summary, when comparing pre-intervention normocapnia to post-intervention normocapnia, there was a statistically significant increase in HR after GTN, whereas there was a statistically significant decrease in HR after MET. Additionally, after MET, when comparing the difference between normo- to hypercapnia (ΔPost), there was a statistically significant increase in MAP, and a statistically significant increase in HR. When comparing the pre-intervention to post-intervention response to the HC (i.e. ΔPre vs. ΔPost) there were no statistically significant differences in the overall response after interventions were given for any measurements. Overall, the differences between conditions were small, and the medians were generally smaller in magnitude than the variability (IQR) of the data.

3.15.1 Pharmacological Interventions Did Not Alter Mean Arterial Blood Pressure or Carotid Artery Blood Velocity, but Did Alter the Heart Rate.

The hypothesis that giving a single dose of pharmacological intervention to healthy participants to lower BP would decrease BP was not supported. When

measured with Dinamap, there was no observed change in the brachial artery BP after GTN or MET. The hypothesis that giving a pharmacological intervention to lower BP would decrease blood flow velocity in the carotid artery was also not supported. Blood flow velocity in the carotid artery, measured with ultrasound to calculate the velocity maximum, did not change after GTN or MET. The hypothesis that giving a pharmacological intervention may alter HR was supported. After GTN, Dinamap pulse oximeter measures of HR increased. Conversely, after MET HR decreased. HR appears to have compensated for the effect of the interventions, hence reducing any possibility of observing a change in BP or velocity. In clinical terms, even a 10 BPM change (within healthy limits) in HR is relatively mild.

GTN Effect on Blood Pressure during Normocapnia

In this study, a statistically significant change in BP after GTN administration was not detected. The basis of GTN as a therapeutic stems from its ability to decrease BP. As a global vasodilator it causes the relaxation of the arteries and a subsequent decrease in peripheral resistance. When peripheral vessels vasodilate and the total peripheral resistance is reduced cardiac output must be increased to maintain BP, which is most easily achieved via increasing HR. Unlike the results shown here in healthy, young participants, previous studies have shown a change in BP after GTN. Firstly, Ghiadoni and colleagues (2019)[93] gave GTN to normo- and hypertensive patients, comparing 25 µg and 400 µg GTN doses, and saw a difference in response to the two doses in both groups. Normotensive participants (N=60, 44.8±11.6 years, 28M), given 400 µg GTN (a dose similar to this chapter) resulted in a decrease in SYS (-2.03±6.90mmHg) and DIA (-5.63±4.39 mmHg) BP. Converted to MAP (using equation 3.1), this would be -4.43 mmHg, almost twice the observed change in MAP shown here

in section 3.12.1. Another reason for a more noticeable change in their study may be because the participants were older, and therefore had systematically less effective homeostasis of the BP, i.e. not as effective compensation mechanisms compared to younger adults. An alternative method, such as Moppett and colleagues (2008)[157], was to give GTN via IV, in healthy participants (N=10, 18-40 years, 3F), to induce a 15% decrease in MAP (from ∼84 to 72 mmHg), which required 0.5–2.5 mg per kg per min. This was different to the study here, as they gave the drug until a set point rather than a single dose, but still saw a decrease in BP. In another study, Shirvani and colleagues (2019)[208] gave 800 µg GTN sublingually to six young, healthy participants (mean age 27.6± 18.5 years, 5M), twice the dose used here. After GTN, systolic and diastolic BP significantly decreased. Unfortunately, the authors only stated the statistical results (systolic p=0.02, diastolic p=0.01), so it is not possible to directly compare absolute values from their study. These studies taken together show that it is possible to lower BP in healthy and patient populations when giving GTN. The GTN dose for this study was chosen on the basis of the dose used in a study previously conducted at the DGHPU (Skirrow and colleagues (2014)[212]). However, to see more noticeable results, it may be appropriate to increase the dose used in this chapter to match the studies above.

GTN Effect on Blood Flow Velocity during Normocapnia

In this study a statistically significant change in blood velocity was not detected following GTN administration. The downstream effects of altering BP via GTN were expected to decrease blood velocity in the carotid artery. This value was of particular interest due to the previous chapter's experimental investigation into blood flow in the brain tissue using a phase contrast velocity and pseudocontinuous arterial spin labelling MR pulse sequences. The previously mentioned study

by Moppett and colleagues (2008)[157], which gave GTN via IV, also observed a small, but significant, decrease in middle carotid artery (MCA) velocity (53 to 48 cm/s) when measured with transcranial doppler (TCD). In another study, Bednarczyk and colleagues (2002)[22] also gave GTN via IV, this time in increasing doses of 0.125, 0.25 and 0.5 g per kg per min to young, healthy volunteers (N=12, 27.5±8.7 mean years, 6F). Blood flow decreased in the right and left MCAs by ∼12% at 0.125 µg per kg per min, ∼17% at 0.25 µg per kg per min and ∼20% at 0.5 µg per kg per min. These results could be considered consistent with the known effect of GTN on cerebral vessels, resulting in a decrease in vascular tone without impairing cerebral autoregulation. Measuring velocity at a different part of the vascular tree could also have had an impact, considering the reactivity of MCAs versus the carotid artery, and this will be discussed in more detail in the discussion's hypercapnia section 3.16.

GTN Effect on Heart Rate during Normocapnia

In this study, there was a statistically significant increase in HR after GTN. This increase is in agreement with previous studies, where HR increased as a compensatory response to GTN. Ghiadoni and colleagues (2019)[93], mentioned above, saw an increase in HR after 400 µg GTN by 5.27±5.52 BPM, a slightly smaller response than seen here in section 3.12.3. Additionally, Moppett and colleagues (2008)[157] also saw a significant increase in HR from 67 to 73 BPM (+6 BPM) after 0.5–2.5 mg per kg per min GTN. These findings taken together may suggest a compensatory HR response to GTN, and explain why there was no change in BP or velocity after GTN in this study.

MET Effect on Blood Pressure during Normocapnia

In this study, a statistically significant change in BP after MET was not detected. When MET is administered beta-1 receptors are blocked, resulting in a decrease in HR. To maintain BP the total peripheral resistance needs to increase. Previous studies have shown a change in BP after administration of metoprolol, which was not reflected in the results from this study. Firstly, Ide and colleagues (1998)[116] studied young healthy participants (N=9, 31±2.0 years (mean±SE), healthy, sex not given) after 0.15 mg per kg MET. MAP at rest was 94±4 mmHg, and decreased to 86±4 mmHg (mean±SE) ($p<0.05$) after MET. In addition, Ogoh and colleagues (2007)[174] also gave 0.15 mg per kg MET to eight healthy men (N = 8M, 22±1 years (mean±SE)), and MAP decreased from 92±4 mmHg to 85±3 mmHg ($p<0.05$) after MET.

However, not all studies show a decrease in BP after MET. Hawkins and colleagues (2009)[109] investigated the difference between Endurance-trained (ET) (n=8, 28±4.6 years) and average-trained athletes (AT; n=8, 26±4.1 years, all male) after 50 mg MET. The results may be more directly comparable to this chapter given they used the same dose. The ET were competitive, long-distance cyclists or runners, whereas the AT took part in moderate aerobic fitness. At rest, the AT SYS non-significantly decreased by -8 mmHg after MET (112±3 mmHg to 103±3 mmHg (mean±SE), whereas the ET SYS non-significantly decreased by -7 mmHg (125±5 mmHg to 118±4 mmHg) after MET. These ET BP values were significantly different to AT baseline and MET BP ($p<0.05$). Additionally, at rest, DIA values showed no statistical difference in BP from baseline to MET (AT: rest 70±2 mmHg, MET 69±2 mmHg (-1), ET: rest 80.3±3 mmHg, MET 71±3 mmHg (difference of -9 mmHg, not significantly different from control or from AT). Using equation 3.1 MAP would therefore be calculated as AT: decreased from 84 mmHg to 80 mmHg (-4 mmHg) after MET, and ET: decreased from

95 mmHg to 87 mmHg after MET (-8 mmHg). In this thesis, participants were only excluded for fitness at a competitive level, and average amounts of exercise were not recorded, which may have increased the variability of the results.

MET Effect on Carotid Artery Blood Flow Velocity during Normocapnia

In this study, no statistically significant change in velocity was found after MET. Other studies have shown different levels of decrease in velocity after MET. Ide and colleagues (1998)[116], already mentioned, used TCD to make measurements of the MCA, and velocity decreased from a mean of 59 cm/s to 56 cm/s (-3 cm/s) after MET. Similarly, Ogoh and colleagues (2007)[174] also measured MCA velocity at rest and saw a decrease, this time significant ($p<0.05$), from 60±2 cm/s to 52±3 cm/s (mean±SE), a difference of -13.4 cm/s after MET. Both these studies gave 0.15 mg per kg metoprolol, measured velocity at the same position, and still saw differing results. This variability may be due to other physiological factors at an individual level e.g. because the β-adrenergic blockade indirectly affects vessels to levels within some participants homeostatic/ autoregulatory range and subsequently results in smaller observed differences from pre- to post- intervention.

MET Effect on Heart Rate during Normocapnia

In this study, HR statistically significantly decreased after MET. The MET mechanism of action involves cardiac-specific beta blockade, including decreasing cardiac output and also heart rate, hence it was expected that this would decrease participants HR. However, in Ide (1998)[116] HR only decreased from 67±4 to 65±3 BPM (mean±SE) after MET. Additionally, Ogoh and colleagues (2007)[174] also saw no change in HR from 66±3 BPM to 67±3 BPM (mean±SE) after MET.

Furthermore, Hawkins and colleagues (2009)[109] in AT observed no change from 77±3 BPM to 71±4 BPM, (mean±SE), a difference of -6 BPM. In contrast, in ET there was a significant decrease from 71±2 BPM to 62±4 BPM after MET, (a difference of -8 BPM ($p < 0.05$). One reason given for the variation between ET and AT participants is that maybe the ET participants had a lower body weight ($P<0.04$) and lower resting HR ($P<0.03$) than the AT participants. However, MET dose was per kilo, so weight should have little influence on the results. Stroke volume may have increased to compensate for the cardiac specific pharmacological intervention and maintain cardiac output, and subsequently the BP.

The BP response remaining unchanged points to stroke volume increasing to keep cardiac output constant. It therefore would have been useful to directly compare these results to the stroke volume and cardiac output responses in this chapter's cohort. It was possible to set the Finapres output to include these measures, calculated indirectly from the peripheral BP measure. However, it is also only possible to record five measures at once and the Finapres results were relegated to the appendix due to problems with the inconsistencies with data variability.

3.16 Response to Hypercapnic Challenge after Pharmacological Interventions

The hypothesis that the pharmacological interventions administered in the study would affect the response to the HC was not supported. This suggests the chosen pharmacological interventions or their dosages do not provide a large enough change in response to the HC to be taken forward to an MRI study.

The Impact of a Hypercapnic Challenge on Mean Arterial Blood Pressure

In this study, there was no change in BP during the hypercapnia condition of the hypercapnic challenge after GTN. However, after MET had been administered between (post-intervention), there was a significant increase in MAP from normo- to hypercapnia condition. Various studies have looked at the response to HCs, whilst measuring different outcomes. Bailliart and colleagues (1993)[17] (N=10 healthy, 32 to 58 years (mean = 38±5), 4F, 6M) compared various gas mixtures, with the 15% O_2, 5% CO_2, 80% N_2 mix the closest to this study. MAP did not significantly increase from a baseline of 89.9±7.1 mmHg to hypercapnia 91.7±8.0 mmHg. Additionally, Starmans-Kool and colleagues (2002)[218] measured carotid BP during a HC of 5% CO_2 with only 15% O_2 in young healthy participants (N=6, 21 years (range 19–23 years), 4M, 2F). SYS and DIA did not change from normo- to hypercapnic condition. Calculated here (using equation 3.1) as a MAP of ∼80.7 mmHg during normocapnia, increasing to ∼81.0 mmHg during hypercapnia. This suggests there were sufficient compensatory mechanisms to maintain BP in healthy participants during a HC, which would explain the lack of change seen in this chapter.

The Impact of a Hypercapnic Challenge Effect on Blood Velocity

In this study, there was no statistically significant change in velocity during the hypercapnic challenge. There was a larger response in the velocity change in the phase contrast velocity (PCV) data during a HC in the previous chapter (18.5% in the ICA (internal carotid arteries) and 21.7% in the vertebral arteries). However, that HC was based on +10 mmHg above the baseline of the individual participant, resulting in a $P_{ET}CO_2$ change of 16.4±4.4% (group mean±std), which may explain the larger change. Another possible reason for this difference between studies may be due to GTN blunting the velocity response to hypercapnia,

whilst MET seems to increase the velocity response to hypercapnia. With a larger number of participants or less variance in the Doppler ultrasound the former (GTN) may still remain non-significant, but the latter (MET) may be more likely to be significant. Additionally, these two studies targeted different blood vessels i.e. internal vs common carotids arteries.

The Starmans-Kool and colleagues (2002)[218] study, mentioned above, measured velocity with B-mode doppler ultrasound at the centre of the right common carotid. With a gas challenge of 5% CO_2 with only 15% O_2 (hypoxia) the peak systolic flow velocity during normocapnia was 104 (90–119) cm/s, which did not change when participants were given a more hypoxic hypercapnia gas mix (101 (74–125) cm/s (mean and range)).

Fortune and colleagues (1992)[83] compared several different gas challenges including normocapnia and hypercapnia (5% CO_2 for 5 minutes) in 20 "normal" participants (neither sex, nor age were given) with Duplex scanning (B-mode & pulsed Doppler shift) higher up the vascular tree at the ICA. Time averaged velocity of ICA blood flow during normocapnia was $\sim$325 ml/min increasing to $\sim$430 ml/min during hypercapnia (approximated from graph results), with a reactivity of 2.3±0.2 %/mmHg, hence they determined duplex was sufficiently sensitive to changes in cerebrovascular response. However, measurements at the ICA do not account for all CBF due to the split into the vertebral system at the common carotid bifurcation. So the results are not directly proportional to common carotid measurements, in addition to the alternative unit measurement method. The same operator performed for all measurements (std of 10.9% of mean), which is generally smaller than measurements from the study presented in this chapter.

Poulin and Robbins, (1996)[191] used doppler ultrasound of the MCA and

various gas challenges in a group of six young, healthy volunteers (20.8±1.7 years (mean±std), sex not given). After inhaling CO_2 to 8.5-9.5 mmHg above individuals normocapnic baseline (targeting an increase of 7.5 mmHg), the right MCA velocity did not change. If the doppler beam is not completely axial, which can result in an error of <13%, velocity measurements may have been underestimated. Additionally, velocity, as a mean velocity, and an index of flow calculated as the total power multiplied by the intensity-weighted mean (IWM) are not directly comparable to results shown in section 3.12.2. N=35 (from repeats of n=6 participants) velocity peak significantly increased from control 57.3±7.6 cm/s to 55.1±7.9 cm/s during hypercapnia ($p<0.05$) and IWM significantly increased from 37.6±6.3 cm/s to 48.3±7.7 cm/s during hypercapnia ($p<0.05$).

Furthermore, Bailliart and colleagues (1993)[17] (N=10 healthy, 32 to 58 years (mean=38±5), 4F, 6M) presented a comparison of ultrasound of both common carotids and MCA measures of blood flow and stated hypercapnia resulted in a 33% increase in carotid BF. They observed a significant increase in the CCA and MCAs, and the common carotid baseline of 290±16 cm^3/min increased to 386±24 cm^3/min ($p<0.001$) during hypercapnia. The simultaneous measurement of MCA velocity baseline 56.2±4.7 cm/s increased to 60.7±5.5 cm/s ($p<0.05$) during hypercapnia. They accounted for inter-operator variability of <7%, and considered changes of >7% to be an actual change. This highlights the importance of considering where in the vascular tree the measurements are taken, along with the method of measurement.

Burley and colleagues (2021)[41] conducted two studies involving breathing 5% CO_2 comparing healthy young and old participants, who were also separated into fit and unfit based on VO_2max (maximum volume of O_2) scores (younger)

or questionnaires (older) (N=18 younger (25±7 years, 7F) and N=12 older (69±4 years, 5F), N=10 young fit adults (22±2 years, 3F), and N=8 older unfit participants (72±4 years, 2F) [41]. Although the baseline measures of CBF for the different modalities (TCD, MCA velocity, PC velocity and flow, perfusion transit time (ASL (arterial spin labelling)) all showed differences between younger and older groups. The CVR measures showed opposing effects of the CO_2 challenge, with TCD showing lower CVR in the younger group, and BOLD and PC showing higher CVR in the younger group. There was also no significant correlation between the TCD or BOLD for CVR measurements. Although the authors noted a similar discrepancy in the literature, the main reasons given were that TCD and BOLD were both indirect measures of CVR and measure different parts of the vascular tree. The different parts of the vascular tree itself can vary in their reactivity to a CO_2 challenge depending on the vessel type. Additionally, there was no correlation between the TCD and PC measures, which may be partly down to methodological differences, given that TCD measures cannot account for changes in vessel diameter during the challenge. Interestingly, there was no difference in CVR measures when comparing fitness levels for either the younger or older groups.

The underlying assumptions about the cerebrovascular bed are important for understanding these different measurements. Piechnik and colleagues (2008)[184] compared different models of the vasculature, and showed different diameters can indeed play an important role in the perceived velocity-flow relationship. By comparing three different models of increasing complexity (a uniform reactive tube model through to a 19 compartments model of varying sizes and reactivities) the microvascular components were shown to play a major role in the overall reactivity of the vascular system, as this is where a substantial volume of the blood is and has higher reactivity than the larger arteries. These results should

be taken in to consideration when comparing the results from this chapter to those acquired at the MCA, and the PC results from the previous chapter.

Hypercapnic Challenge Effect on Heart Rate

Lastly, in this study, the HR slightly increased during the hypercapnia condition of the hypercapnic challenge. Additionally, after MET was administered the post-intervention HR significantly increased from normo- to hypercapnia. Bailliart and colleagues (1993)[17], mentioned above, also found no significant difference in the HR from baseline (72 BPM) to hypercapnia (75 BPM). Starmans-Kool and colleagues (2002)[218], already mentioned, showed no change in HR from normocapnia (70 BPM) to hyperoxic hypercapnia (73 BPM). Note, gas was delivered at 10 L/min vs. the 15 L/min in this study, but still similar to the results shown in this chapter.

3.16.1 Limitations

Blood Pressure Measurements

Although the Dinamap results are presented here, both Finapres and Dinamap measurements of BP were collected. Dinamap was ultimately chosen as the data were less variable and had more consistent baseline results, with smaller IQRs than the Finapres data.

In principle, Finapres is a method that can measure continuous peripheral BP. Silke & McAuley (1998)[210] showed that with calibration at the brachial cuff to a MAP bias of 2.1±8.6 mmHg (mean±std) and precision of 7.6±5.3mmHg (mean±std). However, the Finapres uses a complicated proprietary algorithm that requires several assumptions to be met for reliable results. Schäfer & Vagedes (2013)[203] showed position, specifically movement, standing and

sitting upright, is a particular problem for Finapres measurements. Carrasco and colleagues (1998) showed there is also evidenced of a disagreement between the Finapres and electrocardiography (ECG) (gold standard) HR variability (HRV) and HR values by 12-17% [48]. Participants in the study remained supine, which may have alleviated some of this error, even with a task that increases breathing movement. Another reason there may have been a discrepancy between the Dinamap and Finapres results may be due to Finapres' reliance on Infrared Photoplethysmography (IR-PPG), which has been shown to be less optimal than other methods ([25, 77]). Although these concerns were mainly in clinical groups [76], the overestimation of this methodology may be sub-optimal, even for research purposes.

Furthermore, the Finapres is not accredited for clinical use on the Dable educational trust [114, 71, 205], as the validation by Silke and McAuley (1998) [210] was insufficient for accreditation . In contrast, the Dinamap is considered reliable enough to be accredited by the AAMI and British Hypertension Society [63]. Overall, the trends of the data for the Finapres generally matched those of the Dinamap and are available in the appendix (section C.3).

Participants Physical Characteristics and Sample Size

A practical limitation of the study was the large number of participants (18) withdrawn to achieve the sample size of 10. Several participants were withdrawn due to a BP and/or a HR below the cut off of 100 mmHg SYS and 50 BPM. These cut offs were based on the clinical modified early warning signs (MEWS) of SYS 101–199 mmHg and HR 51–100 BPM [219]. This suggests the 100 mmHg SYS cut off may have been overly conservative for this demographic of young, healthy, fasted and rested participants. Several participants were excluded due to BMI, as fat distribution may contribute to metabolism and subsequently

affect drug metabolism. Unfortunately, growing evidence since the 1970s, including by Keys (1972)[127], suggests BMI (developed by Quetelet (1835)[197]) does not measure the fat percentage or distribution of fat that it is meant to be a surrogate). BMI is known to be especially unreliable across age, racial groups and sexes [3, 89, 243]. Considering participants were recruited from a narrow age range, age is unlikely to be too much of a factor. An alternative option would have been Dual X-ray absorptiometry (DXA) to determine adiposity, but this would have involved a risk from the radiation. Recording participants level of regular exercise may have been more beneficial for assessing fitness.

Single Sex Sample

Only female participants completed both study days. Eugene, (2016)[74] suggested a 50 mg dose of MET in women was similar to 100 mg dose in men. However, this inference was determined graphically from a figure rather than from raw data, and was derived from a tiny sample (Eugene, 2016a [73] using Lundborg & Steen, 1976[142] (N=12, 6=F)). Specifically, this cohort included chronically-ill geriatric in-patients with multiple co-morbidities, other medications, and variable metoprolol doses. Lundborg & Steen, (1976)[142] themselves stated these data would not even have been representative of a geriatric population, so inference to a young healthy female sample would be misplaced. There were individual differences (based on elimination of the drug rates) and more pronounced inter-individual differences in plasma levels across the group overall. Though, the varied plasma levels were deemed to be non-sex related. In relation to this study, the effect inter-/individual absorption rate differences on the intervention's peak time would be of greater concern, in relation to timing the post-intervention HC, as it would have been more likely to cause variability in the results than sex, especially if the peak time was missed.

Use of a Placebo and Double Blind Trials

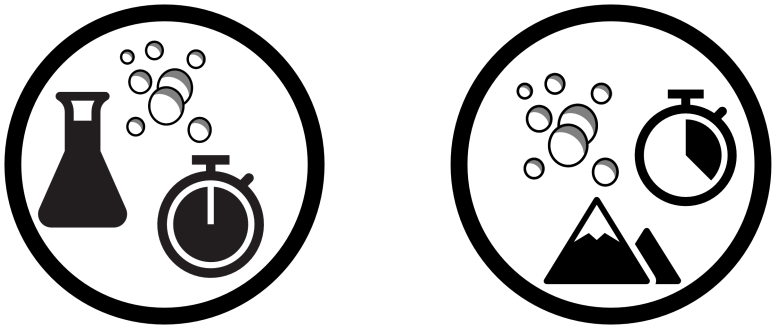
This study used a randomised, but unblinded, administration of GTN and MET. Firstly, the different administration methods (sublingual vs. swallowed with water) would have made unblinding likely. An alternative method of administration, such as IV, would have removed some concerns with unblinding, peak timing and dosage per kg. However, the study was initially planned to be entirely non-invasive. Secondly, this study did not have a placebo condition. Flushing of the face, headaches, etc., due to GTN may still have unblinded the intervention. The original study design intended to include three arms (including LBNP), and adding a fourth placebo arm was a concern for participant retention. Nevertheless, the placebo randomised controlled trial would be the gold standard and more optimal in future studies.

3.16.2 Conclusions

Overall, the young, healthy participants' response to GTN and MET pharmacological interventions and a HC were small. The increase in HR after GTN and a decrease in HR after MET were expected due to the pharmacological mechanisms of the two drugs. This was the most notable observation, and most likely a compensatory mechanism to maintain BP. This may also explain why the results did not correspond well with the chapter's other hypotheses. During the MET Post-intervention challenge the HR and BP increased from normo- to hypercapnia. However, there was no observed difference in the response to the HC when comparing Δ pre- to post-intervention hypercapnia responses for either GTN or MET. The ability to detect changes may have been limited by the sensitivity of the measurements and because the interventions/HC did not exceed the limits of healthy autoregulation. Ultrasound in this chapter had a high standard deviation and was particularly noisy. If it had been possible to

reduce the variance of the measurements, and therefore the standard deviation, it would be more likely to be significant. The theoretical / practical implications of these results suggest that little insight would be gained from performing this study in the MRI in its current format.

4 Implementation of Advanced CVR methods



4.1 Contributions to the Chapter

Colette Milbourn was involved in all stages of the study; the study design, ethics approval, study set-up, participant recruitment, participant screening, MR scanner operator and gas delivery, data collection, writing the preprocessing/processing scripts for data analysis and presentation, manuscript writing/editing.

Dr Nicholas Blockley provided support as the main supervisor, with the design and setup of the study, data analysis, and revisions to the manuscript.

Dr Sebastian Rieger from the Department of Psychiatry, University of Oxford, provided the design for the gas delivery box and the software to drive the system, which was based on an Arduino microcontroller running a custom script.

Stuart Salter assembled the gas delivery box.

Dr Logan Zhang provided an introduction to the multiple post labelling delay (MPLD) pulse sequence on the GE scanner and provided advice on running BASIL in BASH for the eASL section.

Thanks to the Globalink exchange programme funding that made it possible to spend three months with Prof. Jean Chen as a host supervisor in Toronto.

Thanks to Prof. Jean Chen who hosted the knowledge exchange programme at Baycrest Hospital/Rotman Research Institute/ University of Toronto, (Toronto, Canada) and the rest of the Cranium lab who helped with learning about dCVR.

Prof. Jean Chen also helped with setting up the dCVR pipeline, the basis of the dCVR data analysis pipeline i.e. the spherical Laguerre estimation script, originally written by Dr Seyedmohammad Shams.

Jan Paul and Andrew Cooper supported the MR scan sessions.

Dr Martin Craig provided support with troubleshooting the high performance computing cluster software and sbatch scripts.

4.2 Visual Abstract

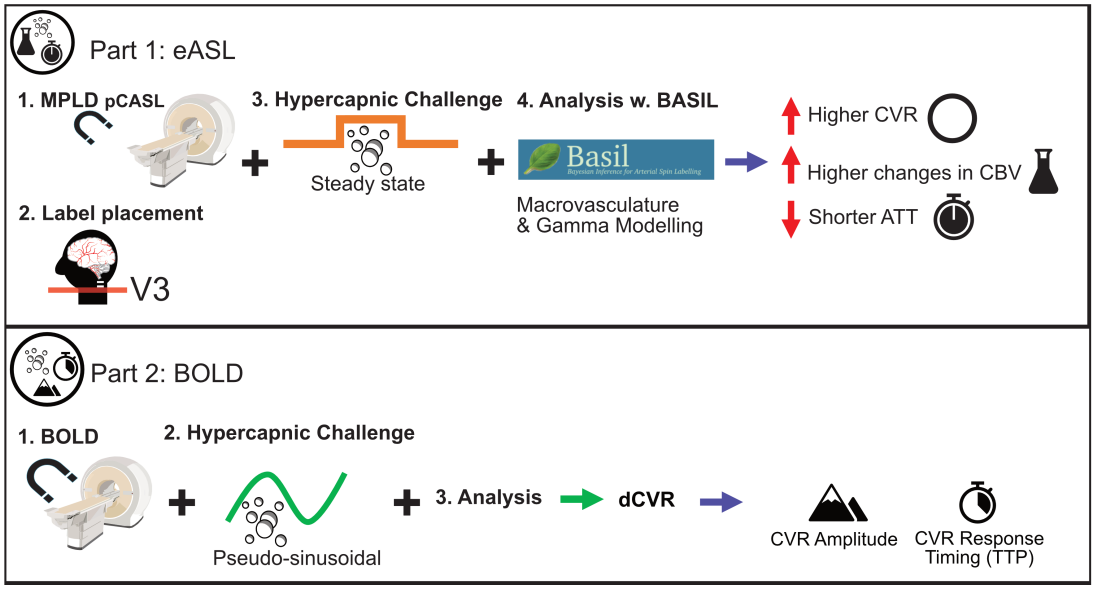


FIGURE 4.1: **Visual Abstract for Chapter 4** Part 1 combined an enhanced pseudocontinuous arterial spin labelling (eASL) multiple post labelling delay (MPLD) sequence with placement of the labelling plane at the V3 segment of the vertebral arteries, a steady state hypercapnic challenge, and a more advanced Bayesian analysis toolbox Bayesian Inference for Arterial Spin Labelling (BASIL). The resulting cerebrovascular reactivity (CVR) and cerebral blood volume (CBV) was higher than in previous studies and the arterial transit time (ATT) was shorter. Part 2 combined a blood oxygen level dependent (BOLD) sequence with a pseudo-sinusoidal hypercapnic challenge and a novel dynamically modelled BOLD analysis method (dCVR), to give measures of CVR amplitude and timing response (time to peak (TTP)).

4.3 Introduction

This chapter is comprised of two sections: the first using multiple post labelling delay (MPLD) pseudocontinuous arterial spin labelling (pCASL) and the second using blood oxygenation level dependent (BOLD) contrast. These datasets were acquired within the same scanning session in young, healthy adults. Both ASL and BOLD were performed with a hypercapnic challenge. The results for the ASL and BOLD datasets are presented separately in this chapter, and are compared directly in the next chapter.

First, this study used an unbalanced, MPLD pCASL magnetic resonance imaging (MRI) sequence. This provides the ability to measure arterial transit time (ATT) and arterial cerebral blood volume (aCBV). It also reduces the sensitivity of cerebral blood flow (CBF) estimates to changes in ATT, or the presence of arterial signal [259]) compared to single post labelling delay (PLD) pCASL. As in chapter 2 part 1, vasodilation was induced via a steady state hypercapnia challenge (high carbon dioxide, (CO_2)) rather than a dynamic gas challenge, as the latter is impractical for MPLD [68] As explored in chapter 2 part 2, the labelling plane was placed at the V3 vertebrae where the main cerebral arteries are most parallel to one another. Here, B_0 and B_1 inhomogeneity is reduced [42]. Bayesian Inference Analysis was used to incorporate an arterial macrovascular component [52, 256] and gamma dispersion modelling [53, 237] to better fit the physiology.

The second part of this study involved analysing multiband BOLD functional MRI (fMRI) with dynamically modelled CVR (dCVR)[206]. This was estimated by using the CO_2-response function with a Basis expansion method with spherical Laguerre basis (BEL) based approach [193]. This involved deconvolving the pseudo-sinusoidal hypercapnic gas challenge time course from the simultaneously

acquired BOLD data. The results demonstrate the feasibility of quantitatively extracting the dCVR amplitude and rise time from BOLD data. This is an advantage over more traditional methods, as it provides a quantitive timing metric.

Recent methodological developments have focused on improving the accuracy of CVR quantification. The longer term goal was to ensure advanced pCASL and BOLD CVR techniques were more practical for clinical use, especially when assessing patients with cerebrovascular disease.

4.3.1 ASL

Multiple Post Labelling Delay ASL

In chapter 2, part 1 and 2 used a single PLD pCASL sequence. This study used a MPLD pCASL sequence in order to measure changes in arterial transit time and arterial cerebral blood volume [228, 242]. This sequence is able to track the bolus at multiple time points as it passes through the tissue and was mentioned in the introduction in Figure 1.20.

This study will focus on the MPLD "enhanced" pCASL technique provided by GE Healthcare which has 7 MPLDs, and was available on the GE MRI scanner at the University of Nottingham Medical school in the Sir Peter Mansfield Imaging Centre (SPMIC) [256]. The GE eASL pCASL sequence is a 'time-encoded' (also known as Hadamard encoded) MPLD technique, which allows it to be more time efficient than other methods [244].
Each 'sub-bolus' has its own unique short labelling and post labelling delays, which results in a mix of signals for each image. These images are then 'decoded' after acquisition. With this sequence it is possible to see the spatial flow of

blood through the brain tissue over time. Figure 4.2 shows how the the 'bolus' appears brighter over time as it is delivered to the brain tissue.

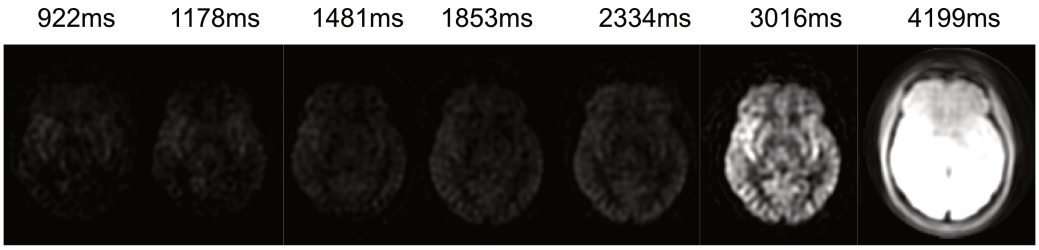


FIGURE 4.2: **Example of seven MPLD eASL at one example slice** The output from the GE eASL sequence shows the pre-subtracted control/label image. At each PLD the bolus appears 'brighter' during the hypercapnic condition. ms (milliseconds).

Furthermore, decreasing the sensitivity of CBF measurements to changes in ATT would be more reliable in clinical conditions, where the CVR response can be less uniform and more varied in the timing dynamics. As mentioned previously, ATT increases in older adults. Choi and colleagues (2017) used a 7 MPLD eASL sequence in older adults with cerebrovascular disease (CVD) and found it to be more diagnostically effective than a single PLD [57]. One advantage of MPLD over single PLD was that the PLD was longer than the ATT, whereas a single PLD would miss the intricacies of the blood flow changes and result in CVR estimation errors. Another advantage of MPLD is that the sequence can be a acquired in a similar time to that of a single PLD sequence and still provide more reliable information [7]. However, one major disadvantage of MPLD, compared to single PLD, is the complex analysis required, which will be discussed further in section 4.13.2.

Labelling Plane Placement

Another acquisition parameter (from chapter 2) that was taken into consideration was the labelling plane placement, in order to reduce error caused by off-resonance effects. Previous publications [263] have found a reasonable reduction in off-resonance effects and pulsatile velocity depending on the labelling placement. The results shown in Chapter 2 Part 2 found placement can indeed make a difference. Hence, it was important to reduce any extra noise or errors where possible in the methods of this chapter. Therefore, the labelling plane was placed at the V3 segment of the VAs,where the main cerebral arteries are most parallel, rather than at 90 mm below the anterior commissure - posterior commissure line (AC-PC).

Hypercapnic Challenge

Chapter 2 part 1 (2.7.2) showed that a steady state hypercapnic challenge delivered as a block challenge for 3 minutes was sufficient to maintain a hypercapnic condition. This was used again in this chapter, in order to induce vasodilation and an increase in blood flow in the brain tissue. A steady state rather than a dynamic hypercapnic challenge was also used to complement the introduction of the MPLD, as the blood flow would need to be consistent across each of the PLDs. An additional reason for choosing a steady state challenge was to test out the new semi-automated gas delivery box (see section 4.9) that was built to replace the RespirAct^{TM}, which was no longer functional after January 2022. Another benefit of the new delivery box was the affordability, costing a few hundred pounds, as it was not financially possible to buy a RespirAct^{TM} Gen 4 at the time. A gas analyser was still required to measure the gas in/expired by the participants at a cost of £10,000, but this was still more affordable than a new RespirAct^{TM} at a cost of circa £50,000-£100,000. Manual switching between gas canisters was a potential option (as used in chapter 3). However, another advantage of the gas delivery box was that it can switch between two (or three) flow meters (one for normocapnia and one for hypercapnia etc.) more immediately to pre-set levels i.e., to 15 L/min. This allows for a quicker change between the two conditions of the hypercapnic challenge (HC) than a manual change to adjust two separate flow meters. Additionally, the timings for the HC paradigm could be pre-set, which would also reduce human error in the gas delivery timings. If the MR vendor provides a trigger box, the start of the HC paradigm can also be started via a trigger from the MRI at the start of the MRI sequence.

The sequential gas delivery (SGD) masks left over from the previous chapter 2 were not easily adaptable to the new gas delivery box set up. Additionally,

the control over the flow rate would not be as good if used with this set up. A similar gas mask delivery set up to chapter 3 was used [221]. One difference was that an extra reservoir was added instead of the rebreathe bag to force expired air out of the mask and into the room. This also provided a fail-safe with the ability to breathe room air if required. The use of single use disposable plastic components that are more widely available than the SGD masks would also reduced the cost of the kit, and make it more accessible and customisable.

Bayesian Inference Analysis

As previously mentioned, one disadvantage of using a MPLD ASL sequence is that it requires more complex analytical methods to process the information and fully take advantage of the additional sensitivity to haemodynamic parameters i.e. ATT and aCBV. Whereas the total CBV is the sum of the blood volume in the arterial, capillary and venous vessels, aCBV is specifically only the arterial CBV. This is a useful measure when investigating CVR. Bayesian Inference for Arterial Spin Labelling (BASIL) (FMRIB Software Library, Oxford, UK) was chosen as it is a free, open-source toolbox that provides both a graphical user interface (GUI) and command line option for MPLD ASL analysis. A comprehensive publication about the toolbox has since been published, which also verified many of the analysis steps that were used in this chapter (for further details see Chappel and colleagues (2023) [51]).

The Bayesian aspect of the toolbox allows for Bayesian inference using a non-linear model [50]. The toolbox uses multiple steps for estimating the distribution of the data (i.e. updates the output estimates as it incorporates an increasingly more complex level of modelling). Priors from the literature can be used as default, or the priors can be over written by the reality of the actual dataset being analysed.

In the first step, perfusion and ATT are inferred, but other parameters are kept fixed. When using MPLD ASL data, BASIL is able to provide the arterial CBV as an output [51]. In the next step, using the CBF and ATT, the macrovascular correction is performed and aCBV is estimated. Then, using the parameters from the previous step, the label duration is corrected (especially if pulsed ASL (PASL)) is used). Next, advanced kinetics are used to estimate the dispersion parameters and correct for the more complex blood-tissue water exchange aspects of the modelling. The dispersion model is important for modelling the flow of the bolus and ensuring that the calculations are also within physiologically realistic limits. The T_1 prior of blood is added in the next step for T_1 correction. Then spatial priors are applied to the perfusion estimate, followed by using spatial regularisation to apply these priors to grey matter (GM) perfusion estimates. The spatial priors are iterative (i.e. the only ones that change from those input at the start of the process) and are based on an average of the neighbouring voxels [51].

Another important aspect of the BASIL tool is the way that it uses results from each of the previous steps to start the next step. This helps the overall estimates of the output parameters to build up complexity gradually whilst remaining robust. The outputs include; calibrated perfusion maps (a CBF flow map in absolute units of ml/100 g/min) that can be partial volume corrected, a grey matter mask, a whole brain mask, ATT maps (absolute value estimated in seconds), the arterial CBV map (estimated aCBV from the macrovascular component, in percentage).

Additionally, the macrovascular contamination as the arterial CBV estimates [52, 183, 256] have recently been compared with and without the gamma dispersion kinetic modelling [53, 188]. BASIL has also been assessed by the open science initiative for perfusion imaging (OSIPI) single PLD ASL analysis challenge and

was found to be favourable in the subsequent results published in Paschoal and colleagues (2024) [178].

4.3.2 BOLD

Multiband BOLD

As well as more advanced pCASL sequences, this chapter also used advanced BOLD sequences. With more modern multi-coil receiver arrays, an MRI scanner can acquire multiple slices simultaneously using multiband [58] (See Fig. 4.3). A single radiofrequency (RF) pulse is used to simultaneously excite multiple slices along the z-axis of the brain at the same time (known as the multiband factor). The signal received is a mixture of all of the simultaneously excited slices. The spatial sensitivity of the coil is used to separate out these slices using parallel imaging techniques like SENSitivity Encoding (SENSE) and Generalized Autocalibrating Partially Parallel Acquisitions (GRAPPA) [194, 103]. The BOLD dataset in this chapter was acquired with a multiband factor of 3 using GE's 'hyperband' method [189]. As a multiband sequence can be used to decrease the total acquisition time or increase the temporal resolution of data acquisition, it is possible to increase resolution or the amount of whole brain coverage. This can be beneficial for HC [199, 200]. The use of this form of sequence, with a shorter scan time, would also be beneficial for clinical use, despite being more complex. One major disadvantage of multiband BOLD is that increasing the number of simultaneous slices requires a higher RF power and subsequently increases the specific absorption rate (SAR).

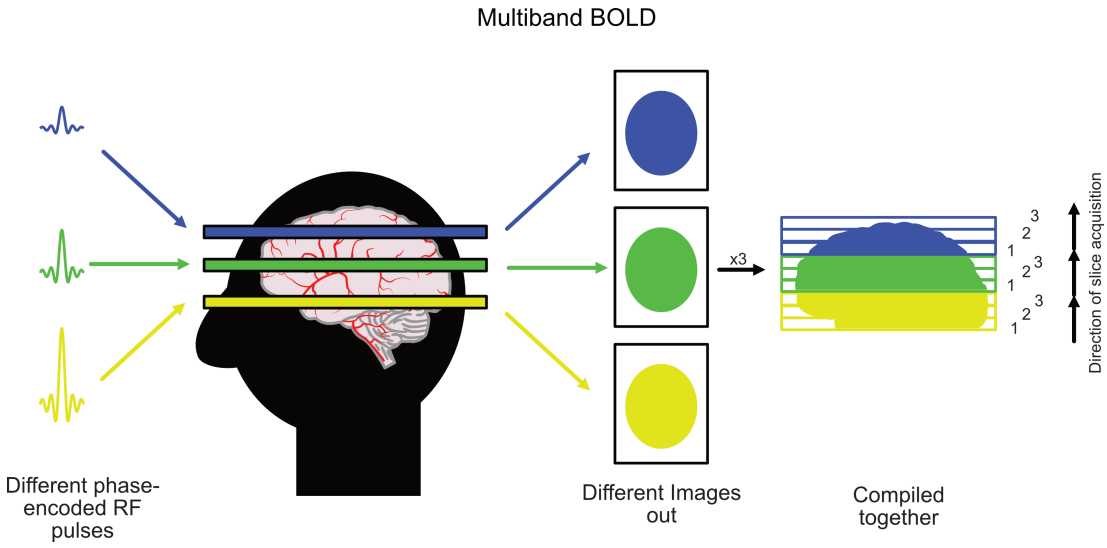


FIGURE 4.3: **Conceptual diagram of multiband BOLD imaging.** To create a multiband pulse a single slice pulse and frequency shift is used to excite a signal at the locations of interest. For example, by adding the pulses together to create a composite pulse it is possible to excite the other two brain slices along the z-axis. This is repeated, and the output images are compiled together to make the complete image. In this example the first slices are taken at the most inferior base of the brain and the subsequent slices are taken in the superior direction until the whole brain has been covered. When the signal is acquired by the scanner, all of the slices are combined together. The scanner then uses the spatial sensitivity of the coil (particularly in the z direction) to separate out the slices. BOLD (blood oxygen level dependent), RF (radio-frequency).

BOLD CVR analysis

Unlike pCASL, traditional methods of BOLD analysis for investigating CVR are not quantitative. Deconvolving the HRF to calculate the task design stimulus (mentioned in Chapter 1, Eqn 1.25), can be modelled with more complex, non-linear methods. In fact, manipulation of inspired CO_2 coupled with BOLD fMRI measurements have long been used for mapping the amplitude of CVR [97, 99, 54]. Additionally, the sensitivity of CVR amplitude to age and related effects can be limited [112]. However, other analytical methods have been developed to map BOLD CVR more quantitatively [98]. Recently, it has also become of interest to map dynamic CVR (dCVR), that is, the response timing (a quantitive measure) in addition to the amplitude of CVR (a qualitative measures) [41, 190, 192].

More specifically, the dCVR analysis method attempts to extract additional timing parameters of the HRF response to CO_2 such as time to peak (TTP) and the full width half maximum (FWHM) of the response function (Fig. 4.4). These parameters are of particular interest in relation to a comparison with eASL CVR outputs. TTP is the time it takes for the response function to reach the most positive peak of the response curve. The FWHM is the width of the response function measured at half the maximum peak (and also relates to dispersion effects). Lastly, CVR is the area under the curve of the response function, which corresponds to the BOLD response to the partial pressure of end-tidal CO_2 ($P_{ET}CO_2$). This chapter used a hypercapnic challenge to induce the CVR response as this has previously been shown to be effective in the previous chapters of this thesis. Hypercapnia has also been used for evaluating more complex response patterns than the traditional simple linear models [82].

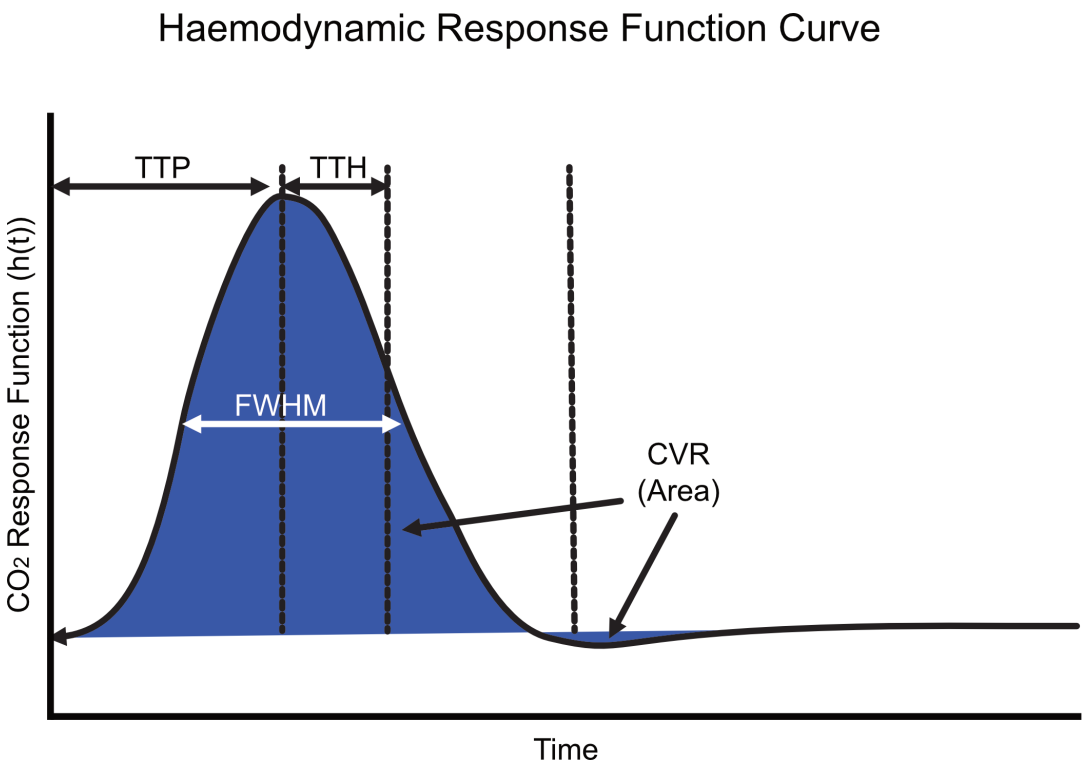


FIGURE 4.4: **Graphical explanation of the dCVR output parameters.** Haemodynamic response function curve in response to a CO_2 challenge i.e. hypercapnia. CO_2 (carbon dioxide), dCVR (dynamically modelled BOLD), TTP (time-to-peak), TTH (time-to-half-maximum), FWHM (full-width at half-maximum, area (the area of h(t), equivalent to the CVR amplitude).

4.3.3 dCVR Analysis

This chapter used an advanced method of data analysis called dCVR to deconvolve the HRF and associated CVR metrics of response magnitude and timing. Most methods of dCVR analysis are based on finding the best linear combinations of two sets of multidimensional variables. In the case of CVR, this would be the BOLD data and PETCO$_2$ data. To demonstrate the feasibility of this dCVR method, this chapter specifically used a novel Basis Expansion method called basis estimation using the spherical Laguerre model (BEL). This process applies signal processing to CVR analysis. BEL uses the spherical Laguerre model as a set of parameters on which to base the starting point of the CVR analysis [148]. A concept diagram with example PETCO$_2$ data is shown in the methods Figure 4.12.

An advantage of using the spherical Laguerre model is that it naturally captures the smooth, delayed response characteristic of BOLD signals and has only a few coefficients. One of the underlying principles of the BEL modelling method is the use of a kernel-based activation function. This means that the model is non-parametric, and that the model has trainable/modifiable parameters (also called a basis set) [202]. BEL estimates the dCVR based on the expansion of this set of parameters. BEL has previously been used for non-linear models of the expansion of the kernels, other physiological models ([60]), and more recently was proposed for analysing CVR [192].

In this chapter, the BEL basis set modelled dCVR using an impulse response h(t). An impulse response is the reaction of a dynamic system in response to some external change. In this method the h(t) is the HRF, which changes in response to CO_2. In this model h(t) starts at zero and decays exponentially

[133, 193]. This is used to estimate the coefficients of the basis function and the expansion of the basis sets. This is done via small changes (i.e. iterations) of each parameter of the basis function to iteratively move the 'estimate' closer to the 'ground truth'. This makes it possible to extract voxelwise results, and therefore regional variation to demonstrate CVR-related differences across the brain.

The BEL model used in this chapter was based on work by Prokopiou (2019) [192], who used non-linear (Volterra kernel) models to analyse dynamic CO_2 reactivity with a discrete time Volterra Model (DVM), of which the Q-th order non-linear system is shown in Eqn. 4.1:

$$y(n) = \sum_{q=0}^{Q} \sum_{m_1} \sum_{...} \sum_{m_q} k_q(m_1, ..., m_q) x(n - m_1)...x(n - m_q), \tag{4.1}$$

where $y(n)$ is the %BOLD change (the output) and $x(n)$ is the $P_{ET}CO_2$ change (the output) at system time n. $k_q(m_1, ..., m_q)$ is the q-th order Volterra kernel of the system, and Q is the model order.

The Volterra kernels were estimated from the data using a functional expansion technique in terms of an orthonormal basis set [148] based on Eqn. 4.2:

$$k_q(m_1, ..., m_q) = \sum_{j_1=0}^{L} \cdots \sum_{j_q=j_{q-1}}^{L} c_{j_1...j_q} b_{j_1}(m_1)...b_{j_q}(m_q), \tag{4.2}$$

where $\{b_j(m) : j = 0, ..., L; m = 0, ..., M\}$ is a set of $L + 1$ orthonormal basis functions, c_j is the unknown expansion coefficient of the j-th order basis function, and M the memory of the system.

The two equations of the DVM (4.1 & 4.2) are then re-formatted in a compact matrix form as Eqn. 4.3:

$$\mathbf{y} = \mathbf{V}\mathbf{c} + \epsilon \tag{4.3}$$

where $\mathbf{V}$ is a matrix of the convolved input ($P_{ET}CO_2$ change) and basis functions values, and ϵ is the residual errors. The vector $\mathbf{c}$ is the unknown expansion coefficients, which can be estimated using ordinary least squares (shown in chapter 1, section 1.8.2) and presented here as Eqn 4.4:

$$\hat{\mathbf{c}}_{\text{LSE}} = [\mathbf{V}^T\mathbf{V}]^{-1}\mathbf{V}^T\mathbf{y}. \tag{4.4}$$

Eqn. 4.5 shows the j-th order discrete time Laguerre function, within the range given for the Laguerre (L) functions parameters ($2 < L < 6$), and alpha (the exponential rate of decline of L) ($0 < \alpha < 0.6$). This was used to prevent over fitting due to low SNR, and potential confounds from breathing rate at resting state using the following:

$$b_j(m) = \alpha^{\frac{m-j}{2}}(1-\alpha)^{\frac{1}{2}}\sum_{k=0}^{j}(-1)^k\binom{m}{k}\binom{j}{k}\alpha^{j-k}(1-\alpha)^k \tag{4.5}$$

where is the basis set parameter α ($0 < \alpha < 1$) determines the rate of exponential decline of these functions. K is the context of the basis expansion. This means that larger values correspond to a slower decay.

Shams and colleagues (2023)[206] showed that modelling CO_2 during task and resting state BOLD with BEL was the most effective of six different dCVR

modelling methods. This included a comparison to Basis expansion using a gamma basis set (BEG) and optimised canonical correlation algorithm (CCA), which use a gamma model. Shams and colleagues (2023) [206] then developed this Laguerre spherical basis function equation into:

$$b_j(n) = \sqrt{\frac{j!}{(j+2)!}} \frac{e^{\frac{n}{2\alpha}}}{\sqrt{\alpha^3}} K_j\left(\frac{n}{\alpha}\right) \tag{4.6}$$

where the basis expansion K is set as:

-
- j = 1, and is the impulse response index
- l is the ordinary least squares for range (0 ... L^{-}1)
- α basis set is set is the2, 4
- L basis set is the0.5, 1

... and this is then rearranged into the associated Laguerre polynomial equation as:

$$K_j(n) = \sum_{r=0}^{1} \binom{1+2}{1-r} \frac{(-n)^r}{r!} \tag{4.7}$$

Overall, HRF modelling has conventionally been challenging due to the noise sensitivity of the deconvolution process [16]. Therefore, the ability to use more complex models to provide a quantitative output from, the traditionally qualitative, BOLD CVR still needs to be proven to be feasible.

4.4 Aims of the study

This chapter was primarily an exploratory study so the aims were based around implementing and developing methods and comparing them to similar results of existing studies.

Part 1: ASL

This section aimed to implement more complex pCASL techniques and compare them to existing studies like Pinto and colleagues (2023) [188]. The first aim was to use an unbalanced MPLD pCASL sequence, with the labelling plane placed perpendicular to the V3 segment of the vertebral arteries (VA) to produce/replicate comparable CVR results. A second aim was to use the BASIL toolbox with more complex modelling of the CVR response to a hypercapnic challenge. Hence:

1. MPLD would provide additional CVR metrics; aCBV and ATT.
2. The labelling plane position at the V3 would reduce B_1 error.
3. The gas delivery box would deliver a steady state CVR challenge, that would be consistent across the PLDs.
4. Better modelling than chapter 2, by using BASIL would provide more CVR metrics i.e. ATT and aCBV.

Part 2: BOLD

One aim for the BOLD section of this chapter was to implement BEL dCVR analysis to an *in vivo*, hypercapnic task-based dataset. Hence:

1. dCVR analysis with BEL would provide timing dynamics of the blood flow such as TTP, which would be comparable to the previous use of CCA dCVR.
2. Test different hypercapnic challenge paradigms with the new semi-automated gas delivery box.

3. The gas delivery box would deliver a pseudo-sinusoidal gas challenge of 1 min on / 1 min off to be similar to the Milbourn, Shams and Chen (2023) [155] results and would induce an increase in dCVR amplitude and change in the TTP.

4.5 Methods

4.6 Participants

Written informed consent was obtained from healthy volunteers following local ethics committee approval; Faculty of Medicine and Health Sciences: 288-1904. Exclusion criteria included; smoking, pregnancy and contraindications to either MRI or the hypercapnia challenge i.e. chronic obstructive pulmonary disease (COPD), does not have adequate understanding of verbal and written information in English sufficient to complete an MRI safety screening and an incomplete dataset (see in/exclusion criteria and screening form in appendix B.1). All datasets presented in this chapter are of young, healthy volunteers (self-reported). N=16 completed the study day (8M, 8F, 23.3±3.1 years) see Table 4.1, of these N=11, 4M/7F, 23.5±3.3 years, 75.1±15.6 kg .70±0.10 m datasets are included in the results section. Screening included; a review of the participant information sheet, a checklist of inclusion/exclusion criteria, a signed consent form, height and weight measurements, a completed MR safety screening form and a tattoo form, if applicable.

TABLE 4.1: **Participant Characteristics** Table of participants characteristics recruited. kg (kilograms), m (metres), F (female), M2F (assigned male at birth, using gender affirming medication for female), M (male), PCV (phase contrast velocity), std (standard deviation).

Participant Number	Age (years)	Sex	Weight (kg)	Height (m)	Notes
1	27	M	67	1.64	No PCV, only 1 BOLD run
2	28	M	80	1.75	Technical error with gas delivery, No PCV, only 1 BOLD
3	20	M	89	1.91	No PCV, only 1 BOLD run
4	21	M	72	1.78	Technical error
5	21	M	85	1.77	
6	23	F	53	1.65	
7	23	F	103	1.63	
8	27	F	70	1.55	
9	28	F	83	1.77	
10	23	M	68	1.73	Incidental Finding
11	19	M	51	1.75	
12	21	F	72	1.67	
13	29	F	72	1.58	
14	23	M	84	1.69	
15	22	F	55	1.61	Technical error for MR data
16	25	F (M2F)	65	1.74	
Mean±std	23.8±3.2	8M/8F	73.1±13.9	1.70±9.1	

4.7 Data Collection

4.8 Respiratory Stimulus

As in Chapter 2, the participant's expired CO_2 was measured using a Gas Analyser. An ADInstruments® Gas Analyser (Product Code ML206) and Powerlab (26 Series with a 6-channel input) were connected to a 2016 Macintosh MacBook Pro (Apple, Cupertino, USA) with LabChart®V8.1.24 (ADInstruments, Dunedin, NZ). This equipment is shown in more detail in figure 4.5. A custom Labchart™ template was used to record continuous O_2 (oxygen) and CO_2, measurements. These were recorded as the percentage content of the gas and later converted to $PETO_2$ (end-tidal partial pressure of O_2) and $PETCO_2$ in mmHg.

4.9 Gases, Gas Analyser and Gas Delivery Box

Figure 4.5 shows the home-built, semi-automated gas delivery system administered two hypercapnic challenges using premixed gas cylinders: medical air (normocapnia: 21% O_2, 79% N_2) and a hypercapnic gas mix (5% CO_2, 21% O_2, 74% N_2). The gas cylinders were connected via medical gas regulators with gas hoses that screwed into the back of the gas delivery box. An Arduino-based electronic control box was used to control three solenoid valves using a script that allowed the gases to either be turned on or off via a button manually, or using a pre-programmed paradigm. The electronic box was connected to the scanner trigger output via a coaxial cable to enable the paradigm to be automatically triggered by the scanner. Medical flow meters at the front of the box were attached with two shorter pieces of gas tubing to a Y-piece, followed by a single tube that was fed through the MR wave guide to the breathing mask. This can be seen

in more detail in the photos in Fig. 4.5 and the conceptual diagram in Fig. 4.6. The breathing circuit was assembled from single use, disposable plastic components (Intersurgical and Cole-Palmer) as shown in Fig. 4.7, based on [221], with a line in from the gas delivery box and a line out to the gas analyser for gas analysis. Additionally, following the line in, four 2 m pieces of open-ended tubing were connected in parallel. This provided a gas reservoir to deal with peaks of high flow during inspiration whilst allowing the participant to breathe room air when the gases were not running. This tubing was connected via a breathing filter to enable reuse whilst maintaining infection control.

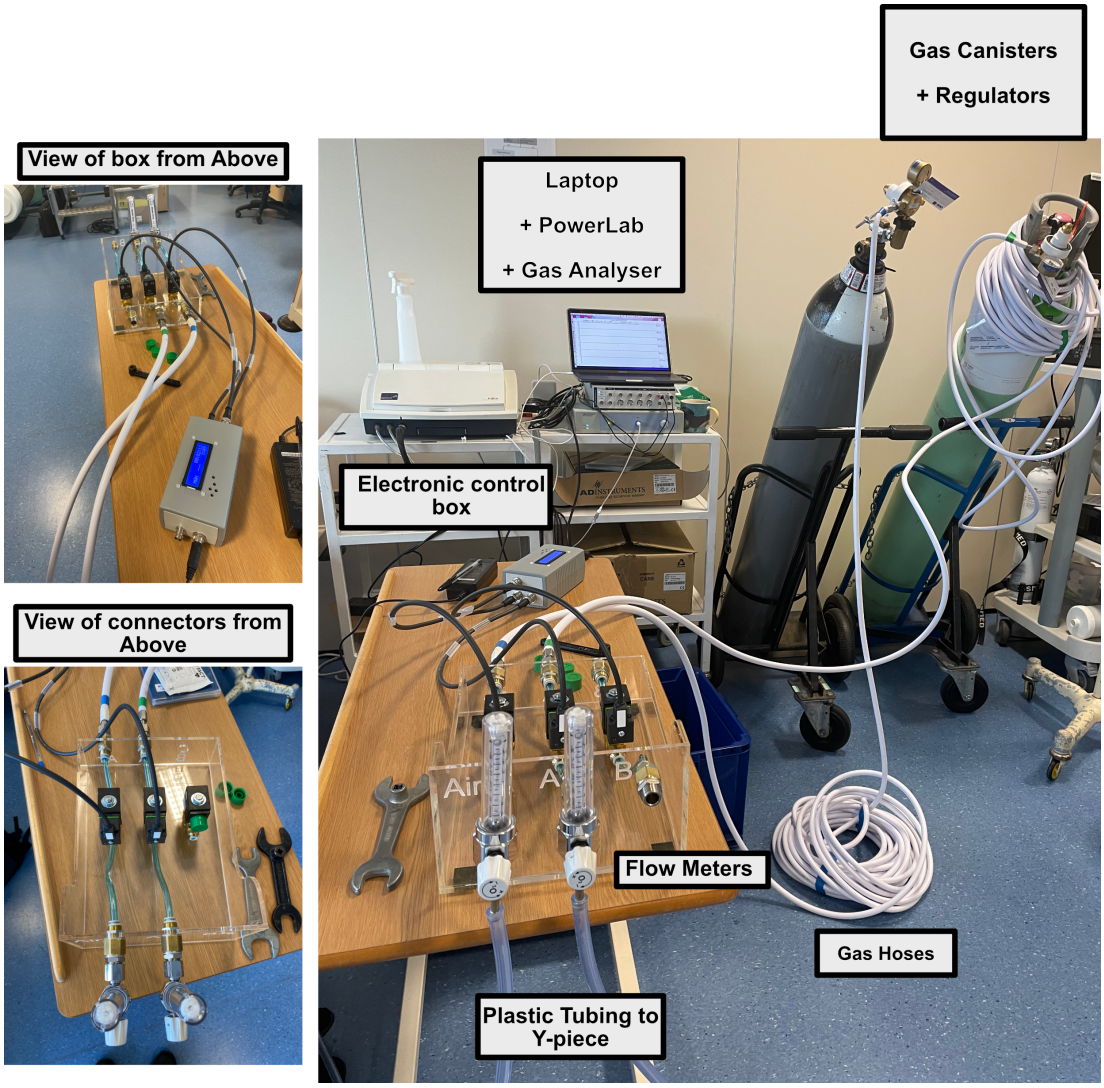


FIGURE 4.5: **Semi-automated Gas Delivery Box Set Up.** The gas cylinders were connected via medical gas regulators and by gas hoses to the back of the gas delivery box. The gas delivery was controlled by an Arduino-based electronic control box.

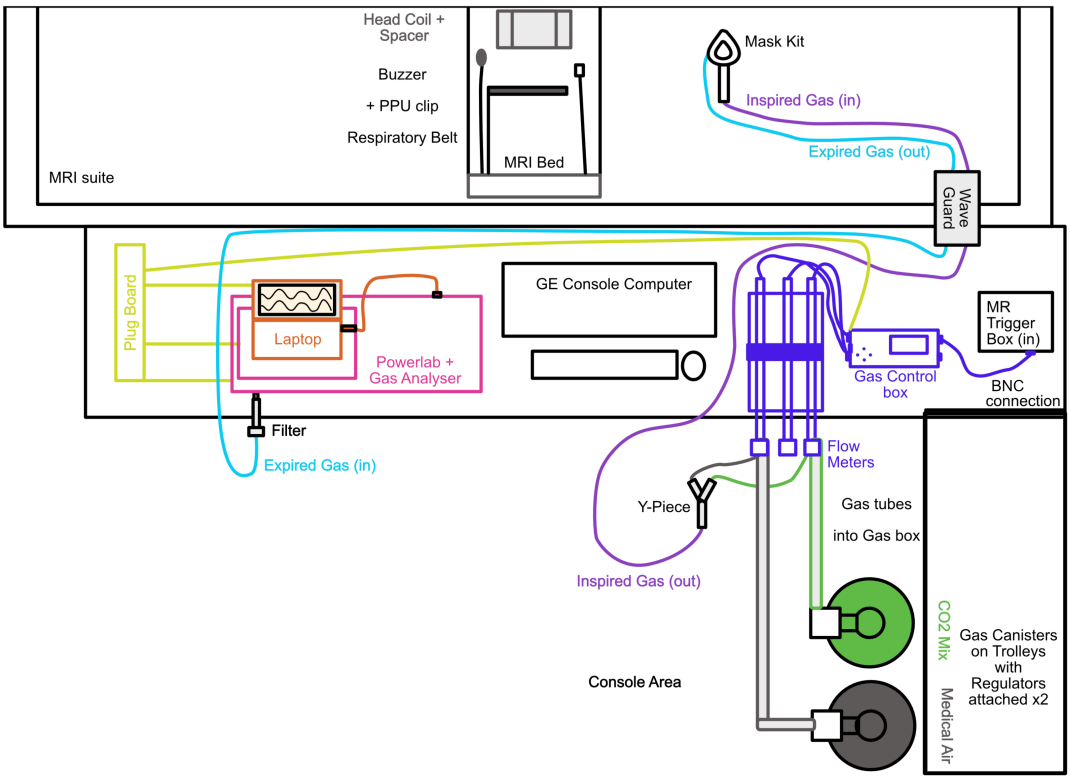


FIGURE 4.6: **Semi-automated Gas Delivery Box Conceptual Diagram.** Diagram showing a conceptual set up of the inputs/outputs for the gas delivery in the GE Healthcare Premier scanner room. Not to scale. BNC (Bayonet Neill–Concelman cable), CO_2 (Carbon dioxide), MRI (magnetic resonance imaging), PPU (peripheral pulse unit).

Breathing Circuit: Gas Delivery qCVR



REF	Name
7294001/7193000	ClearLite, anaesthetic face mask, size 4, adult, green seal, no hook ring, 22F / QuadraLite, anaesthetic face mask, size 3, medium adult, yellow seal, 22F (replaces traditional mask size 3-5)
8724013	Hook Ring for anatomical reprocessable anaesthetic face masks
45502-5	Masterflex Fitting, Nylon, Straight, Female Luer to Smooth Bore Hose Barb Adapter, 3/32" ID; 25/PK
2715000	Monitoring line hydrophobic filter and luer lock connections
2734000	Gas monitoring line, 1.2MM ID male/male luer lock, 3m
1992000	Fixed elbow, 22F-22M
1981000	T-piece 22M-22F-22M
2x 1921000	One-way directional valve 22M flow in - 22F flow out
1963000	Straight connector 22M - 6mm OD stem and cap - 22F –
169000	Flo-Guard breathing filter
2224000	Harness for CPAP mask adult, medium/large
100505	Breathing Circuit Thronhill medical (tubing x4 and connector)

FIGURE 4.7: **Mask Kit.** Tubing from the Y-piece was attached to the following mask set up with a reservoir made up of four 2 m pieces of tubing which were open to room air at one end. Note: the smaller size 3 yellow mask is shown in the photo above, but size 4 was also available and used for most participants. CPAP (Continuous positive airway pressure), F (female connecting), M (male connecting), L (litre), REF (reference number from manufacturer).

4.10 Hypercapnic Challenge Paradigm

4.10.1 Part 1 eASL

In part 1, the gas delivery box was used with the manual mode, to turn the gases on and off for a steady state fixed inspired challenge. Figure 4.8A shows an example respiratory trace for the entire scan protocol i.e. part 1 and part 2 paradigms.

During baseline phase contrast velocity (PCV) and pCASL measurements, a single block of normocapnia was presented to the participant for the duration of both scans (∼120 s PCV + ∼330 s pCASL, totalling ∼450 s). This was followed by presentation of a block of hypercapnia allowing a 30 s delay before the scan started. This was to account for the 30 s lag time taken for the gas to flow through the tubing to the mask and then to the gas analyser. PCV and pCASL measurements were repeated whilst the hypercapnia continued for the duration of the scans (∼120 s PCV + ∼330 s pCASL, totalling ∼480 s).

PCV data were acquired in order to correct for changes in pCASL labelling efficiency, but this has not been implemented so far. It was used as a known constant for the scanner in case it might change between normo- and hypercapnia. However, by using the eASL sequence, which is an unbalanced pCASL implementation, measurements should be less sensitive to changes in blood velocity.

After the participant's CO_2 level had returned to baseline, determined by reading the trace live from LabChart™, the BOLD scans were run.

4.10.2 Part 2 BOLD

For part 2 during the BOLD scans, the gas delivery box was used to deliver a pre-programmed paradigm for the hypercapnic challenge. The 'prep' part

of the BOLD scan was manually started to allow the dummy scans to run before the hypercapnic challenge started. Then the gas box was set to be automatically started with the BOLD scan, via the MR scanner trigger box. A paradigm of 60 s normocapnia followed by 60 s hypercapnia was repeated 3.5 times for a total of ∼420 secs (Fig. 4.8B). Further preparation scans were run, followed by a repeat of the same BOLD scan and simultaneous hypercapnia paradigm. The first two participants were from the developmental scans, and only completed one run of the BOLD scan, so their data was not included in the final results. All the other participants completed two runs of the BOLD scan.

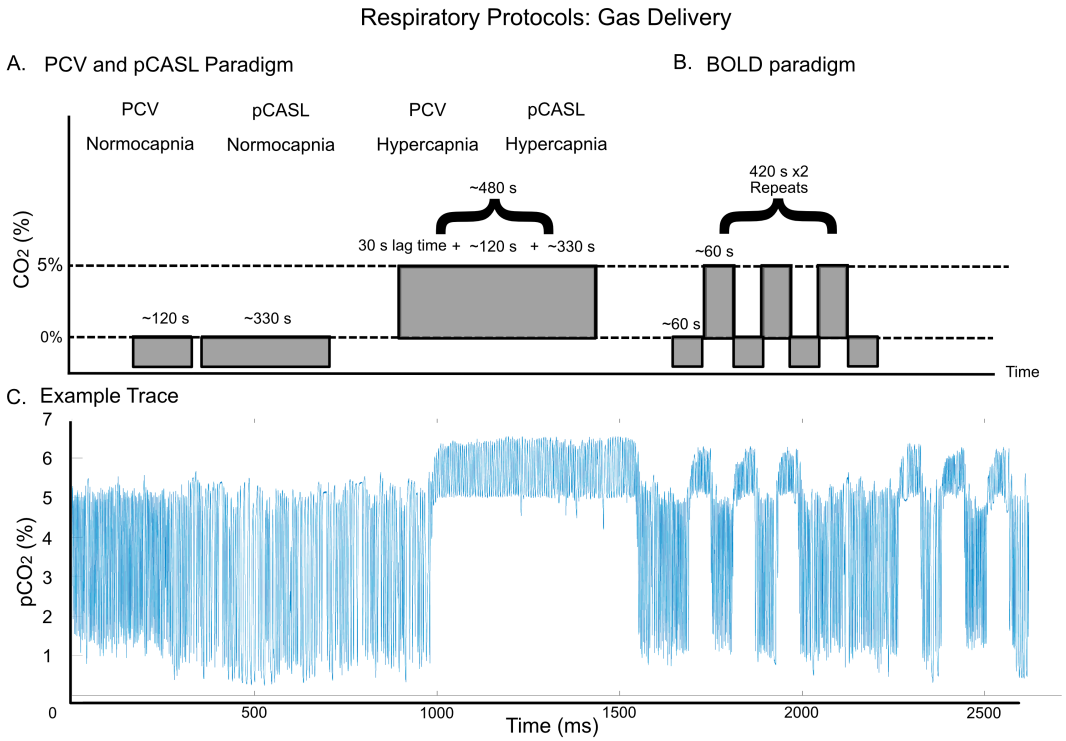


FIGURE 4.8: **Hypercapnic Challenge Paradigms.** A. A block protocol paradigm of normocapnia during the PCV (duration ∼120 s) and the pCASL (duration ∼330 s) scans, followed by hypercapnia for 30 s to account for lag time, and continued during repeated PCV and pCASL scans (total duration ∼480 s). B. A paradigm of 60 s normocapnia followed by 60 s hypercapnia repeated 3.5 times during the BOLD scan (duration ∼420 s). The BOLD scan was repeated twice. C. Example Respiratory trace showing the entire CO_2 trace for one participant. CO_2 (carbon dioxide), BOLD (blood oxygenation level dependent), ms (milliseconds), pCASL (pseudo continuous arterial spin labelling), phase contrast velocity (PCV), % (percent), s (seconds).

4.11 MR

4.11.1 MR Safety Requirements

As mentioned in section 4.6 MR safety forms were completed. Participants were given ear plugs to reduce audio noise from the scanner.

4.11.2 MR Kit

The MR data for parts 1 and 2 of this study were collected as part of the same scanning session. Participants were scanned with a 3T GE Premier (Fig. 1.16) (GE Healthcare, Waukesha, WI, USA) scanner and the vendor's 48 channel head coil. The 'spacer', a piece of plastic that raised the top part of the head coil, was used to provide more room for the breathing mask. This was used for all participants for consistency. The peripheral pulse unit (PPU) and respiratory belt were also used to record the participants' heart rate and respiratory rate.

4.11.3 MR Scan Protocols

Figure 4.10 shows the full MR scan protocol. The full text files of the scan protocols can be found in the Zenodo repository (10.5281/zenodo.10018241). First, a survey and localiser scan were performed. Then a T_1w anatomical (MPRAGE) was acquired [160] for later use in the registration process. The first image in figure 4.10 shows the MPRAGE, which was acquired with TR/TE = 2255/297 ms, flip angle = 8°, slice thickness = 1, matrix = 1.0x1.0x1.0, FOV = 25.6). The second image in the figures is of the time of flight (TOF) magnetic resonance angiography (MRA), which was acquired with 30 slices, slice thickness 50 mm, A-P direction, voxel size 16 x 16 x 50 mm, flip angle 90°, TR/TE set to 'minimum' which was 14/4.9 ms .

The TOF and MPRAGE images were used to determine where to place the imaging plane for the PCV scan.

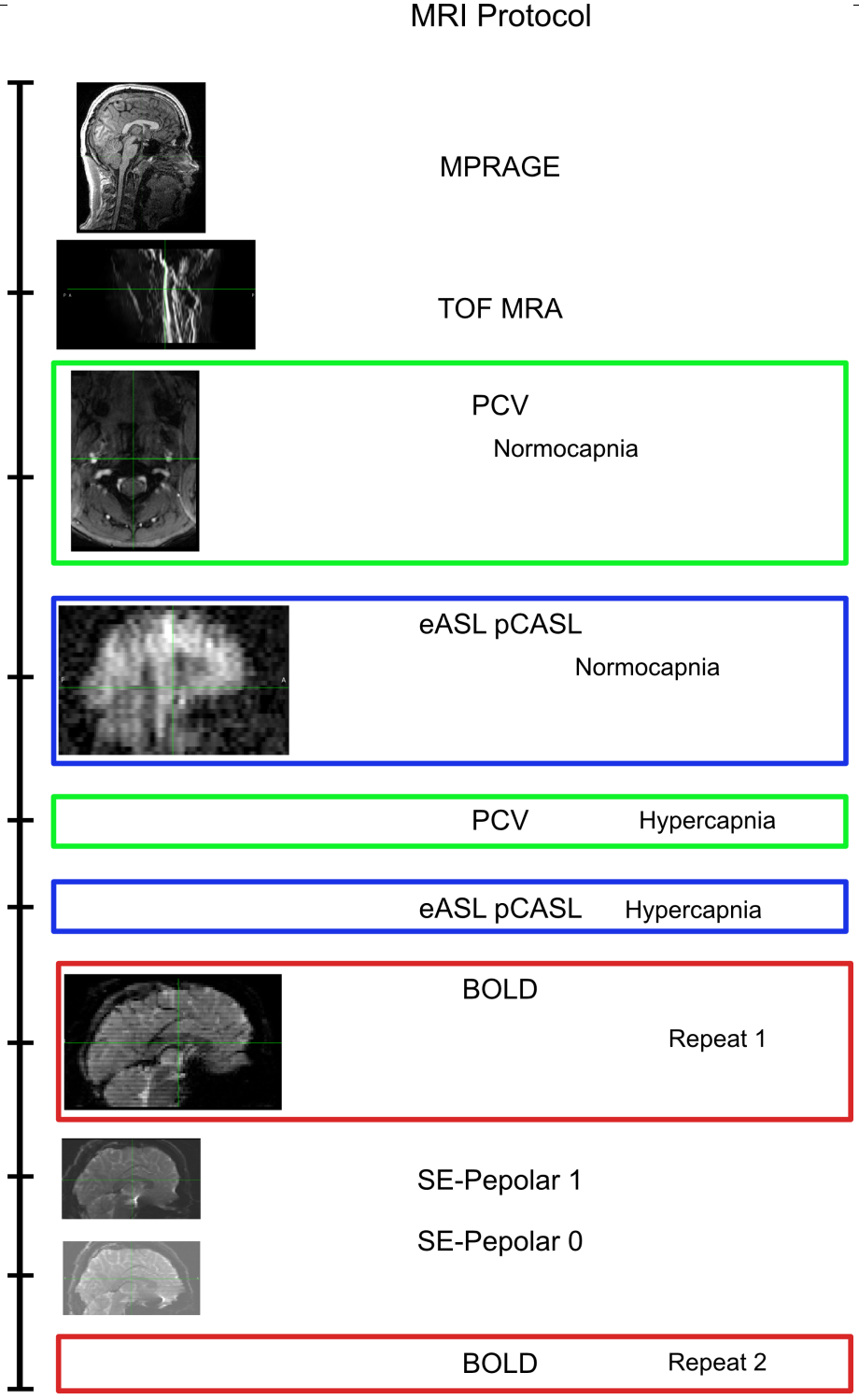


FIGURE 4.9: **MRI Protocol.** Images are an example set from one subject. The sequence for MR scanning was as follows, a localiser survey, MPRAGE (Magnetization Prepared Rapid Acquisition of Gradient Echo), TOF (time of flight) MRA (Magnetic resonance angiography), PCV (phase contrast velocity). eASL (enhanced ASL), BOLD (Blood Oxygen Level Dependent), SE (spin Echo).

4.11.4 Part 1 eASL

For part 1, the placement of the pCASL labelling plane was chosen based on the results from the previous chapter (Chapter 2), with the imaging plane covering as much of the brain as possible. The TOF MRA and PCV images (see 2nd and 3rd images of Fig. 4.10) were used to plan the pCASL labelling plane accordingly. On the GE scanner this required manually moving the base of the imaging plane box 30 mm superior of a plane placed perpendicular to the V3 segment of the VAs and the internal carotid arteries. This was necessary as the labelling plane was hard coded to be 30 mm below the imaging slab.

The MPLD pCASL sequence is a development of the GE 3D-ASL pulse sequence named 'enhanced' ASL (eASL), and was provided by GE Healthcare. The parameters included; seven effective label durations (LD) = 222 ms, 256 ms, 303 ms, 372 ms, 481 ms, 682 ms, 1183 ms , and seven PLDs (i.e. inversion times (TI)) = 922 ms, 1178 ms, 1481 ms, 1853 ms, 2334 ms, 3016 ms, 4199 ms, bolus duration = 1500 ms, 3D spiral readout, acquisition matrix: 4 interleaved spirals x 512 sampling points per interleave, slice thickness = 4.5 cm x 128 slices, FOV = 22 cm, TE = 11.4 ms. The eASL scanner settings automatically set the TR per scan, which for the group was TR = 7529.8±1.0 ms (mean±std). GE eASL sequences use background suppression by default [143]. The 1500 ms bolus duration provides a good balance between signal strength and T_1 decay considerations. The label durations follows an exponential pattern to compensate for T_1 decay, with the longest block (1183 ms) providing substantial signal for the latest time points. The extended TI times mean this sequence is excellent for capturing delayed arterial transit times in pathological conditions. This timing scheme would be particularly useful for patients with cerebrovascular disease where longer transit times are expected, as the extended TI range can better capture delayed perfusion patterns.

4.11.5 Part 2 BOLD

The MPRAGE scan was used to plan the multiband BOLD scan, with the centre of the stack along the AC-PC line, covering as much of the brain as possible. Slice thickness = 1 mm, TE = 35 ms, TR = 1400 ms, voxel size 2 mm x 2 mm x 2 mm, flip angle 68°, matrix 106 x 106, 57 slices. Two sets of spin echo (SE) echo planar imaging (EPI) images with phase encoding applied in opposite directions (A-P and P-A) were acquired to be used in applying distortion correction to the BOLD images.

4.12 Data Analysis

4.12.1 End-tidal Data Analysis

Respiratory data were analysed using similar analysis methods to chapter 2 (see section 2.6) with a custom MATLAB (2021a, Mathworks, Natick, MA, United States) script based pipeline (Fig. 2.7) by windowing (i.e. a section of the $P_{ET}CO_2$ time course was extracted within a time window), and then the 'Findpeaks' function was used to extract the peaks of the trace to calculate the average $P_{ET}CO_2$ (see Fig. 4.10A). Likewise, the CO_2 percentage was converted to $P_{ET}CO_2$ and used to calculate the percentage change as in equation 2.1.

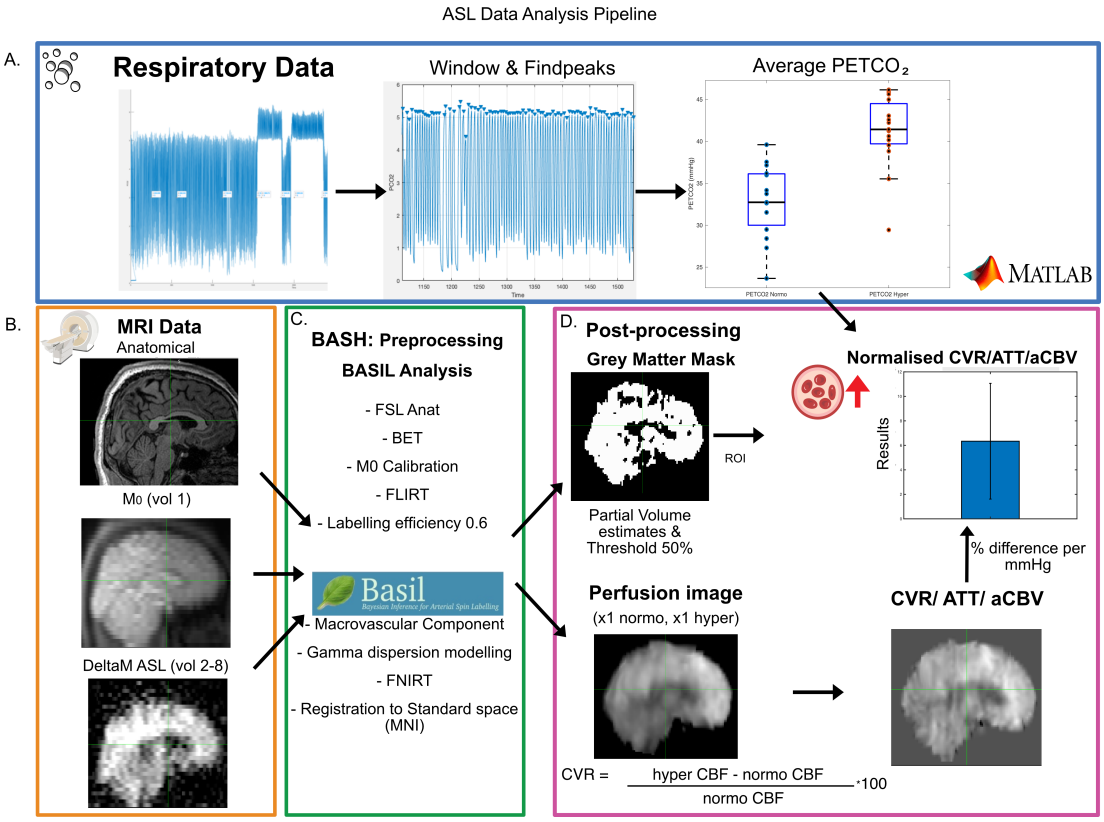


FIGURE 4.10: **pCASL Data Analysis Pipeline.** $PETCO_2$ was windowed and calculated in MATLAB. MRI data were pre-processed using a BASH script and then analysed using Bayesian Inference for Arterial Spin Labelling (BASIL) using gamma dispersion modelling. The grey matter mask and perfusion images were used to calculate the percentage change (%) in blood flow, which was normalised to the individual's $PETCO_2$ to give the percentage change per mmHg. aCBV (arterial cerebral blood volume), ASL (arterial spin labelling), ATT (arterial transit time), BET (brain extraction tool), CVR (cerebrovascular reactivity), DeltaM (difference image i.e. difference between control and tag images), FAST (FMRIB advanced segmentation tool), FLIRT (FSL tool for linear registration), M_0(M zero scan), MNI (Montreal Neurological Institute), MRI (magnetic resonance imaging), $PETCO_2$ (end-tidal partial pressure of carbon dioxide).

4.13 MR Image Analysis

Firstly, digital imaging and communications in medicine (DICOM) data exported from the GE scanner were converted to the Neuroimaging Informatics Technology Initiative (NIFTI) format using MRIcroGL (Chris Rorden, University of South Carolina, SC, USA). The data were pre-processed using a BASH script to re-name and organise them into folders according to the brain imagine data structure (BIDS) format [101].

4.13.1 Grey Matter Mask ROIs

Region of interest (ROI) GM masks were generated using the participant's MPRAGE (T_1w) structural image and M_0 scan using BET (brain extraction tool). For pCASL, this was done as part of the BASIL toolbox processing. For BOLD, the BET needed to be manually adjusted (with thresholding, centring, angle) for each participant in order to achieve a reasonable brain extraction (see Fig. 4.11). These parameters were added to a BASH script. Then the brain extracted T_1w images were transformed into Montreal Neurological Institute (MNI) space (McConnell Brain Imaging Centre, Montreal Neurological Institute, McGill University, Montreal, Quebec, Canada). Then FMRIB's Automated Segmentation Tool (FAST) was used to create grey matter partial volume estimate (PVE) maps [258]. The masked PVE maps were thresholded at 50%, 60%, 70% and 90% to access the best PV threshold. The chosen threshold was 60% for the BOLD data. pCASL data was used with the default thresholding of 50%. These GM ROI masks were used to ensure the BEL analysis was only performed on voxels within the grey matter, rather than running it for the whole brain.

After the brain extracted images were registered to MNI space, this transformation was then used to move the MNI cortical atlas into the eASL native space. This

was followed by using FNIRT [12] to define the GM mask as an ROI (see Fig. 4.11).

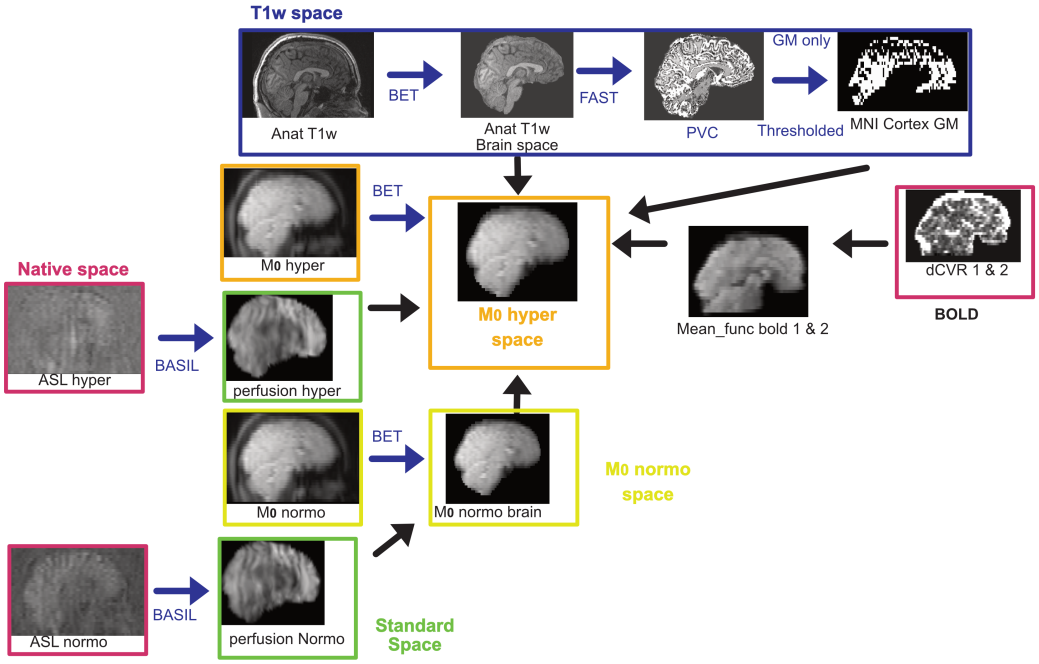


FIGURE 4.11: **Creating GM ROIs.** Tools and transforms used to move the output data from ASL and BOLD datasets into the final M_0 image space. Black arrows denote transforms and blue arrows denote tools/analysis methods. ASL (arterial spin labelling), BASIL (BASIL basil toolbox), BET (brain extraction tool), BOLD (blood oxygen level dependent), dCVR (dynamically modelled BOLD), FAST (FMRIB advanced segmentation tool), FLIRT (FSL tool for linear registration), hyper (hypercapnia), MNI (Montreal Neurological Institute), MRI (magnetic resonance imaging), normo (normocapnia), T1w (T_1 weighted anatomical).

4.13.2 Part 1 eASL - BASIL

MPLD pCASL data were analysed using FMRIB Software Library (FSL) version 6.0.6.3 [252], with BASH and in-house MATLAB scripts (Mathworks, Natick, MA, USA). A BASH script was used to pre-process the pre-subtracted pCASL volumes by using FSLROI. This was used to separate out the first volume as the M_0 volume, and the following volumes 2-8 as the MDelta (i.e. tag-control difference) volumes produced by the scanner. The second part of the BASH script ran the Bayesian Inference program BASIL [50]. After developing the script on a local machine, BASIL was run on the University of Nottingham Augusta high performance cluster (HPC) to process the data faster. This made a difference of taking about four days to run one dataset, to being able to run all datasets parallel over about 4 days. This included using BASIL macrovascular components inference [50, 188, 256]. The gamma dispersion modelling was also used to account for dispersion of the ASL bolus as it travels towards the tissue [188]. This can be modelled to account for variance, otherwise the bolus is treated as square wave. The output metrics from BASIL included CBF, aCBV and ATT.

Unfortunately, motion correction was not possible due to the scanner only providing pre-subtracted pCASL data. Partial volume estimates from BASIL also failed so the 'calib' (calibrated to M_0 images) output images with the PVE from FAST were used instead. Next, FSLmaths was used to calculate the percentage change in blood flow for CVR, which was calculated in the same way as in chapter 2 with Eqn 2.1. Similarly, the percentage changes for aCBV and ATT were calculated. These images were already in eASL native space so required no further transforms. These were then used to calculate

the group mean of medians and standard error of the mean (SEM), to avoid outliers. Further analysis was performed in MATLAB and used to create the bar graphs, which were then formatted as figures using Affinity Designer 2 (Serif, Nottingham, UK).

4.13.3 Part 2 BOLD – dCVR

For the BOLD data, the preprocessing included a BASH script for removing the first two volumes (dummy scans) using FSLROI and motion correction with MCFLIRT [122]. The analysis with FEAT included setting up a design file with the graphical interface (GUI) with pre-processing that consisted of the default values for high pass filtering (120 Hz) [123]. Spatial smoothing was manually checked at 1, 2, 3, 4 and 5 mm, with the final FEAT model running at σ = 3 mm. A sinusoidal model was used to model the BOLD response to the 1 min on / 1 min off HC. Explanatory variable (EV) 1, i.e., waveform, was set as a sinusoid wave form for sin (period 120 s) and EV 2 was set as the cosine wave form (period of 120 s, phase 30 s). Another BASH script was used to run this design file for each of the participants' (both run 1 and 2) BOLD datasets in batch. The preprocessed BOLD data (filtered func) was then used for the next part of the analysis.

For the BOLD data, MATLAB was used to run the BEL algorithm (described in section 4.3.2 of the introduction) on GM voxels to estimate dCVR. The TR was set at 1.4 s for the initial parameters. Each of the BOLD runs (run 1 and 2) were looped separately through the analysis pipeline to total 11 datasets.

The 'Findpeaks' function was used to find the initial $P_{ET}CO_2$. The $P_{ET}CO_2$ time course was interpolated onto the TR of the BOLD data and then normalised

to provide a time course with zero mean and a standard deviation of one in order to fit the BOLD data.

For each voxel the following steps were performed. Firstly, the BOLD time course was normalised in the same way as the PETCO$_2$ time course above. Spherical Laguerres estimation was performed using the normalised PETCO$_2$ and BOLD data to generate an HRF. The MATLAB function conv2 was used to generate a regressor by convolving the PETCO$_2$ time course with this HRF. Regression was performed with the raw BOLD time course and the regressor to estimate the % change in the BOLD signal, which was normalised by the change in PETCO$_2$ to estimate the CVR as % / mmHg. The output from this pipeline provided the HRF from which the peak amplitude, time to peak and full width half maximum were calculated on a voxel by voxel basis. This was performed for each BOLD run using the PETCO$_2$, which is illustrated in Fig. 4.12.

During the initial set up of the dCVR pipeline, running the main analysis script for one dataset took 10 days. Therefore, the HPC was used. The BOLD data were analysed using the University of Nottingham Ada HPC (after being upgraded from Augusta). Due to the HPC time limit of jobs being a maximum of 7 days, the datasets had to be further split into running each of the 57 brain slices separately. A Slurm sbatch script was used to submit the 1,311 individual jobs to the Ada HPC. A BASH script was then used with FSLmerge to recombine the 57 slices back into the whole brain images for each participant.

4.13.4 Statistical Analysis

For all statistical tests, the alpha threshold for significance of tests was set at 0.05. Statistical tests were performed in MATLAB. A Shapiro-Wilks test was

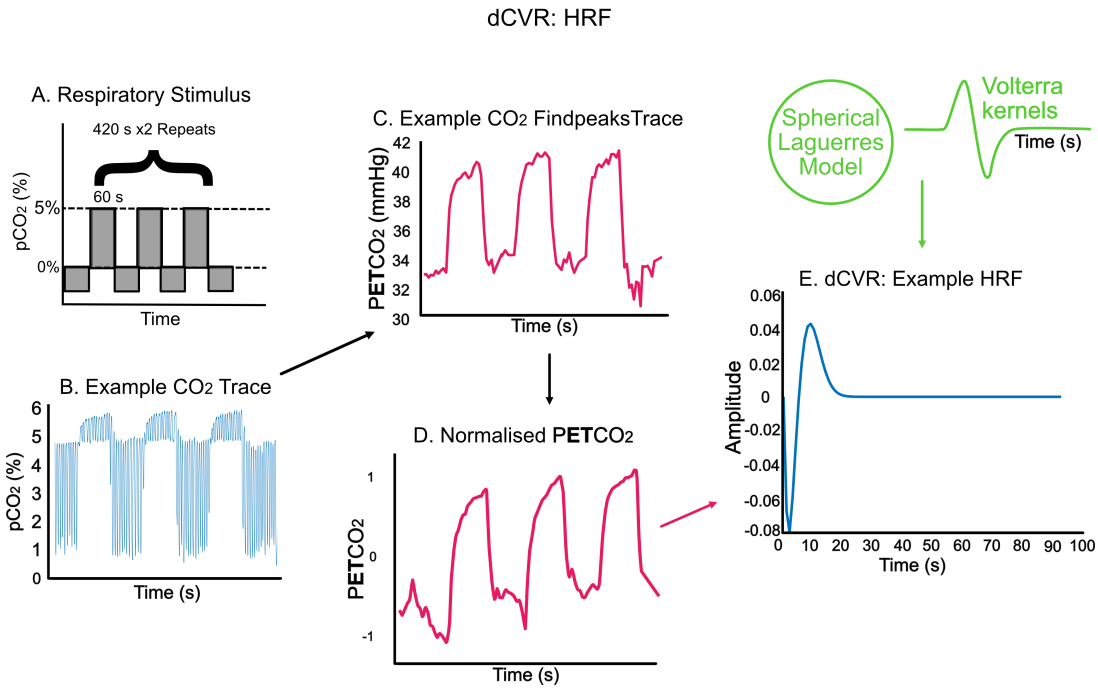


FIGURE 4.12: **dCVR HRF.** Concept diagram showing the respiratory stimuli (A), an example for respiratory trace (B) which was converted to $PETCO_2$, and then processed using the Findpeaks function (C), followed by normalisation (D), and integration with the Spherical Laguerres model (with Volterra kernels), to give an example HRF (E). $PETCO_2$ (end-tidal partial pressure of carbon dioxide), HRF (haemodynamic response function), dCVR (dynamically modelled BOLD (blood oxygen level dependent MRI (magnetic resonance imaging))), s (seconds).

used to confirm the data were normally distributed. Paired students T-tests were used to compare normo- to hypercapnic conditions. The null hypothesis was that there would be no difference between different gas conditions. The test was run for the $PETCO_2$ levels during eASL scanning to compare normo- to hypercapnic conditions. Additionally, the CBF, aCBV and ATT data were compared for normo- and hypercapnia conditions, and the results are shown in the results section 4.16. For part 2, the $PETCO_2$ trace was sinusoidal due to the nature of the 1 min on / 1 min off gas delivery, hence the baseline and average amplitude were calculated to represent 'normocapnia' and 'hypercapnia' conditions. This was for testing if there had been a difference between the two conditions $PETCO_2$ levels.

4.14 Results

4.15 Hypercapnic Challenges

4.15.1 Part 1, eASL Hypercapnic Challenges

The data from one participant were excluded due to image quality (incidental finding), and two datasets were excluded due to technical issues. Eleven participants datasets were included in the pCASL data analysis (N=11, 4M/7F, 23.5±3.3 years, 75.1±15.6 kg .70±0.10 m), and the summary of group mean CO_2 levels are shown in Table 4.2. The response to the hypercapnic challenge during the eASL data acquisition are shown in Table 4.2. At a group level, the response to the hypercapnic challenge showed a significant increase in $P_{ET}CO_2$ from normo- (33.2±4.5 mmHg) to hypercapnia condition (42.7±2.4 mmHg mean±standard deviation) (p=2.31e-06). This was a difference of 9.6±3.4 mmHg, so not disimilar to the +10 mmHg above baseline used in chapter 2 part 1.

TABLE 4.2: **Response to Hypercapnic Challenge: eASL.** Table of participants characteristics and response to the hypercapnic challenge stimulus for the eASL datasets. m (metres), F (female), M (male), m (meters), kg (kilograms), std (standard deviation) % (percent), mmHg (millimetres of mercury), $PETCO_2$ (end tidal partial pressure of carbon dioxide).

Participant Number	Age (years)	Sex	Weight (kg)	Height (m)	Normocapnia (mmHg)	Hypercapnia (mmHg)	Difference (mmHg)
3	20	M	89	1.91	37.5±0.9	43.0±1.5	5.5
5	21	M	85	1.77	36.2±2.2	45.9±0.6	9.7
6	23	F	53	1.65	23.6±1.4	41.0±0.6	17.4
7	23	F	103	1.63	33.7±1.0	42.6±0.5	8.8
8	27	F	70	1.55	32.7±1.2	41.2±1.0	8.5
9	28	F	83	1.77	31.1±0.8	41.7±0.6	10.7
11	19	M	51	1.75	37.1±0.5	45.0±0.4	7.8
12	21	F	72	1.67	32.6±1.7	38.8±1.1	6.2
13	29	F	72	1.58	34.2±1.3	45.6±0.6	11.5
14	23	M	84	1.69	32.7±0.9	40.6±0.9	7.9
16	25	(M2F)	65	1.74	27.3±1.1	41.4±0.8	14.1
Mean±std	23.5±3.3	4M/7F	75.1±15.6	1.70±0.1	33.2±4.5	42.7±2.4	9.6±3.4

4.15.2 Part 2, BOLD Response to Hypercapnic challenge

Part 2 data was acquired at the same participants as part 1. For the BOLD datasets, some participants only had one repeat of the BOLD task, so these were excluded, as they did not have a complete dataset. The other 11 participants had two BOLD repeats to give 11 complete datasets (N=11, 4M, 7F, 23.5±3.3 years). When comparing the $P_{ET}CO_2$ across repeats of the HC, there was no significant difference between run 1 and run 2 for the baseline (run 1 = 31.0±3.4 mmHg, run 2 = 31.7±3.0 mmHg, p=0.076) or amplitude (run 1 = 10.9±1.6 mmHg, run 2 = 10.2±2.2, p=0.241) (median±IQR). Table 4.3 shows the group mean $P_{ET}CO_2$ was 36.2±4.4 mmHg for run 1 and 36.6±4.2 mmHg for run 2 (median±IQR) to give an average of 36.4±2.7 mmHg. When fitted to a sin/cosine model this gave an average baseline of 31.4±3.1 mmHg and amplitude of 10.6±1.9 mmHg, which was a significant increase from baseline (p=1.22e-09).

TABLE 4.3: **Response to Hypercapnic Challenge: BOLD.** Table of participants characteristics and response to the hypercapnic challenge stimulus for the BOLD datasets ($PETCO_2$). F (female), M (male), M2F (male to female medically transitioned) m (meters), kg (kilograms), std (standard deviation) % (percent), mmHg (millimetres of mercury), $PETCO_2$ (end tidal partial pressure of carbon dioxide).

Participant Number	Age (years)	Sex	Weight (kg)	Height (m)	Average (mmHg)	Baseline (mmHg)	Average Amplitude (mmHg)
3	20	M	89	1.91	39.3	34.6	9.4
5	21	M	85	1.77	39.0	34.6	9.1
6	23	F	53	1.65	30.0	25.1	10.6
7	23	F	103	1.63	36.5	30.3	13.2
9	28	F	83	1.77	35.2	29.9	12.1
8	27	F	70	1.55	34.4	28.9	12.5
11	19	M	51	1.75	39.5	35.9	7.6
12	21	F	72	1.67	34.5	30.0	9.6
13	29	F	72	1.58	38.4	32.3	13.0
14	23	M	84	1.69	36.3	30.9	10.8
16	25	(M2F)	65	1.74	36.7	32.7	8.4
Mean±std	23.5±3.3	4M/7F	75.1±15.6	1.70±0.1	36.3±2.8	31.4±3.1	10.6±1.9

4.16 Results: MR

The following results for both eASL and BOLD present values specifically within the grey matter of young, healthy adult brains.

4.16.1 Results: Part 1 eASL

Cerebrovascular Blood Flow

Figure 4.13 shows pCASL measurements of the cerebral blood flow response to the hypercapnic challenge. It shows that CBF significantly increased from normo- to hypercapnic conditions (normo 69.6±4.5 ml/100g/min to hyper 108.0±6.2 ml/100g/min, p=0.0002, group mean of medians±group standard error of the mean).

Figure 4.14 shows that when comparing the percentage change from normo- to hypercapnic conditions, CBF increased by 59.6±11.7% after hypercapnia, which is equivalent to a CVR of 5.8±0.5% for a 1 mmHg change in $P_{ET}CO_2$ (group mean of medians±group standard error of the mean). Normalising by $P_{ET}CO_2$ therefore reduced the standard deviation across the group.

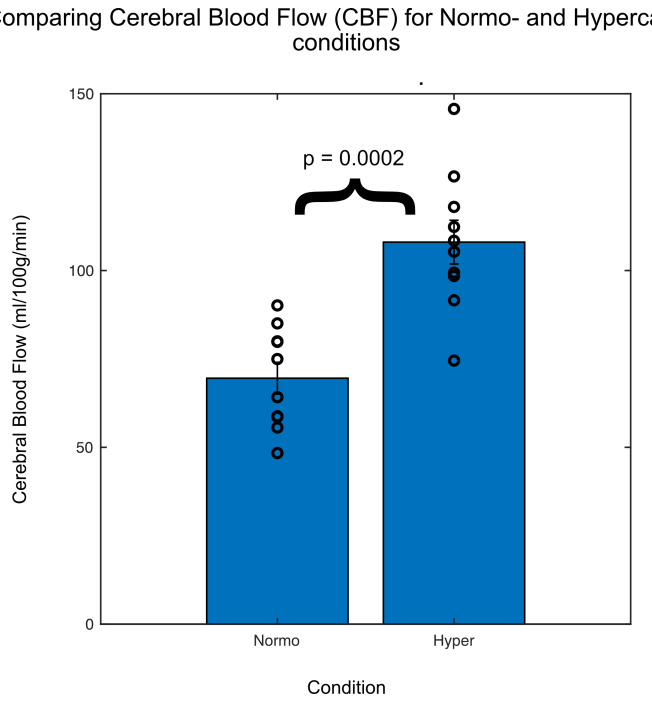


FIGURE 4.13: **Comparing Cerebral Blood Flow (CBF) for Normo- and Hypercapnia Conditions.** Cerebral blood flow (CBF) increased from normo to hypercapnic conditions (p=0.0002). g (grams), hyper (hypercapnia), min (minute), ml (millilitres), normo (normocapnia).

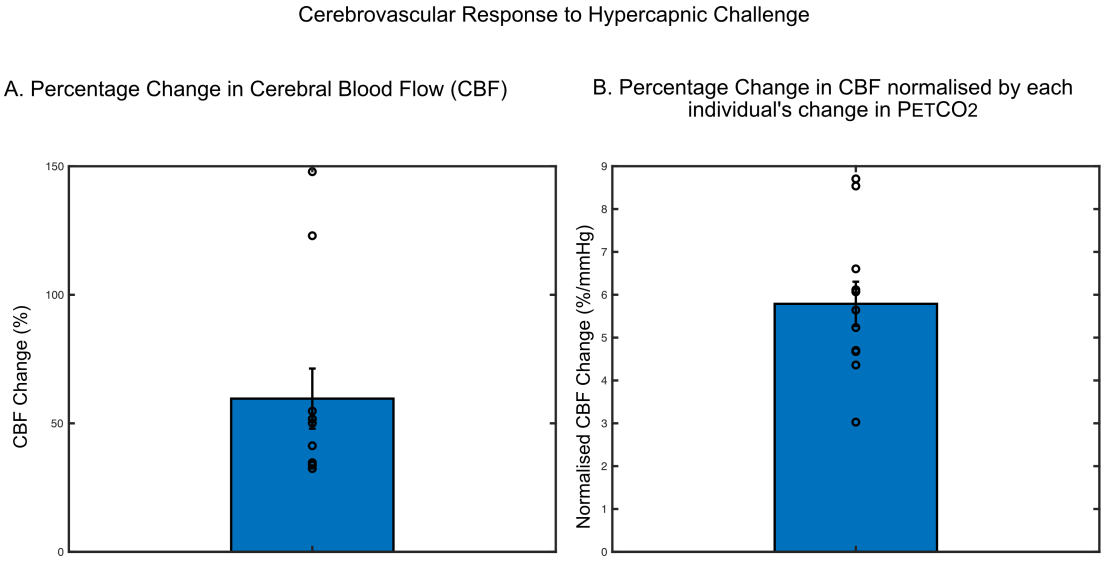


FIGURE 4.14: **Cerebrovascular Response to Hypercapnic Challenge.** Percentage change of cerebral blood flow (CBF) from normo- to hypercapnia. The bar represents the group mean and the error bar represents the standard error of the mean. % (percent), mmHg (millimetres of mercury), $PETCO_2$ (end tidal partial pressure of carbon dioxide).

Cerebral Blood Volume

Figure 4.15 shows that the pCASL measurements of arterial cerebral blood volume showed no change from normo- to hypercapnic conditions (normo 2.3±0.3%, hyper 2.9±0.4%, p=0.4545, group mean of medians±group standard error of the mean).

Figure 4.16 shows that when comparing the percentage change from normo- to hypercapnic conditions, aCBV changed by 44.2±25.6%. This was normalised by each individual's $P_{ET}CO_2$, which was equivalent to a change of 5.2±2.6 %/mmHg (group mean of medians± group standard error of the mean).

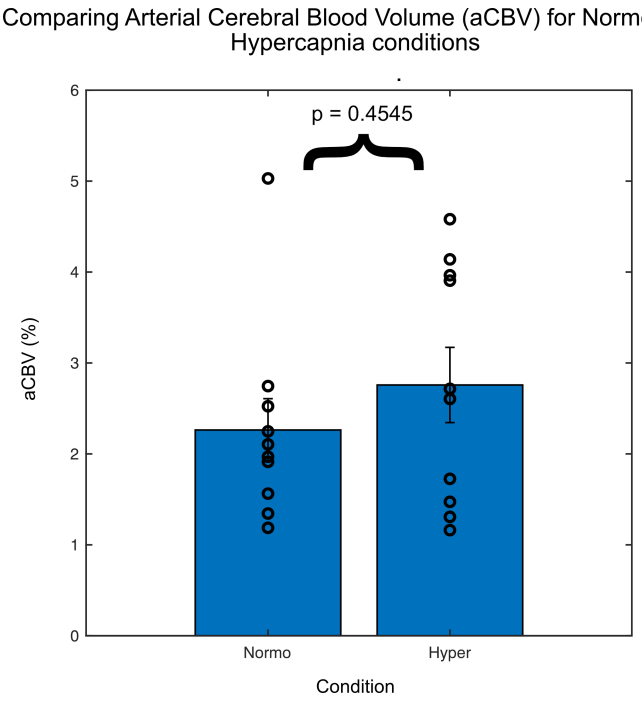


FIGURE 4.15: **Comparing arterial Cerebral Blood volume (aCBV) for Normo- and Hypercapnia Conditions.** aCBV increased from normo- to hypercapnic conditions (p=0.4545). hyper (hypercapnia), normo (normocapnia).

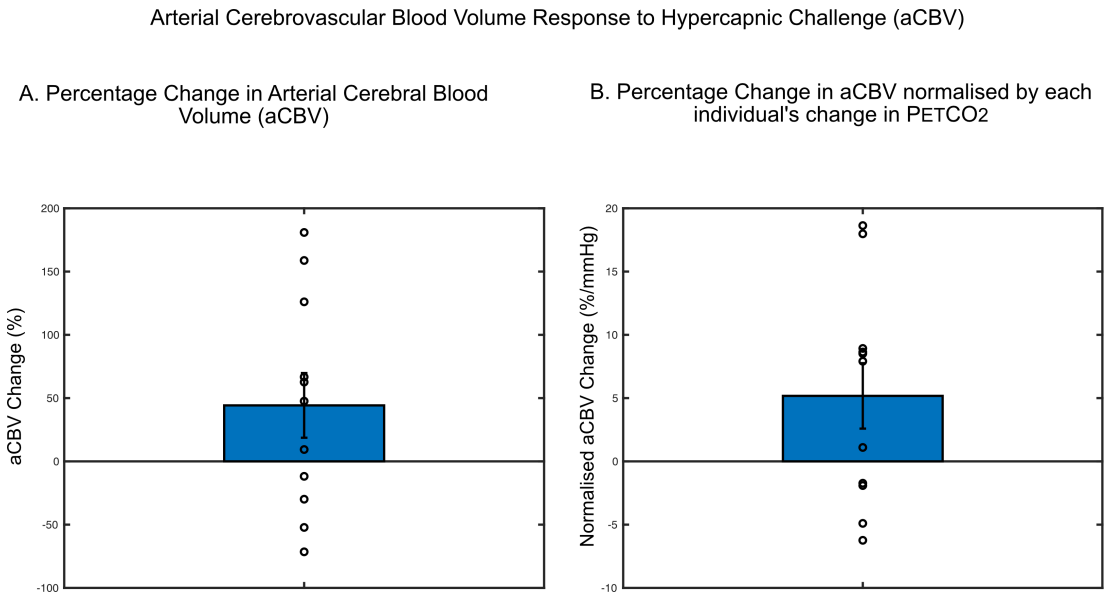


FIGURE 4.16: **Arterial cerebral Blood Volume Response to Hypercapnic Challenge.** Percentage change of aCBV (arterial cerebral blood volume) from normo- to hypercapnia. The bar represents the group mean and the error bar represents the standard error of the mean. % (percent), mmHg (millimetres of mercury), $PETCO_2$ (end tidal partial pressure of carbon dioxide).

Arterial Transit Time

Figure 4.17 shows that when comparing the pCASL measurements of ATT from normo- to hypercapnic conditions, there was a significant decrease from normo- to hypercapnic conditions (normo 1.0±0.01 s, hyper 0.8±0.1 s, p=0.0008, group mean of medians±group standard error of the mean).

Figure 4.18 shows that when comparing the percentage change from normo- to hypercapnic conditions, ATT decreased by -22.0±3.6%. This was normalised by each individual's $P_{ET}CO_2$, which was equivalent to a decrease of -2.2±0.2%/mmHg (group mean of medians± group standard error of the mean).

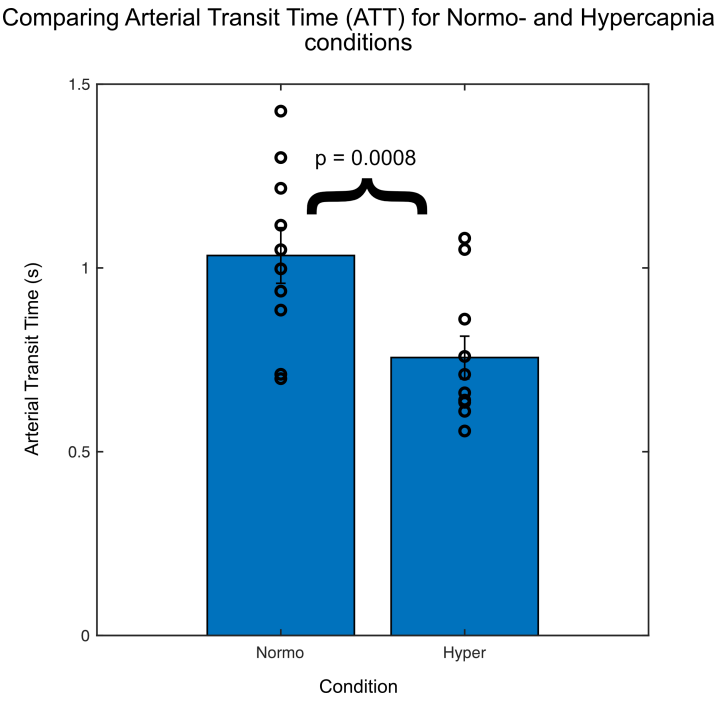


FIGURE 4.17: **Comparing Arterial Transit Time (ATT) for Normo- and Hypercapnia Conditions.** Arterial transit time (ATT) decreased from normo- to hypercapnic conditions (p=0.0008). hyper (hypercapnia), normo (normocapnia), s (seconds).

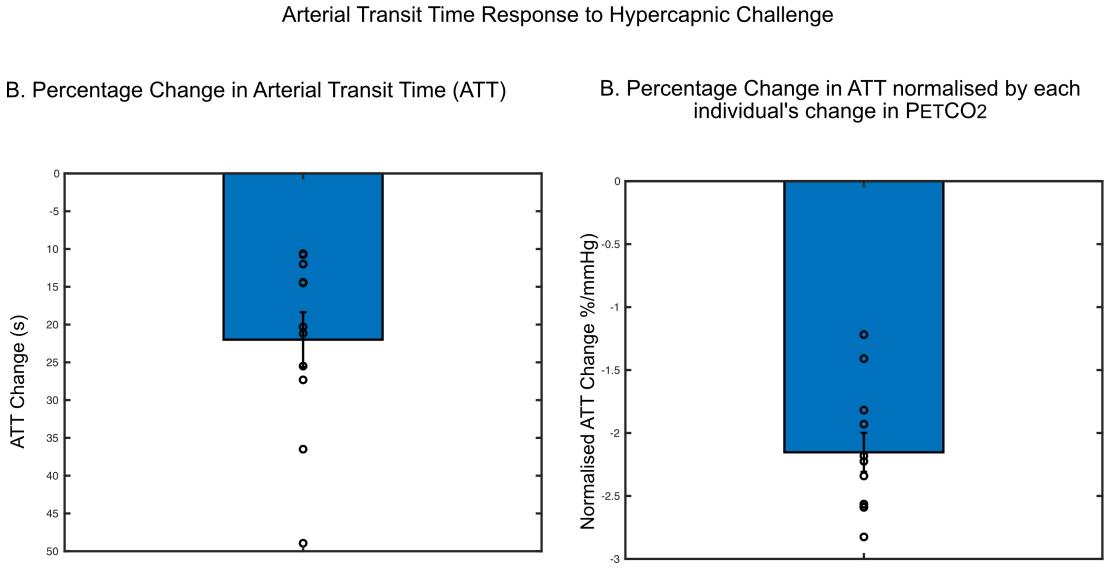


FIGURE 4.18: **Arterial Transit Time Response to Hypercapnic Challenge.** Percentage change of ATT (arterial transit time) from normo- to hypercapnia. The bar represents the group mean and the error bar represents the standard error of the mean. % (percent), mmHg (millimetres of mercury), $PETCO_2$ (end tidal partial pressure of carbon dioxide).

4.16.2 Results: Part 2 dynamically Modelled BOLD CVR

BOLD dCVR: Magnitude

Figure 4.19A shows an example single axial slice of a dCVR magnitude map with the colourbar showing areas of higher CVR magnitude in yellow. Figure 4.19B shows that when comparing the percentage change from normo- to hypercapnic conditions for dCVR magnitude, the BOLD signal in the grey matter increased by 3.2±0.3% after hypercapnia, which is the equivalent to a CVR of 0.3±0.0% per mmHg change in $P_{ET}CO_2$ (group mean of medians±group standard error of the mean) (4.19C).

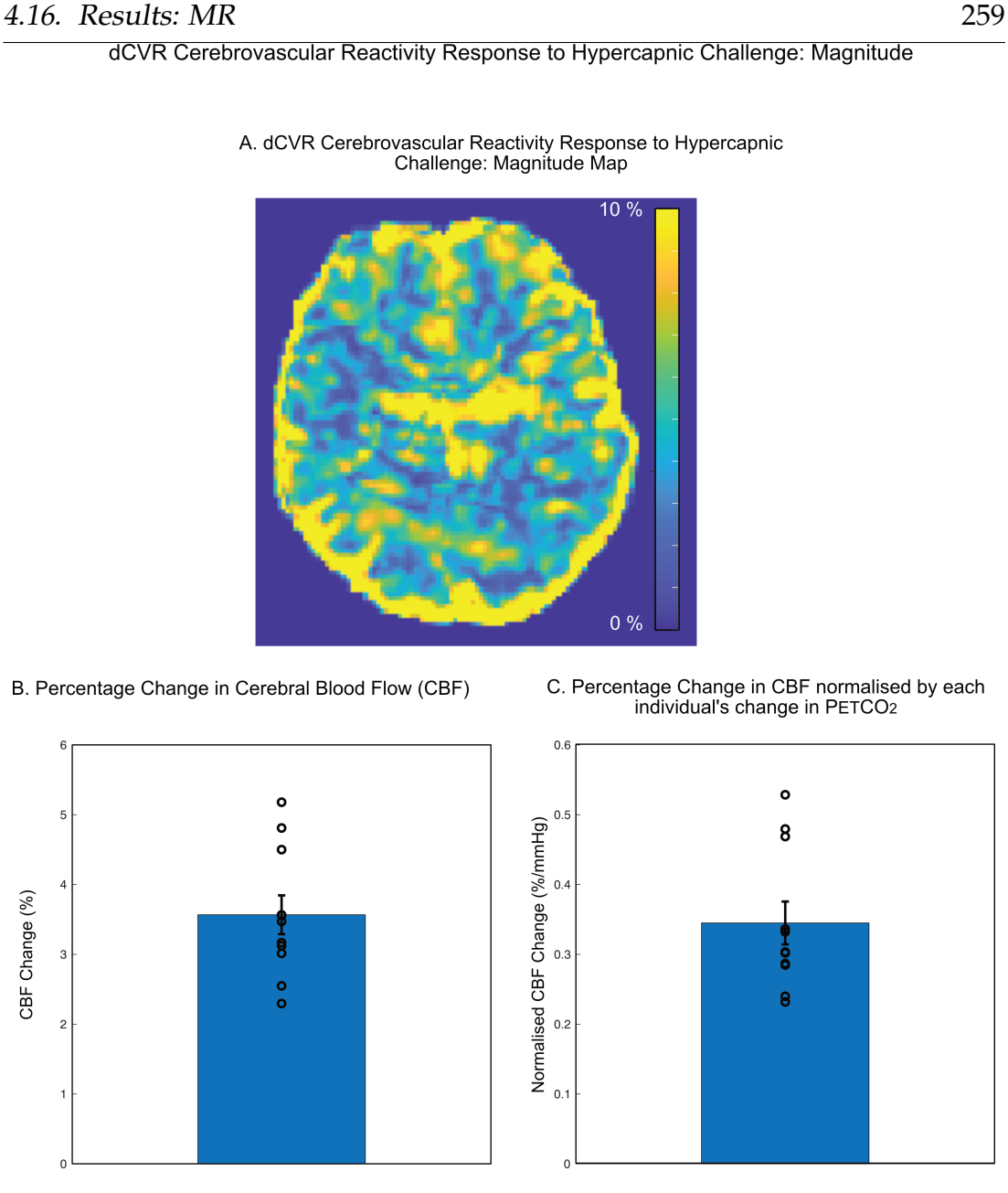


FIGURE 4.19: **dCVR Cerebrovascular Reactivity Response to Hypercapnic Challenge: Magnitude.** A. A single slice, axial example of a dCVR CVR magnitude map showing the response to the hypercapnic challenge. The colour bar shows the higher CVR magnitude in yellow, and lower magnitudes are shown in blue. B. dCVR magnitude of response to a hypercapnic challenge as percentage change of cerebral blood flow (CBF) from normo- to hypercapnia, and C. normalised to the individual participants' $PETCO_2$. The bar represents the group mean and the error bar represents the standard error of the mean. dCVR dynamically modelled BOLD CVR), mmHg (millimetres of mercury), $PETCO_2$ (end tidal partial pressure of carbon dioxide), % (percent)

BOLD CVR: Time to Peak

Figure 4.20A shows an example of a single axial brain slice. This shows the dCVR time to peak map with the colour bar showing areas of longer TTP in yellow and shorter TTP in blue. Figure 4.20B shows that when comparing the percentage change from normo- to hypercapnic conditions for dCVR TTP in the grey matter increased by 30.0±5.2 s after hypercapnia.

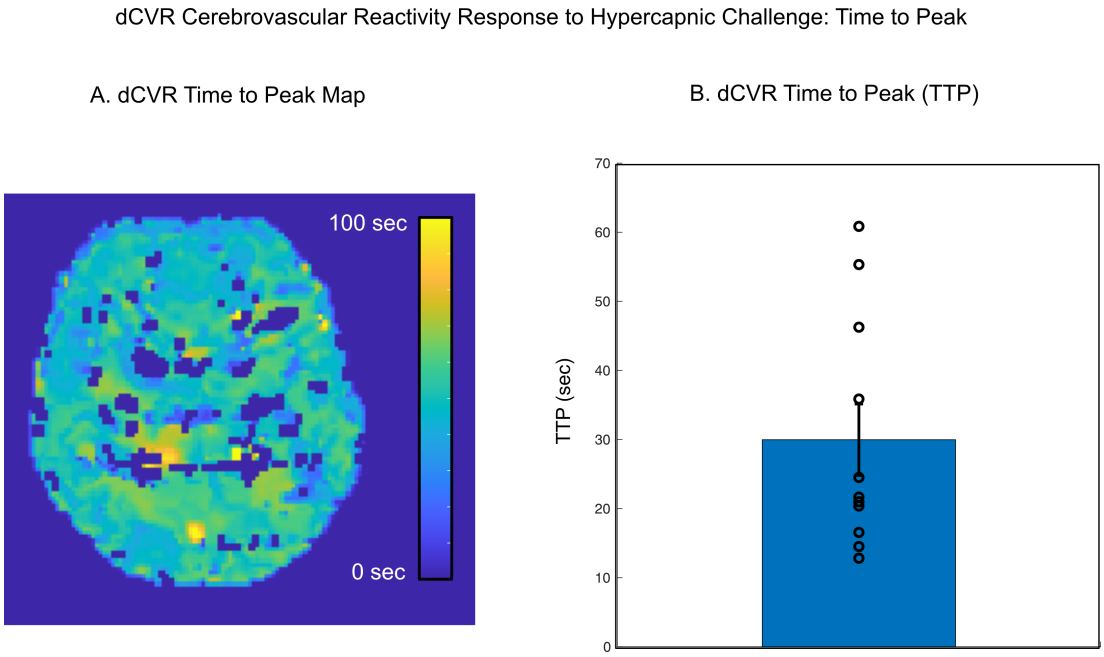


FIGURE 4.20: **dCVR Cerebrovascular Reactivity Response to Hypercapnic Challenge: Time to Peak.** A single slice, axial example of a dCVR dynamically modelled BOLD CVR (dCVR) time to peak (TTP) map showing the response to the hypercapnic challenge. The colour bar shows the longer TTP in yellow, and shorter TTP are shown in blue. , % (percent), s (seconds).

4.17 Discussion

In summary, both the hypercapnic challenges showed a significant change between normo- and hypercapnic conditions. Part 1 used a MPLD eASL sequence with a steady state block HC. The eASL analysis used Bayesian inference with a gamma dispersion model and included modelling for macrovascular components. The CVR increased, the aCBV showed no change, and the ATT decreased. Part 2 used a pseudo-sinusoidal hypercapnic challenge with a multiband BOLD sequence and involved analysis with dynamic modelling of CVR. Here, the CVR magnitude increased and the TTP increased.

4.17.1 Respiratory Stimulus

For part 1, the steady state hypercapnic challenge provided a significant increase in $P_{ET}CO_2$ from normo- to hypercapnia during the eASL scan. This supported the aim to provide a suitable HC using a respiratory stimulus of inhaling 5% CO_2. However, the variation across participants was higher than in chapter 2, during which the $P_{ET}CO_2$ was targeted to the individual participant's baseline using a RespirAct^{TM}. For part 2 during the BOLD scans, the HC was a pseudo-sinusoidal paradigm of 1 min on / 1 min off. The $P_{ET}CO_2$ significantly increased during the HC. This was quite a significant increase of about one third of the baseline value, which also supported the aim to provide a suitable HC.

4.17.2 eASL

Part 1 of this study focused on expanding work by Pinto and colleagues (2023) [188]. Improvements also included using an unbalanced pCASL sequence to enhance the robustness of the CBF estimates. In order to make the most of the

MPLD sequence metrics, a more advanced model was used for the analysis than in chapter 2.

eASL CVR Measured at Normo- and Hypercapnic Conditions

The eASL CVR measurements showed a significant increase in CBF, which suggests that the brain vasculature responded substantially to the hypercapnic challenge. This supported the aim to measure CVR, induced via a steady state HC, with a MPLD eASL sequence. The CBF increase (∼60% or 5.8±0.5 %/mmHg) was similar to the CBF measured with single PLD pCASL in chapter 2 (Params-1: ∼60% increase, equivalent to 6.08±1.45 %/mmHg. The regional variation in velocity across different arteries was an important consideration in chapter 2. However, the effect of changes in blood velocity on the pCASL labelling efficiency should have been decreased, as the MPLD eASL sequence used in this chapter should better account for regional variation.

Pinto and colleagues (2023)[188] analysed a MPLD (6 PLDs) ASL dataset with a +10 mmHg HC [188]. When calculated with BASIL and the dispersion effect model, there was a significant decrease in CBF (∼10–22%). This was compared to analysis without the dispersion modelling, which gave a final result of a ∼33% increase in CBF from normo- to hypercapnia. The CVR response in this chapter was almost double that of Pinto and colleagues (2023), which was calculated here as 3.3 %/mmHg [188]. Donahue and colleagues (2014) [66] had a smaller CBF increase of (8.2%–27.8%), and they used pCASL (MPLD 100 ms, 400 ms, 700 ms, 1,000 ms, 1,300 ms, 1600 ms, 1900 ms) and a constant rate (12 L/minute) 5% inspired CO_2 challenge. Additionally, this was also higher than Ho and colleagues (2011) [111] who used ASL-QUASAR (PASL) technique with Signal Targeting with Alternating Radiofrequency (STAR) labelling) with

an increase in $P_{ET}CO_2$ of $\sim 1/3$ baseline ($\sim$14mmHg) and saw a $\sim$20% increase in CBF, calculated here as $\sim$1.4 %/mmHg.

The Pinto and colleagues (2023) MPLD ASL sequence was a more traditional balanced pCASL sequence, which would have been more sensitive to changes in labelling efficiency. Each pair of TRs had a PLD, which increased for the next pair. These parameters were similar to Params-3 from chapter 2 (Params-3: G_{avg}=0.8, G_{max}=7.8, RF duration=600 ms, RF spacing=400 ms, [13]). Whereas, the eASL sequence used here was a time encoded pCASL sequence, so all of the PLDs were interleaved together and were decoded afterwards. The shorter scan duration for eASL would also be beneficial. Without knowing the 'ground truth,' it is difficult to say for certain which results are fundamentally 'better' than others. It is hard to make assumptions about whether there was more or less under/over estimation of blood flow with the different methods [217].

eASL aCBV Measured at Normo- and Hypercapnic Conditions

The group aCBV increased by $\sim$44%. However, aCBV did not significantly change during hypercapnia, which suggests that the arterial blood volume in the brain was not affected by the CVR response. This did not support the aim to use a HC to increase the aCBV. Alternatively, this lack of significance may be due to the amount of variation i.e. noise in the datasets. Here, individual participants showed a large variation in aCBV, with some increasing and some decreasing during hypercapnia. As Chapter 2 was only a single PLD pCASL sequence the aCBV was not estimated. However, with the BASIL toolbox it is possible to provide rough estimates of aCBV. For single PLD, that method is known to rely heavily on the priors and would not account for regional variation in the aCBV as well as the MPLD analysis. Additionally, there would not be much sensitivity to aCBV in the single PLD analysis, as the sensitivity to

aCBV comes from short PLDs, when the bolus is still in arterial vessels. Given the long PLD used in chapter 2 it would be unlikely that any of the bolus would have remained in the arteries to calculate this accurately.

The results from this chapter, did show a larger difference in aCBV than Pinto nd colleagues (2023)[188], even if this difference was not significant. Pinto and colleagues (2023) results, when including the dispersion model, showed a decrease in aCBV by ∼44-74% compared to without the dispersion model. This gave a final result of a significant ∼30% decrease in aCBV. The individual participants datasets were not presented, so it is not possible to say whether they also saw such a large, and often opposing, variation in aCBV response to the HC. Ho and colleagues (2011)[111] saw an increase in aCBV by 11% in the large arteries. One reason for the more varied results in this chapter may be the use of the semi-automated gas delivery device. This differs from the RespirAct^{TM} used in Pinto and colleagues (2023), which targeted the HC to each participant's baseline. The RespirAct^{TM} was understandably more precise at maintaining consistent $P_{ET}CO_2$ increases across participants.

eASL ATT Measured at Normo- and Hypercapnic Conditions

The eASL ATT values decreased with hypercapnia. This supported the aim to use hypercapnia to decrease ATT. This suggests that the blood velocity, specifically in the arteries, increased during hypercapnia. The reduction in transit time in this study was also larger (∼22%) when compared to some previous studies such as Donahue and colleagues (2014)[66] (4.6%–7.7% decrease). It was also larger than in Pinto and colleagues (2023)[188], who found that, when using the dispersion model, ATT decreased ∼17-26%, which give the final result of a ∼15% ATT decrease.

Fothergill and colleagues (2024)[84] found that the ATT priors inputted into BASIL had a noticeable effect on the resulting ATT. They used ATT priors of 1.3, 1.7, and 2 secs with one simulated dataset [176] and one healthy young adult dataset. The ATT times were chosen to compare healthy and patient ATT times [5, 152]. When comparing a more traditional least-squares model to BASIL, the artificial lesion was more apparent in the least-squares analysis than when using the BASIL analysis. They inferred that this meant the least-squares model was less dependent on the user input ATT priors. As patient groups tend to have longer ATT times than healthy adults [7, 5] it would therefore be important to ensure that the user input ATT times were accurate to the specific patient (or at least patient group) being studied. As the data in this chapter were of healthy participants this bias would be less of a concern. However, this would indeed be an important consideration for later translation of this method to clinical use, especially for datasets with a low SNR.

4.17.3 BOLD dCVR

BOLD dCVR Magnitude Measured with a pseudo-Sinusoidal Hypercapnic Challenge

This study used a novel algorithm called BEL to estimate dCVR magnitude, which defined the amplitude as the area under the HRF curve. The dCVR value of CVR magnitude increased by 3.2%, which was the equivalent of 0.3%/mmHg when normalised by the participants' $P_{ET}CO_2$. This suggests that during the pseudo-sinusoidal HC the CVR also increased.

Of the five different dCVR analysis methods Shams and colleagues (2023)[206] compared, CCA was recommended as a good compromise between reliability and computational power/time. A similar study to this chapter used optimised

CCA (one of the other dCVR methods compared in Milbourn, Shams and Chen, (2023)[155], which was slightly different to the BEL method used here. The CCA algorithm uses a gamma basis in the temporal dimension to prioritise temporal features in the data (info on the algorithm [192, 207]. To estimate the HRF the CCA method therefore prioritises the temporal features of the BOLD and $P_{ET}CO_2$ data [113, 207]. This means that CCA finds the best linear combinations of two sets of multidimensional variables to maximise the correlation between the resulting basis vectors, allowing it to better deconvolve the HRF from noisy data than conventional methods [179].

Milbourn, Shams and Chen (2023)[155] found that the HRF amplitude was 26.3±6.5 %/BOLD/mmHg/s for young adults (18-43 years), which significantly increased for older adults to 72.6±5.75 %/BOLD/mmHg/s (67-85 years). CVR amplitude was also higher in the grey matter compared to the white matter regions of the brain. Although the GM and white matter were not compared in this chapter, the difference across five cortical GM areas are compared in the next chapter.

Atwi and colleagues (2018)[16] used a deconvolution method based on a vascular transfer function to separate the amplitude and timing effects of CVR. The results of this study defined the vascular transfer function (VTF) as the response of vessels to the CO_2 change, and inferred this via the BOLD time series. Additionally, they used very similar CVR metrics to this chapter, defining area under the curve (AUC) as a measure of % BOLD change per mmHg of $P_{ET}CO_2$ (comparable to the dCVR magnitude metric) and time to peak in seconds, both metrics of which should be comparable to those output from the dCVR analysis based on the haemodynamic response function. Of N=60 participants, 18 were healthy controls, 20 had moderate white matter hyperintensities (WMH), 12 had severe WHM, 10 had cerebral autosomal dominant arteriopathy with

subcortical infarcts and leukoencephalopathy (CADASIL). They tested the analysis method on a sinusoidal, box-car, ramp HCs and a 'spontaneous' resting state. These were delivered with a RespirAct^{TM}, with a maximum change of 10 mmHg (other than the resting state). A more conventional linear regression coefficient of BOLD regressed against $P_{ET}CO_2$ was also used to compare to the VTF. They measured the mean conventional CVR in GM (0.26±0.06 %BOLD/mmHg) with the AUC in GM measured to be similar to the result of this chapter (0.3±0.06 %BOLD/mmHg).

Conventional CVR analysis resulted in no difference between healthy controls and patient groups magnitude, when looking at GM, (df=3,F=2.2, p=0.10). VTF magnitude was also no different between groups in GM (df=3, F=0.78, p=0.51). At the one year follow up (N=20 of the 42 patients) the conventional CVR method showed no difference between sessions (0.15) VTF magnitude in the GM was significantly different than the first session (df=1,19, F=5.9, p=0.026, inter class correlation 0.36).

Comparison of Different Magnitude Analysis Methods

Rangaprakash and colleagues (2021) [198] compared two different methods for analysing the HRF. First, deconvolving the HRF from the BOLD time series (to estimate latent neural activity), and second a standard canonical HRF (with two gamma functions). They compared results between healthy (matched controls) and obsessive-compulsive disorder (OCD) patients (both before and after 4 weeks of cognitive behavioural therapy (CBT) treatment) (N=44). They used a HRF deconvolution method based on Wu and colleagues (2013)[253], which is based on the idea that the HRF is not identical to the BOLD activation and is influenced by neurotransmitters release. The metrics they used included response height of the HRF (a measure of magnitude), TTP and FWHM.

There was a significant main effect with all 3 HRF parameters (F=8.65±0.95, p=0.004±0.001). There was also a significant group x time interaction (F=6.89±0.83, p=0.008±0.001) for magnitude and TTP.

Pre-treatment, OCD patients had shorter, quicker, narrower HRFs compared to controls (T=3.23±0.31, effect size: Cohen's =0.78±0.08). Post-treatment OCD patients had taller, longer, broader HRF compared to pre-treatment. Pre- to post-treatment OCD patients HRF magnitude increased (T=3.03±0.27, Cohen's d=0.73±0.09). There was no change between controls or OCD w.o. treatment (wait list) after 4 weeks. Negative association between % change in HRF magnitude and % change in OCD severity after treatment (R=-0.44, R^2=0.19, p=0.0028). This suggested that HRF would be useful for studying patient groups.

BOLD dCVR Timing Measured with a pseudo-Sinusoidal Hypercapnic Challenge

The dCVR timing metric of TTP in this study was measured as the time to the peak of the HRF curve. This chapter found that TTP was increased by 30.0±5.2 s during hypercapnia. Similar to this chapter's results, the Milbourn, Shams and Chen (2023) CCA dCVR results showed time to rise (TTP) also increased with a hypercapnic challenge [155].

However, that dataset used a dual-echo BOLD sequence which can lead to compromises with optimising simultaneous acquisition of a pCASL data. It also used a different hypercapnic challenge, where the sinusoidal modulation of $P_{ET}CO_2$ included hypocapnia $\sim$ 4 mmHg below the participant's baseline as well as hypercapnia $\sim$ 4 mmHg above the participant's baseline for three repeats of 120 seconds [29, 146, 206]. It may be that the benefit of using a more complex analysis shines through in older adults and disease models, where the dCVR methods may be useful for understanding vascular ageing where CVR responses become more varied and less predictable [112].

For the Atwi and colleagues (2018)[16] study, the TTP increase was smaller than this chapter (7.5±1.6 s). TTP was significantly smaller in healthy controls compared to patient groups GM (df=3, F=2.8, p=0.049), but showed no significant pairwise differences ($p > 0.05$). At the one year follow up (N=20 of the 42 patients) VTF TTP in the GM was not different than the first session (p=0.76, interclass interval 0.64).

Comparison of Different Timing Metric Analysis Methods

Rangaprakash and colleagues' (2021)[198] measures of HRF showed that, post-treatment, OCD patients TTP was faster than pre-treatment (T=3.23±0.30, Cohen's d=0.78±0.09). More specifically, the TTP increased in the right caudate tail and left supplementary motor area (T=2.89±0.29, Cohen's d=0.70±0.07). There was no change between controls or OCD without treatment (wait list) after 4 weeks. Post-treatment OCD HRF no different from controls suggests treatment 'normalised' OCD HRF towards control values. This suggests that using HRF analysis methods could be applied to a wider range of neuro-disorders, beyond cerebrovascular diseases.

4.17.4 Limitations

Standardisation of MPLD ASL Acquisition and Analysis

As mentioned in section 4.16.1 the eASL CVR results from this chapter were somewhat different from previous studies. Without knowing the ground truth it is difficult to say for certain that these results are fundamentally 'better' than previous results. The data collection for this chapter started in early 2023. Since then, Woods and colleagues (2024) and OSIPI have published recommendations for the acquisition and analysis of pCASL data [251, 178].

Additionally, this chapter's analysis had already been completed by the autumn of 2023. The results of the OSIPI challenge results for evaluating single pCASL analysis pipeline were only released in 2024. Fortunately, the results for BASIL were favourable [178]. This initiative has more recently been endorsed by the International Society for Magnetic Resonance in Medicine and will soon be expanded to evaluate the analysis of pipelines and toolboxes for MPLD ASL. This chapter followed the key acquisition recommendations for ASL from Woods and colleagues (2024)[251] including: using pCASL, a time-encoded sequence, variable TRs, background suppression, the scan duration was longer than ∼4 min. On the whole, this chapter also followed the key post-processing recommendations including: the minimum reporting of perfusion and ATT, using a kinetic signal model with a model that incorporates variable ATT, and the intravascular signals were modelled (using the macrovascular modelling from the BASIL toolbox). Motion correction is also recommended, therefore a limitation of using the BASIL analysis was that (although attempted) it was not possible to perform motion correction on pre-subtracted (i.e. the label subtracted from the control images), decoded data from the GE scanner. Therefore, this processing pipeline was not able too rectify this acquisition problem. However, discussions with the developers of other toolboxes such as ExploreASL suggest it would be possible overcome this problem [162]. Overall, if the acquisition and analysis of ASL was more standardised it would be possible to make direct comparisons of datasets. Another limitation was that the pipeline takes a long time to run, as one dataset would take over four days locally, and required the use of an HPC in order to analyse more datasets simultaneously.

dCVR Analysis Requirements

BOLD CVR measures tend to be noisy and subsequently have a low SNR, though generally less noisy than ASL. Another complication with BOLD CVR is that the frequency of the BOLD and $P_{ET}CO_2$ time courses often overlap increases the difficulty of deconvolving the HRF. BEL performs well even under these circumstances, however this does come at a cost. A major limitation of the BEL method is the lengthy time it takes to set up and run the analysis pipeline. For one dataset, it took over 10 days to run locally, whereas the CCA method only took about 24 hours to run one dataset. Therefore, CCA may provide a better compromise between the reliability / robustness of the results and the time required to run the pipeline [155]. It was also computationally heavy and the use of a HPC may not be as universally accessible as more simple analysis that can be run locally on a laptop. Therefore, the choice of model depends on if the analysis performed prioritises accuracy or speed. So far, this method of dCVR requires a HC or other task, and as previously described it would be more beneficial to perform clinical scans without the need for HC equipment due to cost, space and training etc.

Kazan and colleagues (2016)[125] aimed to improve sensitivity of resting state fMRI (without a task) using a method called vascular auto rescaling (VasA) , which was based on analysing slow oscillations of less than 0.1 Hz caused by natural variation in respiration rate. It did however use residuals of task-related fMRI to approximate the amplitude of the small CO_2 oscillations. They used open source datasets (Human connectome project [20]) to estimate directly from the time series data [249]. The analysis method involved using a general linear model for the time series of each voxel, and the resulting residuals map was then Fourier transformed. Then the averaged square root of the power within the freq band of 0.01-0.08 Hz and the rescaling derived from linear

regression plots. They found a strong positive correlation between the Vascular-Space-Occupancy (VASO) low-frequency %CBV maps and the VasA maps (R=0.76, $p < 0.05$, N=3), and within the single subject (R=0.39, $p < 0.05$).They also found functional sensitivity average increased by 10%. At a group level, this increased voxel activation by up to 42% for tasks and t-scores around 30% (visual cortex), average around 10% though. They also compared these results to CVR and CBV maps (from 7T VASO) to show vascularisation differences. Results suggested that this method reduced inter-individual vascularisation variations that modulate the BOLD signal. They pointed out that increasing from 1.5 T to 4 T produces a 20% increase in sensitivity, so this VasA improvement was substantial. Therefore, investigating the dCVR sensitivity measures would be a useful next step, as well as more directly comparing dCVR to eASL CVR metrics.

It is important to note that a lot of the previous application of HRF analysis has been to infer latent neuronal activity. This is because neural activity is proposed to influence the HRF via neurovascular coupling (NVC), which in turn influences CBF, vasodilation/vasoconstriction mechanisms and subsequently CVR. Additionally, certain psychological symptoms are often related to neurotransmitter imbalances. In terms of NVC, glutamatergic and GABAergic interneurons release neurometabolic modulators which then effect CBF [45]. This in turn will contribute to the BOLD effect and therefore the HRF [38]. For example, glutamate acts on N-methyl-D-aspartate (NMDA) receptors which will result in vasodilation near neurons ([43] influencing the HRF. High glutamate therefore results in taller, quicker, narrower HRFs (via nitric oxide release). Whereas, high GABA will result in the opposite [161]. Serotonin is a vasoconstrictor which alters the blood brain barrier permeability for modulating NVC [161]. CVR has still been investigated in psychological conditions with both pCASL

and BOLD MRI, (including HRF analysis), showing differences in HRF with both Doppler and infrared spectroscopy measures [135, 134, 232, 72]. In terms of the clinical application of this vascular physiology knowledge, it is harder to make inferences about psychological conditions, as they have traditionally been defined by behavioural symptoms rather than the underlying physiology that causes the behavioural symptoms. Though cerebrovascular diseases often results in psychological problems, such as cognitive decline.

However, the information sought in this chapter is purely vascular based. This information is often dismissed as noise in BOLD functional connectivity studies and is removed or ignored, despite providing information that will in fact provide insight in to many clinical conditions. For carotid stenosis, stroke and vascular dementia, which are defined more by their physiological and vascular abnormalities than these more complex psychological conditions. This means inference of a CVR biomarker would likely be more directly applicable to these conditions compared to the psychological conditions.

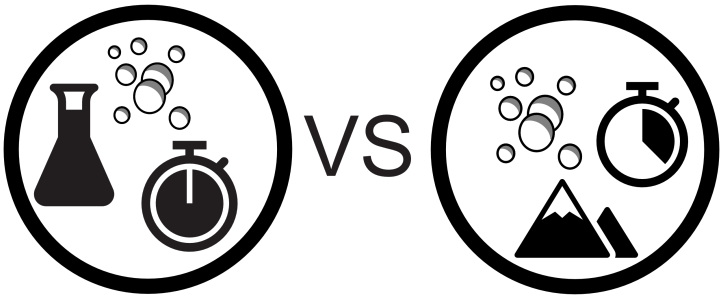
4.17.5 Conclusions

The CVR metrics from this chapter measured using a MPLD eASL and BASIL methods showed a higher CVR, higher changes in aCBV and smaller changes in ATT than recent results [188]. This may be due to smaller/minimal changes in labelling efficiency between normocapnic and hypercapnic conditions with the pCASL variant used in this study. Greater variability in the hypercapnic challenge was observed than in previous work (chapter 2, [188]). This is potentially due to the use of a hypercapnic challenge based on a fixed inspired challenge.

The CVR metrics from the BOLD dataset analysed with the BEL dCVR method provided a qualitative measure for CVR magnitude, but potentially more robust

than more traditional analysis methods, especially in ageing and disease. Additionally, the dCVR analysis provided a quantitative measure for timing with time to peak. To continue this investigation, the next chapter will go on to more directly compare the differences between eASL and dCVR across different brain regions.

5 Comparing the Effect of a Hypercapnic Challenge on eASL, sinCVR and dCVR



5.1 Contributions to the Chapter

The dataset and data analysis for this chapter lead on from the work presented in the previous chapter. Hence the contributions to this chapter 4.1 also apply.

5.2 Visual Abstract

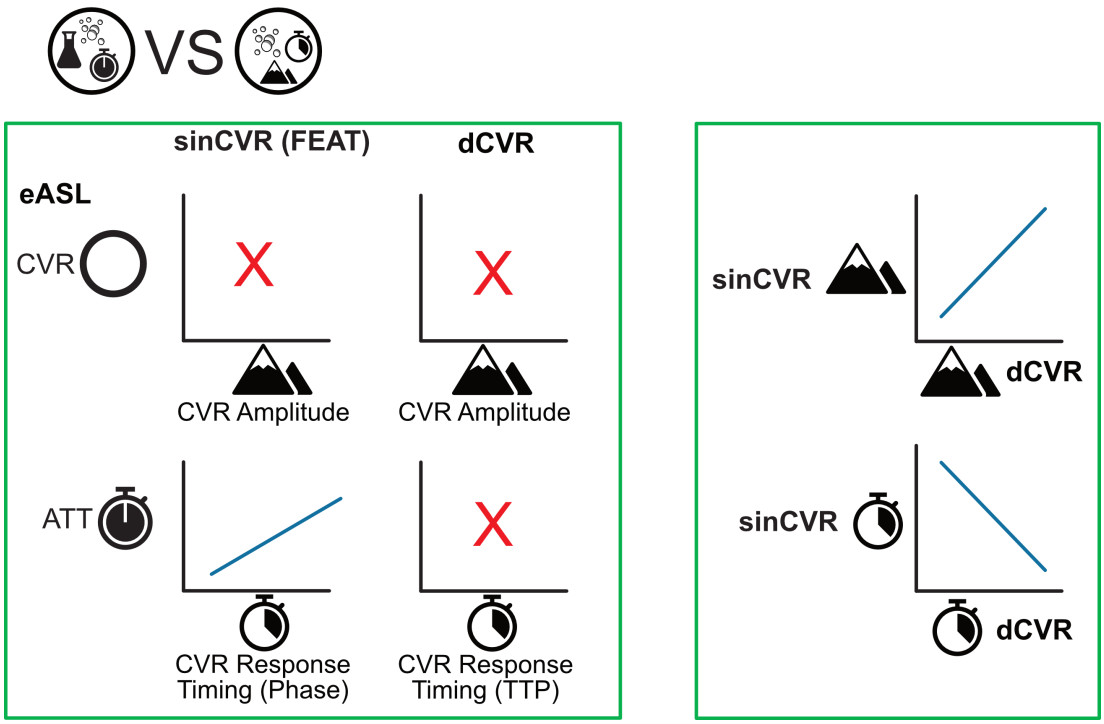


FIGURE 5.1: **Visual Abstract for Chapter 5.** This chapter compares the eASL and BOLD (dCVR) analyses from the previous chapter, along with an additional BOLD analysis (sinCVR), to investigate if there are correlations between these methods across five grey matter cortices. The measure of CVR magnitude from eASL did not correlate with those of sinCVR or dCVR. Measures of blood flow timing from eASL (ATT), correlated with those of sinCVR (phase), but not dCVR (TTP). sinCVR and dCVR CVR magnitude were positively correlated, but their timing measures were negatively correlated. ATT (arterial transit time), BOLD (blood oxygen level dependent), CVR (cerebrovascular reactivity), dCVR (dynamically modelled BOLD), eASL (enhstanced pseudocontinuous arterial spin labelling), sinCVR (sinusoidally modelled BOLD), TTP (time to peak).

5.3 Introduction

Building on the work from Chapter 4, this chapter directly compared the enhanced arterial spin labelling (eASL) and blood oxygen level dependent (BOLD) datasets. The results from Chapter 2 showed that blood velocity increases during a hypercapnia challenge (HC), and therefore affects the labelling efficiency of pseudocontinuous arterial spin labelling (pCASL) cerebrovascular reactivity (CVR) measurements likely vary across the brain. Therefore, it was also of interest to explore how the eASL and BOLD metrics varied across brain regions. Understanding the physiological basis of different CVR measurement techniques would help to identify the relative strengths and limitations of each method. This chapter also compared a more traditional sinusoidally modelled BOLD (sinCVR) output from FEAT (FSL, FMRIB software library), and the more complex dynamically modelled BOLD (dCVR) model [206]. sinCVR was named after the sinusoidally modelled BOLD technique, as this analysis was based on a sinusoidal waveform model created in FEAT ([252]). This was chosen as a more traditional method of BOLD analysis for CVR, so that the dCVR metrics could be compared with a simpler analysis. Comparison of sinCVR and dCVR to eASL CVR metrics included the eASL cerebral blood flow (CBF) to dCVR and sinCVR magnitude. Timing metrics included eASL arterial transit time (ATT) compared to dCVR time to peak (TTP) and sinCVR phase. Confidence in these metrics will be important for clinicians to implement quantitative CVR metrics in clinical practice.

5.3.1 Comparing Two Different BOLD Analysis Models to eASL

The eASL from the previous chapter used a multiple post labelling delay (MPLD) pCASL sequence, and was analysed with Bayesian Inference Arterial Spin

Labelling (BASIL) toolbox. This provided absolute, quantitative values of CVR magnitude, via CBF and arterial cerebral blood volume (aCBV). The BOLD data from the previous chapter was analysed with a novel dCVR method, which provided qualitative outputs of CVR magnitude. The more traditional sinCVR method was expected to provide a similar measure of CVR magnitude to dCVR. For the blood flow metrics, eASL CBF and dCVR magnitude are the most similar to compare, as both originate from estimates designed for evaluating CVR [206, 52]. Where as, sinCVR and dCVR have a more similar signal origin, as they are both derived from BOLD.

BASIL analysis of eASL also provided a quantitative CVR timing metric via ATT. In contrast, the sinCVR timing metric of phase is more indirectly derived from the BOLD data. Whereas, dCVR BOLD provided quantitive timing metrics via TTP, and the sinCVR analysis provided a timing metric via phase. For timing metrics, eASL ATT and dCVR TTP are the most likely to be similar to compare, as ATT considers the transit time of the bolus and TTP considers the time from the start of the haemodynamic response function (HRF) response to the peak of the HRF. While ATT specifically measures arterial changes, BOLD timing metrics encompasses both arterial and venous vascular changes. The relationship between these two measures is less clear as the physiological basis of ATT is more direct than the derived TTP estimate.

If robust measures of CVR can be better defined, then an important next step for translation to a clinical setting will be the feasibility of interpreting the CVR measures. Linders and colleagues (2023) 'grey paper' recommended simply using a qualitative, visual inspection of CVR maps in a clinical setting [138]. However, given the results from the previous chapter and many other previous studies there is plenty of potential insight into clinical conditions to be gained from considering the quantitative CVR metrics. Some hospitals already use

CVR with hypercapnic challenges, however this application is rare and limited to research focused institutions (e.g. Western Ontario Hospital, Sunnybrooke Hospital, Baycrest Hospital, Toronto, Canada). Additionally, decisions on how to best proceed with the interpretation and inference of the CVR metrics will need to include a better understanding of the modelling and analysis steps required. First, each analysis method requires different resources in terms of financial cost, time investment, and computational power, each with their own cost-benefit trade-offs. Basic requirements to be able to run and analyse these scans are high, which alone may be unfeasible in a hospital setting regardless of the usefulness of the results. Second, the level of detail implemented in the models and what metrics are available from the output for inference will determine how useful the results are for prognosis and diagnosis of cerebrovascular disease (CVD). Third, test-retest reliability, accuracy and plausibility of the basic physiological assumptions are also critical if these methods are going to be adopted more widely. When comparing simper, quicker and more traditional methods of BOLD (e.g. sinCVR) to more complex, time consuming and computationally heavy methods (e.g. dCVR) these considerations are likely to influence the model chosen.

5.3.2 Comparing Different Brain Regions

Liu and colleagues (2023) brain atlas is shown in figure in chapter 1 (Fig. 1.4), and showed how different major arteries (anterior, middle and posterior cerebral arteries (ACA, MCA, PCA) supply different vascular territories and hence different brain regions and sub-regions (open source licence link [140]). This is important for understanding how the label dispersal for eASL is transported to the brain tissue, and how the blood supply in BOLD measures can be influenced by vascular structure.

Figure 5.2 shows the five main cortical grey matter regions, which are of interest for CVR metrics; Frontal Lobe (cyan), Insula (red), Occipital Lobe (green), Parietal Lobe (blue) and Temporal Lobe (magenta). Previous studies have used pCASL and BOLD to measure CVR across brain regions and brain networks [144]. Furthermore, MRI research has started to shift from studying brain activity within structurally distinct, specialised regions, to examining functional networks i.e. multiple areas that work together. This shift has been particularly important for understanding CVR changes in health and disease in relation to cognition. Understanding regional variation of both eASL and BOLD metrics provides further insight into understanding brain physiology for both the vascular and the neuronal systems. However, cognitive-level analysis is beyond the scope of the exploratory study in this chapter.

In this chapter, the eASL data and BOLD data (CVR magnitude and timing) from the previous chapter were compared across each of the five main cortices. The process of which is explained in more detail in the methods section 5.4.3.

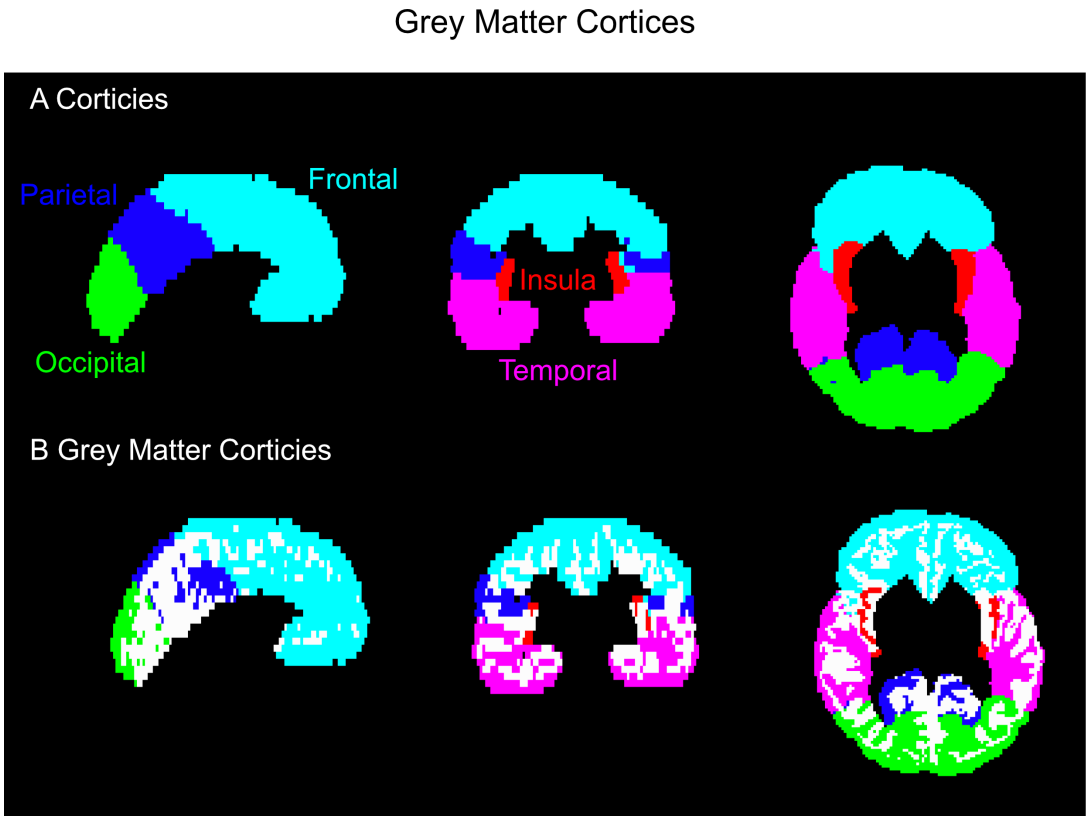


FIGURE 5.2: **Grey matter cortices.** A: Shows the five main cortices of interest for grey matter CVR. B: Shows an example grey matter mask superimposed over the top of the five cortices. Frontal Lobe (cyan), Insula (red), Occipital Lobe (green), Parietal Lobe (blue) and Temporal Lobe (magenta). Created using the MNI (Montreal Neurological Institute) atlas and an example dataset from this chapter.

5.3.3 Aims

This chapter aimed to compare the eASL and BOLD datasets from the previous chapter across the five main grey matter (GM) cortices. This chapter also aimed to compare a more traditional sinCVR method to the dCVR analysis, in order to compare the benefits and limitations of the two models. It aimed to compare the magnitude and timing metrics of the CVR response of the different analysis methods, in order to gain a deeper understanding of the underlying mechanisms and relationships between eASL and BOLD measures of CVR.

5.3.4 Hypothesis

The first hypothesis was that there would be a high correlation between the eASL and sinCVR/dCVR magnitude measurements.

The second hypothesis was that there would be a high correlation between the eASL and sinCVR/dCVR timing metrics.

The third hypothesis was that there would be a high correlation between the sinCVR and dCVR measurements for both magnitude and timing metrics.

5.4 Methods

5.4.1 Data Collection

Methods for the data collection are outlined in sections 4.16.1 (eASL) and 4.16.2 (BOLD) of chapter 4.

5.4.2 Data Analysis

5.4.3 Masks for Regions of Interest

Regions of interest (ROI) masks from chapter 4 were used to create individual masks for the five main GM cortices (Frontal Lobe, Insula, Occipital Lobe, Parietal Lobe, Temporal Lobe), which were then binarised to create cortical masks (see Fig. 5.4). However, in this case the eASL analysis used the same GM ROI masks as the BOLD analysis for consistency. This meant that both of the datasets GM ROIs were thresholded at 60%, so that the masks would cover exactly the same brain regions.

5.4.4 Data Analysis for eASL

The preprocessing steps for the eASL data were based on the previous chapter (using a BASH script that split the M_0 volume from the perfusion data). Next BASIL was run with the same parameters as the previous chapter, with the addition of user specified M_0 BET masks [50, 52, 53]. This step was added so that the eASL and BOLD registration would be closer than using the BASIL automated brain extraction tool (BET) images. BASIL was run on the ADA high performance cluster (HPC) using an updated slurm sbatch script.

Another difference to the previous chapter was that the data were registered to the eASL hyper M_0 space first, and then the CBF, aCBV and ATT change values were calculated. Figure 5.4 shows the analysis pipeline used for this. The brain extracted M_0 for normocapnia was first transformed into the brain extracted M_0 hypercapnia condition. This transform was then applied using applywarp to the normocapnia calibrated perfusion map images and ATT map images output from BASIL. Then with both the normocapnia and hypercapnia images in the same image space, the perfusion images (as a percentage difference) were calculated (Eqn 2.1).

5.4.5 Data analysis for sinCVR and dCVR

For the BOLD data, as in Chapter 4, the preprocessing included a BASH script for removing the first two volumes (dummy scans) using FSLROI and motion correction with MCFLIRT [122]. The analysis with FEAT included setting up a design file with the graphical interface (GUI) with pre-processing that consisted of the default values for high pass filtering (120 Hz) [123]. Spatial smoothing was manually checked at 1, 2, 3 ,4 and 5 mm, with the final FEAT model running at σ = 3 mm. Running FEAT took about 20-3minutes per dataset. A sinusoidal model was used to model the BOLD response to the 1 min on / 1 min off HC. EV (explanatory variable (EV), i.e., waveform) 1 was set as a sinusoid wave form for sine (period 120 s) and EV 2 was set as the cosine wave form (period of 120 s, phase 30 s). Another BASH script was used to run this design file for each of the participants' (both run 1 and 2) BOLD datasets in batch. The preprocessed BOLD filtered func data files were then used for the next part of the analysis for dCVR, as in the previous chapter. Running the dCVR modelling section of the pipeline took a 1-2 days on the HPC.

The sinCVR parameters, CVR magnitude and CVR phase, were calculated from the output of the FEAT data using FSLmaths. FSLmaths was used to take the square root of cope 2 added to the square root of cope 3, which was then square rooted and divided by the "mean func" data (Eqn 5.1a). The phase images for the BOLD data were calculated as cope2 divided by cope 3, and then the arc tangent function was used (Eqn 5.1b).

$$\sqrt{\frac{\sqrt{COPEsin^2} + \sqrt{COPEcos^2}}{mean_func}} \tag{5.1a}$$

$$CVR_{phase} = arctan\left(\frac{COPEsin}{COPEcos}\right) \tag{5.1b}$$

Figure 5.3 illustrates how this sinusoidal model was deconvolved with the BOLD data to give an HRF.

Figure 5.4 shows in more detail how these data were transformed into eASL hyper M_0 space. The filtered func data from the FEAT output was used to estimate CVR magnitude/phase, and these resulting images were then transformed into M_0 space. These where then further refined by restricting the ROI to each of the five main GM cortices. This was performed by co-registering the Montreal Neurological Institute (MNI) Cortical Atlas (McConnell Brain Imaging Centre, Montreal Neurological Institute, McGill University, Montreal, Quebec, Canada), via the MNI standard brain to the structural image and transforming it into M_0 space via the T1w image using FSL FLIRT and convert XFM.

The mean_func image from FEAT was used as a reference image to transform the sinCVR magnitude and phase images into M_0 space. FLIRT was used to provide the transform values and then 'applywarp' was used to transform the BOLD images into M_0 space [136, 150] .

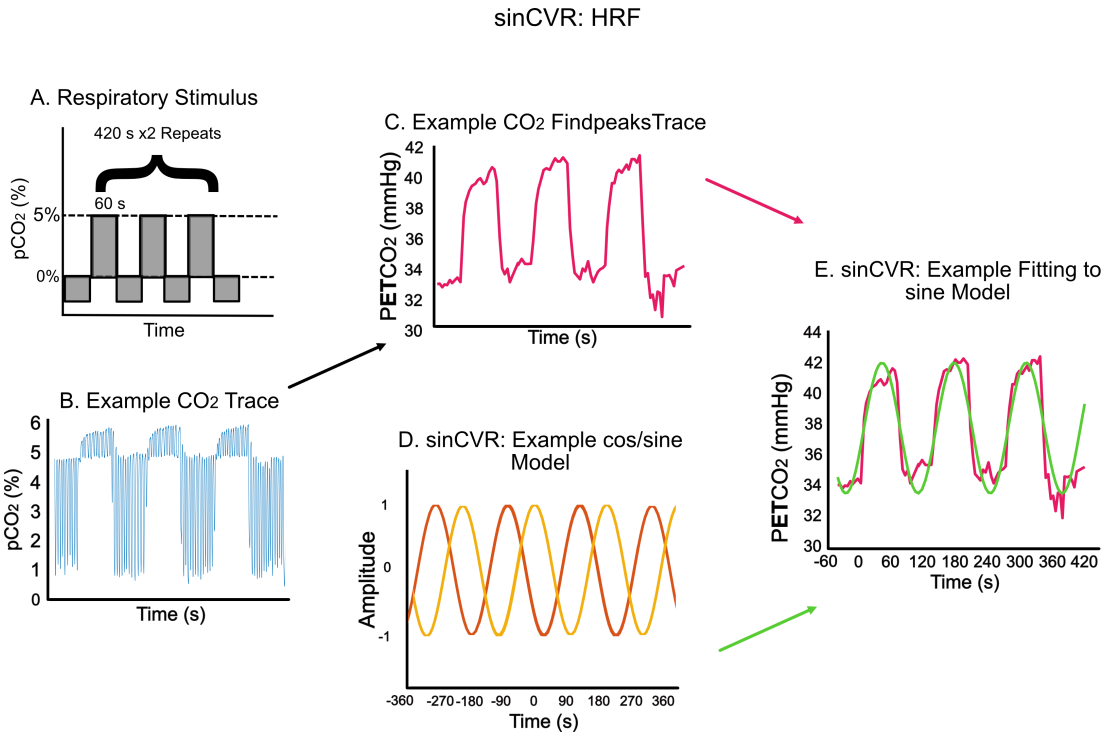


FIGURE 5.3: **sinCVR HRF.** Concept diagram showing the respiratory stimuli (A), an example for respiratory trace (B) which was converted to $PETCO_2$, and then processed using the Findpeaks function (C), and integration with the cos/sine model (D), to give an example HRF (E). $PETCO_2$ (end-tidal partial pressure of carbon dioxide), HRF (haemodynamic response function), sinCVR (sinusoidally modelled BOLD (blood oxygen level dependent MRI (magnetic resonance imaging))), s (seconds).

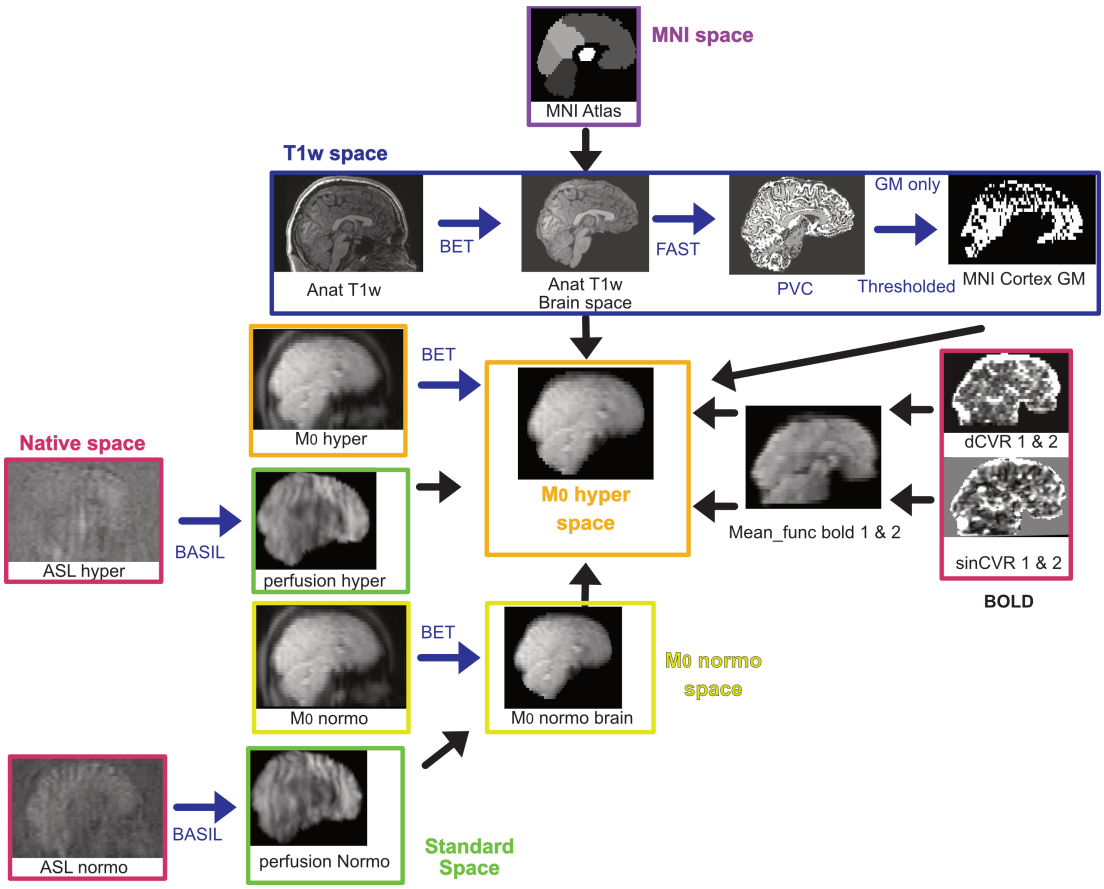


FIGURE 5.4: **Creating GM ROIs for the five main cortices.** Tools and transforms used for the eASL and BOLD datasets, moved into the eASL hyper M_0 space. Black arrows denote transforms and blue arrows denote tools/analysis methods. ASL (arterial spin labelling), BASIL (BASIL toolbox), BET (brain extraction tool), BOLD (Blood oxygen level dependent), dCVR (dynamically modelled BOLD), FAST (FMRIB advanced segmentation tool), hyper (hypercapnia), MNI (Montreal Neurological Institute), normo (normocapia), sinCVR (sinusoidally modelled BOLD, T1w ($T1_1$ weighted anatomical).

The FMRIB advanced segmentation tool (FAST) was used for the anatomical segmentation of the ROIs. The bash script that run this also ran the registration and the transforms to ROIs, which took about 30 minutes for participant's combined (sinCVR, dCVR and eASL (normo- and hypercapnia) data) dataset. Further analysis was performed in MATLAB (Mathworks, Natick, MA) to plot the eASL CVR vs. sinCVR magnitude values and the eASL ATT vs. sinCVR phase values in order to compare these measures across the five main GM cortices. The mean of the two BOLD runs was calculated as the first BOLD run plus the second BOLD run, divided by 2. The CVR magnitude for dCVR was used because the dCVR analysis used the regressed convolution of the partial pressure of end-tidal CO_2 ($P_{ET}CO_2$) and the HRF from the BOLD dataset. Therefore, the assumption made was that it would be a more refined regressor than assuming a sinusoid model. Hence, the dCVR and sinCVR magnitude values were also compared.

Similarly, a Matlab script was used to create the graphs and tables presented in the results, where the dCVR parameters were plotted as eASL CVR vs. dCVR magnitude values and the eASL ATT vs. dCVR time to peak (TTP). Additionally, the dCVR TTP was compared to the sinCVR phase.

5.4.6 Statistical Analysis

R^2 calculations were performed in MATLAB, with values of <0.2 considered to be uncorrelated, 0.2-0.5 as a small correlation, 0.5-0.7 as a medium correlation and >0.8 as a strong correlation. The differences between brain cortices were calculated with a one-way ANOVA, and results were considered statistically signifiant if the alpha was $p<0.05$.

5.5 Results

5.5.1 Comparison of CVR Magnitude

Comparison of eASL CVR and sinCVR Magnitude

Figure 5.5A shows that when comparing the percentage change from normo- to hypercapnic conditions, for the five GM ROIs, eASL CVR increased 62.3±5.6 % and sinCVR magnitude increased 3.2±0.2 % (group mean of medians across all five cortices±group standard error of the mean). There was no correlation, with an R^2 value of only 0.07 (p=0.0514). When these values were normalised by individuals $P_{ET}CO_2$, eASL CVR was 6.1±0.6 %/mmHg and sinCVR magnitude was 0.3±0.02 %/mmHg (group mean of medians±group error of the mean). There was no correlation, with an R^2 value of 0.00 (p=0.9400) (Fig. 5.5B). A table with a breakdown of each of the main five cortices is in the appendix D.2.2. There was no significant difference between the five different brain regions (eASL p=0.9211, sinCVR p=0.5214).

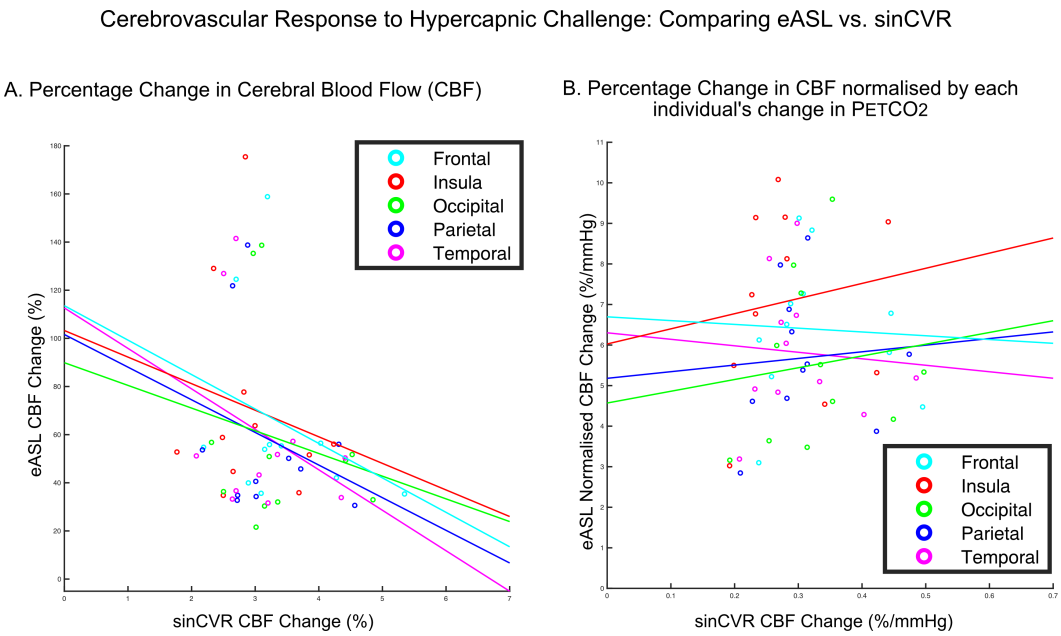


FIGURE 5.5: **Comparison of eASL CVR and sinCVR magnitude.** eASL and sinCVR were not correlated either before (A) or after normalisation to participant's individual $PETCO_2$ (B) (R^2=0.07 and R^2=0.00). Cerebrovascular reactivity (CVR), eASL (enhanced pseudocontinuous arterial spin labelling), hyper (hypercapnia), % (percent), mmHg (millimetres of mercury), $PETCO_2$ (end tidal partial pressure of carbon dioxide), sinCVR (sinusoidal modelled BOLD (blood oxygen level dependent)).

Comparison of CVR and dCVR Magnitude

Figure 5.6A shows that when comparing the percentage change from normo- to hypercapnic conditions, across the five GM ROIs, eASL CVR increased 62.3±5.6 % and dCVR magnitude increased 3.5±0.1 % (group mean of medians±group error of the mean). These results had no correlation, with an R^2 value of 0.07 (p=0.0506). When normalised by the individual's $PETCO_2$ eASL CVR increased 6.1±0.6 %/mmHg and dCVR increased 0.3±0.0 %/mmHg (group mean of medians±group standard error of the mean), which had no correlation with an R^2 value of 0.000163 (p=0.9260) (Fig. 5.6B). There was no significant difference between the five different brain regions (eASL p=0.9211, dCVR p=0.8867).

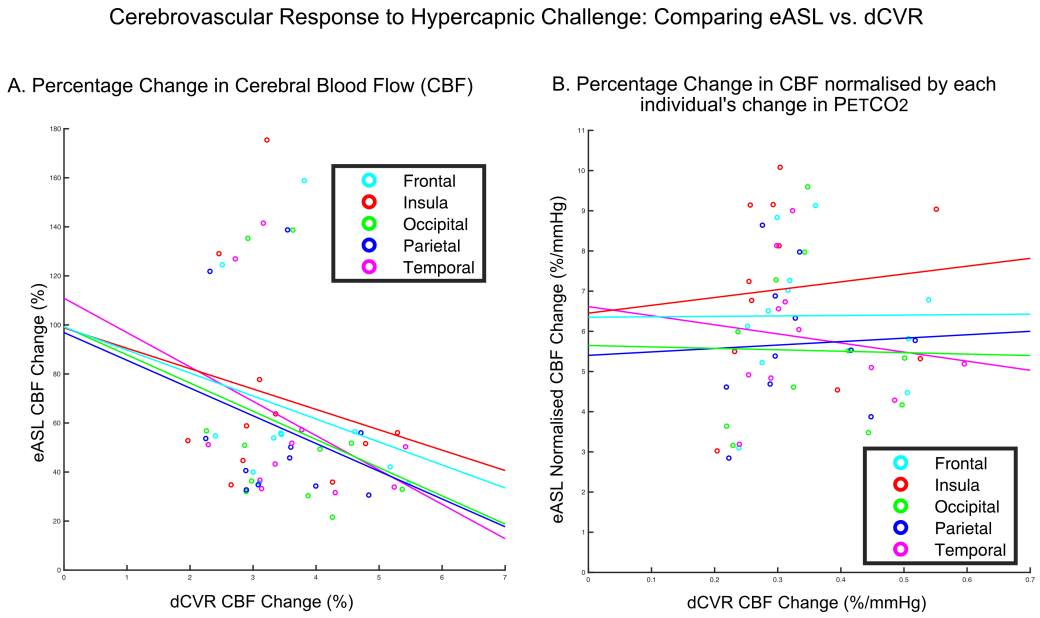


FIGURE 5.6: **Comparison of eASL CVR and dCVR magnitude** eASL and dCVR magnitdue were not correlated either before (A) or after normalisation to individuals' $PETCO_2$ (B) (R^2=0.07 and R^2=0.00). Cerebrovascular reactivity (CVR), dCVR (dynamically modelled BOLD) eASL (enhanced pseudocontinuous arterial spin labelling), hyper (hypercapnia), mmHg (millimetres of mercury), $PETCO_2$ (end tidal partial pressure of carbon dioxide).

Comparison of sinCVR and dCVR Magnitude

Figure 5.7A shows that when comparing the percentage change from normo- to hypercapnic conditions, for the five GM ROIs, the sinCVR magnitude increased 3.2±0.2 % and the dCVR magnitude increased 3.5±0.1 % (group mean of medians±group standard error of the mean). This showed a strong, positive correlation with an R^2 value of 0.832 (p=3.32e-22) (Fig. 5.7B). There increased no significant difference between the five GM ROIs (sinCVR p=0.5214, dCVR p=0.8867).

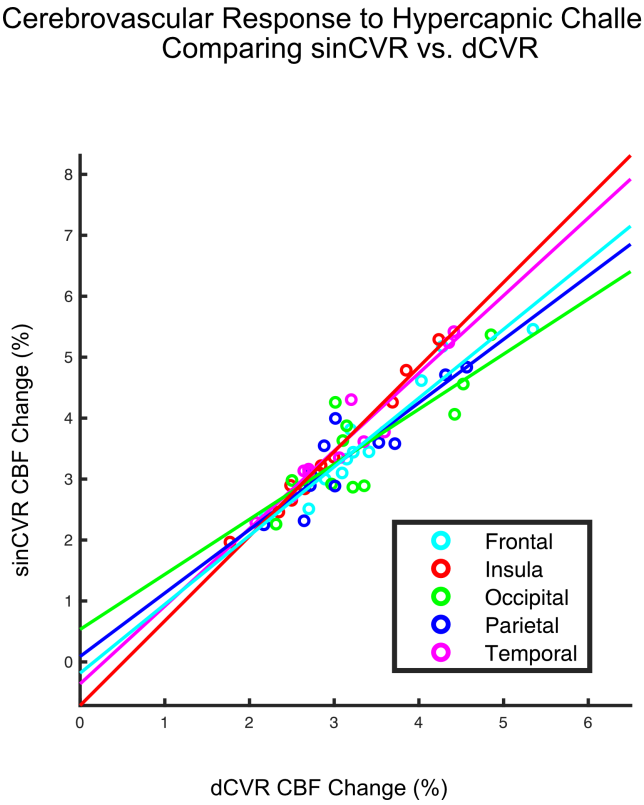


FIGURE 5.7: **Comparison of sinCVR and dCVR magnitude.** sinCVR and dCVR magnitude values had a strong positive correlation (R^2=0.82). Cerebral vascular reactivity (CVR), dCVR (dynamically modelled BOLD), hyper (hypercapnia), normo (normocapnia), sinCVR (sinusoidal modelled BOLD).

5.5.2 Comparison of Timing Measures

Comparison of eASL ATT and sinCVR Phase

Figure 5.8 shows that when comparing the change from normo- to hypercapnic conditions, across the five GM ROIs, timing metrics for the eASL ATT decreased -20.8±5.2 s and the sinCVR phase increased 0.4±0.0 radians (group mean of medians±group standard error of the mean). This showed a small, positive correlation, with an R^2 value of 0.263 (p=6.57e-05). There was no significant difference between the five different brain regions (eASL ATT p=0.1686, sinCVR phase p=0.9343).

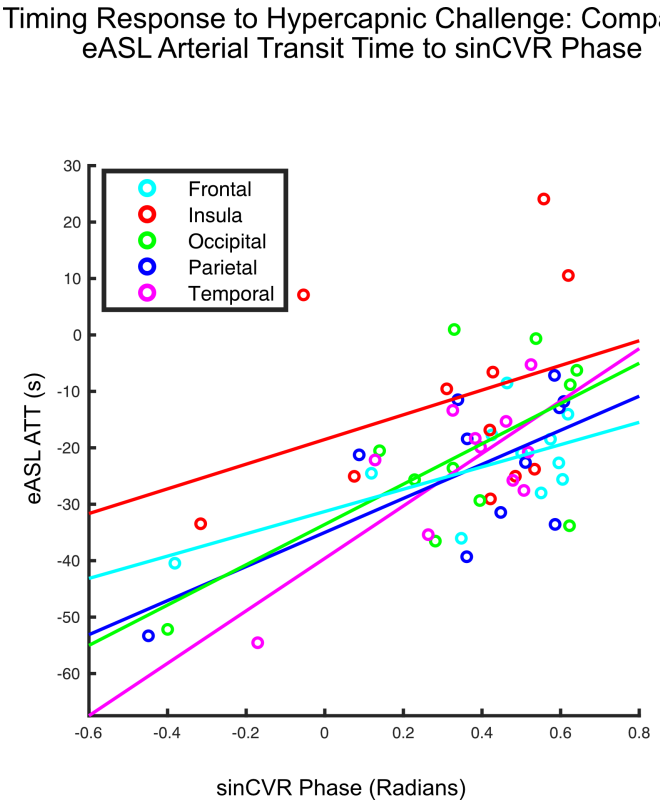


FIGURE 5.8: **Comparison of eASL ATT and sinCVR phase.** sinCVR and dCVR timing measures had a weakly positively correlation (R^2=0.26). Timing delay and phase data had a small positive correlation. ATT (Arterial Transit Time), eASL (enhanced pseudocontinuous arterial spin labelling), s (seconds), sinCVR (sinusoidal modelled BOLD), BOLD (blood oxygen level dependent).

Comparison of eASL ATT and dCVR TTP

Figure 5.9 shows that when comparing the absolute change from normo- to hypercapnic conditions, across the five GM ROIs, timing metrics for the eASL ATT decreased -20.8±5.2 s and the dCVR TTP increased 30.2 ±1.6 s (group mean of medians±group standard error of the mean). This was also not correlated, with an R^2 value of 0.05 (p=0.1140). There was no significant difference between different brain regions (eASL ATT p=0.1686, dCVR TTP p=0.9765).

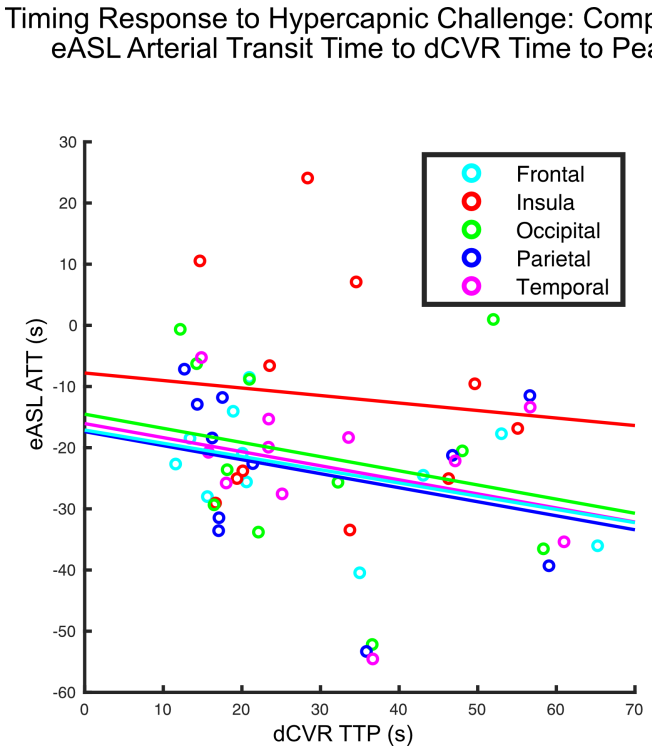


FIGURE 5.9: **Comparison of eASL Arterial Transit Time and dCVR Time To Peak.** Timing measures from eASL and dCVR were not correlated (R^2=0.05). dCVR (dynamically modelled BOLD), ATT (Arterial Transit Time) in s (seconds), eASL (enhanced pseudocontinuous arterial spin labelling), hyper (hypercapnia), normo (normocapnia), s (seconds), TTP (time to peak).

Comparison of sinCVR Phase and dCVR TTP

Figure 5.10 shows that when comparing the percentage change from normo- to hypercapnic conditions, across the five GM ROIS, the sinCVR phase increased 0.4±0.0 radians and the dCVR TTP increased 30.2 ±1.6 s (group mean of medians±group standard error of the mean), with an R^2 value of 0.22 (p=0.0003) this showed a small, negative correlation. There was no significant difference between brain regions (sinCVR phase p=0.9343, dCVR TTP p=0.9765).

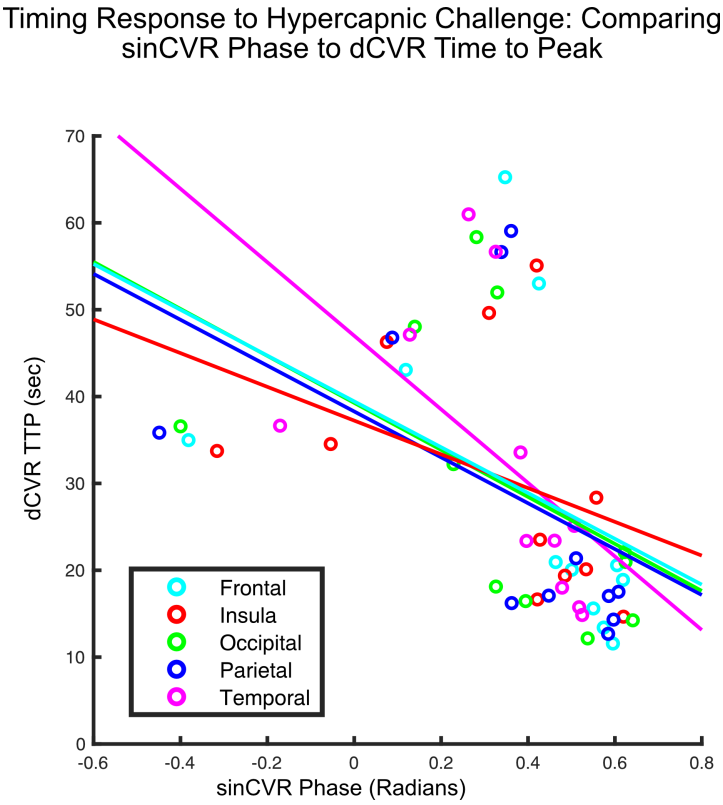


FIGURE 5.10: **Comparison of sinCVR phase and dCVR Time To Peak.** Timing measures from sinCVR and dCVR were weakly correlated (R^2=0.22). dCVR (dynamically modelled BOLD), hyper (hypercapnia), normo (normocapnia), s (seconds), TTP (time to peak), sinCVR (sinusoidal modelled BOLD), BOLD (blood oxygen level dependent).

5.6 Discussion

In summary, when comparing eASL, sinCVR and dCVR methods of calculating CVR magnitude, there was no correlation between eASL with either sinCVR or dCVR metrics. There was a small, positive correlation between eASL and sinCVR timing metrics, but no correlation between eASL and the dCVR timing metrics. When comparing sinCVR and dCVR, there was a strong, positive correlation between CVR magnitude measures and a small, negative correlation between the CVR timing metrics.

5.6.1 Respiratory Stimulus

The pCASL and BOLD datasets were collected with different HCs using a novel, semi-automated gas delivery box. As mentioned in the previous chapter, both HC paradigms appeared to induce a significant change in $P_{ET}CO_2$ from baseline, which resulted in a CVR response. Although, to account for this the data was normalised by the $P_{ET}CO_2$ change per subject for each paradigm. One of the reasons for the lack of correlation between eASL and BOLD datasets may have been due to using different HCs. Due to these differences, the time to peak at 5% $P_{ET}CO_2$ and length of time spent at the peak may have also been different. A 3 minute steady state challenge was used for eASL, and this more simple design may have resulted in a more exponential rise to the peak $P_{ET}CO_2$ level. The shorter blocks of 1 min on, 1 min off repeated three times for the BOLD, which was close to a sinusoidal HC. This presented a smoother, more naturalistic pattern, but this may have resulted in less overall time at the peak $P_{ET}CO_2$ compared to the eASL scan. Though previous publications have still referred to this type of paradigm as a block paradigm [264, 81], the naming as pseudo-sinusoidal was used because the observed response in the

$P_{ET}CO_2$ was closer to a sinusoid waveform. Additionally, the FEAT analysis model was also based on a sinusoid waveform. As noted in the previous chapter, a limitation of the HCs used here was that the mask kit used was not an SGD mask, as used by the RespirAct^{TM}. When using a non-rebreathing mask and a fixed inspired HC the subsequent end-tidal $P_{ET}CO_2$ is dependent on the ventilation rate and the participants CO_2 production rate. Whereas, when using a SGD mask, the alveolar gas ventilation is heavily influenced by the flow rate of fresh gas into the mask, with the rest of the minute ventilation filled with rebreathed gas. Hence, when ventilation rate increases the $P_{ET}CO_2$ will not initially reduce, as the alveolar ventilation is still fixed. The additional minute ventilation is effectively neutral in respect to the gas exchange. Therefore, when participants in this study breathed in the normocapnia gas mix it filled the alveoli in the lungs. Then the gas mixture will have mixed with the dead space air in the lungs, and some metabolic CO_2 would have been breathed out. When the participants then breathed in hypercapnia gas and it will have mixed with the dead space air, and the next breath exhaled will have included some of the hypercapnia gas CO_2 in addition to the metabolically created CO_2. In contrast, an SGD mask does not allow for as much mixing with the air in the dead space. Hence, $P_{ET}CO_2$ equilibrates over a few breath, which means the resulting $P_{ET}CO_2$ trace will more faithfully match the CO_2 paradigm trace, as will the arterial PCO_2, which drives the change in CBF. Computed end-tidal targeting to each individual participants $P_{ET}CO_2$ (as in chapter 2), would be one way to deliver CO_2 more precisely. A possible improvement for using the semi-automatic gas delivery box in this chapter would be to first manually adjust the flow rate to be set to the participant's breathing rate/volume during hypercapnia before starting the MR scan. The breathing rate would need to be set so that their breathing equalled the exchange rate of the alveoli. This

would ensure the dead space was topped up with previously expired gas and maintain a more consistent CO_2 level, and be more equal to the last breath [81]. This would require a SGD mask, and a limitation of this is that these masks are not commercially available.

Ito and colleagues (2008) validated the use of the RespirAct^{TM} with an SGD mask. They collected duplicate arterial blood samples, measuring partial pressure of carbon dioxide in the blood ($PaCO_2$), and assessed repeatability [119]. Across a sample of middle aged males (N=5, one smoker, one mild asthmatic), they found that there was an agreement between $PETCO_2$ and $PaCO_2$ for a range of 35, 40, 45 and 50 mmHg x 3 min HCs (mean difference: 0.5±1.7 mmHg p=0.53, 95% confidence interval (CI) -2.8 to 3.8 mmHg). There was also good repeatability between duplicate $PaCO_2$ samples (mean difference -0.1±1.6 mmHg, 95% CI: -3.7 to 2.6 mmHg). Therefore, their study demonstrated that, for respiratory rates greater than 12 breaths/min, when using an SGD $PETCO_2$ provides an accurate measurement of direct arterial blood analysis (i.e. $PaCO_2$). This is beneficial as it is a non-invasive method compared to taking a blood sample. Similar validation of the semi-automated gas delivery box used in this chapter would be useful for increasing confidence in future research projects.

5.6.2 Magnitude

eASL vs. BOLD Magnitude

The hypothesis that there would be a correlation between the eASL and sinCVR measurements of CVR magnitude was not supported, as there was no correlation between the eASL and sinCVR magnitude data. Additionally, the hypothesis that there would be a correlation between eASL and dCVR magnitude was also not supported, as the eASL perfusion and the dCVR magnitude data

were not correlated. This was in contrast to previous studies that have seen a strong correlation between ASL and BOLD data. For example, Mandell and colleagues (2008) previously found that BOLD and ASL datasets of patients with steno-occlusive disease (narrowing/blocking of blood vessels) had a strong correlation in the GM (r=0.83) [144]. Notably, their study used single PLD, pulsed ASL, which would have been limited by the CBF estimates sensitivity being confounded by changes in ATT. Additionally, they used a PLD of only 1000 ms, which was far less than current recommendations for healthy adults (1500 ms) or patients (2000 ms) [7].

A more recent study by Zhou and colleagues (2015) used a similar HC to this chapter with a 1 min on / 1 min off 5% CO_2 gas-mixture paradigm in healthy, older adults (37.8±14.3 years) [264]. They found a correlation between pCASL (PLD 1230 ms) and BOLD measures of GM CVR response at a whole brain level (r=0.61, p=0.01). However, they observed slightly lower values of CVR in the GM for both ASL CBF derived CVR (5.11±0.87 %/mmHg) and BOLD magnitude (0.23±0.04 %/mmHg). The most significant correlations they found between BOLD and ASL were in the occipital cortex (6.8 %/mmHg), which was higher than that of the frontal and parietal lobes (4.5 %/mmHg). Whereas, in this chapter, the ASL magnitude results were highest in the insula (7.1 %/mHg), followed by the frontal lobe (6.4 %/mmHg), but were not significantly different.

sinCVR vs. dCVR Magnitude

The hypothesis that the sinCVR and dCVR magnitude data would correlate was supported, as the sinCVR magnitude and dCVR magnitude were strongly correlated. As both sinCVR and dCVR magnitude metrics should have essentially been measuring the same underlying BOLD signal, it was reassuring that these metrics correlated.

In this chapter, the sinCVR magnitude was largest in the frontal and occipital lobes followed closely by the parietal, temporal and insula lobes, and all values were ∼0.3 %/mmHg change during hypercapnia. Whereas, the dCVR magnitude values were largest in the frontal followed closely by the temporal, occipital, parietal and then insula lobe, and were also ∼0.35 %/mmHg. In Zhou and colleagues (2015), the highest BOLD signal magnitude was in the occipital lobe (∼0.33 %/mmHg), followed by the parietal lobe [264]. So the pattern of occipital lobe then the parietal lobe matches the results of this chapter. However, these lobes were not the two highest magnitudes out of the five investigated in this chapter. Though it is worth pointing out that there was no significant difference between the values of the five different brain regions for eASL, sinCVR or dCVR, which may explain some of this discrepancy.

Many different analysis methods have been used for calculating CVR maps from BOLD. One study similar to this was by Blockley and colleagues (2011), who also used a 1 min on/off hypercapnic challenge (although delivered by a RespirAct^{TM}), and used a fast Fourier transform and linear least squares fitting analysis [29]. They estimated the BOLD signal in GM as greater than 2% (peak-to-peak signal amplitude change), which was slightly lower than the sinCVR (3.2%) and dCVR (3.5%) magnitude estimates.

Bright and colleagues (2009) investigated BOLD signal change and CVR delay using breath holds (BH) to induce hypercapnia, cued deep breathing (CDB) to induce hypocapnia and a 4% CO_2 inhalation task [34]. They interpolated the BOLD signal timecourse of each voxel using splines to a temporal resolution of 0.3 s for a voxel-by-voxel basis. They found BOLD signal in the GM changed by 0.5–3%, with larger responses in the tissue near large veins. The absolute timing of the extrema of the BOLD response curve were thresholded using a

20-second window centred on the mean response for that participant. They estimated the % BOLD signal change to be 0.23±0.08% for BH and 0.30±0.17% signal change for CDB, which was closer to the results in this chapter than in Blockley and colleagues (2011) [29].

Comparing Data Analysis Methods

Goode and colleagues (2009) investigated the reliability and reproducibility of BOLD measures of CVR with a 10% CO_2 HC with a non-rebreathing mask (N=16, 7F, 27.7 years) [100]. They used FEAT to analyse the BOLD signal percentage change in the GM. They compared a box car analysis method to an automated regression analysis, and found that in the GM the results were similar, but a little lower than this chapter (2.93%±0.68% (boxcar) vs 2.73%±0.48% (automated)). These results were also quite similar to the sinCVR results from this chapter calculated with FEAT. Reproducibility was measured with short-term reproducibility (COV) and was 6.6-9.0% (non-normalized) in the GM. The reliability in data normalised by $P_{ET}CO_2$) (24-27% COV) was unexpectedly poorer than the non-normalise data. Between-subject variation (COV) was 11.3-23.1% for non-normalised data, and 32.7-39% for normalised data. It was lower for the automated method vs the boxcar method. Of note is that this study was conducted on a 1.5 T system, and the HC was twice that of this chapter. Therefore, proportional to the HC, the response to the % per mmHg was much smaller than the normalised data from this chapter, i.e. $\sim$0.03% per mmHg change to 10% CO_2 vs. $\sim$0.03% change per mmHg to 5% CO_2. Additionally, this suggests that it was still worth investigating more complex analyses than FEAT.

This chapter is also not the first to compare different methods of calculating

HRF and timing metrics from BOLD data. Mayer and colleagues (2014) used a similar non-linear regression to the dCVR analysis, though with a double gamma variate function, to determine where in the brain the HRF differed as a function of time [149]. This was also compared to more traditional methods, and they used voxel wise analysis (ANCOVA). They investigated trauma (mild traumatic brain injury (mTBI)), and their results with the traditional method did not show any significant differences between healthy (matched controls) and mTBI participants. This included no differences in the shape of the HRF. For the group x time interaction mTBI patients showed an increased activation at 2 seconds post stimulus for most ROIs. A qualitative comparison of magnitude with the non-linear method showed mTBI patients also had a larger peak amplitude and area under the curve (AUC) (magnitude) during the positive phase of the HRF response in several ROIs. The volume of activation was larger for the mTBI group (309.90 mL) than the controls (138.62 mL). More specifically, in the visual cortex the positive peak was 0.40 % for mTBI vs. 0.29 % for healthy participants, and the negative peak was -0.38 % mTBI vs. -0.38 % healthy controls, positive AUC in mTBI 0.69 vs. 0.4 and in negative AUC mTBI 0.81 % vs. 1.04 % . This supports the idea that HRF varies across brain regions, which was not found in this chapter's results. Although these results are not directly comparable to using a HC to estimate CVR, it is reassuring that a similar method performed better than traditional methods when used in a clinical cohort. This supports the hope that the dCVR method will also do well in clinical cohorts.

5.6.3 Timing Metrics

eASL vs. BOLD Timing

The hypothesis that the eASL and sinCVR timing metrics would be correlated was supported, as there was a weak correlation between the eASL ATT and the sinCVR phase data. This showed that as the transit time in the arteries increased, so did the phase, which suggests some form of relationship between the two methods. The hypothesis that eASL and dCVR temporal data would be correlated was not supported, as there was no correlation between the eASL ATT and the dCVR TTP data.

While the sinCVR and dCVR magnitude were expected to be similar, the phase from sinCVR and the time to peak from dCVR appear to originate from different components of the physiological response to hypercapnia signal. Further work is required to understand the different origins of these metrics.

sinCVR Phase vs. dCVR TTP Timing

The hypothesis that the sinCVR and the dCVR temporal metrics would be correlated was supported, as the sinCVR phase and dCVR TTP were weakly correlated. However, the trend was negative, rather than positive, for the temporal data.

The Blockley and colleagues (2011) study, mentioned previously, also investigated CVR timing metrics, and found that GM delays were 14.3±3.4 s, which was similar, but lower than dCVR in this chapter (30.2±1.6 s) [29]. Also they used phase relative to the GM average, which was then converted to seconds. sinCVR phase here was measured in radians (0.4±0.0 radians), which would need to be converted to be more directly comparable. Additionally, in this chapter there were no significant differences between any brain regions ($p<0.05$), for

any timing metrics, whereas Blockley and colleagues (2011) found significant difference across different lobes ($p<0.0001$). More specifically, they found that the frontal lobe reacted significantly earlier than the occipital lobe ($p<0.001$), and the parietal lobe was earlier than the occipital lobe ($p=0.004$). A major limitation of the use of sinCVR phase as a timing metric was that it is not quantitative, where as the dCVR TTP was measured in absolute units (seconds).

Bright and colleagues (2009) [34], mentioned previously, found delays of 19.6±1.8 s for BH, and 27.3±2.0 s for cued deep breathing, which was closer to the dCVR results in this chapter (than Blockley (2011)). They found differences in the BOLD delay of up to 6 s across regions. However, they calculated timing results quite differently, by normalising the mean response timing in voxels that survived after two thresholding steps (one to remove voxels with less than 1% absolute BOLD signal change, and one to remove voxels on the edges of the temporal window). They found broadly similar results to the Blockley and colleagues (2011) study, with shorter delays in the GM, insula and basal ganglia, and longer delays in the posterior regions [29]. One benefit of the CDB approach, compared to the gas inhalation, was that it would be easier for patients to perform than BH, and did not require gas canisters. However, one disadvantage was that they were not able to calculate timing delay for the 4% CO_2 inhalation task using their analysis method.

Comparing Data Analysis Methods

Mayer and colleagues (2014), mentioned previously, used a non-linear regression method, which was more similar to dCVR, and was therefore able to provide a quantitive timing metric using TTP. This timing metric suggests dCVR may also provide insight into disease. They found that when looking at TTP for both the positive and negative phases of the HRF curve, the mTBI patients

had an earlier HRF compared to healthy participants [149]. For example, for positive TTP: mTBI V1 2.3 s vs. healthy controls 2.6 s, negative TTP: mTBI primary visual cortex 4.77 s vs. healthy participants 5.43 s. They found that modelling three (i.e., a single gamma variate function) or eight free parameters (i.e., a double gamma variate function) increased the chances of modelling many different signal types (i.e., noise) rather than the actual HRF. Therefore, this reiterates that the amount of noise in the data is another limitation of using more complex models to analyse the HRF. Another concern was that the changes in the vasculature and metabolism in mTBI may alter the BOLD signal phases, which could be lost if using a deconvolution with a canonical HRF. However, the simpler, single gamma variate analysis was not be able to provide details of the undershoot (negative) phase of the HRF. Whereas, the double gamma function was able to provide more metrics for this, which was beneficial. Notably, their interest was more in the functional (cognitive testing), neuronal pathology of mTBI, where as the study here was actually more interested in the vascular changes. Unfortunately, with their method the HRF signal to noise ratio (SNR) was too low to analyse on a voxel-wise basis, and so only showed group level analysis. Therefore, applying dCVR, which can be performed at a voxel level, would be more advantageous, as it may provide more insight into the changes in vascular and neuronal decoupling in mTBI and other clinical cohorts. Alternatively, it could also be optimised to a method that is able to provide regional information (as in dCVR), so that the HC in this chapter was no longer required.

A limitation of the dCVR method is that it is not clear how well it deals with time lags. Regressor Interpolation at Progressive Time Delays (RIPTiDe) is a strategy/ method to deal with this 'noise' present in rsfMRI, especially time lags [87]. More specifically, low frequency oscillations (sLFOs) (0.01-0.15 Hz)

cause BOLD signal variance and the frequency band overlaps with those of brain connectivity. RIPTiDe is a cross-correlation model run at a voxel level to provide blood arrival times via iterative 'bootstrap sharpening' to recover the source signal. Tong and colleagues (2019) tested RIPTiDe (and other methods) and found that sLFOs account for ∼30% of low frequency variance in GM and are likely to be more usefully defined as potential biomarkers than 'noise'. The range of delays across the brain was about 6.5 s, increasing to a ∼6.7 s transit time from the carotid to sagittal sinus. This method performed better than traditional models (explaining 16% of the variance rather than only 1-5%). It was especially useful for looking at fluctuations in $P_{ET}CO_2$ as a possible cause of these low frequency oscillations. A major limitation of this method was that is may struggle with inhomogeneous time delays and needs careful regressor selection. A newer version of this method called RAPIDTIDE is available open source at

this link https://hpc.nih.gov/apps/rapidtide.html

and on Github https://github.com/bbfrederick/rapidtide.

In this chapter, dCVR implementation does not account for regional delays in CO_2 arrival very well. Performing a preprocessing step, via a pre-calibration of sorts, using a method like RAPIDTIDE or sinCVR may be useful for experimenting with for future dCVR analyses, in order to strengthen its performance with larger timing lags.

5.6.4 Limitations

Respiratory Stimulus

For evaluating the timing metrics, it may be useful to calculate the percentage change per mmHg as well, to normalise any difference in response to $P_{ET}CO_2$.

It may reduce the standard deviation, but less clear about how much greater insight it would provide. Sleight and colleagues (2021) suggested the variation in the delivery of hypercapnia may also result in different CVR responses [214]. This disparity was highlighted by Kastrup and colleagues (1998) [124] that investigated regional BOLD responses to hypercapnia and showed that the frontal lobe had the slowest response to hypercapnia. This is in opposition to later work by Bright & Blockley that suggested the fastest response was observed in the frontal regions. However, the timing metrics in these studies were calculated differently, making any inference about the underlying physiology by directly comparing them difficult.

Other elements may bias the CVR results that appear to be related to the HC, but are actually indirectly affecting the results. For example, even if two participants experienced the same level of HC, variation in datasets in terms of SNR for the MR data would also influence the regional CVR response results [137]. Zhou and colleague's (2015) HC was only given at 1 L/min, as they used Douglas bags rather than a more direct delivery from canisters. Douglas bags are generally filled before the experiment, so the flow rate is not as comparable. However, there can be a bigger delay when switching gases, as the participant has to inhale all of the remaining gas in the lines before getting to the new gas. It is likely that study would therefore also have a different SNR to the studies that used end-tidal targeted gas delivery methods.

One reason for the lack of correlation between BOLD and eASL data in this chapter may also be due to the type of HC used with the BOLD data. Due to the sinusoidal wave form of the resulting $P_{ET}CO_2$ trace, this may have led to some modelling misestimation and a higher risk that it would be out of phase with the BOLD signal [158].

Another limitation it that there is often a concern that the HCs are not tolerable for patients or older participants. Suri and colleagues (2021) asked members of the Whitehall II imaging cohort at wave MRI-1 (2012-2016) and wave MRI-2 (2019-2023 but paused in 2020) to complete a questionnaire about their experience of a HC CVR task (5% CO_2), (N=$\sim$200 of the >65 years) [221]. They reported (of N=21) that 24% noticed when breathing different gases, 5% noticed change in smell or taste, 43% reported scanner-related discomfort, 43% reported mask/gas-related discomfort, 14% reported no discomfort. Even though some participants reported discomfort, 90% would still have been willing to do a similar study again, which suggests it was considered to be tolerable. Although, there was no follow-up questionnaire in this chapter, no participants asked to stop scanning or made obvious comments about discomfort. It may be possible to speculate that scanning a younger cohort may have found the HC more tolerable. Additionally, a post-scan questionnaire to gather more data on the tolerance of HCs has been suggested for standard research practice by the Imaging Cerebral Physiology Network (2017) [35]

5.6.5 Acquisition Methods Limitations

Many studies use either BOLD or ASL, but not both. This also makes it harder to directly compare the results from this chapter to existing literature [36, 37]. Both methods of data acquisition have their own strengths and limitations, but they can also be complementary [38]. With more information it is often possible to provide a better interpretation of the data.

An advantage of eASL is that it provides a direct measure of blood flow and uses quantifiable physiological units. A limitation of eASL is that it is particularly sensitive to motion, but only provided subtracted images, which meant it was not possible to perform motion correction on the data using BASIL [241]. Additionally,

pCASL has a lower temporal resolution than BOLD, so may not able to capture dynamic changes as well.

sinCVR may be sufficient enough for periodic (block) stimuli (i.e. simple box car paradigms). However, phase is relative, and may miss non-periodic responses (i.e. more naturalistic sinusoidal waveform). It may be necessary to compare the regional data to a reference such as the global whole brain or whole grey matter average signals. Whereas, dCVR appears to be better than sinCVR for stimuli more complex than block paradigms. Another benefit is that the timing metrics are given in quantitive units. However, the assumptions of the HRF may not be as good at accounting for local delays. This could potentially lead to missing regional variations in response timings. Furthermore, the processing computation and time requirements were much higher.

A multi-modal approach combining both ASL and BOLD methods might provide more comprehensive understanding, but this is rarely done due to practical constraints. For example, to ensure both the BOLD and ASL responses to HC are more similar, another option would be to acquire the MR data simultaneously e.g. using a dual-echo sequence (e.g. as in [154]). However, the sequence would then lose the MPLD element and therefore the timing metric's sensitivity. Additionally, the dual-echo sequence may compromise the SNR of either the ASL or BOLD data. For example, the ASL data acquisition would be favoured by the background suppression and increase the ASL SNR. However, this would also lower the BOLD SNR.

5.6.6 Analysis Methods Limitations

Duffin and colleagues (2017) showed that the response to increasing CO_2, when looking at BOLD data, fitted well with a sigmoidal response model [69]. They

suggested this was explained by the physiology of the network of the vascular bed and associated changes in vascular resistance during hypercapnia. However, this relied on the assumptions of a simplistic model of the vasculature with a slow ramp stimulus, and also that local perfusion pressure had remained constant. There is also evidence that the response to CO_2 varies in shape (i.e. not always sigmoidal) depending on region, especially in patients [82]. As dCVR analysis uses a transformation from $PETCO_2$ to BOLD signal, the transform does not have to be linear, or even sigmoidal, to estimate the HRF. The model is essentially more data driven. However, sinCVR analysis may be less adaptable, and therefore less applicable to disease states that require a more rigid model. Therefore, future studies could investigate how dCVR performs in ageing, and then disease states, to see if the model is still reliable in clinical cases, with an altered vascular system.

Another option for the underlying physiological mechanisms estimated by BOLD and pCASL to be more similar would be to mask out the veins in the BOLD data, so that it would more closely match the arterial data of the pCASL. However, this is difficult to achieve accurately for individual participants, as most methods rely on using statistically based atlases. Conversely, an advantage of ASL is that it does not include the veins in the CBF values.

Registration and masking procedures in this chapter were verified. Though manual correction of BET was time-consuming, and further preprocessing with motion correction with BASIL was not possible due to subtraction of tag and control images on the GE scanner, as part of the eASL acquisition.

Modelling the Physiology

For understanding pathology, it would be preferable to have more information for regional responses, rather than whole brain CVR values. Ideally, these

measures better account for distance from blood vessels, and subsequently the different tissue responses. Additionally, more detailed regional information would account for any potential "CVR steal phenomenon", which is where (especially in pathology) the brain prioritises blood supply to specific regions [230, 36, 200].

In the Bright and colleagues (2009) study they acknowledged that the differences in CVR delay across cortices were not entirely explained by blood transit times alone, which suggested they were measuring local reactivity phenomena as well as passive blood flow properties. These regional timing differences were found to be consistent across healthy participants, so may suggest this represents normal physiological variation rather than measurement artifacts. Furthermore, there have previously been some inconsistencies in estimates of CVR when comparing CO_2 versus carbogen (a mixture of CO_2 and oxygen), which also complicates drawing inferences from these different kinds of comparisons [146].

As mentioned, a long term aim for clinical use would be to remove the need for a HC. However, this would require high sensitivity to changes in the naturally varying CO_2 that occurs simply from changes in breathing rate and pattern. There have been a variety of methods at acquisition and analysis stages implemented to improve the analysis of BOLD for measuring CVR. Methods for improving the sensitivity that could be applied to the BOLD data here include: taking into account an individual's variation by rescaling to their own baseline, using reference scans (PCV and VASO etc), and complex modelling.

A major limitation of this chapter, as always, was the small sample. Therefore it would be beneficial to perform this analysis on a larger sample size to increase the statistical power of the comparison results. In relation to this chapter,

chapter 2 and 3, comparing both the MRI and physiological measures e.g. BP, may also prove useful for understanding the underlying physiology of the CVR response. With a larger cohort, it may be possible to create a protocol that is more effective than the ones used in this thesis.

Suri and colleagues (2020) used the large Whitehall II imaging cohort to investigate if cardiovascular risk was associated with risk to the brain e.g. a predetermination of vascular dementia (N=543, M=444) [222]. Additionally, they started investigating Whitehall II imaging cohort at wave MRI-1 (2012-2016) and wave MRI-2 (2019-2023 but paused in 2020) Suri and colleagues (2021). They analysed BOLD data using cross-subject voxel-wise statistics using higher-level FEAT, however only a single participant's data was presented. The thresholded activation images showed BOLD signal changes during hypercapnia blocks relative to air (z-statistic values between 3.1 and 26.8). Unfortunately, data collection was paused due to COVID-19 restrictions. Considering this cohort has been followed for over 35 years, it will be interesting to see how this develops in future. As the Whitehall II dataset is open access, it will present a great opportunity to test out the different methods of analysis used in this chapter on a larger sample size (once the next phase is released).

Furthermore, this presents an opportunity learn how to adapt the physiology study in chapter 3 to be combined with the MRI study in this chapter. Suri and colleagues (2020) used the Whitehall II imaging cohort to investigate aortic pulse wave velocity (PWV) measurements to CBF data [222]. PWV measurements are as a measure of aortic stiffening, and calculated as the distance between two measuring sites divided by the time it takes for the arterial pulse to travel from the proximal to the distal measuring site. The PWV data were collected in 2007–2009 (mean age 63.9±5.2 years) and a four-year follow-up in 2012–2013

(mean age 68.0±5.2 years). The imaging data were collected from 2012 to 2016 (mean age 69.8±5.2 years). The CBF data was from a MPLD pCASL sequence with a TR of 4240 ms, TE 13 ms, labelling duration 1400 ms, PLDs 250 ms 500 ms, 750 ms, 1000 ms, 1250 ms, 1500 ms, and 1750 ms ([222] supplementary material). The BASIL toolbox, with the general linear model, was used to calculate the CBF with a voxel-based analysis. They found that the mean PWV significantly increased by 0.7±1.6 m/s over the 4 years ($p<0.0001$), at a rate of 0.2±0.4 m/s per year (mean±std). In a sub-set of N=112 participants faster aortic stiffening was associated with a significantly lower CBF in 18.4% of GM. This was specifically observed in the frontal (-10.85 ml/100g/min, 95% CI: -17.91 to -3.79) and parietal lobes (-12.75 ml/100g/min, 95% CI: -21.58 to -3.91), which was significant after Bonferroni correction ($p<0.0125$). In terms of cognitive performance, lower baseline PWV was associated with significantly lower semantic fluency (B = -0.47, 95% CI: -0.76 to -0.18) and poorer verbal learning (B = -0.36, 95% CI: -0.60 to -0.12), which was also significant after Bonferroni correction ($p<0.007$). This suggested cognitive function was more closely related to baseline arterial stiffness, than to the rate of arterial stiffening, and therefore indicate early intervention here may be crucial for preventing a cognitive decline. One reason for the association between PWV, CBF and cognitive perfusion may be that a higher PWV damages the microvasculature that regulates CBF, and therefore disrupts the supply of blood to the neuronal system that facilitates the cognitive tests. This damage to the vasculature system would also likely have knock on effect on CVR. They surmised that this would agree with other studies that hypotheses a link between Dementia and arterial stiffening. It would have tied in nicely with the work from chapter 3 that was looking at the whole body relationship from blood pressure to CVR, if it had progressed to MR. PWV is considered a more comprehensive measure for

understanding cardiovascular risk than traditional blood pressure measurement alone, so could improve on the BP measures used in chapter 3. An MR conditional BP and heart rate monitor had been purchased, however it was not used due to no longer continuing the physiology study, but could be useful for future studies.

A limitation of this study was that this cohort was a specific demographic of mostly male, older civil servants. Authors highlighted that this cohort would therefore be biased by a high educational attainment, survival bias, and lack of ethnic or socioeconomic diversity.

5.6.7 Conclusions

This study compared three different approaches to modelling CVR estimates: enhanced arterial spin labelling, sinusoidally modelled CVR, and dynamically modelled CVR. The results reveal important insights about the relationships between these methodologies and the potential complementary roles in CVR assessment. ASL and BOLD magnitude did not show a correlation, but the two BOLD methods (dCVR and sinCVR) did. There was a significant correlation between ATT and phase and between phase and TTP. However, there was no correlation between ATT and TTP.

ASL and BOLD based measures did not align with previous studies that directly compared the two methods, as this chapter did not find a strong correlation between these two methods. However, there is also plenty of previous research that highlights the distinct physiological bases of ASL and BOLD signals, and the impact that has on differing results for CVR i.e. capturing different aspects of the cerebrovascular response. Although there were no significant differences seen here between the cortical regions for either ASL or BOLD, there were

some similarities between the regional differences compared to previous studies. However, there was also a large variation in the results depending on the study, methods used for MR acquisition and HC delivery. Therefore, there is still a need to standardise the methodology before translation to clinical use.

6 Discussion

6.1 Summary of Interest

Robustness of magnetic resonance imaging (MRI) data acquisition and data analysis is needed for more reliable clinical diagnosis and prognosis of cerebrovascular disease. This thesis aimed to investigate robust measures of the change in blood flow in the brain using MRI, via cerebrovascular reactivity (CVR) measurements. It also aimed to advance the implementation of hypercapnic challenges (HC) for inducing CVR. Additionally, it explored the application of more advanced arterial spin labelling (ASL) and blood oxygen level dependent (BOLD) analysis for investigating CVR measurements, including timing metrics. This chapter is divided into a reflection on the discussion points for data chapters covering CVR measurements using HCs, MRI acquisition, ASL and BOLD CVR analysis methods. In each of these parts, the main findings are summarised, followed by discussions on the contributions that this work makes towards robust measurements of CVR using pseudocontinuous ASL (pCASL), BOLD, and HCs (inhaling high carbon dioxide gas (CO_2)). The limitations of the thesis are also reviewed and future directions of research are proposed.

6.2 Optimising Robust Quantification of Cerebrovascular Reactivity using pseudocontinous ASL

Chapter 2 part 1 investigated validating robust measures of the change in blood flow in the brain using MRI via CVR measurements. These results showed that blood flow in the brain measured with pCASL increased when using a steady state HC and resulted in different measures of CVR when comparing three different sets of preparation parameters. These differences are likely due to changes in blood velocity and its effect on labelling efficiency. The measurements of CVR across large feeding arteries in the brain also varied when measured with phase contrast velocity (PCV) was also greater in the internal carotid arteries (ICAs) compared to the vertebral arteries (VAs), and greater on the left than the right side of the brain. Params-1 appeared to be more robust to these changes in velocity. This finding has important implications for labelling efficiency and territory-specific perfusion assessment. The observed asymmetry between left and right vessels agreed with known anatomical variations in vessel diameter and flow dynamics, which suggests a more nuanced approached to CVR quantification is needed.

Part 2 investigated whether hyperventilation altered the B_0 at the labelling plane, and also two different labelling plane positions. This chapter used the pCASL preparation parameters from part 1 (Params-1 [233]) and found only a small difference between normal ventilation and hyperventilation in terms of the B_0 inhomogeneity at the labelling plane. Investigation of magnetic field effects revealed a measurable ($\sim$30%) increase in B_0 value range during hyperventilation, though absolute changes were modest compared to previous studies. There was also only a small difference in the B_1^+ when comparing the two different labelling plane measurements (one at the V3 segment and one at

90 mm below the AC-PC line (anterior commissure-posterior commissure). B_1 field characteristics showed optimal performance (∼97% of nominal flip angle) at the V3 vertebral artery segment, representing more favourable conditions than previously reported (∼83%) when the labelling plane was placed 90 mm below the AC-PC line.

Overall, this study demonstrated that CVR measurements exhibit significant parameter-dependent variations, influenced by physiological changes in blood velocity and subtle magnetic field effects (B_1 and B_0). These findings highlight the importance of optimising pCASL preparation parameters for robust CVR quantification, and the need for standardised protocols in clinical applications. The study's sample size of <10 aligned with current literature, but was a considerable limitation. Additionally, technical constraints included single post labelling delay (PLD) implementation and spatial resolution trade-offs in PCV acquisition. For example, single PLD acquisitions were insensitive to changes in ATT, and limited PCV spatial resolution means the results might have underestimated blood velocity. Additionally, the practical requirements of using a HC would present challenges in clinical settings such as extra equipment, training, time and cost.

Future work should focus on developing more efficient and standardised approaches to CVR assessment, particularly for clinical implementation. The 'Grey Paper' [138], released suggested to focus on purely observing CVR from clinical images. However, this would leave out a lot of potential insight from the quantitive measures available. It will be interesting to see when the next 'White Paper' is released and how the standardisation can be improved. For example, through community efforts such as the open source initiative for perfusion imaging (OSIPI) challenges to standardise pipelines, nomenclature, and reporting of

study details in the literature. Respiratory stimuli could also be better standardised, as mentioned in Moreton and colleagues (2016) [158].

6.3 Investigating the Effect of Pharmacological Interventions on Blood Pressure and Velocity during a Hypercapnic Challenge

Chapter 3 aimed to investigate a pharmacological challenge and advance the implementation of HCs for inducing CVR. This chapter investigated the effect of anti-hypertensive pharmacological interventions on systemic blood pressure (BP), heart rate, and carotid artery blood flow during a HC. The results revealed several important findings that contributed to the decision not proceed to MRI with this protocol, and highlighted several considerations for future research. For example, pharmacological interventions resulted in some observations that were expected based on their known mechanisms of action. Glycerol trinitrate (GTN) administration induced significant heart rate increases, whilst Metoprolol (MET) induced significant heart rate decreases. The heart rate changes ($\sim$10 beats per minute (BPM)) indicated relatively modest cardiovascular effects in this healthy cohort. However, the findings did not align with the initial hypotheses, as neither intervention significantly altered BP or carotid artery blood flow, which suggests robust compensatory mechanisms maintained cardiovascular homeostasis. Analysis of HC responses revealed no significant differences between pre- and post-intervention conditions. BP stability during hypercapnia aligns with previous research that has demonstrated effective autoregulation in healthy subjects. Velocity measurements showed less pronounced changes compared to previous studies, potentially due to methodological variations

in measurement location and technique. However, sensitivity to detect subtle haemodynamic changes did not match the previous chapter's pCASL and PCV measurements during a HC.

A practical limitation was that the conservative BP cut-off (100 mmHg systolic) may have unnecessarily restricted participation, whilst body mass index (BMI)-based exclusion criteria potentially failed to optimally characterise body composition. The exclusively female sample and absence of placebo control were also limiting.

Overall, these findings suggest that young, healthy individuals maintain robust cardiovascular homeostasis after pharmacological interventions were given, even when administered in conjunction with a HC. Compensatory mechanisms, particularly heart rate adjustments, appear to have effectively preserved BP. However, the modest size of the observed changes indicates limited utility for direct implementation in MRI studies without further protocol refinement.

6.4 Implementation of advanced CVR methods

Chapter 4 explored the implementation of more advanced ASL and BOLD analysis for investigating CVR measurements. This chapter investigated CVR using two distinct approaches: a steady-state HC with a multi-PLD ASL (MPLD) sequence, and a pseudo-sinusoidal HC with a dynamically modelled BOLD (dCVR) analysis. Both methods demonstrated significant physiological responses to hypercapnic conditions, though with some notable differences from previous literature.

In part 1, the "enhanced" ASL (eASL) study showed a substantial CVR response

(∼60% increase or 5.8±0.5 %/mmHg), which was higher than similar previous studies. While arterial cerebral blood volume (aCBV) showed an average increase of ∼44%, this change wasn't statistically significant and displayed considerable inter-subject variability. The arterial transit time (ATT) decreased by ∼22% during hypercapnia, exceeding previous findings in the literature. These results suggest that while the MPLD ASL sequence effectively captured CVR changes, the variability in aCBV measurements may reflect limitations in the semi-automated gas delivery system compared to more precise methods like the RespirAct^{TM}.

In part 2, the BOLD dynamic CVR analysis showed a 3.2% increase in CBF (0.3%/mmHg when normalized by end-tidal partial pressure of CO_2 ($P_{ET}CO_2$)) and demonstrated increased time-to-peak during the HC. These findings aligned with previous research, particularly regarding age-related differences in the CVR response. However, in part 2, the dynamically modelled BOLD (dCVR) Basis expansion method with spherical Laguerre basis (BEL) method used for analysis, while robust, proved computationally intensive, requiring over 10 days for processing a single dataset locally. In comparison, for sinCVR, the modelling via FSL Feat only took about 20-30 minutes per dataset. When parallelised on the HPC, the sinCVR could run all of the datasets processing simultaneously. The post-processing stage was the same for dCVR and sinCVR as they were integrated into the same scripts as the eASL data.

The study highlighted the need for standardisation in MPLD ASL acquisition and analysis, following recent recommendations from OSIPI and other initiatives. The inability to perform motion correction on pre-subtracted data represented a technical limitation, although alternative toolboxes might offer solutions. The computational demands of the dCVR analysis, while providing reliable results, raises questions about clinical practicality. This work advances the

understanding of cerebrovascular reactivity measurement techniques, whilst highlighting important methodological considerations for future research and potential clinical applications.

A future aim for improving the eASL analysis would be further test-retest reliability and reproducibility. This would be beneficial to increase confidence in the CVR metrics output from BASIL. A future project could compare the actual difference between the results here with and without the gamma dispersion model. This would more closely follow the work of Pinto and colleagues (2023). Both modelling options were run on the datasets in chapter 4, but only the combined model results were included in section 4.16.1.

A future aim for improving the dCVR analysis would be to translate the deconvolution method to resting state CVR estimation, so that the gas kit set up would not be required and this would be more practical for patients. Another future direction would be to apply the BEL and optimised canonical correlation algorithm (CCA) analysis methods to the pCASL CBF. Another possible future directions for BEL dCVR analysis would be to measure dCVR in older adults, to see if there are similar differences across ageing as seen with the CCA method, and subsequently expand feasibility testing to patient datasets (e.g. with the open source Whitehall cohort dataset).

6.5 Comparing the Effect of a Hypercapnic Challenge on eASL, sinCVR and dCVR

Chapter 5 compared the two different methods from chapter to measure CVR: eASL, and dynamic CVR dCVR. Additionally, sinusoidal CVR (sinCVR), a simpler, traditional analysis method was used. This revealed complex relationships

between these methodologies. The comparison showed no correlation between eASL and either sinCVR or dCVR magnitude measurements, though there was a weak positive correlation between eASL and sinCVR timing measures. Whilst eASL and dCVR timing measures showed no correlation, sinCVR and dCVR perfusion measures demonstrated a strong positive correlation, with their timing measures showing a weak negative correlation. Results deviated significantly from anticipated outcomes, as the theory was that these comparisons may follow previous literature, however the underlying physiology of the different MR methodologies appeared to be too different. These varying relationships likely stem from the methodological differences, particularly the MR and respiratory stimulus protocols: eASL was acquired with a 3-minute steady-state challenge, whereas shorter blocks of 1-minute on/off repeated three times was used with BOLD. Consequently, for eASL, there were results from before and after the HC, whereas the BOLD results showed the change with the baseline and peak being estimated from a model. This would likely influence the difference in the timing measures more than the magnitude metrics. The lack of correlation between ASL and BOLD-based measures notably contrasted with previous studies, which have found strong correlations (e.g. R^2=0.83 [144]). This disparity may be explained by several factors, including different HC paradigms, technical limitations of the gas delivery system, regional variations in response to hypercapnia, and fundamental differences in the physiological mechanisms measured by the MR techniques.

This study identified several methodological considerations and limitations, including the need for more precise, but affordable CO_2 delivery methods, the importance of regional variations in CVR response, potential impacts of vein masking in BOLD data, and the role of signal-to-noise ratio in affecting

regional CVR responses. Other limitations included technical constraints with the gas delivery system, difficulties with motion correction due to the spiral eASL data requiring decoding and subtraction on the scanner, time-consuming manual corrections needed for brain extraction, and the non-quantitative nature of the BOLD sequence used. This chapter highlighted the complementary nature of different CVR measurement techniques while emphasising the need for careful consideration of methodological choices in CVR assessment. The findings suggest that while these methods may capture different aspects of cerebrovascular response. Each contributes valuable information to our understanding of brain vascular physiology, particularly in the context of potential clinical applications and the investigation of cerebrovascular health.

Future improvements could implement semi-manual end-tidal targeting for more precise CO_2 delivery, e.g. through development of an sequential gas delivery (SGD) circuit and switching between gases with a fixed flow rate. Another method may be to develop better simultaneous BOLD and MPLD ASL acquisition methods via dual-echo sequences. Alternatively, a 'calibrated' BOLD analysis method could be used. Additionally, future work could analyse approaches used to quantify BOLD CVR, and investigating these methods in disease states such as stroke, vascular dementia, carotid stenosis and Moya Moya disease. In future, it would also be of interest to investigate why different measures of CVR magnitude and timing metrics were not correlated even more closely, and where the differences between the analytics originate from in a more physiological sense.

6.6 General Limitations and Future Directions

A major limitation of all of the studies in this thesis is the small sample numbers, and hence an often small effect size that did not produce significant results. However, this could be improved by recruiting a larger cohort for the studies, which would also provide an opportunity to investigate the replication and reproducibility of these results.

For the study in chapter 3, the order of the pharmacological interventions being given was randomised. Other than this, none of the studies were randomly controlled and/or double-blinded. As the hypercapnia response often induces hyperventilation it would have been hard to blind participants to the HCs. The application of the HCs were not randomised or interleaved, i.e. they were always done in the same order to reduce time required for recovery from a hypercapnic state. The order of scans within the protocol were also performed in the same order for each participant i.e. eASL then BOLD, which could have resulted in habituation, or differences in response depending on which one was done first. There was already quite large noise/ variation in these small datasets, despite recruiting a relatively narrowly defined cohort.

In summary, for more general future directions the work in Chapter 2 could be extended to investigate the origin of the systematic differences in the pCASL preparation parameters and if they can be further optimised.

For example, through the use simulations as in Milbourn and Blockley (2021) [156] and might be aided by the use of MPLD ASL, as was used in Chapter 4/5.

Chapter 3 was not viable for use in the MR, so was not pursued further, but provided valuable experience in the design and application of a pharmacological

study which could be used in future studies.

Chapter 4 showed lower correlation between ASL and BOLD measurements than expected, but could be investigated further by applying dCVR analyis method to the ASL data. However, this would require an eASL dataset with a dynamic HC rather than a steady state block challenge. Additionally, this could be investigated further through simulations.

Chapter 5's comparison of dCVR and eASL across brain regions could be extended to white matter regions, in order to be applicable to a wider range of cerebrovascular diseases. Ideally the dCVR analysis will be sensitive enough to be applied to resting state data. However, this may take substantial adaptations, in order to distinguish such small changes in $P_{ET}CO_2$ seen in non-HC breathing. Overall, these findings highlight the need for more robust methodological frameworks. Though, hopefully these findings contribute to small steps towards optimised CVR data acquisition and analysis methods, which has implications for improving the accuracy and reliability of cerebrovascular assessment in both research and clinical settings.

6.6.1 Recommendations

The exploratory nature of this work revealed numerous avenues for future investigation. Going forward, the following recommendations would be advised when measuring CVR:

Data Acquisition - using different MRI methods, sequences and parameter sets:

- Sample Size: An obvious recommendation would be to increase sample size, where possible of inter- and/or intra-participant datasets. Various limitations resulted in a small sample size including that the research

timeline was significantly impacted by global pandemic restrictions, necessitating substantial modifications to data collection protocols. The possible scope of the research grant was limited by the expense of MR scanning time. Additionally, some datasets had to be removed due to quality control and incidental findings. However, larger cohorts will be required for formal clinical trials.

- Placebo and interleaving: ideally with unlimited resources it would be preferred to use double-blind, random control set up for these studies. However, when interleaving a HC into a random order it will be important to ensure a suitable recovery time after the hypercapnic condition, before doing the normocapnic condition.
- Repeatability: would be another obvious follow up study, to see if these results could be repeated and/or replicated at another site or by another research group.
- Standardisation: The fMRI sequences used here may not directly transfer to other vendors. Cross-scanner validation would be important to check which pCASL preparation parameter sets, that performed best here, would be suitable to use on other vendors. Though, it may be important to decide if this would come at the cost of a standardised sequence, that works well on all scanners, or optimising it for the best-of-the-best sequence that may only work well on one scanner.
- MPLD sequences: MPLD improved the speed of data acquisition compared to single PLD pCASL MRI. MPLD is preferable over single PLD pCASL, to determine quantitive, multi-parametric values i.e. ATT and aCBV. So, this would be preferable over a single PLD pCASL sequence.
- Improve simulations: for estimating labelling efficiency for pCASL preparation

parameter sets e.g. progress from laminar flow to the more recent pulsatility models. The phase contrast velocity and pCASL data from chapter 2 could still be used to model these.

- Phantoms for CBF: to provide a more direct 'ground truth' for quality assurance of the CBF measurements for specific pCASL preparation parameters as well as comparison between the PCV and BOLD datasets.
- Multi-band BOLD: improved the speed of data acquisition for BOLD CVR. So this would also be benificial for clinical use over more traditional BOLD sequences.
- More general Quality Metrics: although the MRI system had routine quality assurance, there is scope for individual subject thresholds for data exclusion criteria, temporal SNR maps and CVR reliability maps (e.g., coefficient of variation across runs). As these would be less biased than the visual inspection and basic checks used here.

Hypercapnic Challenges - using different gas delivery methods:

- Equipment issues necessitated alternative approaches, therefore cheaper, open-source and repairable equipment (i.e. see the new right to repair laws in the European Union) would be more beneficial in future to improve accessibility of the kit.
- Standardised HCs: 3-minute paradigms shown here conform with the move towards standardisation of steady-state paradigms, so would be recommended for future studies using MPLD pCASL.
- Fixed-target $P_{ET}CO_2$ devices: are expensive, but the computer controlled gas delivery is useful for more complex paradigms. For steady-state

paradigms, a semi-automated gas delivery box will be sufficient, cheaper, and provide more controlled paradigms than manual gas delivery.

- Resting state: in an ideal world there would be no need for a HC, and the dCVR could be applied to resting state data and sufficiently predict the HRF. This removes the need for inhaling CO_2 or performing breath holds, which may be difficult for some patients. Although, dCVR of resting state data was trialled, it was unsucessful therefore the data was not included in this thesis, but perhaps future refinement may be more fruitful.

Data analysis - using standard, Bayesian and more complex HRF analysis:

- Standardisation of pipelines: there are multiple pipelines available for CVR data analysis, the BASIL toolbox is open-source and facilitates various modelling options. The gamma distribution and macrovascular modelling performed well here, and there is transparency and accessibility in the application of a toolbox compared to the custom, in-house scripts used in Chapter 2.

- Robust statistical analyses: Bayesian analysis typically deal with outliers better and the use of the priori values provides more physiologically plausible results. It would also be recommended to use models that can provide the wider metrics of MPLD pCASL i.e. aCBV, and ATT.

- Regions of interest: this thesis focused on grey matter areas of the brain, though white matter ROIS may be of interest for a broader range of neurological diseases e.g. multiple sclerosis.

- Scanning patients: it was not possible to scan older adults or patients, and it would be important to ensure that the theories about the robustness

of the pCASL / BOLD CVR methods used here actually hold up in practice, i.e. within clinical populations.

A Professional Internship Programme Reflective Statement

Note to examiners: This statement is included as an appendix to the thesis in order that the thesis accurately captures the PhD training experienced by the candidate as a BBSRC Doctoral Training Partnership student. The Professional Internship for PhD Students is a compulsory 3-month placement which must be undertaken by DTP students. It is usually centred on a specific project and must not be related to the PhD project. This reflective statement is designed to capture the skills development which has taken place during the student's placement and the impact on their career plans it has had.

A.1 Professional Internship Placement Reflective Statement

Where you went on placement, and the project you worked on During my three-month professional internship placement at Cerca Magnetics Limited, I have enjoyed working with the fantastic team on the 'Innovate' regulatory work packages for usability and device equivalence of OPM-MEG (Optically pumped magnetometers – magneto-encephalography). Working with Cerca gave me a greater understanding of the approval process and user requirements needed to translate your visions of OPM-MEG into a clinically approved device. Cerca is a spin out company from the University of Nottingham (UoN) created

to commercialise new brain imaging software called OPM-MEG. Compared to conventional MEG, OPMs do not require helium for cryogenic cooling, and the sensors can therefore be placed in a helmet that can be fit to individual being scanned. Cerca sell, install and service the OPM scanning set up, which includes collaborations with Magnetic Shields Limited for the magnetically shielded rooms and QSPIN for the sensors. Cerca had several projects ongoing as part of an 'Innovate' grant aiming to apply for medical device approval with the FDA. The projects I was working on included working with a UoN/Cerca PhD student (Zoe) with their OPM to MEG equivalence package. This involved being scanned on my first day in both the conventional MEG and the OPM-MEG systems with a Braille stimulus task. This project aims to show the equivalence of the data for the new Neuro1 OPM device with existing approved MEG devices. The main project I was working on was to compare OPM to a clinically approved EEG device. This was to compare the usability of the hardware and software of both devices. The other project I was working on was the development of the usability and feasibility documentation for OPM to become a clinically approved device.

The outcomes of your placement project For Zoe's project, I created documents for an MRI protocol to collect the anatomical MRI images on the GE scanner and collected the MR data for a couple of participants as a scanner operator. The MR images are used in OPM/MEG data analysis for co-registration and allowed me to bring in my practical knowledge of MRI from the PhD into the placement. For the EEG project, I was able to conduct EEG data collection with the clinical, 25 electrode set up as well as the EEG cap. Unfortunately, the EEG cap did not arrive until almost two months into the placement. However, I was still able to collect EEG data both independently and concurrently with conventional MEG and OPM-MEG. I was able to start the set up of an MNE

pipeline (python based package) for preliminary results. I also created detailed documentation on how to set up and use the EEG and Braille stimuli device. For the usability project, I was able to integrate the use of concurrent EEG with OPM into the activity diagrams and use FEMA documents.

What skills you developed whilst on placement Interactions with collaborators from UoN, QuSPIN and Magnetic Shields Limited gave me a greater appreciation of the wider team and physical components involved in building the pre-install system. Additionally, the site visit to Young Epilepsy gave me better comprehension of the integration of OPM-MEG into epilepsy research by neurophysiology clinicians and researchers. Assisting the Cerca team with writing questionnaires and conducting interviews with current MEG users, with a focus on evaluating current clinical practice, enhanced my understanding of the potential developments and challenges of developing a clinically approved OPM-MEG system. Furthermore, by creating detailed instructions of this process and Activity diagrams for the Failure Modes and Effects Analysis (FMEA), I was able to provide my own usability feedback for the system.

Any impact your placement has had on your career plans This placement introduced me to different career plans within industry and shifted my career perspective. While I had previously focused exclusively on post-doctoral research opportunities, my experience at Cerca revealed dynamic possibilities within industry research. The role combined academic research with practical applications in a new way. When Chris mentioned an opening for a Scientific Researcher Role at Cerca, I recognised how such a position would allow me to apply my research skills while contributing to tangible healthcare improvements. The collaborative environment and the opportunity to bridge academic and commercial research particularly appealed to me.

B Appendix Chapter 2

B.1 Chapter 2 Methods

Figure B.1 shows the Consent form for chapters 2, 4 and 5.

Figure B.1 shows the basic MR safety screening questionnaire for chapters 2, 4 and 5. Figure shows the tattoo safety screening questionnaire, required if a participant had a tattoo.

University of Nottingham
UK | CHINA | MALAYSIA

Faculty of Medicine & Health Sciences
School of Life Sciences

CONSENT FORM
(Version 1.0: 29/01/2019)

Title of Study: **Robust quantification of cerebrovascular reactivity for use in clinical research**

REC ref: 246-1902

Name of Researcher: _____

Name of Participant: _____

1. I voluntarily agree to take part in the above study. ☐
2. I confirm that I have read and understand the information sheet version number _____ dated _____ for the above study and have had the opportunity to ask questions. ☐
3. I understand that my participation is voluntary and that I am free to withdraw at any time, without giving any reason, and without my legal rights being affected. I understand that should I withdraw then the information collected so far cannot be erased and that this information may still be used in the project analysis. ☐
4. I understand that relevant sections of data collected in the study may be looked at by authorised individuals from the University of Nottingham, the research group and regulatory authorities where it is relevant to my taking part in this study. I give permission for these individuals to have access to these records and to collect, store, analyse and publish information obtained from my participation in this study. I understand that my personal details will be kept confidential. ☐
5. I agree to comply with the reasonable instructions of the supervising investigator and will notify him/her immediately of any unexpected unusual symptoms or deterioration of health. ☐
6. I authorise the investigators to disclose the results of my participation in the study but not my name. ☐
7. I understand that information about me recorded during the study will be kept in a secure database. If data is transferred to others it will be made anonymous. Data will be kept for 7 years after the results of this study have been published. ☐
8. I understand that I can ask for further instructions or explanations at any time. ☐
9. I understand that I am free to withdraw from the study at any time, without having to give a reason for withdrawing. ☐
10. I confirm I have disclosed relevant medical information before the study. ☐
11. I may receive an inconvenience allowance of £25. If I withdraw from the study for medical reasons not associated with the study a payment will be made to me proportional to the length of the period of participation, but if I withdraw for any other reason, the payment to be made, if any, shall be at the discretion of the supervising investigator. ☐

12. **Optional: Consent for storage and possible use in future research** I agree that the samples I give and the data gathered about me can be stored by the SPMIC research team at the University of Nottingham for possible use in future studies (approved by an Ethics Committee). I understand that some of these studies may be carried out by researchers other than the current team at SPMIC, who ran the first study, including researchers working for commercial companies. Any samples or data used will be anonymised, and I will not be identified in any way. ☐

13. I have not been a subject in any other research study in the last three months which involved: taking a drug; being paid a disturbance allowance; having an invasive procedure (e.g. blood sample >50ml) or exposure to ionising radiation. ☐

Abnormal Findings in Scans

14. I understand that the SPMIC is not a clinical diagnostic facility and so does not routinely inspect images for abnormalities. I understand that my MR scans will NOT be reviewed by a radiologist (or any other medically qualified person) to look for any signs of disease, and it is unlikely that any abnormalities that may be present will be detected. ☐

15. I understand that if one of the investigators notice any potentially significant abnormality on my MR scans they will show my scans to a radiologist who will contact my GP to organise any further action required. ☐

16. I understand the if an abnormality were detected on my scan it may affect my ability to get life insurance. ☐

17. I agree to my GP being informed of any medically relevant information gained from the study. ☐

GP Name: _____

Surgery Address: _____

_____

Telephone Number: _____

_____	_____	_____
Name of Participant	Date	Signature

Information below to be completed by the researcher:

I confirm that I have fully explained the purpose of the study and what is involved to:

_____

I have given the above named a copy of this form together with the information sheet.

_____	_____	_____
Name of Investigator	Date	Signature

_____	_____
Ethics Code	Study Volunteer Number

University of Nottingham
Sir Peter Mansfield Imaging Centre

MR Volunteer Safety Screening Questionnaire

Name:	Scan Date:	Date of Birth:
Address:	Volunteer Number:	
	Ethics Code:	
Phone number:	Weight:	Height:

MR scanning uses strong magnetic fields. For your own safety and the safety of others it is **very important** that you do not go into the magnet halls with any metal in or on your body or clothing. Please answer the following questions carefully and ask if anything is not clear. All information is held in the strictest confidence.

Do you have any implants in your body *(e.g. replacement joints, drug pumps)*? ***Please provide details overleaf***	Y/N
Do you have aneurysm clips (clips put around blood vessels during surgery)?	Y/N
Do you have a pacemaker or artificial heart valve? *(These stop working near MR scanners)*	Y/N
Have you ever had any surgery? ***Please give brief details overleaf*** *(We do not need to know about uncomplicated caesarean delivery, vasectomy or termination of pregnancy)*	Y/N
Do you have any foreign bodies in your body *(e.g. shrapnel)*?	Y/N
Have you ever worked in a machine tool shop without eye protection?	Y/N
Do you wear a hearing aid or cochlear implant?	Y/N
Could you be pregnant? *(Pregnancy tests are available in the female toilets)*	Y/N
Have you ever suffered from tinnitus?	Y/N
Do you wear dentures, a dental plate or a brace?	Y/N
Are you susceptible to claustrophobia?	Y/N
Do you suffer from blackouts, epilepsy or fits?	Y/N
Do you have any tattoos? ***If yes, you may be asked to read and sign another form***	Y/N
Do you have any body piercing jewellery that cannot be removed?	Y/N
Do you have any skin patches (trans-dermal patches)?	Y/N
Do you have a coil in place (IUD) for contraception? Do you know what type?	Y/N
Do you have any condition that may affect your ability to control your temperature? *(e.g. Do you have a fever, cardiovascular disease, hypertension, diabetes or cerebrovascular disease?)*	Y/N
Will you remove all metal including coins, body-piercing jewellery, false teeth hearing aids etc before entering the magnet hall? (*Lockers are available by the changing rooms)*	Y/N
Is there anything else you think we should know?	Y/N

Please turn over to complete the form

Details of any surgery/implants here (if applicable):

I have read and understood all of the questions.

Signature:	Date:

FOR SCANNER OPERATORS/MR ASSISTANTS ONLY

Is this volunteer safe to be scanned? Y/N

Signature:	Date:

The University of Nottingham
UNITED KINGDOM · CHINA · MALAYSIA

SPMIC Sir Peter Mansfield Imaging Centre Nottingham

Tattoo Form

On the safety screening form you have indicated that you have a tattoo. Please read the following information and we will go through it with you, ask if anything is unclear.

What are the risks?

During an MRI scan, certain types of tattoos may heat up if they are inside the region being scanned; in exceptional conditions burning may occur around the tattoo (in extreme cases leading to blistering).
For people with facial or genital tattoos or large tattoos (greater than 7.5cms across), such burning could be inconvenient or uncomfortable and may require medical care.
People may feel tingling at the site of the tattoo during scanning if it is going to heat up; this provides a warning of a potential problem.
We advise not scan within 48 hours of a fresh tattoo as it may cause the ink to bleed and smudge the artwork.

What should I do if I feel any heating or tingling?

If you feel any heating or tingling in your tattoo alert the scanner operator using the call bell. We will stop the scan and remove you from the scanner. If there are any signs of heating we will apply a cold compress. In extreme situations we will seek medical help. Terminating the scan does not affect any inconvenience allowance you may be due from participating in the study.

What should I do now?

If you no longer want to participate in the study, just tell the researcher. If you would still like to participate please continue reading.

Statement of consent.

I confirm that:	**Please initial box**
The researcher has explained the risk of having a scan with a tattoo	
That I want to proceed with the scan	
That I will alert the operator if I feel any heating or tingling in my tattoo(s)	
I understand that if this happens then the MR scan will be terminated	
I understand that terminating the scan will not affect any inconvenience allowance due to me for study participation	

Participant's Signature: .....

Date: .....

Investigator's Signature: .....

Date: .....

B.2 Chapter 2 Results

B.2.1 Respiratory Stimulus

Table B.1 summarises the results for chapter 2 participant characteristics.

	Part 1
PCV	N=10, 5M/5F, 21.7±1.6 years, 64.1±14.1 kg, 1.66±0.01 m
pCASL	N=9, 4F/5M, 21.3±1.2 years
	Part 2
B_0/B_1	N=6 2F/4M, 25.8±1.7 years, 76.7±14.5 kg, 1.73±0.97 m

TABLE B.1: Summary of participants characteristics for Chapter 2. Group mean±standard deviation. F (female), kg (kilograms), m (metres), M (male), std (standard deviation).

B.2.2 $P_{ET}CO_2$ Data for pCASL Params-1, -2 and -3

Table B.1 of all the $P_{ET}CO_2$ data for params-1, -2 and -3, comparing the normo-, hypercapnia and the difference data. There was no significant difference between the three parameters for the pCASL data $P_{ET}CO_2$ levels during normocapnia conditions, and there was no significant difference during the three hypercapnia conditions (ANOVA p=0.0000).

					Normocapnia $PETCO_2$ (mmHg)			Hypercapnia $PETCO_2$ (mmHg)			Δ $PETCO_2$ (mmHg)		
Participant Number	**Age**	**Sex**	**Weight (kg)**	**Height (cm)**	**P1**	**P2**	**P3**	**P1**	**P2**	**P3**	**P1**	**P2**	**P3**
1	23	M	65	169	40.3±1.7	41.1±2.9	38.4±1.2	46.4±0.6	45.3±1.5	45.9±0.3	6.1	4.1	7.5
2	22	M	90	161	41.7±0.5	41.9±0.7	43.0±0.8	48.4±0.3	49.3±0.2	50.7±0.2	6.7	7.4	7.7
3	23	F	49	158	41.03±0.8	40.8±0.6	40.1±0.9	47.2±0.4	47.2±0.4	46.9±0.4	6.2	6.4	6.9
5	20	M	57	173	40.8±1.0	40.7±1.3	40.0±0.4	47.9±0.3	48.8±0.3	47.1±0.3	7.1	8.1	7.1
6	20	F	69	175	39.0±0.4	38.8±0.8	39.0±0.7	45.9±0.7	46.0±0.4	46.0±0.4	6.8	7.1	7.1
7	25	F	60	160	36.0±0.8	36.1±1.1	35.4±1.0	44.8±0.4	44.7±0.4	44.8±0.4	8.8	8.6	9.3
8	22	M	64	178	41.0±1.2	39.8±0.6	39.0±0.4	48.9±0.3	47.1±0.4	45.5±0.3	7.9	7.3	6.5
9	21	F	85.2	163	39.7±0.6	39.5±0.7	39.3±0.4	47.4±0.2	47.2±0.4	47.0±0.3	7.7	7.7	7.7
10	20	M	50	162	41.6±1.2	43.9±0.6	44.4±0.5	49.0±0.2	50.7±0.4	51.2±0.4	7.4	6.7	6.9
Group Mean±SD	**21.8±1.7**	**5M, 4F**	**65.4±14.2**	**166.6±7.3**	**40.1±0.9**	**40.3±1.0**	**39.8±0.7**	**47.3±0.4**	**47.3±0.5**	**47.2±0.3**	**7.2±0.9**	**7.0±1.3**	**7.4±0.8**

FIGURE B.1: **Respiratory Stimulus pCASL.** Comparison the three pCASL (pseudocontinuous Arterial Spin Labelling) labelling parameter sets $PETCO_2$. Group mean±standard deviation. Δ (Change in $PETCO_2$ between normocapnia and hypercapnia $PETCO_2$), millimetres of mercury (mmHg), % (percentage), Pseudocontinuous Arterial Spin Labelling (pCASL), Params-1/2/3 (P1/2/3), end-tidal partial pressure of carbon dioxide ($PETCO_2$), N=9.

Table B.2 shows a summary of the respiratory stimulus during the B_1 scan.

Condition	**PETCO$_2$ (mmHg)**
Normal ventilation	50.2±1.3
Hyperventilation	46.8±1.6
Δ	-3.4±3.5
ANOVA	p=0.9374

TABLE B.2: Respiratory Stimulus for B_1. Group mean±standard deviation. There was no significant difference between normal and hyperventilation PETCO$_2$. Analysis of Variance (ANOVA), Difference between normal and hyperventilation (Δ), End-tidal partial pressure of carbon dioxide (PETCO$_2$).

Table B.3 shows the effect of hypercapnia on pCASL parameters median flow change and resulting CVR measurements.

Parameter Set	**Median Flow Change (%/mmHg)**	**Normalised by PETCO$_2$ (mmHg)**
Params-1	43.98±13.35	6.08±1.45
Params-2	29.47±14.35	4.05±1.61
Params-3	37.63±13.11	5.06±1.51
ANOVA	p=0.0315	p=0.0976
Tukey-Kramer test	Params-1 and Params-2	p=0.030

TABLE B.3: Part 1 Effect of Hypercapnia on Different pCASL Parameters. Group mean±standard deviation. Analysis of Variance (ANOVA), millimetres of mercury (mmHg), percentage change per mmHg (%/mmHg).

Table B.4 show a summary of the effect of hypercapnia on PCV across Arteries.

Artery and Condition	**Velocity (cm/s) Stats**	
ICA Normocapnia	44.4±9.3	
ICA Hypercapnia	52.6±11.7	
VA Normocapnia	22.6±5.1	
VA Hypercapnia	27.5±6.8	
	Condition	
Δ hypo- to normocapnia	ANOVA	p=0.0121
Post-hoc Tukey's HSD test	NSFD	
	Arteries	
Δ normo- and hypercapnia	ANOVA	p=0.0017
Post-hoc Tukey's HSD test	NSFD	
	Normalised by $P_{ET}CO_2$	
Δ hypo- to normocapnia	ANOVA	p=0.0036
Δ normo- to hypercapnia	ANOVA	p=0.0032
Tukey's HSD test	NSFD	

TABLE B.4: Part 1 Effect of Hypercapnia on PCV across Arteries. Group mean±standard deviation. Analysis of Variance (ANOVA), Centimetres per second (cm/s), Honestly Significant Difference (HSD). Not significantly difference (NSFD).

Table B.5 shows a summary of Part 2 Effect of Hyperventilation on B_0.

	Δ Normal to hyperventilation, single slice (Hz)
RICA	4.8±2.9 Hz
LICA	3.5±9.3 Hz
LVA	3.6±3.6 Hz
RVA	4.4±6.6 Hz
Kruskal-Wallis Tests	
Arteries	p=0.2611
Conditions	p=0.3312
	Range of B_0 offsets textbf(Hz)
RICA	-1.8±8.1
LICA	-3.2±2.7
LVA	9.1±16.6
RVA	8.1±14.9

TABLE B.5: Range of B_0 offsets was estimated as the difference between 2nd and 98th, for normal breathing and hyperventilation. Left/right (L/R) internal carotid arteries (ICA) and vertebral arteries (VA), Hertz (Hz).

Table B.6 shows a summary of B_0 across arteries.

Artery	**B_0 (Hz)**
RICA	18.7±4.8
LICA	23.0±6.2
LVA	21.5±10.2
RVA	28.2±12.9
Kruskal-Wallis Test	p=0.0162

TABLE B.6: B_0 Arteries. Left/right (L/R) internal carotid arteries (ICA) and vertebral arteries (VA), Hertz (Hz).

Table B.7 shows the B_0 across normo- and hyperventilation conditions.

Condition (Hz)	**B_0**
Normal ventilation	22.0±4.2
Hyperventilation	23.1±11.5
Kruskal-Wallis Test	p=0.4704
Mann Whitney U test between Conditions for Individual arteries	
Artery	**P-value**
RICA vs LICA	p=0.0086
RICA vs RVA	p=0.0056
RICA vs LVA	p=0.2140
LICA vs LVA	p=0.4355
LICA vs RVA	p=0.2364
LVA vs RVA	p=0.1658

TABLE B.7: B_0 across Conditions. Mann Whitney U test between conditions for individual arteries. Hertz (Hz).

Table B.8 shows a summary of the effect of labelling plane placement on B_1.

Artery	**At V3 Percentage (%)**	
RICA	94.2±2.9	
LICA	98.2±3.4	
LVA	100.3±5.9	
RVA	94.5±7.7	
Kruskal-Wallis Test	p=0.0934	
Artery	**At 90 mm below AC-PC line Percentage (%)**	
RICA	78.5±10.4	
LICA	83.3±7.2	
LVA	94.2±15.9	
RVA	93.0±8.4	
Kruskal-Wallis Test	p=0.0419	
Artery	**Comparing Conditions**	**Mann Whitney U**
RICA	+12.9±-8.1	p=0.0374
LICA	+14.5±-4.8	p=0.0065
LVA	+3.7±-11.8	p=0.4233
RVA	0.0±+0.0	p=0.7488

TABLE B.8: Part 2 Effect of Labelling Plane Placement on B_1. median±interquartile range. Left/right (L/R) internal carotid arteries (ICA) and vertebral arteries (VA), Percentage (%).

C Appendix Chapter 3

C.1 Chapter 3: Methods and Materials

Figure C.1 shows the basic health questionnaire used for screening participants and the in/exclusion criteria.

Volunteer Screening Form

Study Title: Pilot study to Determine the Effect of Low Blood Pressure Interventions on Carotid Artery Velocity during a Hypercapnic Challenge.

Investigators:
Dr Nicholas Blockley
Colette Milbourn
Aline Nixon

PERSONAL INFORMATION

Subject Number _____ Date ___/____/___

1. **Name** ……..

2. **Contact Address** ……..

……..

……..

3. **Contact Telephone number** .....……..

4. **E mail address**……

5**. Date of Birth** ……./……./…….

6. **GP Surgery Name and Address** ……..

……..

……..

7. **GP Surgery Phone Number** ……..

8. **GP Name** (if known) ……..

GENERAL HEALTH

1. In general would you say your health is;
Please tick one response

a. ☐ *Excellent*
b. ☐ *Very good*
c. ☐ *Good*
d ☐ *Fair*
e. ☐ *Poor*

2. Compared to one year ago, how would you rate your health in general now?
Please tick one response

a. ☐ *Much better than a year ago*
b. ☐ *Somewhat better than a year ago*
c. ☐ *About the same*
d. ☐ *Somewhat worse than a year ago*
e. ☐ *Much worse than a year ago*

3. The following questions are concerned with any medical conditions you might have.

Please tick one box on each line

	No	*Yes*	*Don't Know*
Diabetes			
Epilepsy			
Depression			
Hayfever			
Asthma			
Eczema			
High blood pressure			
Heart problems			
Breathing problems *			
Indigestion / heartburn			
Irritable bowel syndrome			
Any other medical condition not listed above (please detail below)			

*** other than asthma**

Please detail any other medical condition/s
……
……

If you answered '*yes*' to any of the above, when did you first start having the problem and what medication (if any) do you use?
……
……
……
……

4.

More specifically have you any history of any of the following?

- Angina/chest pain
- Heart disease
- Changes on an ECG (Electrocardiogram measurement of your heart) e.g. Cardiomyopathy, arrythmias or heart block
- Hypertension
- Adult respiratory distress syndrome
- Closed angle glaucoma
- Postural hypotension
- Cardiac comorbidities e.g. valve disorders
- Migraines
- Phosphodiesterase inhibitors e.g. Cialis
- Blood abnormalities

If you answered 'yes' please detail below

……
……
……

Medication Have you recently taken or are you currently taking any other medication that you have not previously mentioned on this form?

.....
.....

5. **Have you ever fainted or do you have a tendency to faint in certain situations?**
E.g. on standing, in a warm room, after fasting, during exercise, blood.

☐ ***Yes*** ☐ ***No*** ☐ ***Don't Know***

6. **Smoking** On average, how many cigarettes do you smoke a day?
(If a non – smoker, please put '*none*') ……

7. Do you suffer from any **allergies**? ☐ ***Yes*** ☐ ***No*** ☐ ***Don't Know***

If '*yes*', what are you allergic to?

……
……

7. **Alcohol** On average, how many units of alcohol do you drink in a week?

…….Units

(pint of beer/lager =3 units, pub measure of wine / spirits =1 unit)

8. **Have you taken part, or do you intend to take part in any other trials within the three months prior to or following this particular study?** ☐ ***Yes*** ☐ ***No***

……
……

9. **Have you given blood in the last three months or do you plan to give blood in the next three months?**.....
……
……

PHYSIOLOGICAL MEASUREMENTS

1. **Height** ……cm

2. **Weight** ……kg

3. **BP** (Lying) **……./…….**
   BP (Standing 1 minute) **……./…….**
   BP (Standing 3 minutes) **……./…….**

4. **HR** (Lying)**:** **……..**
   HR (Standing 1 minute)**:** **……..**
   HR (Standing 3 minutes)**:** **……..**

BMI = ……..

Bloods:

- **FBC**
- **LFT**
- **U&Es**

Date Phoned:

For Reference - In/Exclusion Criteria

Exclusion based on consent grounds:

- Does not have adequate understanding of verbal and written information in English, sufficient to complete safety screening.

Exclusion based on those with extreme physiology (not a health risk but not representative of 'average healthy' population):

- History or current psychiatric illness
- History or current neurological condition (e.g. epilepsy)
- Having taken part in a research study in the last 3 months involving invasive procedures or an inconvenience allowance
- Those with extremely different cardio-respiratory/ carbon dioxide sensitivity physiology (e.g. Extreme/endurance athletes (e.g. lifelong performance swimmers), wind/brass instrument players / vocalists etc) may be excluded at the discretion of the lead investigator.
- Clinically significant abnormalities on screening

Exclusion based on contraindicators for any of the interventions:

- Pregnant or breast feeding (drugs only licenced for over 18years)
- Taking routine medication (except contraceptive)
- Any major cardiorespiratory disease including asthma, metabolic and endocrine disease or any other significant medical condition or individuals taking any medication. Other specific contraindications which we will ask for at screening include significant migraines and glaucoma.

Contraindications at screening e.g.:

- Any blood abnormalities, specifically anemia and out of range liver function tests
- Resting systolic BP <100mmHg
- A significant postural drop of >20 mmHg from sitting to standing
- Postural drop of >20 mmHg from sitting to standing
- ECG abnormalities e.g. cardiomyopathy, arrythmias or heart block
- Migraine / headache sufferers

C.1.1 Withdrawn Participants

The following table C.1 lists the participants who were withdrawn, with the reason for withdrawal. Some demographic information was not recorded due to withdrawal before that part of the screening. Four more participants (not listed below) also withdrew due to problems with rescheduling study days.

Number	Age (years)	Weight (kg)	Height (m)	Sex	Sex	Reason for
1	25	67.2	158	F	Screening	High BMI >25 + Bloods MCV 81.9 (low)
2	21	70.6	177	F	Study day 1	Failed to cannulate
3	19	60.7	163	M	Study day 1	Low HR <50BPM
4	20	Not recorded	Not recorded	M	Screening	Asthma
5	20	75.1	177.5	M	Screening	Low HR <50BPM
6	20	83.2	177	M	Screening	High BMI >25
7	19	85.2	185	M	Screening	ECG contraindication
8	Met exclusion criteria before recording	87	180	M	Pre-Screening	High BMI >25
9	30	76.2	177	M	Study day 1	Low HR & BP <50BPM, SYS <100mmHg
10	21	53	160	F	Bloods	Low Bloods (MCV, MCH, MCHC low, RDW-CV High , Alkaline Phosphatase low)
11	19	53.3	160	F	Study day 1	Low BP and HR <50BPM &SYS <100mmHg
12	21	55	155	F	Study day 1	Low BP SYS <100mmHg
13	23	52	166	F	screening	LowBP <100mmHg
14	18	63	169	F	after screening	participant withdrew
Mean	**21.2**	**67.8**	**169.6**	NA	NA	NA
Standard deviation	**3.2**	**12.8**	**9.8**	NA	NA	NA

FIGURE C.1: **Participant Recruitment, Withdrawn participants**. The mean and standard deviation for the participants of the low blood pressure study; m (metres), F (female), kg (kilograms), M (male), SD (standard deviation).

C.1.2 Lower Body Negative Pressure Device

Note there was originally a third arm of the study intending to use a non-pharmacological device to lower BP. The Lower body negative pressure (LBNP) device was later removed from the study due to practical, feasibility and safety concerns, see Fig. C.2.

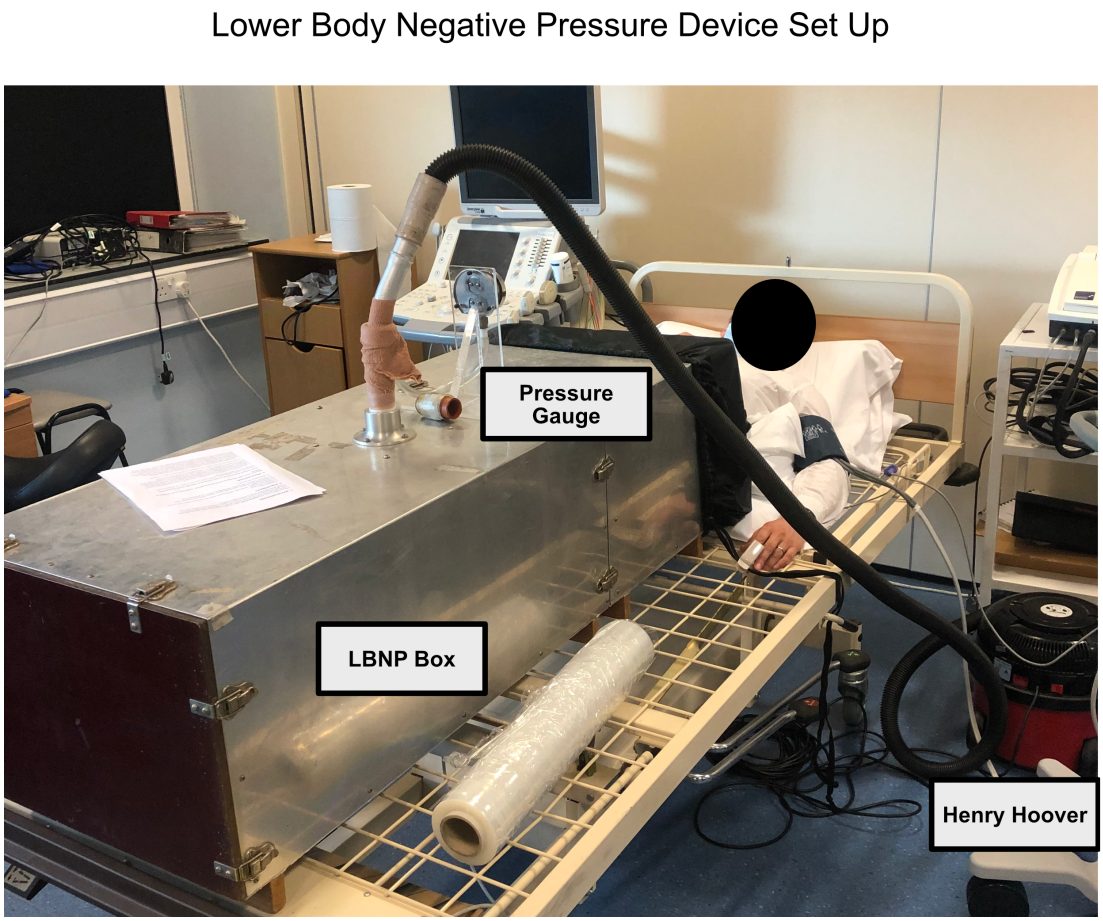


FIGURE C.2: **Lower Body Negative Pressure Device**. Lower Body Negative Pressure (LBNP) device, which was removed from the study design during development.

C.1.3 Ultrasound

Length of the minor axis of the vessel. Dist2 A 99.9 (mm)

*1: Either of the following two methods can be preset to calculate the flow volume.
The trace for the item (Vm_peak or Vm_mean) to be used for calculating the flow volume is displayed in light blue.
The trace for the item not used for calculation is displayed in dark blue.

- $Flow\ Vol(L/\min) = Vm_peak(cm/s) \times 60(s/\min) \times Area(mm^2)/100/1000$
- $Flow\ Vol(L/\min) = Vm_mean(cm/s) \times 60(s/\min) \times Area(mm^2)/100/1000$

*2: Whether Vmin or Ved is used for calculating PI can be preset.

- $PI = (Vmax - Vmin)/Vm_peak$
- $PI = (Vmax - Ved)/Vm_peak$

*3: Whether Vmin or Ved is used for calculating RI can be preset.

- $RI = (Vmax - Vmin)/Vmax$
- $RI = (Vmax - Ved)/Vmax$

*4: S/D calculation formula

- $S/D = Vmax/Ved$

*5: This item is measured and displayed when Auto Trace or Auto Range is selected as the trace method.

*6: This item is measured and displayed when Vel Trace is selected as the trace method.

FIGURE C.3: **Ultrasound Flow Volume calculations continued**
Page of the manual that shows the calculations for flow

In-house Matlab scripts were then used to calculate group median averages and plot the figures seen in the results section.

C.2 Chapter 3: Dinamap Results

Chapter 3 results for Dinamap data are summarised in Figure C.4.

	PRE INTERVENTION				POST INTERVENTION				PRE to POST Intervention	
Measurement	Pre Normo	Pre Hyper	ΔPre	ΔPre p-value	Post Normo	Post HYPER	ΔPost	ΔPost p-value	ΔNormo p-value	ΔPre to ΔPost p-value
GTN										
MAP (mmHg)	79.0±9.0	81.5 ± 10.0	0.5±4.0	p=0.5570	74.0±9.0	77.0±6.0	3.0±6.0	p=0.0740	p=0.0350	p=0.3360
HR (BPM)	62.5±11.0	68.0±12.0	-1.5±5.0	p=0.0273	72.5±12.0	78.5±17.0	2.0±9.0	p=0.0390	p=0.0020	p=0.0250
Vmax (cm/s)	82.2 ± 26.8	96.7±12.6	3.3±10.1	p=0.8457	93.2 ± 24.8	89.1±27.1	2.4±10.1	p=0.3200	p =0.770	p=0.9220
MET										
MAP (mmHg)	77.5±9.0	80.5±7.0	2.5±4.0	p=1.000	79.0±7.0	84.5±6.0	3.2±3.1	p=0.0040	p=0.895	p=0.8830
HR (BPM)	62.0±15.0	71.0±17.0	-0.5±8.0	p=0.8460	54.0±12.0	63.5±11.0	2.5±5.0	p=0.0060	p=0.0040	p=0.1680
Vmax (cm/s)	91.3 ± 16.9	98.5±112.0	0.3±17.5	p=0.0370	93.9 ± 36.6	113.6±18.6	6.4±15.0	p=0.0200	p=1.000	p=0.0273

FIGURE C.4: **Dinamap Results Summary.** Summary table of chapter 3 results. BPM (beats per minute), cm/sec (centimetres per second), ΔPre (difference between normocapnia and hypercapnia, during the HC, pre-intervention), ΔPost (difference between normocapnia and hypercapnia, during the HC, post-intervention), GTN (glyceryl trinitrate), HC (hypercapnic challenge), Hyper (hypercapnia), Normo (normocapnia), N-N (normocapnia pre- vs. normocapnia post-intervention), MET (metoprolol), mmHg (millimetres of mercury).

C.3 Chapter 3: Finapres Results

C.4 Finapres: Does the Pharmacological Intervention influence the Normocapnic Condition?

Table C.1 shows the baseline measurements taken at the beginning of the study day for the 10 participants. These measurements were similar for both study days, showing a relatively consistent baseline before starting the experiment.

TABLE C.1: **Baseline Measurements.** Baseline measurements (group median ± interquartile range, N=10) after participants had been resting, breathing room air, for 30minutes. BPM (beats per minutes), cm/s (centimeters per second), GTN (glyceryl trinitrate), MAP (mean arterial pressure), MET (Metoprolol), mmHg (millimetres of mercury), Vmax (Velocity Maximum).

Measurement	Day 1	Day 2
MAP	92.1±8.9	86.7±9.2
HR	68.4±17.1	63.8±10.4

C.4.1 Finapres: Mean Arterial Pressure

Figure C.5 shows the blood pressure values represented by the MAP data for each individual participant (coloured lines) along with the group median and interquartile range (IQR) (black bared lines) measured using a Finapres. Qualitatively, during the hypercapnic challenge, both before and after an intervention was given, the MAP did not vary much. Overall, these two figures show a slightly greater variability in the GTN data (Fig C.5A) compared to MET (Fig C.5B).

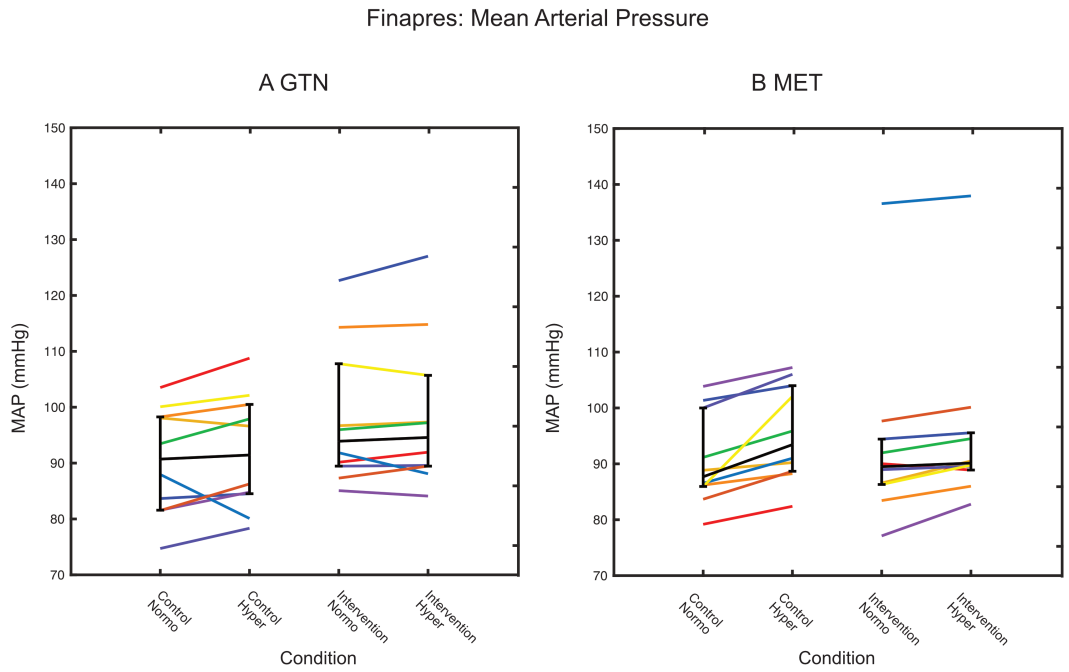


FIGURE C.5: **Finapres: Mean Arterial Pressure.** Coloured lines are for showing change in MAP within each participant across the whole experiment chronologically, the black line represents group median and interquartile range. N=10. GTN (glyceryl trinitrate), Hyper (hypercapnia), MAP (mean arterial pressure), MET (Metoprolol), mmHg (millimetres of mercury), Normo (normocapnia).

The blood pressure during control and intervention normocapnia conditions were compared to see if there was a noticeable effect of the pharmacological interventions on lowering the blood pressure i.e. did these medications produce the expected drop in blood pressure. Qualitatively, when the blood pressure was measured with Finapres (shown in Figure C.6) the control and intervention MAP data show little change for both GTN (Fig. C.6A) (median±IQR control to intervention MAP data; Finapres GTN=90.7±316.7 mmHg to 93.9±18.3 mmHg) and MET (Fig. C.6B) (Finapres MET=87.7±314.0 mmHg to 89.5±8.1 mmHg).

The two normocapnia conditions were compared with a Wilcox Sign Rank tests to see if there was a significant difference in MAP before or after the pharmacological interventions were given. Figures C.7 shows the blood pressure during normocapnia at a group level after the interventions were given, had a marginally significant difference between the MAP during control (left boxplots) or intervention (right boxplots) normocapnia conditions for GTN Finapres p=0.048 (Fig.C.6A), but not for MET Finapres p=1.000 (Fig.C.6B)). These results showed no change after correcting for multiple comparisons.

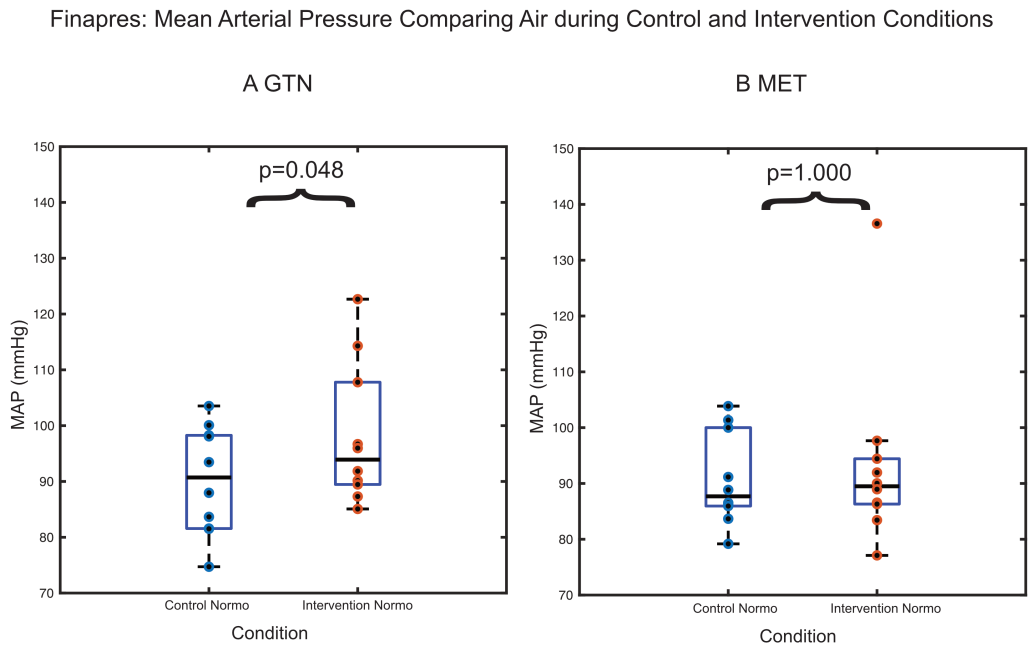


FIGURE C.6: **Finapres: Mean Arterial Pressure Comparing Normocapnia during Control and Intervention Conditions.** Shows the control (left boxplot) and intervention (right boxplot) MAP during normocapnia. The circles show the individual participants and the black line represents group median and interquartile range. N=10. There was a significant difference between the control and intervention normocapnia data for MAP when GTN (p=0.048) but not MET (p=1.000) was given. GTN (glyceryl trinitrate), MAP (mean arterial pressure), MET (Metoprolol), mmHg (millimetress of mercury), Normo (normocapnia).

C.4.2 Finapres: Difference Between Control and Intervention Normocapnia Conditions: Mean Arterial Pressure

The difference between the control and intervention blood pressure during normocapnia condition were calculated to see if there was any noticeable difference in blood pressure after interventions had been given. Qualitatively, the results again showed little change in MAP after either of the interventions was given (median±IQR difference control to intervention MAP data; Finapres GTN=4.8±12.2mmHg (Fig. C.7A), Finapres MET=-1.0±17.8mmHg (Fig. C.7B).

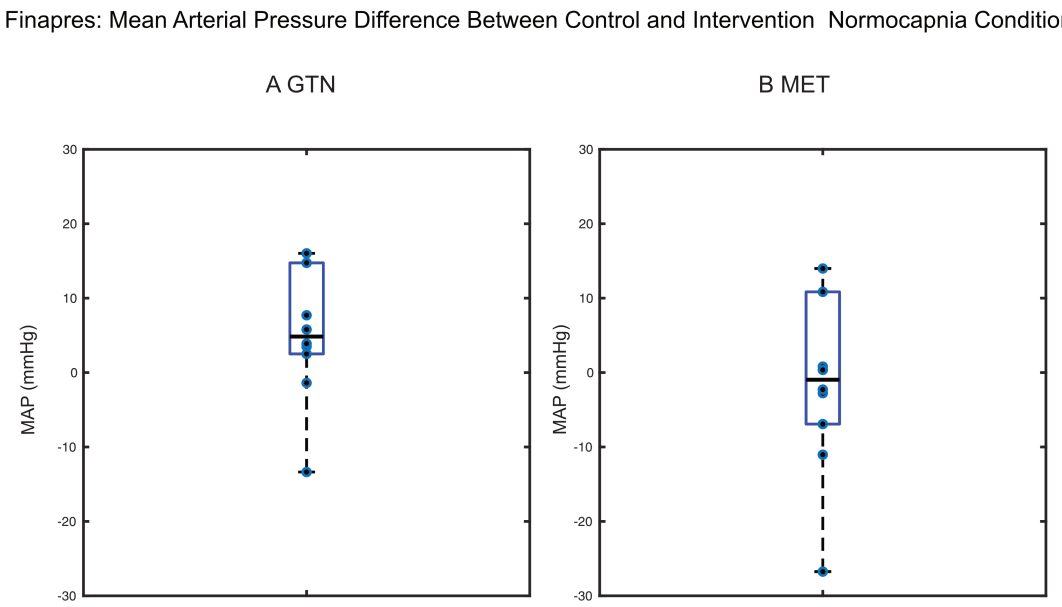


FIGURE C.7: **Finapres: Mean Arterial Pressure Difference Between Control and Intervention Normocapnia Conditions.** Shows the difference between the control and intervention MAP during normocapnic conditions. The circles show the individual participants and the black line represents group median and interquartile range. N=10. GTN (glyceryl trinitrate), MAP (mean arterial pressure), MET (Metoprolol), mmHg (of mercury).

C.4.3 Finapres: Heart Rate

The heart rate (in beats per minute (BPM)) was measured as a secondary finding to investigate HR as an adaptation or compensatory mechanism to the GTN or MET influence on blood pressure. Figures C.8 shows the heart rate for each individual participant (coloured lines) with the group median and IQR (black bar lines). There was more variation in the HR after the pharmacological interventions were given for MET (Fig.C.8B) (median±IQR control to intervention values; Finapres MET=67.1±12.5 BPM to 58.4±17.5BPM) compared to GTN (Fig.C.8A) (Finapres GTN = 62.5±12.0BPM to 73.9±5.5BPM).

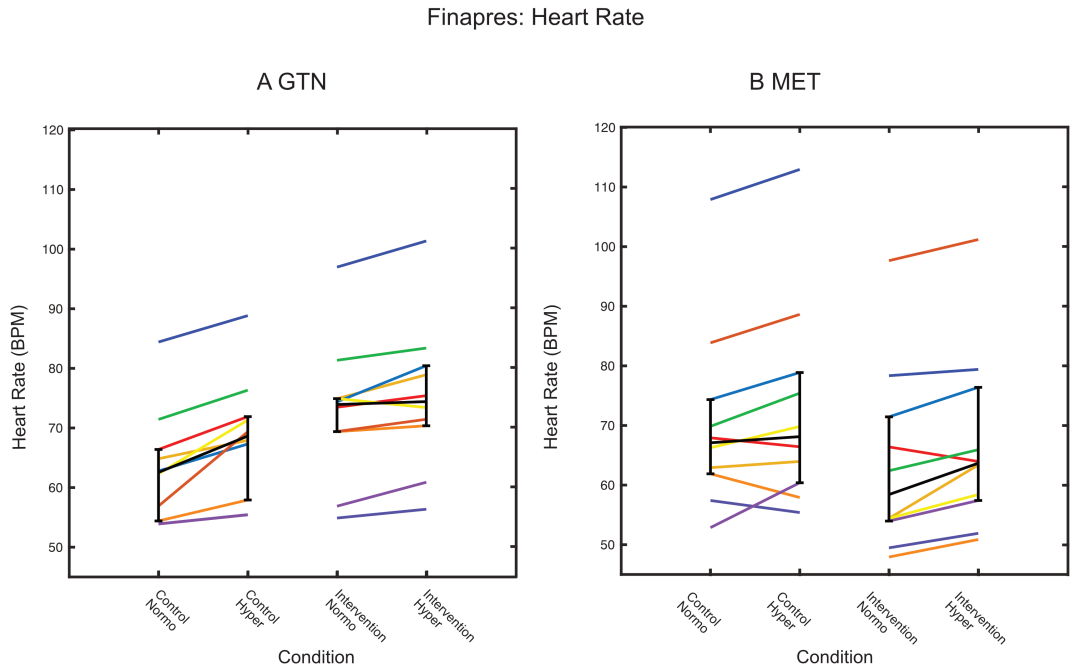


FIGURE C.8: **Finapres: Heart Rate.** Coloured lines show the change in HR within each participant across the whole experiment chronologically, the black line represents group median and interquartile range. N=10. BPM (beats per minute), GTN (glyceryl trinitrate), HR (heart rate), Hyper (hypercapnia), MET (Metoprolol), Normo (normocapnia).

C.4.4 Finapres: Heart Rate Difference in Control and Intervention Normocapnia conditions

When comparing the control and intervention heart rate during normocapnia, data show little change for Finapres measurements (Figure C.9).

There was a significant differences between the control (left boxplots) and intervention (right boxplots) normocapnia conditions for HR for Finapres GTN $p=0.002$ (Fig.C.9A), but not for Finapres MET $p=0.064$ (Fig.C.9B). The change in HR after GTN was still observed after correcting for multiple comparisons, but were not 'highly significant' using alpha of $p<0.001$.

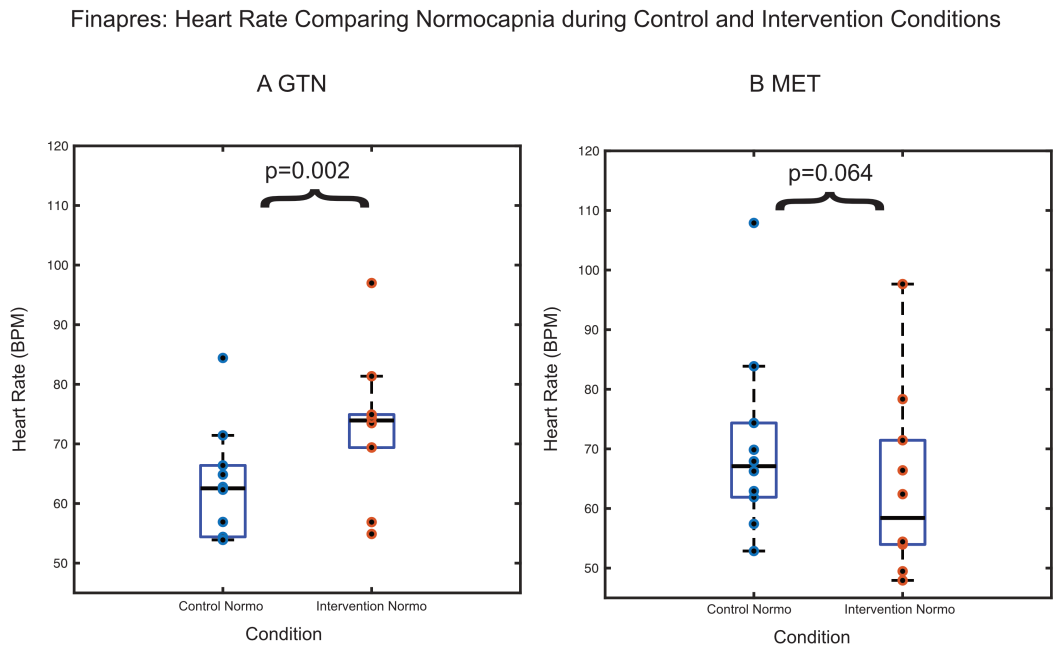


FIGURE C.9: **Finapres: Heart Rate Comparing Normocapnia during Control and Intervention Conditions.** Shows the control (left boxplot) and intervention (right boxplot) normocapnia heart rates. The circles show the individual participants and the black line represents group median and interquartile range. N=10. There was a significant difference between the control and intervention normocapnia conditions for HR when GTN was given (p=0.002) but not for MET (p=1.000) was given. BPM (beats per minute), GTN (glyceryl trinitrate), HR (heart rate), MET (Metoprolol), Normo (normocapnia).

At first glance, HR during normocapnia showed a more noticeable difference comparing control to intervention normocapnia conditions compared to the MAP and VMax data. Interestingly there was an increase in HR after GTN median±IQR difference control to intervention HR; Finapres GTN=10.8±5.5 BPM (Fig. C.10A), whereas there was a decrease in HR after MET Finapres MET=-7.7±10.3 BPM (Fig. C.10B). Additionally, HR data showed slightly more variability in the MET data during both normocapnia conditions.

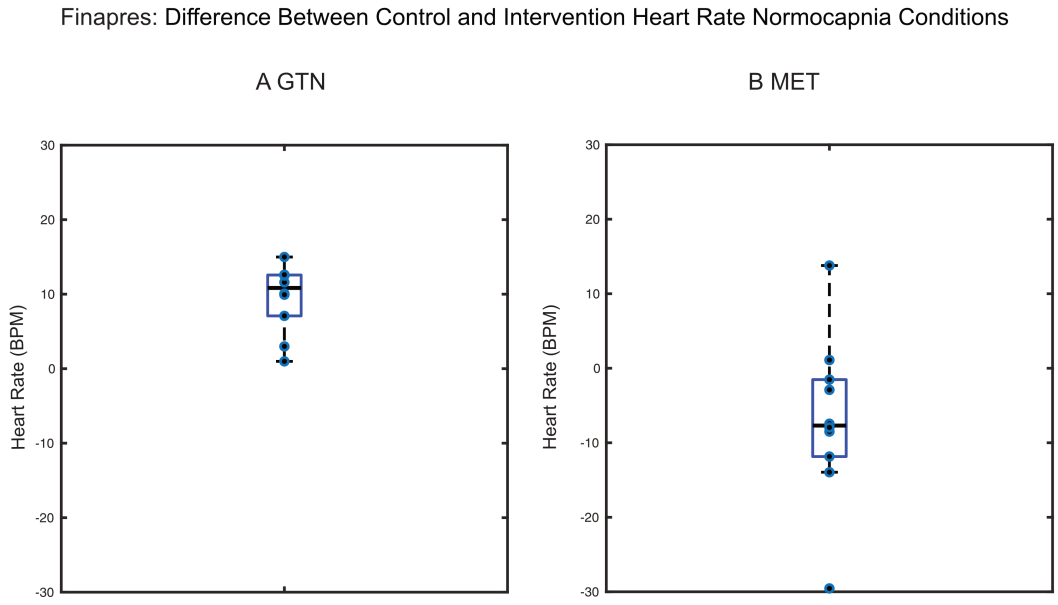


FIGURE C.10: **Finapres: Difference Between Control and Intervention Heart Rate Normocapnia Conditions.** Shows the difference between the control and intervention normocapnia heart rates. The circles show the individual participants and the black line represents group median and interquartile range. BPM (beats per minute), GTN (glyceryl trinitrate), HR (heart rate), MET (Metoprolol).

C.5 Finapres: Does the Intervention have an effect on the change between Normocapnia and Hypercapnia during the Hypercapnic Challenge?

The second outcome to investigate was to determine if the interventions had an effect on the physiological measurements (BP, velocity, HR) during the hypercapnic challenge. These results show the difference between the normocapnia and hypercapnic measurements both control and intervention.

C.5.1 Finapres: Difference during Hypercapnic Challenge: Mean Arterial Pressure

When comparing the difference in MAP between normocapnia and hypercapnia conditions, Finapres showed a small decrease in MAP after GTN (median±IQR difference between normocapnia and hypercapnia MAP, comparing control to intervention Finapres GTN=2.7±3.6 to 0.6±2.8mmHg (Fig. C.11A), and small decrease in MAP after MET (Finapres MET=3.9±2.4 to 2.5±2.3mmHg (Fig. C.11B). However, there was no significant difference between the normocapnia and hypercapnia conditions when comparing pre to post intervention change for MAP for either intervention (Finapres GTN ($p=0.322$) or Finapres MET ($p=0.105$)).

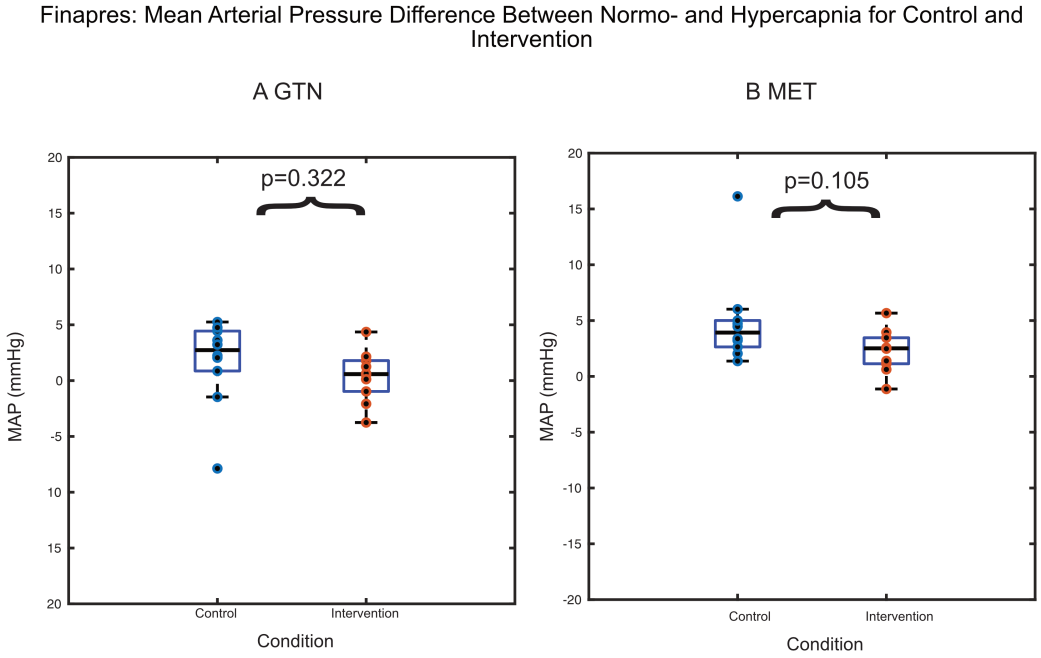


FIGURE C.11: **Finapres: Difference Between Normo- and Hypercapnia for Control and Intervention Mean Arterial Pressure.** Shows the difference between hypercapnia and normocapnia for control (left boxplot) and intervention (right boxplot) MAP. The circles show the individual participants and the black line represents group median and interquartile range. There was no significant difference between the change from normo- to hypercapnia conditions when comparing control to intervention change for MAP when GTN (p=0.322) or MET (p=0.105) was given. GTN (glyceryl trinitrate), MAP (mean arterial pressure), MET (Metoprolol), mmHg (millimetress of mercury).

C.5.2 Finapres: Difference during Hypercapnic Challenge: Heart Rate

Figure C.12 shows further secondary findings, that there was very little difference in HR during the hypercapnic challenge either before or after either of the interventions was given; Finapres: GTN 4.5±2.3BPM to 2.1±2.5BPM (Fig. C.12A), MET 4.0±6.6BPM to 3.5±1.6BPM (Fig. C.12B).

Additionally, there was no significant difference between the change from normocapnia to hypercapnia conditions when comparing control to intervention for HR when GTN was given when measured with Finapres (p=0.131). Finally, there was no significant difference between the change from normo- to hypercapnia conditions when comparing control to intervention change for HR when MET was given when measured with Finapres (p=0.846).

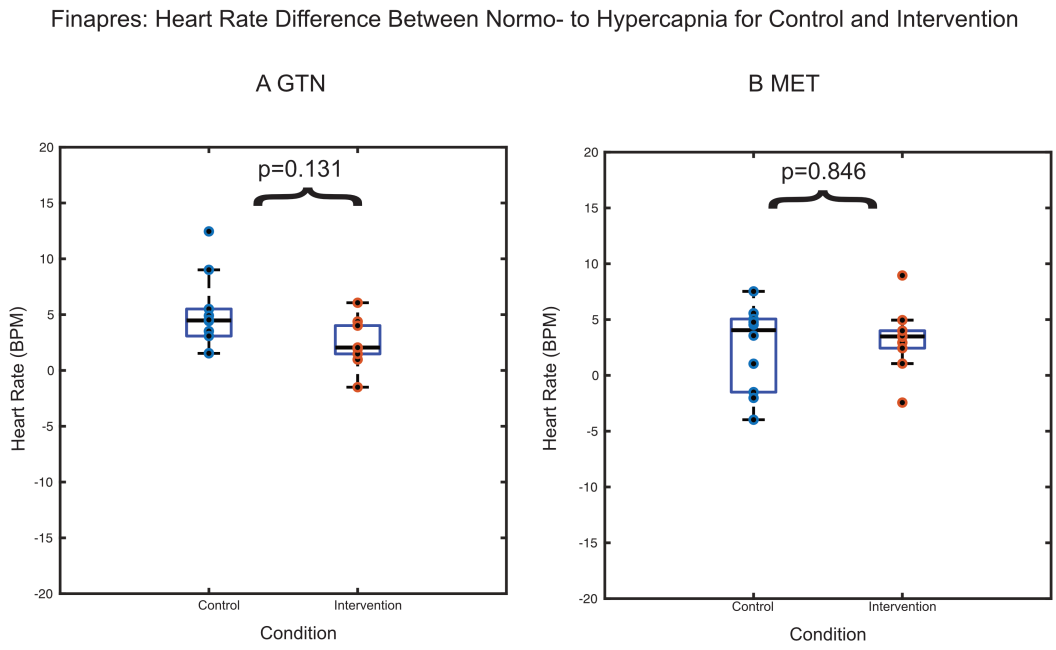


FIGURE C.12: **Finapres: Heart Rate Difference Between Normo- to Hypercapnia for Control and Intervention.** Shows the difference between hypercapnia and normocapnia for control (left boxplot) and intervention (right boxplot) heart rates. The circles show the individual participants and the black line represents group median and interquartile range. There was no significant difference between the change from normocapnia to hypercapnia conditions when comparing control to intervention for HR when GTN (p=0.131) or MET (p=0.846) was given. BPM (beats per minute), GTN (glyceryl trinitrate), HR (heart rate), MET (Metoprolol).

D Appendix

D.1 Chapter 4 Appendix: Methods and Materials

Figure D.1 shows more details of the BOLD sequence parameters.

BOLD fMRI Data Collection Details

Scanner			
	Recommended	Manufacturer	GE Healthcare
		Scanner Model	Signa Premier
		Magnetic field strength (tesla)	3T
	useful	Software version	29\LX\\RX29.1_R02_2131.a
Hardware Options:			
	Recommended	Rx coil type	GE 48 Channel head coil
Spatial encoding			
	Recommended	Pulse seuqence type	EPI
		number of shots if >1	1
		PE acceleration factor if >1	3
		PE acceleration type if used	Multiband acceleration Factor Phase=2, hyperband slice =3, slice =1
		PE partial fourier scheme (if used)	
	useful	PE direction	phase encoding polarity =1 (reverse)
		Phase over sampling(if used)	
		Read gradient bandwidth	250
		Readout echo spacing(ms)	spacing =0
	supplemental	Pulse sequence name	epiSPMIC, fmri MB3_ARC2_fMRI
Spatial Parameters			
	Recommended	In-plane FOV (mm x mm)	freq FOV= 21.2, Phase FOV= 1
		in plane matrix	acq voxel size 2.0x2.0x2.0
		In-plane inline filtering (if any)	intensity filter =none
		slice thickness (mm)	2
		inter-slice gap(mm)	spacing0, spacing between slices 2
		Number of slices	60
		slice acquisition order	freq dir = R/L, phase acquisition order = interleaved
		slice orientation	scan plane = oblique
Timing Parameters			
	Recommended	TR (ms)	1400
		TE (ms)	35
		No of volumes in time series	299 total volumes per dataset
		No of averages/ volumes if >1	
RF& Contrast			
	Recommended	Excitation flip angle (deg)	68
		Fat suppression scheme	spectral-spatial FatSat=0 (off)
	supplemental	Excitation RF pulse shape	excitation mode= selection, RF drive mode= quadr
Customisation			
	Recommended	Sparse sampling delay (if used)	delay after acq = minimum
		Prospective motion correction scheme (if used)	Motion correction done with MCFLIRT(FSL)
		Cardiac gating(if used)	yes
	supplemental	shim routine	shim = off, shim setting= 14,-6,-184

FIGURE D.1: **BOLD Data Collection supplementary details.** BOLD data collection supplementary details. EPI (echo planar imaging), FOV (field-of-view), mm (millimetres), ms (milliseconds), PE (phase encode), Rx (Radiofrequency (RF) receiver), SPMIC (Sir Peter Mansfield Imaging Centre), Tx (Radiofrequency (RF) transmitter), T (tesla) TE (echo time), TR (repetition time).

D.2 Chapter 4 Appendix: Results

D.2.1 Summary of Chapter 4 Results: Respiratory Stimulus

The following results are from Participants: N = 16, 23.8±3.2 years, 8M/8F, 73.1±13.9 kg, 1.70±0.10, of which there are Datasets: N=11, 4M/7F, 23.5±3.3 years, 75.1±15.6 kg, 1.70±0.10 m.

Table D.1 shows the respiratory stimulus results for Part 1, eASL Hypercapnic Challenges.

TABLE D.1: **Respiratory Stimulus, Part 1, eASL Hypercapnic Challenges.** Group mean ± standard deviation, N=11. end-tidal partial pressure of carbon dioxide ($P_{ET}CO_2$), millimetres of mercury (mmHg).

Condition	$P_{ET}CO_2$ (mmHg)
Normocapnia	33.2±4.5
Hypercapnia	42.7±2.4
Difference	+9.6±3.4
T-test	p=2.31e-06

Table D.2 shows the respiratory stimulus results for Part 2, BOLD Hypercapnic Challenges.

TABLE D.2: **Respiratory Stimulus, Part 2, BOLD Hypercapnic Challenges.** Group mean ± standard deviation, N=11. End-tidal partial pressure of carbon dioxide ($P_{ET}CO_2$), millimetres of mercury (mmHg).

Condition	$P_{ET}CO_2$ (mmHg)
Baseline	
Run 1	31.0±3.4
Run 2	31.7±3.0
T-Test	p=0.076
Amplitude	
Run 1	10.9±1.6
Run 2	10.2±2.2
T-Test	p=0.241
Group Means $P_{ET}CO_2$	
Run 1	36.2±4.4
Run 2	36.6±4.2
Average	36.4±2.7
Average baseline	31.4±3.1
Average amplitude	10.6±1.9
T-Test Baseline to Amplitude	p=1.22e-09

D.2.2 Summary of Chapter 4 Results: MR

Table D.3 shows the MR results for Part 1, eASL Hypercapnic Challenges.

TABLE D.3: **Part 1, eASL Hypercapnic Challenges, MR.** Medians±group standard error of the mean, N=11. Difference between normo and hypercapnia (Δ), Normo (normocapnia), End-tidal partial pressure of carbon dioxide ($PETCO_2$), millimetres of mercury (mmHg).

Condition	Measurement
CBF (ml/100g/min)	
Normo	69.6±4.5
Hyper	108.0±6.2
T-test	p=0.0002
Δ	+59.6±11.7%
Normalised by $PETCO_2$	5.8±0.5%
aCBV (%)	
Normo	2.3±0.3
Hyper	2.9±0.4
T-test	p=0.4545
Δ	+44.2±25.6
Normalised by $PETCO_2$	+5.2±2.6 %/mmHg
ATT (s)	
Normo	1.0±0.01
Hyper	0.8±0.1
T-test	p=0.0008
Δ	-22.0±3.6%
Normalised by $PETCO_2$	-2.2±0.2%/mmHg

Table D.4 shows the MR results for Part 2, BOLD Hypercapnic Challenges.

TABLE D.4: **Part 2, BOLD Hypercapnic Challenges, MR.** Medians±group standard error of the mean, N=11. End-tidal partial pressure of carbon dioxide ($PETCO_2$), millimetres of mercury (mmHg), Time to Peak (TTP), percentage (%).

BOLD dCVR: Magnitude	**Percentage Change**
BOLD after hypercapnia	+3.2±0.3%
Normalised by $PETCO_2$	0.3±0.0%
BOLD dCVR: TTP	**Percentage Change**
dCVR TTP after hypercapnia	+30.0±5.2 s

Table D.5 shows the different magnitude and timing metrics for eASL and BOLD for each of the five main grey matter cortices.

TABLE D.5: **Grey Matter Cortices eASL and BOLD data.** Break down of the metrics for each of the five main grey matter cortices. ANOVA (Analysis of Variance), ATT (arterial transit time), dCVR (dynamically modelled BOLD), s (seconds), sinCVR (sinusoidally modelled BOLD), TTP (Time to Peak).

Cortex	eASL (%)	ATT (s)	sinCVR Magnitude (%)	sinCVR Phase (Radians)	dCVR magnitude (%)	TTP (s)
Frontal	64.79 ± 12.46	-23.35 ± 2.86	3.40 ± 0.27	0.40 ± 0.10	3.66±0.31	28.85 ± 5.75
Insula	71.00 ± 13.88	-11.63 ± 5.41	2.92 ± 0.22	0.31 ± 0.10	3.34±0.30	31.09 ± 4.44
Occipital	57.80 ± 12.79	-21.47 ± 5.08	3.40± 0.26	0.32 ± 0.10	3.60±0.28	30.10 ± 5.17
Parietal	58.12 ± 12.08	-23.94 ± 4.43	3.20± 0.23	0.37 ± 0.10	3.43±0.26	28.60 ± 5.64
Temporal	59.78 ± 12.32	-23.56 ± 4.18	3.14± 0.23	0.33 ± 0.07	3.65±0.30	32.32 ± 5.12
ANOVA	p=0.9211	p=0.1686	p=0.5214	p=0.9343	p=0.8867	p=0.9765

E Appendix Chapter 5

E.1 Chapter 5 Results

Table E.1 shows the MR results summary for chapter 5.

TABLE E.1: **Chapter 5 Results Summary.** Average across the Five GM Cortices. Group mean of medians±group standard error of the mean, N=11.

Comparison	Of	Methods	R^2	p-value
Comparison of CVR Magnitude				
	eASL CVR	**sinCVR magnitude**		
CBF	62.3±5.6 %	3.2±0.2 %	0.07	p=0.0514
CVR	6.1±0.6 %/mmHg	0.3±0.02 %/mmHg	0.00	p=0.9400
	eASL CVR	**dCVR magnitude**		
CBF	62.3±5.6 %	3.5±0.1 %	0.07	p=0.0506
CVR	6.1±0.6 %/mmHg	0.3±0.0 %/mmHg	0.000163	p=0.9260
	sinCVR magnitude	**dCVR magnitude**		
CBF	3.2±0.2 %	3.5±0.1 %	0.832	p=3.32e-22
Comparison of Timing Measures				
	eASL ATT sinCVR Phase			
Timing	-20.8±5.2 s	0.4±0.0 radians	0.263	p=6.57e-05
	eASL ATT	**dCVR TTP**		
Timing	-20.8±5.2 s	30.2 ±1.6 s	0.05	p=0.1140
	sinCVR Phase	**dCVR TTP**		
Timing	0.4±0.0	30.2 ±1.6 s	0.22	p=0.0003

Bibliography

[1] Ahmed Abdel Khalek Abdel Razek, Mona Talaat, Lamiaa El-Serougy, Gada Gaballa, and Mohamed Abdelsalam. Clinical Applications of Arterial Spin Labeling in Brain Tumors. *Journal of Computer Assisted Tomography*, 43(4):525–532, 2019.

[2] Hunar Abdulrahman and Richard N. Henson. Effect of trial-to-trial variability on optimal event-related fMRI design: Implications for Beta-series correlation and multi-voxel pattern analysis. *NeuroImage*, 125:756–766, 2016.

[3] Kenneth F.; Adams, Arthur; Schatzkin, Tamara B.; Harris, Victor; Kipnis, Traci; Mouw, Rachel; Ballard-Barbash, Albert; Hollenbeck, and Michael F. Leitzmann. Overweight Obesity and Mortality in a Large Prospective Cohort of Persons 50 to 71 Years Old Enhanced Reader. *The New England Journal of Medicine*, 355(8), 2006.

[4] Philip N. Ainslie, Leo Celi, Ken McGrattan, Karen Peebles, and Shigehiko Ogoh. Dynamic cerebral autoregulation and baroreflex sensitivity during modest and severe step changes in arterial PCO2. *Brain Research*, 1230:115–124, 2008.

[5] Sarah Al-Bachari, Rishma Vidyasagar, Hedley C.A. Emsley, and Laura M. Parkes. Structural and physiological neurovascular changes

in idiopathic Parkinson's disease and its clinical phenotypes. *Journal of Cerebral Blood Flow and Metabolism*, 37(10):3409–3421, 2017.

[6] D. C. Alsop and J. A. Detre. Reduced transit-time sensitivity in noninvasive magnetic resonance imaging of human cerebral blood flow. *Journal of Cerebral Blood Flow and Metabolism*, 16(6):1236–1249, 1996.

[7] David Alsop. Recommended Implementation of ASL Perfusion MRI for Clinical Applications. 2015.

[8] David C. Alsop and John A. Detre. Multisection cerebral blood flow MRI imaging with continuous arterial spin labeling. *Radiology*, 208(2):410–416, 1998.

[9] María Guadalupe Mora Álvarez, Robert Wayne Stobbe, and Christian Beaulieu. High resolution continuous arterial spin labeling of human cerebral perfusion using a separate neck tagging RF coil. *PLoS ONE*, 14(4):1–11, 2019.

[10] Franck Amyot, Kimbra Kenney, Carol Moore, Margalit Haber, L. Christine Turtzo, Christian Shenouda, Erika Silverman, Yunhua Gong, Bao Xi Qu, Leah Harburg, Hanzhang Y. Lu, Eric M. Wassermann, and Ramon Diaz-Arrastia. Imaging of Cerebrovascular Function in Chronic Traumatic Brain Injury. *Journal of Neurotrauma*, 35(10):1116–1123, 2018.

[11] Franck Amyot, Cillian E. Lynch, John Ollinger, J. Kent Werner, E. Silverman, Carol Moore, Cora Davis, L. Christine Turtzo, Ramon Diaz-Arrastia, and Kimbra Kenney. Cerebrovascular Reactivity Measures Are Associated With Post-traumatic Headache Severity in Chronic TBI; A Retrospective Analysis. *Frontiers in Physiology*, 12(May):1–8, 2021.

[12] J L R Andersson, M Jenkinson, and S Smith. Non-linear registration, aka spatial normalization (FMRIB technical report TR07JA2). (June), 2010.

[13] Sina Aslan, Feng Xu, Peiying L. Wang, Jinsoo Uh, Uma S. Yezhuvath, Matthias Van Osch, and Hanzhang Lu. Estimation of labeling efficiency in pseudocontinuous arterial spin labeling. *Magnetic Resonance in Medicine*, 63(3):765–771, 2010.

[14] Vahan Aslanyan, Wendy J. Mack, Nancy E. Ortega, Ilya M. Nasrallah, Nicholas M. Pajewski, Jeff D. Williamson, and Judy Pa. Cerebrovascular reactivity in Alzheimer's disease signature regions is associated with mild cognitive impairment in adults with hypertension. *Alzheimer's and Dementia*, 20(3):1784–1796, 2024.

[15] Iris Asllani, Ajna Borogovac, and Truman R. Brown. Regression algorithm correcting for partial volume effects in arterial spin labeling MRI. *Magnetic Resonance in Medicine*, 60(6):1362–1371, 2008.

[16] Sarah Atwi, Han Shao, David E. Crane, Leodante da Costa, Richard I. Aviv, David J. Mikulis, Sandra E. Black, and Bradley J. MacIntosh. BOLD-based cerebrovascular reactivity vascular transfer function isolates amplitude and timing responses to better characterize cerebral small vessel disease. *NMR in Biomedicine*, 32(3):1–12, 2019.

[17] O. Bailliart, Ph Bonnin, A. Capderou, E. Savin, A. W. Kedra, and J. P. Martineaud. Simultaneous ultrasonic measurement of carotid blood flow and intracerebral haemodynamics in man. *Archives of Physiology and Biochemistry*, 101(2):149–154, 1993.

[18] Peter A. Bandettini, Eric C. Wong, R. Scott Hinks, Ronald S. Tikofsky, and James S. Hyde. Time course EPI of human brain function during

task activation. *Magnetic Resonance in Medicine*, 25(2):390–397, 1992.

[19] Robert B. Banzett, Ronald T. Garcia, and Shakeeb H. Moosavi. Simple contrivance 'clamps' end-tidal PCO2 and PO2 despite rapid changes in ventilation. *Journal of Applied Physiology*, 88(5):1597–1600, 2000.

[20] Deanna M. Barcha, Steven E. Petersena c d e Bradley L. Schlaggarc d e f Maurizio Corbettac d e Matthew F. Glasserd Sandra Curtissd Sachin Dixitb Cindy Feldtb Dan Nolanb Edward Bryantb Tucker Hartleyb Owen Footerb J Gregory C. Burgessd, Michael P. Harmsb, and David C. Van Essend for the WU-Minn HCP Consortium aDepartment. Function in the Human Connectome: Task-fMRI and Individual Differences in Behavior. *NeuroImage*, 80:169–189., 2013.

[21] Laia Bécares, Dharmi Kapadia, and James Nazroo. Neglect of older ethnic minority people in UK research and policy. *The BMJ*, 368(February):11–12, 2020.

[22] E. M. Bednarczyk, D. S. Wack, M. Y. Kassab, K. Burch, K. Trinidad, M. Haka, and J. Gona. Brain blood flow in the nitroglycerin (GTN) model of migraine: Measurement using positron emission tomography and transcranial Doppler. *Cephalalgia*, 22(9):749–757, 2002.

[23] Eleanor S.K. Berry, Peter Jezzard, and Thomas W. Okell. Off-resonance correction for pseudo-continuous arterial spin labeling using the optimized encoding scheme. *NeuroImage*, 199(February):304–312, 2019.

[24] BHSOC. *BHSOC*. PhD thesis, 2023.

[25] Philip E. Bickler, John R. Feiner, and John W. Severinghaus. Effects of skin pigmentation on pulse oximeter accuracy at low saturation.

Anesthesiology, 102(4):715–719, 2005.

[26] Jonathan Birns, J. Jarosz, H. S. Markus, and L. Kalra. Cerebrovascular reactivity and dynamic autoregulation in ischaemic subcortical white matter disease. *Journal of Neurology, Neurosurgery and Psychiatry*, 80(10):1093–1098, 2009.

[27] Bharat Biswal, F. Zerrin Yetkin, Victor M. Haughton, and James S. Hyde. Functional connectivity in the motor cortex of resting human brain using echo-planar mri. *Magnetic Resonance in Medicine*, 34(4):537–541, 1995.

[28] F. Bloch. Nuclear induction. *Physical Review*, 70(7-8):460–474, 1946.

[29] Nicholas P. Blockley, Ian D. Driver, Susan T. Francis, Joseph A. Fisher, and Penny A. Gowland. An improved method for acquiring cerebrovascular reactivity maps. *Magnetic Resonance in Medicine*, 65(5):1278–1286, 2011.

[30] Nicholas P. Blockley, Valerie E.M. Griffeth, Michael A. Germuska, Daniel P. Bulte, and Richard B. Buxton. An analysis of the use of hyperoxia for measuring venous cerebral blood volume: Comparison of the existing method with a new analysis approach. *NeuroImage*, 72:33–40, 2013.

[31] Nicholas P. Blockley, James W. Harkin, and Daniel P. Bulte. Rapid cerebrovascular reactivity mapping: Enabling vascular reactivity information to be routinely acquired. *NeuroImage*, 159(January):214–223, 2017.

[32] PA Bottomley and JR Griffith. *Handbook of Magnetic Resonance Spectroscopy In Vivo. MRS Theory, Practice and Applications*. John Wiley & Sons, Chichester, UK, 2014.

[33] Geoffrey M. Boynton, Stephen A. Engel, Gary H. Glover, and David J. Heeger. Linear systems analysis of functional magnetic resonance imaging in human V1. *Journal of Neuroscience*, 16(13):4207–4221, 1996.

[34] Molly G. Bright, Daniel P. Bulte, Peter Jezzard, and Jeff H. Duyn. Characterization of regional heterogeneity in cerebrovascular reactivity dynamics using novel hypocapnia task and BOLD fMRI. *NeuroImage*, 48(1):166–175, 2009.

[35] Molly G. Bright, Erin L. Mazerolle, Olivia Sobczyk, Audrey P Fan, Matthias JP van Osch, Clarisse I. Mark, Laurentius Huber, Avery J.L. Berman, Daniel P. Bulte, Bruce G. Pike, Claudine J. Gauthier, and Nicholas P. Blockley. Clinical mapping of cerebrovascular reactivity using MRI: a framework for reaching consensus. In *International Society for Magnetic Reonance in Medicine 2017*, 2017.

[36] Molly G. Bright and Kevin Murphy. Reliable quantification of BOLD fMRI cerebrovascular reactivity despite poor breath-hold performance. *NeuroImage*, 83:559–568, 2013.

[37] Molly G. Bright, Joseph R. Whittaker, Ian D. Driver, and Kevin Murphy. Vascular physiology drives functional brain networks. *NeuroImage*, 217(June 2019):116907, 2020.

[38] Gregory G. Brown, Lisa T.Eyler Zorrilla, Bassem Georgy, Sandra S. Kindermann, Eric C. Wong, and Richard B. Buxton. BOLD and perfusion response to finger-thumb apposition after acetazolamide administration: Differential relationship to global perfusion. *Journal of Cerebral Blood Flow and Metabolism*, 23(7):829–837, 2003.

[39] Harald Bruhn, Andreas Kleinschmidt, Henning Boecker, Klaus Dietmar

Merboldt, Wolfgang Hänicke, and Jens Frahm. The effect of acetazolamide on regional cerebral blood oxygenation at rest and under stimulation as assessed by MRI. *Journal of Cerebral Blood Flow and Metabolism*, 14(5):742–748, 1994.

[40] D. J. Bryant, A. Payne, D. N. Firmin, and D. B. Longmore. Measurement of flow using NMR imaging. *Journal of Computer*, 8(4):588–598, 1984.

[41] Claire V. Burley, Susan T. Francis, Kate N. Thomas, Anna C. Whittaker, Samuel J.E. Lucas, and Karen J. Mullinger. Contrasting Measures of Cerebrovascular Reactivity Between MRI and Doppler: A Cross-Sectional Study of Younger and Older Healthy Individuals. *Frontiers in Physiology*, 12(April):1–17, 2021.

[42] Adam Bush, Yaqiong Chai, So Young Choi, Lena Vaclavu, Scott Holland, Aart Nederveen, Thomas Coates, and John Wood. Pseudo continuous arterial spin labeling quantification in anemic subjects with hyperemic cerebral blood flow. *Magnetic Resonance Imaging*, 47(October 2017):137–146, 2018.

[43] David W. Busija, Ferenc Bari, Ferenc Domoki, and Thomas Louis. Mechanisms Involved in the Cerebrovascular Dilator Effects of N-methyl-D-aspartate in Cerebral Cortex David. *Brain Res Rev.*, 56(1):89–100, 2007.

[44] Richard B. Buxton, Lawrence R. Frank, Eric C. Wong, Bettina Siewert, Steven Warach, and Robert R. Edelman. A general kinetic model for quantitative perfusion imaging with arterial spin labeling. *Magnetic Resonance in Medicine*, 40(3):383–396, 1998.

[45] György Buzsáki, Kai Kaila, and Marcus Raichle. Inhibition and Brain

Work György. *Neuron*, 56(5):771–783, 2007.

[46] Paul T. Callaghan. *Translational Dynamics and Magnetic Resonance: Principles of Pulsed Gradient Spin Echo NMR*. Oxford Academic, Oxford, 2011.

[47] Keri L.H. Carpenter, Marek Czosnyka, Ibrahim Jalloh, Virginia F.J. Newcombe, Adel Helmy, Richard J. Shannon, Karol P. Budohoski, Angelos G. Kolias, Peter J. Kirkpatrick, Thomas Adrian Carpenter, David K. Menon, and Peter J. Hutchinson. Systemic, local, and imaging biomarkers of brain injury: More needed, and better use of those already established? *Frontiers in Neurology*, 6(FEB):1–20, 2015.

[48] S. Carrasco, R. González, J. Jiménez, R. Román, V. Medina, and J. Azpiroz. Comparison of the heart rate variability parameters obtained from the electrocardiogram and the blood pressure wave. *Journal of Medical Engineering and Technology*, 22(5):195–205, 1998.

[49] M. A. Chappell, A. R. Groves, B. J. MacIntosh, M. J. Donahue, P. Jezzard, and M. W. Woolrich. Partial volume correction of multiple inversion time arterial spin labeling MRI data. *Magnetic Resonance in Medicine*, 65(4):1173–1183, 2011.

[50] Michael A. Chappell, Adrian R. Groves, Brandon Whitcher, and Mark W. Woolrich. Variational Bayesian inference for a nonlinear forward model. *IEEE Transactions on Signal Processing*, 57(1):223–236, 2009.

[51] Michael A. Chappell, Thomas F. Kirk, Martin S. Craig, Flora A. Kennedy McConnell, Moss Y. Zhao, Bradley J. MacIntosh, Thomas W. Okell, and Mark W. Woolrich. BASIL: A toolbox for perfusion quantification using arterial spin labelling. *Imaging Neuroscience*, 1(November):1–16, 2023.

[52] Michael A. Chappell, Bradley J. MacIntosh, Manus J. Donahue, Matthias Günther, Peter Jezzard, and Mark W. Woolrich. Separation of macrovascular signal in multi-inversion time arterial spin labelling MRI. *Magnetic Resonance in Medicine*, 63(5):1357–1365, 2010.

[53] Michael A. Chappell, Mark W. Woolrich, Samira Kazan, Peter Jezzard, Stephen J. Payne, and Bradley J. MacIntosh. Modeling dispersion in arterial spin labeling: Validation using dynamic angiographic measurements. *Magnetic Resonance in Medicine*, 69(2):563–570, 2013.

[54] J. Jean Chen and Claudine J. Gauthier. The Role of Cerebrovascular-Reactivity Mapping in Functional MRI: Calibrated fMRI and Resting-State fMRI. *Frontiers in Physiology*, 12(March), 2021.

[55] Jingyuan E. Chen, Gary H. Glover, Nina E. Fultz, Bruce R. Rosen, Jonathan R. Polimeni, and Laura D. Lewis. Investigating mechanisms of fast BOLD responses: The effects of stimulus intensity and of spatial heterogeneity of hemodynamics. *NeuroImage*, 245(February):118658, 2021.

[56] Zhiqiang Chen, Jian Zhang, and Jonathan S. Stamler. Identification of the enzymatic mechanism of nitroglycerin bioactivation. *Proceedings of the National Academy of Sciences of the United States of America*, 99(12):8306–8311, 2002.

[57] Seong-Cheol Choi, Doh-Hun Gwon, Keon-Yeong Kim, Min-Su Lee, and Dong-Seong Kim. Usefulness Study of 7 Delays eASL(Enhanced Arterial Spin Labeling) in Comparison to Single Delay ASL. *Journal of the Korean Society of MR Technology*, 27(1):45–55, 2017.

[58] Alexander D. Cohen, Andrew S. Nencka, and Yang Wang. Multiband

multi-echo simultaneous ASL/ BOLD for task-induced functional MRI. *PLoS ONE*, 13(2):1–21, 2018.

[59] Mandy M.A. Conijn, Johannes M. Hoogduin, Yolanda van der Graaf, Jeroen Hendrikse, Peter R. Luijten, and Mirjam I. Geerlings. Microbleeds, lacunar infarcts, white matter lesions and cerebrovascular reactivity - A 7T study. *NeuroImage*, 59(2):950–956, 2012.

[60] Aditi S. Dabir, Chintan A. Trivedi, Yeontack Ryu, Paritosh Pande, and Javier A. Jo. Fully automated deconvolution method for on-line analysis of time-resolved fluorescence spectroscopy data based on an iterative Laguerre expansion technique. *Journal of Biomedical Optics*, 14(2):024030, 2009.

[61] Weiying Dai, Dairon Garcia, Cedric De Bazelaire, and David C. Alsop. Continuous flow-driven inversion for arterial spin labeling using pulsed radio frequency and gradient fields. *Magnetic Resonance in Medicine*, 60(6):1488–1497, 2008.

[62] Weiying Dai, Ajit Shankaranarayanan, and David C. Alsop. Volumetric measurement of perfusion and arterial transit delay using hadamard encoded continuous arterial spin labeling. *Magnetic Resonance in Medicine*, 69(4):1014–1022, 2013.

[63] Annemarie De Greeff and Andrew H. Shennan. Clinical assessment of the DINAMAP ProCare monitor in an adult population according to the British Hypertension Society Protocol. *Blood Pressure Monitoring*, 12(2):107–111, 2007.

[64] J. B. De Vis, J. Hendrikse, A. Bhogal, A. Adams, L. J. Kappelle, and E. T. Petersen. Age-related changes in brain hemodynamics; A calibrated MRI

study. *Human Brain Mapping*, 36(10):3973–3987, 2015.

[65] Manus J. Donahue, Michael Ayad, Ryan Moore, Matthias Van Osch, Robert Singer, Paul Clemmons, and Megan Strother. Relationships between hypercarbic reactivity, cerebral blood flow, and arterial circulation times in patients with moyamoya disease. *Journal of Magnetic Resonance Imaging*, 38(5):1129–1139, 2013.

[66] Manus J. Donahue, Carlos C. Faraco, Megan K. Strother, Michael A. Chappell, Swati Rane, Lindsey M. Dethrage, Jeroen Hendrikse, and Jeroen C.W. Siero. Bolus arrival time and cerebral blood flow responses to hypercarbia. *Journal of Cerebral Blood Flow and Metabolism*, 34(7):1243–1252, 2014.

[67] Manus J. Donahue, Peter Jan Van Laar, Peter C.M. Van Zijl, Robert D. Stevens, and Jeroen Hendrikse. Vascular space occupancy(VASO) cerebral blood volume-weighted MRI identifies hemodynamic impairment in patients with carotid artery disease. *Journal of Magnetic Resonance Imaging*, 29(3):718–724, 2009.

[68] J. Duffin. Measuring the respiratory chemoreflexes in humans. *Respiratory Physiology and Neurobiology*, 177(2):71–79, 2011.

[69] James Duffin, Olivia Sobczyk, Adrian Crawley, Julien Poublanc, Lashmi Venkatraghavan, Kevin Sam, Alan Mutch, David Mikulis, and Joseph Fisher. The role of vascular resistance in BOLD responses to progressive hypercapnia. *Human Brain Mapping*, 38(11):5590–5602, 2017.

[70] Allen D. Elster. Questions and Answers in MRI, 2020.

[71] Ayten Elvan-Taşpinar, Leonore A.M.Schoot Uiterkamp, J. Marko Sikkema, Michiel L. Bots, Hein A. Koomans, Hein W. Bruinse, and

Arie Franx. Validation and use of the Finometer™ for blood pressure measurement in normal, hypertensive and pre-eclamptic pregnancy. *Journal of Hypertension*, 21(11):2053–2060, 2003.

[72] Allison C Engstrom, John Paul Alitin, Arunima Kapoor, Shubir Dutt, Trevor Lohman, Isabel J Sible, Anisa J Marshall, Fatemah Shenasa, Aimée Gaubert, Farrah Ferrer, Amy Nguyen, David Robert Bradford, Kathleen Rodgers, Lorena Sordo, Elizabeth Head, Xingfeng Shao, Danny JJ Wang, and Daniel A Nation. Spontaneous cerebrovascular reactivity at rest in older adults with and without mild cognitive impairment and memory deficits. 2024.

[73] Andy Eugene. Metoprolol Dose Equivalence in Adult Men and Women Based on Gender Differences: Pharmacokinetic Modeling and Simulations. *Medical Sciences*, 4(4):18, 2016.

[74] AR Eugene. Gender based Dosing of Metoprolol in the Elderly using Population Pharmacokinetic Modeling and Simulations. *International Journal of Clinical Pharmacology & Toxicology*, 5(3):209–215, 2016.

[75] Hongli Fan, Henk J.M.M. Mutsaerts, Udunna Anazodo, Daniel Arteaga, Koen P.A. Baas, Charlotte Buchanan, Aldo Camargo, Vera C. Keil, Zixuan Lin, Thomas Lindner, Lydiane Hirschler, Jian Hu, Beatriz E. Padrela, Mohammad Taghvaei, David L. Thomas, Sudipto Dolui, and Jan Petr. ISMRM Open Science Initiative for Perfusion Imaging (OSIPI): ASL pipeline inventory. *Magnetic Resonance in Medicine*, 91(5):1787–1802, 2024.

[76] Ashraf Fawzy, Tianshi David Wu, Kunbo Wang, Matthew L. Robinson, Jad Farha, Amanda Bradke, Sherita H. Golden, Yanxun Xu, and Brian T. Garibaldi. Racial and Ethnic Discrepancy in Pulse Oximetry and

Delayed Identification of Treatment Eligibility among Patients with COVID-19. *JAMA Internal Medicine*, 182(7):730–738, 2022.

[77] John R. Feiner, John W. Severinghaus, and Philip E. Bickler. Dark skin decreases the accuracy of pulse oximeters at low oxygen saturation: The effects of oximeter probe type and gender. *Anesthesia and Analgesia*, 105(SUPPL. 6), 2007.

[78] Li Feng, Leon Axel, Hersh Chandarana, Kai Tobias Block, Daniel K. Sodickson, and Ricardo Otazo. XD-GRASP: Golden-angle radial MRI with reconstruction of extra motion-state dimensions using compressed sensing. *Magnetic Resonance in Medicine*, 75(2):775–788, 2016.

[79] J. Fierstra, O. Sobczyk, A. Battisti-Charbonney, D. M. Mandell, J. Poublanc, A. P. Crawley, D. J. Mikulis, J. Duffin, and J. A. Fisher. Measuring cerebrovascular reactivity: What stimulus to use? *Journal of Physiology*, 591(23):5809–5821, 2013.

[80] D. N. Firmin, G. L. Nayler, R. H. Klipstein, S. R. Underwood, R. S. O. Rees, and D. B. Longmore. In Vivo Validation of MR Velocity Imaging. *Journal of Computer Assisted Tomography*, 11(5):751–756, 1987.

[81] Joseph A. Fisher and David J. Mikulis. Cerebrovascular Reactivity: Purpose, Optimizing Methods, and Limitations to Interpretation – A Personal 20-Year Odyssey of (Re)searching. *Frontiers in Physiology*, 12(April), 2021.

[82] Joseph A. Fisher, Olivia Sobczyk, Adrian Crawley, Julien Poublanc, Paul Dufort, Lashmi Venkatraghavan, Kevin Sam, David Mikulis, and James Duffin. Assessing cerebrovascular reactivity by the pattern of response to progressive hypercapnia. *Human Brain Mapping*, 38(7):3415–3427,

2017.

[83] John B.; Fortune, Devon; Bock, Marie Kupinski; Kupinski, Howard H.; Stratton, Dhiraj; Shah, and Paul J. Feustel. Human Cerebrovascular Resposnse to Oxygen and Carbon Dioxide as Determined by Internal Carotid Artery Duplex Scanning. 32(2), 1992.

[84] Aisling Fothergill, Thomas Kirk, David Higgins, Aaron Oliver-Taylor, Logan Zhang, Martin Craig, Michael A Chappell, and Parkes Laura M. Impact of Bayesian-Inference vs Least-Squares Fitting on Multi-Delay Arterial Spin LLabelling Parameter Estimation. *ISMRM 2024 Proceedings*, 2024.

[85] J. Frahm, A. Haase, K.D Matthai, K.D. Merboldt, and W. Hanicke. Rapid NMR imaging using stimulated echoes. *J Magn Reson*, 65(130-135), 1985.

[86] J. Frahm, K. D. Merboldt, W. Hanicke, and A Haase. Stimulated echo imaging. *J Magn Reson*, 64:81–93, 1985.

[87] Blaise deB. Frederick, Lisa D. Nickerson, and Yunjie Tong. Physiological denoising of BOLD fMRI data using Regressor Interpolation at Progressive Time Delays (RIPTiDe) processing of concurrent fMRI and near-infrared spectroscopy (NIRS). *Neuroimage*, 60(3):1913–1923, 2012.

[88] K J Friston, C D Frith, R Turner, and R S Frackowiak. Characterizing evoked hemodynamics with fMRI, 1995.

[89] D. Gallagher, S. B. Heymsfield, M. Heo, S. A. Jebb, P. R. Murgatroyd, and Y. Sakamoto. Healthy percentage body fat ranges: An approach for developing guidelines based on body mass index. *American Journal of Clinical Nutrition*, 72(3):694–701, 2000.

[90] Claudine J. Gauthier, Cécile Madjar, Laurence Desjardins-Crépeau, Pierre Bellec, Louis Bherer, and Richard D. Hoge. Age dependence of hemodynamic response characteristics in human functional magnetic resonance imaging. *Neurobiology of Aging*, 34(5):1469–1485, 2013.

[91] GE. *GE Manual*. 0.

[92] Sanna Gevers, Aart J. Nederveen, Karin Fijnvandraat, Sandra M. Van Den Berg, Pim Van Ooij, Dennis F. Heijtel, Harriët Heijboer, Paul J. Nederkoorn, Marc Engelen, Matthias J. Van Osch, and Charles B. Majoie. Arterial spin labeling measurement of cerebral perfusion in children with sickle cell disease. *Journal of Magnetic Resonance Imaging*, 35(4):779–787, 2012.

[93] Lorenzo Ghiadoni, Martina Francesconi, Stefano Taddei, and Rosa Maria Bruno. Hemodynamic and autonomic effects of low-dose glyceryl trinitrate used to test endothelium-independent vasodilation of the brachial artery. *Vascular Pharmacology*, 120(June):106576, 2019.

[94] Lidia Glodzik, Catherine Randall, Henry Rusinek, and Mony J. De Leon. Cerebrovascular reactivity to carbon dioxide in alzheimer's disease. *Journal of Alzheimer's Disease*, 35(3):427–440, 2013.

[95] Gary H. Glover. Deconvolution of impulse response in event-related BOLD fMRI. *NeuroImage*, 9(4):416–429, 1999.

[96] Gary H. Glover. The Canonical HRF. In *ISMRM*, 2024.

[97] Ali M. Golestani, Jonathan B. Kwinta, Stephen C. Strother, Yasha B. Khatamian, and J. Jean Chen. The association between cerebrovascular reactivity and resting-state fMRI functional connectivity in healthy

adults: The influence of basal carbon dioxide. *NeuroImage*, 132:301–313, 2016.

[98] Ali M. Golestani, Luxi L. Wei, and J. Jean Chen. Quantitative mapping of cerebrovascular reactivity using resting-state BOLD fMRI: Validation in healthy adults. *NeuroImage*, 138:147–163, 2016.

[99] Ali M. Golestani, Luxi L. Wei, and J. Jean Chen. Quantitative mapping of cerebrovascular reactivity using resting-state BOLD fMRI: Validation in healthy adults. *NeuroImage*, 138:147–163, 2016.

[100] S. D. Goode, S. Krishan, C. Alexakis, R. Mahajan, and D. P. Auer. Precision of cerebrovascular reactivity assessment with use of different quantification methods for hypercapnia functional MR imaging. *American Journal of Neuroradiology*, 30(5):972–977, 2009.

[101] Krzysztof J. Gorgolewski, Tibor Auer2, Vince D. Calhoun, R. Cameron Craddock, Samir Das, Eugene P. Duff, Guillaume Flandin, Satrajit S. Ghosh, Tristan Glatard, Yaroslav O. Halchenko, Daniel A. Handwerker, Michael Hanke, David Keator, Xiangrui Li, Zachary Michael, Camille Maumet, B. Nolan Nichols, Thomas E. Nichols, John Pellman, Jean-Baptiste Poline, Ariel Rokem, Gunnar Schaefer, Vanessa Sochat, William Triplett, Jessica A. Turner, and Gaël Varoquaux29 Russell A. Poldrack1. The brain imaging data structure, a format for organizing and describing outputs of neuroimaging experiments. *Encyclopedia of Genetics, Genomics, Proteomics and Informatics*, pages 208–208, 2008.

[102] M. Grade, J. A. Hernandez Tamames, F. B. Pizzini, E. Achten, X. Golay, and M. Smits. A neuroradiologist's guide to arterial spin labeling MRI in clinical practice. *Neuroradiology*, 57(12):1181–1202, 2015.

[103] Mark A. Griswold, Peter M. Jakob, Robin M. Heidemann, Mathias Nittka, Vladimir Jellus, Jianmin Wang, Berthold Kiefer, and Axel Haase. Generalized Autocalibrating Partially Parallel Acquisitions (GRAPPA). *Magnetic Resonance in Medicine*, 47(6):1202–1210, 2002.

[104] M Guenther. Highly efficient accelerated acquisition of perfusion inflow series by Cycled Arterial Spin Labeling. *Proc. Intl. Soc. Mag. Reson. Med. 15*, 15:380, 2007.

[105] Matthias Gunther, Michael Bock, and Lothar R. Schad. Arterial spin labeling in combination with a look-locker sampling strategy: Inflow turbo-sampling EPI-FAIR (ITS-FAIR). *Magnetic Resonance in Medicine*, 46(5):974–984, 2001.

[106] Sheliza Halani, Jonathan B. Kwinta, Ali M. Golestani, Yasha B. Khatamian, and J. Jean Chen. Comparing cerebrovascular reactivity measured using BOLD and cerebral blood flow MRI: The effect of basal vascular tension on vasodilatory and vasoconstrictive reactivity. *NeuroImage*, 110:110–123, 2015.

[107] Julia J. Harris, Clare Reynell, and David Attwell. The physiology of developmental changes in BOLD functional imaging signals. *Developmental Cognitive Neuroscience*, 1(3):199–216, 2011.

[108] Martin Havlicek, Dimo Ivanov, Alard Roebroeck, and Kamil Uludağ. Determining excitatory and inhibitory neuronal activity from multimodal fMRI data using a generative hemodynamic model. *Frontiers in Neuroscience*, 11(NOV):1–20, 2017.

[109] Megan N. Hawkins, Quinton Barnes, Sushmita Purkayastha, Wendy Eubank, Shigehiko Ogoh, and Peter B. Raven. The effects of aerobic

fitness and β1-adrenergic receptor blockade on cardiac work during dynamic exercise. *Journal of Applied Physiology*, 106(2):486–493, 2009.

[110] Einar Heiberg, Jane Sjögren, Martin Ugander, Marcus Carlsson, Henrik Engblom, and Håkan Arheden. Design and validation of Segment - freely available software for cardiovascular image analysis. *BMC Medical Imaging*, 10:1–13, 2010.

[111] Yi Ching Lynn Ho, Esben Thade Petersen, Ivan Zimine, and Xavier Golay. Similarities and differences in arterial responses to hypercapnia and visual stimulation. *Journal of Cerebral Blood Flow and Metabolism*, 31(2):560–571, 2011.

[112] Kenneth R. Holmes, David Tang-Wai, Kevin Sam, Larissa Mcketton, Julien Poublanc, Adrian P. Crawley, Olivia Sobczyk, Melanie Cohn, James Duffin, Maria Carmela Tartaglia, Sandra E. Black, Joseph A. Fisher, Bruce Wasserman, and David J. Mikulis. Slowed Temporal and Parietal Cerebrovascular Response in Patients with Alzheimer's Disease. *Canadian Journal of Neurological Sciences*, 47(3):366–373, 2020.

[113] Gholam Ali Hossein-Zadeh, Babak A. Ardekani, and Hamid Soltanian-Zadeh. Activation detection in fMRI using a maximum energy ratio statistic obtained by adaptive spatial filtering. *IEEE Transactions on Medical Imaging*, 22(7):795–805, 2003.

[114] Http://www.dableducational.org/. Dabl Educational, 2023.

[115] G. D. Iannetti and Richard G. Wise. BOLD functional MRI in disease and pharmacological studies: room for improvement? *Magnetic Resonance Imaging*, 25(6):978–988, 2007.

[116] K. Ide, F. Pott, J. J. Van Lieshout, and N. H. Secher. Middle cerebral

artery blood velocity depends on cardiac output during exercise with a large muscle mass. *Acta Physiologica Scandinavica*, 162(1):13–20, 1998.

[117] Louis J. Ignarro. After 130 years, the molecular mechanism of action of nitroglycerin is revealed. *Proceedings of the National Academy of Sciences of the United States of America*, 99(12):7816–7817, 2002.

[118] Ben P.M. Imholz, Wouter Wieling, Gert A. Van Montfrans, and Karel H. Wesseling. Fifteen years experience with finger arterial pressure monitoring: Assessment of the technology. *Cardiovascular Research*, 38(3):605–616, 1998.

[119] Shoji Ito, Alexandra Mardimae, Jay Han, James Duffin, Greg Wells, Ludwik Fedorko, Leonid Minkovich, Rita Katznelson, Massimiliano Meineri, Tamara Arenovich, Cathie Kessler, and Joseph A. Fisher. Non-invasive prospective targeting of arterial PCO2 in subjects at rest. *Journal of Physiology*, 586(15):3675–3682, 2008.

[120] Hesamoddin Jahanian, Douglas C. Noll, and Luis Hernandez-Garcia. B 0 field inhomogeneity considerations in pseudo-continuous arterial spin labeling (pCASL): Effects on tagging efficiency and correction strategy. *NMR in Biomedicine*, 24(10):1202–1209, 2011.

[121] Andy Jahn. *Andy's Brain Book*. University of Michigan, Michigan, 2024.

[122] Mark Jenkinson, Peter Bannister, Michael Brady, and Stephen Smith. Improved Optimization for the Robust and Accurate Linear Registration and Motion Correction of Brain Images. *NeuroImage*, 17(2):825–841, 2002.

[123] Mark Jenkinson, Christian F Beckmann, Timothy E J Behrens, Mark W Woolrich, and Stephen M Smith. FSL. *NeuroImage*, 62:782–790, 2012.

[124] Andreas Kastrup, Johannes Dichgans, Matthias Niemeier, and Martin Schabet. Changes of cerebrovascular CO2 reactivity during normal aging. *Stroke*, 29(7):1311–1314, 1998.

[125] Samira M. Kazan, Siawoosh Mohammadi, Martina F. Callaghan, Guillaume Flandin, Laurentius Huber, Robert Leech, Aneurin Kennerley, Christian Windischberger, and Nikolaus Weiskopf. Vascular autorescaling of fMRI (VasA fMRI) improves sensitivity of population studies: A pilot study. *NeuroImage*, 124:794–805, 2016.

[126] Kimbra Kenney, Franck Amyot, Margalit Haber, Angela Pronger, Tanya Bogoslovsky, Carol Moore, and Ramon Diaz-Arrastia. Cerebral Vascular Injury in Traumatic Brain Injury. *Experimental Neurology*, 275:353–366, 2016.

[127] Ancel Keys, Flaminio Fidanza, Martti J. Karvonen, Noburu Kimura, and Henry L. Taylor. Indices of relative weight and obesity. *International Journal of Epidemiology*, 43(3):655–665, 1972.

[128] Connor C. ; Adnan-Ghufran;Schaller Derek J. Kim, Kyle H.;Kerndt. *Nitroglycerin*. StatPearls Publishing, Treasure Island (FL), 2023.

[129] Seong-Gi -G Kim. Quantification of relative cerebral blood flow change by flow-sensitive alternating inversion recovery (FAIR) technique: Application to functional mapping. *Magnetic Resonance in Medicine*, 34(3):293–301, 1995.

[130] Kenneth K. Kwong, John W. Belliveau, David A. Chesler, Inna E. Goldberg, Robert M. Weisskoff, Bridgitte P. Poncelet, David N. Kennedy, Bernice E. Hoppel, Mark S. Cohen, Robert Turner, Hong-Ming Cheng, Thomas J. Brady, and Bruce R. Rosen. Dynamic magnetic resonance

imaging of human brain activity during primary sensory stimulation. *Proc Natl Acad Sci USA*, 89:5675–5679, 1992.

[131] G. J. Langewouters, J. J. Settels, R. Roelandt, and K. H. Wesseling. Why use Finapres or Portapres rather than intra-arterial or intermittent non-invasive techniques of blood pressure measurement? *Journal of Medical Engineering and Technology*, 22(1):37–43, 1998.

[132] So Mi Lee, Soonhak Kwon, and Yun Jeong Lee. Diagnostic usefulness of arterial spin labeling in MR negative children with new onset seizures. *Seizure*, 65(January):151–158, 2019.

[133] Boris Leistedt and Jason D. McEwen. Exact wavelets on the ball. *IEEE Transactions on Signal Processing*, 60(12):6257–6269, 2012.

[134] Harald Lemke, Ana Gómez Carrillo de Castro, Peter Schlattmann, Isabella Heuser, and Peter Neu. Cerebrovascular reactivity over time-course - From major depressive episode to remission. *Journal of Psychiatric Research*, 44(3):132–136, 2010.

[135] T. K. Len and J. P. Neary. Cerebrovascular pathophysiology following mild traumatic brain injury. *Clinical Physiology and Functional Imaging*, 31(2):85–93, 2011.

[136] Renata F. Leoni, Kelley C. Mazzetto-Betti, Afonso C. Silva, Antonio C. dos Santos, Draulio B. de Araujo, João P. Leite, and Octavio M. Pontes-Neto. Assessing Cerebrovascular Reactivity in Carotid Steno-Occlusive Disease Using MRI BOLD and ASL Techniques. *Radiology Research and Practice*, 2012:1–10, 2012.

[137] Oleg Leontiev, David J. Dubowitz, and Richard B. Buxton. CBF/CMRO2 Coupling Measured with Calibrated-BOLD fMRI: Sources of Bias.

Neuroimage, 36(4):1110–1122, 2007.

[138] Thomas Lindner, Divya S. Bolar, Eric Achten, Frederik Barkhof, António J. Bastos-Leite, John A. Detre, Xavier Golay, Matthias Günther, Danny J.J. Wang, Sven Haller, Silvia Ingala, Hans R. Jäger, Geon Ho Jahng, Meher R. Juttukonda, Vera C. Keil, Hirohiko Kimura, Mai Lan Ho, Maarten Lequin, Xin Lou, Jan Petr, Nandor Pinter, Francesca B. Pizzini, Marion Smits, Magdalena Sokolska, Greg Zaharchuk, and Henk J.M.M. Mutsaerts. Current state and guidance on arterial spin labeling perfusion MRI in clinical neuroimaging. *Magnetic Resonance in Medicine*, 89(5):2024–2047, 2023.

[139] S. Lindskog and J. E. Coleman. The catalytic mechanism of carbonic anhydrase. *Proceedings of the National Academy of Sciences of the United States of America*, 70(9):2505–2508, 1973.

[140] Chin Fu Liu, Johnny Hsu, Xin Xu, Ganghyun Kim, Shannon M. Sheppard, Erin L. Meier, Michael I. Miller, Argye E. Hillis, and Andreia V. Faria. Digital 3D Brain MRI Arterial Territories Atlas. *Scientific Data*, 10(1):1–17, 2023.

[141] Peiying Liu, Jill B. De Vis, and Hanzhang Lu. Cerebrovascular reactivity (CVR) MRI with CO2 challenge: A technical review. *NeuroImage*, 187(November 2017):104–115, 2019.

[142] P. Lundborg and B. Steen. Plasma Levels and Effect on Heart Rate and Blood Pressure of Metoprolol after Acute Oral Administration in 12 Geriatric Patients. *Acta Medica Scandinavica*, 200(1-6):397–402, 1976.

[143] Nasim Maleki. Optimization of background suppression for arterial spin labeling perfusion imaging. *NIH Public Access*, 25(2):127–133, 2012.

[144] Daniel M. Mandell, Jay S. Han, Julien Poublanc, Adrian P. Crawley, Andrea Kassner, Joseph A. Fisher, and David J. Mikulis. Selective reduction of blood flow to white matter during hypercapnia corresponds with leukoaraiosis. *Stroke*, 39(7):1993–1998, 2008.

[145] M. Z. Mariyaselvam, R. E. Heij, D. Laba, J. A. Richardson, E. J. Hodges, C. A. Maduakor, J. J. Carter, and P. J. Young. Description of a new non-injectable connector to reduce the complications of arterial blood sampling. *Anaesthesia*, 70(1):51–55, 2015.

[146] Clarisse I. Mark, Marat Slessarev, Shoji Ito, Jay Han, Joseph A. Fisher, and G. Bruce Pike. Precise control of end-tidal carbon dioxide and oxygen improves BOLD and ASL cerebrovascular reactivity measures. *Magnetic Resonance in Medicine*, 64(3):749–756, 2010.

[147] Michael Markl and Jochen Leupold. Gradient echo imaging. *Journal of Magnetic Resonance Imaging*, 35(6):1274–1289, 2012.

[148] Vasilis Z. Marmarelis. Identification of nonlinear biological systems using laguerre expansions of kernels. *Annals of Biomedical Engineering*, 21(6):573–589, 1993.

[149] Andrew R. Mayer, Trent Toulouse, Stefan Klimaj, Josef M. Ling, Amanda Pena, and Patrick S.F. Bellgowan. Investigating the properties of the hemodynamic response function after mild traumatic brain injury. *Journal of Neurotrauma*, 31(2):189–197, 2014.

[150] J. Mazziotta, A. Toga, A. Evans, P. Fox, J. Lancaster, K. Zilles, R. Woods, T. Paus, G. Simpson, B. Pike, C. Holmes, L. Collins, P. Thompson, D. MacDonald, M. Iacoboni, T. Schormann, K. Amunts, N. Palomero-Gallagher, S. Geyer, L. Parsons, K. Narr, N. Kabani,

G. Le Goualher, D. Boomsma, T. Cannon, R. Kawashima, and B. Mazoyer. A probabilistic atlas and reference system for the human brain: International Consortium for Brain Mapping (ICBM). *Philosophical Transactions of the Royal Society B: Biological Sciences*, 356(1412):1293–1322, 2001.

[151] James McCarthy. FSLeyes, 2022.

[152] John Mcfadden, Julian Matthews, Lauren Scott, Karl Herholz, Ben Dickie, Hamied Haroon, Oliver Sparasci, Saadat Ahmed, Natalia Kyrtata, and Hedley C A Emsley. Oxygen Extraction Fraction is higher in elderly participants with a higher cardiovascular disease risk; a combined QSM and ASL study. (Table 2):21–23, 2025.

[153] David J. Mikulis, Gregory Krolczyk, Hubert Desal, William Logan, Gabrielle DeVeber, Peter Dirks, Michael Tymianski, Adrian Crawley, Alex Vesely, Andrea Kassner, David Preiss, Ron Somogyi, and Joseph A. Fisher. Preoperative and postoperative mapping of cerebrovascular reactivity in moyamoya disease by using blood oxygen level-dependent magnetic resonance imaging. *Journal of Neurosurgery*, 103(2):347–355, 2005.

[154] Colette Milbourn and Nicholas Blockley. Improving measures of cerebrovascular reactivity using a sinusoidal hypercapnic challenge and dual-echo pseudocontinuous ASL. *Joint Annual Meeting ISMRM-ESMRMB ISMRT 31st Annual Meeting*, pages 2021–2023, 2022.

[155] Colette Milbourn, Seyedmohammad Shams, and Jean Chen. Age-related differences in dynamic cerebrovascular reactivity based on CO2-response modelling. *2023 ISMRM & ISMRT Annual Meeting*, pages 2022–2024, 2023.

[156] Colette C Milbourn, Thomas W Okell, and Nicholas P Blockley. Moving Towards Robust Quanti cation of Cerebrovascular Reactivity (CVR) using Pseudocontinuous Arterial Spin Labelling (pCASL) Step protocol used for Phase Contrast Velocity (PCV) measurements made in the main feeding arteries of the brain by alteri. pages 10–13, 2020.

[157] I. K. Moppett, R. W. Sherman, M. J. Wild, J. A. Latter, and R. P. Mahajan. Effects of norepinephrine and glyceryl trinitrate on cerebral haemodynamics: Transcranial Doppler study in healthy volunteers. *British Journal of Anaesthesia*, 100(2):240–244, 2008.

[158] Fiona C. Moreton, Krishna A. Dani, Colin Goutcher, Kevin O'Hare, and Keith W. Muir. Respiratory challenge MRI: Practical aspects. *NeuroImage: Clinical*, 11:667–677, 2016.

[159] Jason Morris, Ayoola O. Awosika, and Alexis Dunham. *Metoprolol*. 2023.

[160] John P. Mugler and James R. Brookeman. Three-dimensional magnetization-prepared rapid gradient-echo imaging (3D MP RAGE). *Magnetic Resonance in Medicine*, 15(1):152–157, 1990.

[161] Suresh D. Muthukumaraswamy, C. John Evans, Richard A.E. Edden, Richard G. Wise, and Krish D. Singh. Individual variability in the shape and amplitude of the BOLD-HRF correlates with endogenous GABAergic inhibition. *Human Brain Mapping*, 33(2):455–465, 2012.

[162] Henk J.M.M. Mutsaerts, Jan Petr, Paul Groot, Pieter Vandemaele, Silvia Ingala, Andrew D. Robertson, Lena Václavů, Inge Groote, Hugo Kuijf, Fernando Zelaya, Owen O'Daly, Saima Hilal, Alle Meije Wink, Ilse Kant, Matthan W.A. Caan, Catherine Morgan, Jeroen de Bresser, Elisabeth Lysvik, Anouk Schrantee, Astrid Bjørnebekk, Patricia Clement, Zahra

Shirzadi, Joost P.A. Kuijer, Viktor Wottschel, Udunna C. Anazodo, Dasja Pajkrt, Edo Richard, Reinoud P.H. Bokkers, Liesbeth Reneman, Mario Masellis, Matthias Günther, Bradley J. MacIntosh, Eric Achten, Michael A. Chappell, Matthias J.P. van Osch, Xavier Golay, David L. Thomas, Enrico De Vita, Atle Bjørnerud, Aart Nederveen, Jeroen Hendrikse, Iris Asllani, and Frederik Barkhof. ExploreASL: An image processing pipeline for multi-center ASL perfusion MRI studies. *NeuroImage*, 219(June), 2020.

[163] James Y Nazroo. Addressing inequalities in healthy life expectancy Future of an ageing population : evidence review. *Government Office for Science*, 2015.

[164] Kay Nehrke and Peter Börnert. DREAM-a novel approach for robust, ultrafast, multislice B1 mapping. *Magnetic Resonance in Medicine*, 68(5):1517–1526, 2012.

[165] J.D. Nguyen and H. Duong. *Anatomy, Head and Neck, Anterior, Common Carotid Arteries*. StatPearls [Internet], Treasure Island (FL), 2020.

[166] NHS. NHS GTN, 2024.

[167] NHS. NHS Metoprolol, 2024.

[168] NICE and BNF. Acetazolamide, 2025.

[169] Sei Nishida, Toshihiko Aso, Shigetoshi Takaya, Yuki Takahashi, Takayuki Kikuchi, Takeshi Funaki, Kazumichi Yoshida, Tomohisa Okada, Takeharu Kunieda, Kaori Togashi, Hidenao Fukuyama, and Susumu Miyamoto. Resting-state Functional Magnetic Resonance Imaging Identifies Cerebrovascular Reactivity Impairment in Patients

with Arterial Occlusive Diseases: A Pilot Study. *Clinical Neurosurgery*, 85(5):680–688, 2019.

[170] Nobel Prize Outreach AB 2025. The Nobel Prize in Physiology or Medicine 2003, 2003.

[171] James P.B. O'Connor, Jessica K.R. Boult, Yann Jamin, Muhammad Babur, Katherine G. Finegan, Kaye J. Williams, Ross A. Little, Alan Jackson, Geoff J.M. Parker, Andrew R. Reynolds, John C. Waterton, and Simon P. Robinson. Oxygen-enhanced MRI accurately identifies, quantifies, and maps tumor hypoxia in preclinical cancer models. *Cancer Research*, 76(4):787–795, 2016.

[172] S. OGAWA, T. M. LEE, A. R. KAY, and TANK D. W. T. Brain magnetic resonance imaging with contrast dependent on bloodoxygenation. *Proc Natl Acad Sci U S A*, 87:9868–9872, 1990.

[173] Gbenga Ogedegbe and Thomas Pickering. Principles and Techniques of Blood Pressure Measurement. *Cardiology Clinics*, 28(4):571–586, 2010.

[174] S. Ogoh, M. K. Dalsgaard, N. H. Secher, and P. B. Raven. Dynamic blood pressure control and middle cerebral artery mean blood velocity variability at rest and during exercise in humans. *Acta Physiologica*, 191(1):3–14, 2007.

[175] Thomas W. Okell, Meritxell Garcia, Michael A. Chappell, James V. Byrne, and Peter Jezzard. Visualizing artery-specific blood flow patterns above the circle of Willis with vessel-encoded arterial spin labeling. *Magnetic Resonance in Medicine*, 81(3):1595–1604, 2019.

[176] Aaron Oliver-taylor, Thomas Hampshire, Nadia A S Smith, Michael Stritt, Jan Petr, Johannes Gregori, Matthias Günther, Henk J Mutsaerts,

and Xavier Golay. ASLDRO: Digital reference object software for Arterial Spin Labelling. *Proceedings of International Society for Magnetic Resonance In Medicine 2022*, 2022.

[177] Jérémie Papassin, Olivier Heck, Eric Condamine, Johan Pietras, Olivier Detante, and Alexandre Krainik. Impaired cerebrovascular reactivity is associated with recurrent stroke in patients with severe intracranial arterial stenosis: A C02 BOLD fMRI study. *Journal of Neuroradiology*, 2020.

[178] Andre M. Paschoal, Joseph G. Woods, Joana Pinto, Esther E. Bron, Jan Petr, Flora A. Kennedy McConnell, Laura Bell, Maria Eleni Dounavi, Cassandra Gould van Praag, Henk J.M.M. Mutsaerts, Aaron Oliver Taylor, Moss Y. Zhao, Irène Brumer, Wei Siang Marcus Chan, Jack Toner, Jian Hu, Logan X. Zhang, Catarina Domingos, Sara P. Monteiro, Patrícia Figueiredo, Alexander G.J. Harms, Beatriz E. Padrela, Channelle Tham, Ahmed Abdalle, Paula L. Croal, and Udunna Anazodo. Reproducibility of arterial spin labeling cerebral blood flow image processing: A report of the ISMRM open science initiative for perfusion imaging (OSIPI) and the ASL MRI challenge. *Magnetic Resonance in Medicine*, 92(2):836–852, 2024.

[179] N.A.; Patterson. *Robust, non-parametric method to identify outliers and improve final yield and quality*. CS Mantech, Boston, 2012.

[180] K. T.S. Pattinson. Functional magnetic resonance imaging in anaesthesia research. *British Journal of Anaesthesia*, 111(6):872–876, 2013.

[181] Stephen J. Payne. *Cerebral Autoregulation*. Springer, 2016.

[182] J. Penaz, Albert A, Vogt W, and Hellig W. Photoelectric measurement

of blood pressure, volume and flow in the finger. In *Digest of the 10th International Conference on Medical and Biological Engineering*, page 104, Dresden, 1973. Dresden: International Federation for Medical and Biological Engineering, 1973.

[183] Esben Thade Petersen, Tchoyoson Lim, and Xavier Golay. Model-free arterial spin labeling quantification approach for perfusion MRI. *Magnetic Resonance in Medicine*, 55(2):219–232, 2006.

[184] Stefan K. Piechnik, Peter A. Chiarelli, and Peter Jezzard. Modelling vascular reactivity to investigate the basis of the relationship between cerebral blood volume and flow under CO2 manipulation. *NeuroImage*, 39(1):107–118, 2008.

[185] Jay J Pillai. Clinical utility of cerebrovascular reactivity mapping in patients with low grade gliomas. *World Journal of Clinical Oncology*, 2(12):397, 2011.

[186] Jay J. Pillai and D. J. Mikulis. Cerebrovascular reactivity mapping: An evolving standard for clinical functional imaging. *American Journal of Neuroradiology*, 36(1):7–13, 2015.

[187] Jay J. Pillai and Domenico Zacà. Comparison of BOLD cerebrovascular reactivity mapping and DSC MR perfusion imaging for prediction of neurovascular uncoupling potential in brain tumors. *Technology in Cancer Research and Treatment*, 11(4):361–374, 2012.

[188] Joana Pinto, Nicholas P Blockley, James W Harkin, and Daniel P Bulte. Modelling spatiotemporal dynamics of cerebral blood flow using multiple-timepoint arterial spin labelling MRI. *Frontiers in physiology*, 14(May):1142359, 2023.

[189] Benedikt A. Poser and Kawin Setsompop. Pulse sequences and parallel imaging for high spatiotemporal resolution MRI at ultra-high field. *Physiology & behavior*, 168(1):101–118, 2018.

[190] Julien Poublanc, Adrian P. Crawley, Olivia Sobczyk, Gaspard Montandon, Kevin Sam, Daniel M. Mandell, Paul Dufort, Lashmikumar Venkatraghavan, James Duffin, David J. Mikulis, and Joseph A. Fisher. Measuring cerebrovascular reactivity: The dynamic response to a step hypercapnic stimulus. *Journal of Cerebral Blood Flow and Metabolism*, 35(11):1746–1756, 2015.

[191] Marc J. Poulin and Peter A. Robbins. Indexes of flow and cross-sectional area of the middle cerebral artery using Doppler ultrasound during hypoxia and hypercapnia in humans. *Stroke*, 27(12):2244–2250, 1996.

[192] Prokopis C. Prokopiou, Kyle T.S. Pattinson, Richard G. Wise, and Georgios D. Mitsis. Modeling of dynamic cerebrovascular reactivity to spontaneous and externally induced CO2 fluctuations in the human brain using BOLD-fMRI. *NeuroImage*, 186(June 2018):533–548, 2019.

[193] Prokopis C. Prokopiou, Alba Xifra-Porxas, Michalis Kassinopoulos, Marie Hélène Boudrias, and Georgios D. Mitsis. Modeling the Hemodynamic Response Function Using EEG-fMRI Data During Eyes-Open Resting-State Conditions and Motor Task Execution. *Brain Topography*, 35(3):302–321, 2022.

[194] Klaas P. Pruessmann, Markus Weiger, Markus B. Scheidegger, and Peter Boesiger. SENSE: Sensitivity encoding for fast MRI. *Magnetic Resonance in Medicine*, 42(5):952–962, 1999.

[195] E. M. Purcell. To th tor. *Phys. Rev*, 69(681):681, 1946.

[196] Qin Qin and Peter C.M. van Zijl. Velocity-selective-inversion prepared arterial spin labeling. *Magnetic Resonance in Medicine*, 76(4):1136–1148, 2016.

[197] Lambert Adolphe Quételet. Sur l'homme et le développement de ses facultés ou Essai de physique sociale. Tome seconde. *Paris: Bachelier*, 44(0):327, 1835.

[198] D. Rangaprakash, Reza Tadayonnejad, Gopikrishna Deshpande, Joseph O'Neill, and Jamie D. Feusner. FMRI hemodynamic response function (HRF) as a novel marker of brain function: applications for understanding obsessive-compulsive disorder pathology and treatment response. *Brain Imaging and Behavior*, 15(3):1622–1640, 2021.

[199] Harshan Ravi, Peiying Liu, Shin Lei Peng, Hanli Liu, and Hanzhang Lu. Simultaneous multi-slice (SMS) acquisition enhances the sensitivity of hemodynamic mapping using gas challenges. *NMR in Biomedicine*, 29(11):1511–1518, 2016.

[200] Harshan Ravi, Binu P. Thomas, Shin Lei Peng, Hanli Liu, and Hanzhang Lu. On the optimization of imaging protocol for the mapping of cerebrovascular reactivity. *Journal of Magnetic Resonance Imaging*, 43(3):661–668, 2016.

[201] Diego San Millán Ruiz, Bradley P. Barnett, and Philippe Gailloud. Craniocervical Vascular Anatomy. *Image-Guided Interventions: Expert Radiology Series, Third Edition*, pages 454–472, 1 2020.

[202] Simone Scardapane, Steven Van Vaerenbergh, Simone Totaro, and Aurelio Uncini. Kafnets: Kernel-based non-parametric activation functions for neural networks. *Neural Networks*, 110:19–32, 2019.

[203] Axel Schäfer and Jan Vagedes. How accurate is pulse rate variability as an estimate of heart rate variability?: A review on studies comparing photoplethysmographic technology with an electrocardiogram. *International Journal of Cardiology*, 166(1):15–29, 2013.

[204] F. Schmitt, D. Grosu, C. Mohr, D. Purdy, K. Salem, K. T. Scott, and B. Stoeckel. 3 Tesla MRI: Successful results with higher field strengths. *Radiologe*, 44(1):31–48, 2004.

[205] A. E. Schutte, H. W. Huisman, J. M. Van Rooyen, N. T. Malan, and R. Schutte. Validation of the Finometer device for measurement of blood pressure in black women. *Journal of Human Hypertension*, 18(2):79–84, 2004.

[206] Seyedmohammad Shams, Prokopis Prokopiou, Azin Esmaelbeigi, Georgios D. Mitsis, and J. Jean Chen. Modeling the dynamics of cerebrovascular reactivity to carbon dioxide in fMRI under task and resting-state conditions. *NeuroImage*, 265(November 2022):119758, 2023.

[207] Seyyed Mohammad Shams, Gholam Ali Hossein-Zadeh, and Hamid Soltanian-Zadeh. Multisubject activation detection in fMRI by testing correlation of data with a signal subspace. *Magnetic Resonance Imaging*, 24(6):775–784, 2006.

[208] Saba Shirvani, Paweł Tokarczuk, Ben Statton, Marina Quinlan, Alaine Berry, James Tomlinson, Peter Weale, Bernd Kühn, and Declan P. O'Regan. Motion-corrected multiparametric renal arterial spin labelling at 3 T: reproducibility and effect of vasodilator challenge. *European Radiology*, 29(1):232–240, 2019.

[209] Robert G. Shulman, Douglas L. Rothman, Kevin L. Behar, and Fahmeed

Hyder. Energetic basis of brain activity: Implications for neuroimaging. *Trends in Neurosciences*, 27(8):489–495, 2004.

[210] B. Silke and D. McAuley. Accuracy and precision of blood pressure determination with the Finapres: An overview using re-sampling statistics. *Journal of Human Hypertension*, 12(6):403–409, 1998.

[211] M. Skarpathiotakis, D. M. Mandell, R. H. Swartz, G. Tomlinson, and David J. Mikulis. Intracranial atherosclerotic plaque enhancement in patients with ischemic stroke. *American Journal of Neuroradiology*, 34(2):299–304, 2013.

[212] Sarah Louise Skirrow. Human forearm immobilisation: impact on muscle mass, function and glucose disposal. *PQDT - UK & Ireland*, (July), 2014.

[213] Emilie Sleight. Emilie Sleight Doctor in Philosophy The University of Edinburgh 2023. 2023.

[214] Emilie Sleight, Michael S. Stringer, Ian Marshall, Joanna M. Wardlaw, and Michael J. Thrippleton. Cerebrovascular Reactivity Measurement Using Magnetic Resonance Imaging: A Systematic Review. *Frontiers in Physiology*, 12(February), 2021.

[215] Marat Slessarev, Jay Han, Alexandra Mardimae, Eitan Prisman, David Preiss, George Volgyesi, Cliff Ansel, James Duffin, and Joseph A. Fisher. Prospective targeting and control of end-tidal CO2 and O2 concentrations. *Journal of Physiology*, 581(3):1207–1219, 2007.

[216] Stephen M. Smith. Fast robust automated brain extraction. *Human Brain Mapping*, 17(3):143–155, 2002.

[217] O. Sobczyk, A. Battisti-Charbonney, J. Fierstra, D. M. Mandell, J. Poublanc, A. P. Crawley, D. J. Mikulis, J. Duffin, and J. A. Fisher. A conceptual model for CO2-induced redistribution of cerebral blood flow with experimental confirmation using BOLD MRI. *NeuroImage*, 92:56–68, 2014.

[218] Mirian J. Starmans-Kool, Alice V. Stanton, Shunzhi Zhao, X. Yun Xu, Simon A.M. Thom, and Alun D. Hughes. Measurement of hemodynamics in human carotid artery using ultrasound and computational fluid dynamics. *Journal of Applied Physiology*, 92(3):957–961, 2002.

[219] C. P. Subbe, M. Kruger, P. Rutherford, and L. Gemmel. Validation of a modified early warning score in medical admissions. *QJM - Monthly Journal of the Association of Physicians*, 94(10):521–526, 2001.

[220] Cathie Sudlow, John Gallacher, Naomi Allen, Valerie Beral, Paul Burton, John Danesh, Paul Downey, Paul Elliott, Jane Green, Martin Landray, Bette Liu, Paul Matthews, Giok Ong, Jill Pell, Alan Silman, Alan Young, Tim Sprosen, Tim Peakman, and Rory Collins. UK Biobank: An Open Access Resource for Identifying the Causes of a Wide Range of Complex Diseases of Middle and Old Age. *PLoS Medicine*, 12(3):1–10, 2015.

[221] Sana Suri, Daniel Bulte, Scott T. Chiesa, Klaus P. Ebmeier, Peter Jezzard, Sebastian W. Rieger, Jemma E. Pitt, Ludovica Griffanti, Thomas W. Okell, Martin Craig, Michael A. Chappell, Nicholas P. Blockley, Mika Kivimäki, Archana Singh-Manoux, Ashraf W. Khir, Alun D. Hughes, John E. Deanfield, Daria E.A. Jensen, Sebastian F. Green, Veronika Sigutova, Michelle G. Jansen, Enikő Zsoldos, and Clare E. Mackay. Study Protocol: The Heart and Brain Study. *Frontiers in Physiology*, 12(March):1–19, 2021.

[222] Sana Suri, Scott T. Chiesa, Enikő Zsoldos, Clare E. Mackay, Nicola Filippini, Ludovica Griffanti, Abda Mahmood, Archana Singh-Manoux, Martin J. Shipley, Eric J. Brunner, Mika Kivimäki, John E. Deanfield, and Klaus P. Ebmeier. Associations between arterial stiffening and brain structure, perfusion, and cognition in the Whitehall II imaging sub-study: A retrospective cohort study. *PLoS Medicine*, 17(12):1–19, 2020.

[223] Yuriko Suzuki, Patricia Clement, Weiying Dai, Sudipto Dolui, Maria Fernández-Seara, Thomas Lindner, Henk JMM Mutsaerts, Jan Petr, Xingfeng Shao, Manuel Taso, and David L Thomas. ASL lexicon and reporting recommendations: A consensus report from the ISMRM Open Science Initiative for Perfusion Imaging (OSIPI). *Magn, Reson Med.*, 2023.

[224] S. Lalith Talagala, Frank Q. Ye, Patrick J. Ledden, and Scott Chesnick. Whole-brain 3D perfusion MRI at 3.0 T using CASL with a separate labeling coil. *Magnetic Resonance in Medicine*, 52(1):131–140, 2004.

[225] Felipe B. Tancredi, Claudine J. Gauthier, Cécile Madjar, Divya S. Bolar, Joseph A. Fisher, Danny J.J. Wang, and Richard D. Hoge. Comparison of pulsed and pseudocontinuous arterial spin-labeling for measuring CO2-induced cerebrovascular reactivity. *Journal of Magnetic Resonance Imaging*, 36(2):312–321, 2012.

[226] Alexei Taylor, Fengqing Zhang, Xin Niu, Ashley Heywood, Jane Stocks, Gangyi Feng, Karteek Popuri, Mirza Faisal Beg, and Lei Wang. Investigating the temporal pattern of neuroimaging-based brain age estimation as a biomarker for Alzheimer's Disease related neurodegeneration. *NeuroImage*, 263, 2022.

[227] Amanda J. Taylor, Jung Hwan Kim, and David Ress. Characterization of the hemodynamic response function across the majority of human

cerebral cortex. *NeuroImage*, 173(March):322–331, 2018.

[228] Wouter M. Teeuwisse, Sophie Schmid, Eidrees Ghariq, Ilya M. Veer, and Matthias J.P. Van Osch. Time-encoded pseudocontinuous arterial spin labeling: Basic properties and timing strategies for human applications. *Magnetic Resonance in Medicine*, 72(6):1712–1722, 2014.

[229] Eric Peter Thelin, Tamara Tajsic, Frederick Adam Zeiler, David K. Menon, Peter J.A. Hutchinson, Keri L.H. Carpenter, Maria Cristina Morganti-Kossmann, and Adel Helmy. Monitoring the neuroinflammatory response following acute brain injury. *Frontiers in Neurology*, 8(JUL):1–14, 2017.

[230] Binu P. Thomas, Uma S. Yezhuvath, Benjamin Y. Tseng, Peiying Liu, Benjamin D. Levine, Rong Zhang, and Hanzhang Lu. Life-long aerobic exercise preserved baseline cerebral blood flow but reduced vascular reactivity to CO2. *Journal of Magnetic Resonance Imaging*, 38(5):1177–1183, 2013.

[231] Adam L. Urback, Bradley J. MacIntosh, and Benjamin I. Goldstein. Cerebrovascular reactivity measured by functional magnetic resonance imaging during breath-hold challenge: A systematic review. *Neuroscience and Biobehavioral Reviews*, 79(May):27–47, 2017.

[232] Adam L. Urback, Arron W.S. Metcalfe, Daphne J. Korczak, Bradley J. MacIntosh, and Benjamin I. Goldstein. Reduced cerebrovascular reactivity among adolescents with bipolar disorder. *Bipolar Disorders*, 21(2):124–131, 2019.

[233] Lena Vaclavu, Magdalena Sokolska, Aart J Nederveen, and David L Thomas. Accounting for pCASL labelling efficiency variation in

patients with low and high arterial blood flow velocities. *Proceedings of International Society for Magnetic Resonance In Medicine*, pages 1–3, 2018.

[234] Nederveen AJ Thomas DL. Vaclavu L, Sokolska M. Accounting for pCASL labelling efficiency variation in patients with low and high arterial blood flow velocities. *Proc. Intl. Soc. Mag. Reson. Med.*, 26:#5530, 2008.

[235] Achala S. Vagal, J. L. Leach, M. Fernandez-Ulloa, and M. Zuccarello. The acetazolamide challenge: Techniques and applications in the evaluation of chronic cerebral ischemia. *American Journal of Neuroradiology*, 30(5):876–884, 2009.

[236] Pierre François Van de Moortele, Josef Pfeuffer, Gary H. Glover, Kamil Ugurbil, and Xiaoping Hu. Respiration-induced Bo fluctuations and their spatial distribution in the human brain at 7 Tesla. *Magnetic Resonance in Medicine*, 47(5):888–895, 2002.

[237] Merlijn C.E. van der Plas, Martin Craig, Sophie Schmid, Michael A. Chappell, and Matthias J.P. van Osch. Validation of the estimation of the macrovascular contribution in multi-timepoint arterial spin labeling MRI using a 2-component kinetic model. *Magnetic resonance in medicine*, 87(1):85–101, 1 2022.

[238] Federico von Samson-Himmelstjerna, Vince Istvan Madai, Jan Sobesky, and Matthias Guenther. Walsh-ordered hadamard time-encoded pseudocontinuous ASL (WH pCASL). *Magnetic Resonance in Medicine*, 76(6):1814–1824, 2016.

[239] Ahmet Vural and Esin Derin Çiçek. Is the asymmetry between the vertebral arteries related to cerebral dominance? *Turkish Journal of*

Medical Sciences, 49(6):1721–1726, 2019.

[240] Danny J.J. Wang, Jeffry R. Alger, Joe X. Qiao, Matthias Gunther, Whitney B. Pope, Jeffrey L. Saver, Noriko Salamon, and David S. Liebeskind. Multi-delay multi-parametric arterial spin-labeled perfusion MRI in acute ischemic stroke - Comparison with dynamic susceptibility contrast enhanced perfusion imaging. *NeuroImage: Clinical*, 3:1–7, 2013.

[241] Jiongjiong Wang, Geoffrey K. Aguirre, Daniel Y. Kimberg, Anne C. Roc, Lin Li, and John A. Detre. Arterial spin labeling perfusion fMRI with very low task frequency. *Magnetic Resonance in Medicine*, 49(5):796–802, 2003.

[242] S. Wang, I. Z. Wang, J. C. Bulacio, C. J. Mosher, J. Gonzalez-Martinez, A. V. Alexopoulos, I. M. Najm, and K. N. So. Ripple classification helps to localize the seizure-onset zone in neocortical epilepsy. *Epilepsia*, 54(370–376), 2013.

[243] J. C.K. Wells. A Hattori chart analysis of body mass index in infants and children. *International Journal of Obesity*, 24(3):325–329, 2000.

[244] Jack A. Wells, Mark F. Lythgoe, David G. Gadian, Roger J. Ordidge, and David L. Thomas. In vivo Hadamard encoded Continuous arterial spin labeling (H-CASL). *Magnetic Resonance in Medicine*, 63(4):1111–1118, 2010.

[245] Karel H. Wesseling, Jos J. Settels, Gerard M.A.Van Der Hoeven, Jannes A. Nijboer, Michelle W.T. Butijn, and Joop C. Dorlas. Effects of peripheral vasoconstriction on the measurement of blood pressure in a finger. *Cardiovascular Research*, 19(3):139–145, 1985.

[246] John B. West. A Web-based course of lectures in respiratory physiology. *American Journal of Physiology - Advances in Physiology Education*, 35(3):249–251, 2011.

[247] Christina E. Wierenga, Chelsea C. Haysa, and Zvinka Z. Zlatara. Cerebral Blood Flow Measured by Arterial Spin Labeling MRI as a Preclinical Marker of Alzheimer's Disease. *J Alzheimers Dis.*, 42(1):1S411–S419, 2014.

[248] Donald S. Williams, Weiguo Zhang, Alan P. Koretsky, and Sheldon Adler. Perfusion imaging of the rat kidney with MR. *Radiology*, 190(3):813–818, 1994.

[249] Richard G. Wise, Kojiro Ide, Marc J. Poulin, and Irene Tracey. Resting fluctuations in arterial carbon dioxide induce significant low frequency variations in BOLD signal. *NeuroImage*, 21(4):1652–1664, 2004.

[250] Eric C. Wong. Vessel-encoded arterial spin-labeling using pseudocontinuous tagging. *Magnetic Resonance in Medicine*, 58(6):1086–1091, 2007.

[251] Joseph G. Woods, Eric Achten, Iris Asllani, Divya S. Bolar, Weiying Dai, John A. Detre, Audrey P. Fan, María A. Fernández-Seara, Xavier Golay, Matthias Günther, Jia Guo, Luis Hernandez-Garcia, Mai Lan Ho, Meher R. Juttukonda, Hanzhang Lu, Bradley J. MacIntosh, Ananth J. Madhuranthakam, Henk Jan Mutsaerts, Thomas W. Okell, Laura M. Parkes, Nandor Pinter, Joana Pinto, Qin Qin, Marion Smits, Yuriko Suzuki, David L. Thomas, Matthias J.P. Van Osch, Danny J.J. Wang, Esther A.H. Warnert, Greg Zaharchuk, Fernando Zelaya, Moss Zhao, and Michael A. Chappell. Recommendations for quantitative cerebral perfusion MRI using multi-timepoint arterial spin labeling: Acquisition,

quantification, and clinical applications. *Magnetic Resonance in Medicine*, 92(2):469–495, 2024.

[252] Mark W. Woolrich, Brian D. Ripley, Michael Brady, and Stephen M. Smith. Temporal autocorrelation in univariate linear modeling of FMRI data. *NeuroImage*, 14(6):1370–1386, 2001.

[253] Guo Rong Wu, Wei Liao, Sebastiano Stramaglia, Ju Rong Ding, Huafu Chen, and Daniele Marinazzo. A blind deconvolution approach to recover effective connectivity brain networks from resting state fMRI data. *Medical Image Analysis*, 17(3):365–374, 2013.

[254] Yang Ji, Joseph G. Woods, Hongwei Li, and Thomas W. Okell. Dynamic B0 field shimming for improving pseudo-continuous arterial spin labeling at 7 Tesla. *Centre for Integrative Neuroimaging*, (July 2024):1674–1689, 2024.

[255] Harumi Yoshinaga, Tomoyuki Nakahori, Yoko Ohtsuka, Eiji Oka, Yoshihiro Kitamura, Hideki Kiriyama, Kazumasa Kinugasa, Keiichi Miyamoto, and Toru Hoshida. Benefit of simultaneous recording of EEG and MEG in dipole localization. *Epilepsia*, 43(8):924–928, 2002.

[256] Logan X. Zhang, Joseph G. Woods, Thomas W. Okell, and Michael A. Chappell. Examination of optimized protocols for pCASL: Sensitivity to macrovascular contamination, flow dispersion, and prolonged arterial transit time. *Magnetic Resonance in Medicine*, 86(4):2208–2219, 2021.

[257] Weiguo Zhang, Afonso C. Silva, Donald S. Williams, and Alan P. Koretsky. NMR Measurement of Perfusion Using Arterial Spin Labeling Without Saturation of Macromolecular Spins. *Magnetic Resonance in Medicine*, 33(3):370–376, 1995.

[258] Yongyue Zhang, Michael Brady, and Stephen Smith. Segmentation of brain MR images through a hidden Markov random field model and the expectation-maximization algorithm. *IEEE Transactions on Medical Imaging*, 20(1):45–57, 2001.

[259] Chenyang Zhao, Ze Wang, and Danny Wang. A digital brain perfusion phantom for validation of ASL data postprocessing software. pages 11–13, 2021.

[260] Li Zhao, Marta Vidorreta, Salil Soman, John A. Detre, and David C. Alsop. Improving the robustness of pseudo-continuous arterial spin labeling to off-resonance and pulsatile flow velocity. *Magnetic Resonance in Medicine*, 78(4):1342–1351, 2017.

[261] Moss Y. Zhao, Audrey P. Fan, David Yen Ting Chen, Yosuke Ishii, Mohammad Mehdi Khalighi, Michael Moseley, Gary K. Steinberg, and Greg Zaharchuk. Using arterial spin labeling to measure cerebrovascular reactivity in Moyamoya disease: Insights from simultaneous PET/MRI. *Journal of Cerebral Blood Flow and Metabolism*, 42(8):1493–1506, 2022.

[262] Moss Y. Zhao, Audrey P. Fan, David Yen Ting Chen, Magdalena J. Sokolska, Jia Guo, Yosuke Ishii, David D. Shin, Mohammad Mehdi Khalighi, Dawn Holley, Kim Halbert, Andrea Otte, Brittney Williams, Taghi Rostami, Jun Hyung Park, Bin Shen, and Greg Zaharchuk. Cerebrovascular reactivity measurements using simultaneous 15O-water PET and ASL MRI: Impacts of arterial transit time, labeling efficiency, and hematocrit. *NeuroImage*, 233(October 2020):117955, 2021.

[263] Moss Y. Zhao, Melvin Mezue, Andrew R. Segerdahl, Thomas W. Okell, Irene Tracey, Yingyi Xiao, and Michael A. Chappell. A systematic study of the sensitivity of partial volume correction methods for

the quantification of perfusion from pseudo-continuous arterial spin labeling MRI. *NeuroImage*, 162(August):384–397, 2017.

[264] Yongxia Zhou, Zachary B. Rodgers, and Anderson H. Kuo. Cerebrovascular reactivity measured with arterial spin labeling and blood oxygen level dependent techniques. *Magnetic Resonance Imaging*, 33(5):566–576, 2015.